Summer 8-13-2010

# Single Molecule investigations of DNA Looping Using the Tethered Particle Method and Translocation by Acto-Myosin Using Polarized Total Internal Reflection Fluorescence Microscopy

John F. Beausang

*University of Pennsylvania*, beausang@sas.upenn.edu

# Single Molecule investigations of DNA Looping Using the Tethered Particle Method and Translocation by Acto-Myosin Using Polarized Total Internal Reflection Fluorescence Microscopy

**Abstract**

Single molecule biophysics aims to understand biological processes by studying them at the single molecule level in real time. The proteins and nucleic acids under investigation typically exist in an aqueous environment within approximately ten degrees of room temperature. These seemingly benign conditions are actually quite chaotic at the nanoscale, where single bio-molecules perform their function. As a result, sensitive experiments and statistical analyses are required to separate the weak single molecule signal from its background. Protein-DNA interactions were investigated by monitoring DNA looping events in tethered particle experiments. A new analysis technique, called the Diffusive hidden Markov method, was developed to extract kinetic rate constants from experimental data without any filtering of the raw data; a common step that improves the signal to noise ratio, but at the expense of lower time resolution. In the second system, translocation of the molecular motor myosin along its actin filament track was studied using polarized total internal reflection (polTIRF) microscopy, a technique that determines the orientation and wobble of a single fluorophore attached to the bio-molecule of interest. The range of resolvable angles was increased 4-fold to include a hemisphere of possible orientations. As a result, the handedness of actin filament twirling as it translocated along a myosin-coated surface was determined to be left-handed. The maximum time resolution of a polTIRF setup was increased 50-fold, in part by recording the arrival times and polarization state of single photons using a modified time-correlated single photon counting device. A new analysis, the Multiple Intensity Change Point algorithm, was developed to detect changes in molecular orientation and wobble using the raw time-stamped data with no user-defined bins or thresholds. The analysis objectively identified changes in the orientation of a bifunctional-rhodamine labeled calmodulin that was attached to a myosin V molecule translocating along an actin filament. Long intervals corresponding to stable positions between tilting motions of the lever arm during each step were routinely observed. Substeps in the cycle that preceded these long dwells were measured, but only occasionally most likely because of the low number of photons detected during these rapid events.

**Degree Type**
Dissertation

**Degree Name**
Doctor of Philosophy (PhD)

**Graduate Group**
Physics & Astronomy

**First Advisor**
Philip C. Nelson

SINGLE MOLECULE INVESTIGATIONS OF DNA LOOPING USING THE

TETHERED PARTICLE METHOD AND TRANSLOCATION BY ACTO-MYOSIN

USING POLARIZED TOTAL INTERNAL REFLECTION FLUORESCENCE

MICROSCOPY

John F. Beausang

A DISSERTATION

in

Physics and Astronomy

Presented to the Faculties of the University of Pennsylvania in Partial
Fulfillment of the Requirements for the Degree of Doctor of Philosophy

2010

_____
Philip C. Nelson
Professor of Physics and Astronomy
Supervisor of Dissertation

_____
Yale E. Goldman
Professor of Physiology
Co-Supervisor

_____
Ravi Sheth
Associate Professor of Physics and Astronomy
Graduate Group Chairperson

Dissertation Committee
A. T. Charlie Johnson, Jr., Associate Professor of Physics and Astronomy
Mark Goulian, Associate Professor of Biology
E. Mike Ostap, Professor of Physiology

# Acknowledgments

There are many people that I would like to thank during my past six years at Penn. I am grateful to Chiara Zurla in Laura Finzi's lab at Emory for providing the tethered particle data, and to Rob Phillips at Caltech for suggesting to Phil that we analyze it using the hidden Markov method. I'd also like to thank Rob for numerous visits to his lab at Caltech, especially the Biological physics bootcamp. Seth Blumberg and Lin Han in his lab were particularly helpful in discussing results from tethered particle experiments.

I have been fortunate to work with so many excellent people in Yale's lab. Jody Dantzig-Brody was continuously helpful and ensured that the lab ran smoothly. I received lots of help from Travis Gorkin, Pritish Agarwal, and Pete Cianfrani on writing several LabView programs and building electronic circuits that made the myosin experiments possible. There would have been no protein to study if it wasn't for Xiaonan Cui, Huy Pham, Rama Khudaravalli and Tianming Lin (in Mike Ostap's lab). I benefitted from numerous conversations and assistance from the fellow graduate students and post docs in the lab: John Lewis, Trey Schroeder, and Yujie Sun. Also, Chris Mitchell was a big help with Westerns.

I was very fortunate to receive 3 years of funding from the Penn-Drexel IGERT, which I was very grateful for, as well as a Dissertation Completion Fellowship from SAS during my

last year.

I would especially like to thank my advisors Phil and Yale. I learned a tremendous amount and consider myself very fortunate to have been able to work with them both.

Lastly, I'd like to thank my family which has always been exceedingly supportive in everything I've pursued. Best of all during these last few years in Philadelphia, I met my wife, Dana, who has been more than I could ask for.

ABSTRACT

SINGLE MOLECULE INVESTIGATIONS OF DNA LOOPING USING THE TETHERED

PARTICLE METHOD AND TRANSLOCATION BY ACTO-MYOSIN USING POLARIZED TOTAL

INTERNAL REFLECTION FLUORESCENCE MICROSCOPY

John F. Beausang

Philip C. Nelson and Yale E. Goldman

Single molecule biophysics aims to understand biological processes by studying them at the single molecule level in real time. The proteins and nucleic acids under investigation typically exist in an aqueous environment within $\sim$ ten degrees of room temperature. These seemingly benign conditions are actually quite chaotic at the nanoscale, where single bio-molecules perform their function. As a result, sensitive experiments and statistical analyses are required to separate the weak single molecule signal from its background. Protein-DNA interactions were investigated by monitoring DNA looping events in tethered particle experiments. A new analysis technique, called the Diffusive hidden Markov method, was developed to extract kinetic rate constants from experimental data without any filtering of the raw data; a common step that improves the signal to noise ratio, but at the expense of lower time resolution. In the second system, translocation of the molecular motor myosin along its actin filament track was studied using polarized total internal reflection (polTIRF) microscopy, a technique that determines the orientation and wobble of a single fluorophore attached to the bio-molecule of interest. The range of resolvable angles was increased 4-fold to include a hemisphere of possible orientations. As a result, the handedness of actin filament twirling as it translocated along

a myosin-coated surface was determined to be left-handed. The maximum time resolution of a polTIRF setup was increased 50-fold, in part by recording the arrival times and polarization state of single photons using a modified time-correlated single photon counting device. A new analysis, the Multiple Intensity Change Point algorithm, was developed to detect changes in molecular orientation and wobble using the raw time-stamped data with no user-defined bins or thresholds. The analysis objectively identified changes in the orientation of a bifunctional-rhodamine labeled calmodulin that was attached to a myosin V molecule translocating along an actin filament. Long intervals corresponding to stable positions between tilting motions of the lever arm during each step were routinely observed. Substeps in the cycle that preceded these long dwells were measured, but only occasionally most likely because of the low number of photons detected during these rapid events.

# Contents

# Chapter 1

# Introduction

For over 20 years, researchers have been struggling to measure single molecules. Why? In many ways it is the logical next step in the scientific approach where complex systems are broken into smaller and smaller parts in order to understand how they work. In biology, single macromolecules such as nucleic acids and proteins are the fundamental building blocks that are responsible for many of the basic functions in a cell. For example, many forms of cell motility can be reduced to just two proteins: actin and myosin, which in the presence of ATP can produce force and movement relative to one another. Understanding how these two proteins work together helps explain the complex macroscopic phenomena that are built upon them.

Historically, experiments involving large numbers of molecules have always been studied from a statistical view that relied on determining the mean and variance of the ensemble of molecules. The single molecule approach instead aims to construct the distribution of molecules one at a time [1]; but in the end, the characterization of its mean and variance

should be the same as found from the ensemble approach. The difference, however, is that the properties and behavior of individual molecules can be studied and transient features such as short-lived states and rare, but important fluctuations that were lost in the ensemble average are revealed. In order to obtain such information in an ensemble experiment, techniques to synchronize a majority of molecules are required so that their collective signal can be measured during the short time before the random nature of the individual molecular processes dissipates the signal (see Reference [2] for examples).

Single molecule experiments differ from ensemble measurements in several key ways. In single molecule experiments, kinetics are directly measured by recording the trajectory of the molecule over time, where rare events and random fluctuations can be measured directly. Force is also a unique variable in many single molecule experiments that can be used to probe the function of motor proteins (i.e., their "mechanochemistry") or denature proteins in unfolding experiments. Single molecule experiments can provide a useful link that connects the extremely detailed, yet static structures from X-ray crystallography, cryo-EM and NMR with biochemical experiments that determine rates into a single picture, or more appropriately a movie, of how the molecule performs its function.

There are many excellent reviews of single molecule research, including reviews devoted to the sub-field of single molecule biophysics. Several good early reviews include References [1, 3, 4] and more recent ones by Greenleaf et al. [5] and Ritort [6] survey many of the current experimental tools and recent results. Numerous books reviewing the field are also available [7–10].

This introduction will review some of the landmark developments in single molecule bio-

physics with particular attention to the areas of DNA mechanics and the molecular motor myosin. Subsequent chapters begin with a separate introduction that reviews the background relevant for that section. The material presented here is intended to put those chapters into the wider context of the single molecule biophysics field. Next, non-fluorescence based single molecule experiments will be briefly summarized followed by a discussion of fluorescence based research.

### 1.0.1   Non-Fluorescence based single molecule experiments

The first experiment with single molecule sensitivity was performed by Neher and Sakmann in 1976 on the acetylcholine receptor using a current probe known as a patch clamp that measured the change in conductance as a single ion channel opened and closed [11]. Since this pioneering work, electrical measurements on single ion channels have developed into a separate field, nearly independent from the other areas of research that are typically grouped into the phrase "single molecule biophysics". This review will also focus on non-channel related single molecule experiments.

Outside of the ion channel field, non-fluorescence single molecule experiments awaited development of two key devices: the optical trap in 1970 [12] and the atomic force microscope (AFM)[1] in 1985 [13]. An optical trap consists of a laser beam that is focused on to a small spot, typically using a microscope objective in an aqueous medium. Small particles such as microspheres with diameter 0.1–1 $\mu$m and an index of refraction greater than water are confined to the focal point of the laser by the highly refracted beam. Arguably, 1987

---

[1]A glossary of common abbreviations can be found at the end of the manuscript

might be considered the first year for a single molecule biophysics experiment when Ashkin and Dziedzic [14] used an optical trap to capture and manipulate single bacteria and tobacco mosaic viruses, while viewing them in an optical microscope. Optical traps have since been used in countless biophysical experiments to exert 1-100 pN of force on individual biological molecules. For example, they have been used to unfold molecules such as titin [15] and exert forces on molecular motors such as kinesin [16], RNA polymerase [17], myosin [18], and the $\phi 29$ bacteriophage DNA packaging motor [19].

An AFM consists of a small cantilever with an extremely sharp tip that is scanned across a surface. Small deflections of the tip, due either to direct contact with the surface or indirect interactions with fields such as van der Waals forces, are magnified by a laser that is reflected from the back of the cantilever onto an optical sensor. AFM is traditionally considered a surface imaging device, but it can also be used to manipulate single molecules. Typical AFM experiments involve pulling one end of a molecule off of a surface and recording unfolding events in force-extension curves. Typically, AFMs operate at larger forces (20-10 000 pN) than optical traps. The classic example of an AFM pulling experiment is the unfolding of the gigantic muscle protein titin, which was first performed by Rief et al. [20] in 1997. Titin and other multi-domain proteins are well-suited for AFM pulling experiments because each domain unfolds sequentially, resulting in a repeatable pattern of events that can be distinguished from spurious interactions with the surface. Many proteins also reversibly refold as the force is reduced so that the process can be repeated multiple times with the same molecule. AFMs have since become one of the most widely used single molecule instruments [6].

**Single molecule investigations of DNA**

The first single molecule manipulation of DNA was by Chu in 1991 [21] when his lab used an optical trap to measure the elastic response of a DNA molecule attached to a bead. Shortly thereafter [22], the elasticity of single molecules of DNA in solution were investigated by attaching one end of the DNA to a surface and the other to a magnetic bead. Fluid flow or magnetic force could be used to stretch out the entropic elasticity and elongate the molecule with forces up to 30 pN. The resulting force-extension curves were in good agreement with the wormlike chain theory, which predicts the mechanical properties of the polymer assuming that adjacent segments are related by an elastic bending energy. A few years later, experiments were performed that pulled the DNA with higher forces into a nonlinear elastic regime where it was stretched to $\sim 1.7\times$ its original length at a constant force of $\sim 65$ pN using either a micropipette [23] or optical trap [24]. The influence of the DNA helix on its elasticity was investigated by twisting the DNA while pulling on it using a "magnetic tweezers" [25]. Similar to optical traps, a magnetic tweezer uses a magnetic field to control the orientation of a small magnetic bead attached to the free end of a surface-tethered DNA molecule. They determined that slightly unwinding the DNA helix dramatically reduced the amount of force required to disturb the DNA structure. This is relevant to biological molecules such as topoisomerases and helicases, which unwind DNA as part of their function and may utilize this asymmetry *in vivo*.

These experiments all investigated the role of force on DNA structure; a method to study DNA-protein interactions under no external load was developed in 1995 by Finzi and Gelles [26]. They observed the Brownian motion of a small bead attached to the microscope surface

via a DNA tether. The DNA contained a sequence from the lac operon, where a single repressor protein can simultaneously bind to the DNA at two distinct sites and form a loop. Loop formation shortened the DNA and abruptly changed the motion of the tethered particle. Dissociation of the protein allowed the loop to break, and the process to repeat at a rate dictated in part by the concentration of protein in solution. A new method to determine the kinetics of DNA loop formation and breakdown in tethered particle experiments is the subject of Sect. 2.

Recent high resolution AFM experiments of DNA adhered to a surface estimated the elastic properties of the DNA on the 5–100 nm length scale. They determined that DNA is more flexible at these short lengths than predicted by the wormlike chain model [27]. The elasticity of DNA at short length scales was also investigated using tethered particle experiments [28] by engineering the spacing between protein binding sites on the DNA so that only small loops, which theoretically have a prohibitively high bending energy, can form. Comparing the looping probability for different length loops, including comparison to a Monte Carlo simulation with no free parameters [29], indicated that short loops form more often than predicted by the wormlike chain model.

### 1.0.2   Fluorescence-based single molecule experiments

Several investigators [3,30] credit Hirschfeld [31] with detecting the first optical detection of a single molecule, an antibody labeled with 80-100 fluoresceine isothiocyanate, in 1976. Other early fluorescence measurements of single molecules included DNA [32] and cell surface receptors [33], in both cases each molecule of interest was decorated with $\sim 100$ fluorophores. In 1984, single actin filaments labeled with multiple rhodamine-phalloidin molecules were

observed using epifluorescence as they translocated on myosin-coated cover slips [34]; a technique now commonly referred to as a gliding filament assay. True single molecule sensitivity was first accomplished in 1989 by detecting a single fluorescence molecule of *p*-terphenyl embedded in a crystal at extremely low temperature (1.6 K), albeit by using an absorption measurement [35]. Using the same experimental system, the first fluorescence measurement with single molecule sensitivity was achieved a year later [36].

In the intervening years fluorescence has overwhelmingly become the preferred method for optical detection of single molecules. A major advance for eventual biological applications came in 1990 when the first single fluorophore was detected at room temperatures [37]. The experiment involved confocal detection of single fluorophores suspended in an aqueous environment; as the molecules transiently diffused into the small detection volume, a large burst of fluorescence was detected. This technique has evolved into the field of fluorescence correlation spectroscopy (FCS) [38]. A few years later, single fluorescence molecules, immobilized on a surface, were detected using near-field [39] and far-field [40, 41] scanning optical microscopy (SOM). These experiments were notable achievements, but they were not amenable to wide-spread biological research.

A more common biological tool is fluorescence microscopy, where single molecule detection was first achieved in wide-field epifluorescence in 1995 [30, 42]. Funatsu et al. [42] mentioned several steps that were necessary to obtain the reduction in background required to detect single molecules: choosing the proper combination of fluorophore and optical filters/dichroic; using low autofluorescence immersion oil and objectives; minimizing the amount of contaminating dust; and using low auto-fluorescence quartz instead of glass for cover slips

and/or microscope slides. These modifications reduced the background $\sim$ 40-fold, allowing them to detect single Cy3-labeled myosin molecules adhered to the surface using a sensitive CCD camera [42]. They reduced the background another $\sim$ 40-fold by using total internal reflection (TIR) illumination, which only excited a thin region of the sample close to the quartz surface. Combining TIR excitation with fluorescence microscopy (i.e., TIRF) and a fluorescent ATP analog, they were able to detect single hydrolysis events by a myosin molecule adhered to the surface [42]. Individual fluorescent molecules were also detected using a low-background epifluorescence microscope (without TIR), which was used in a gliding assay to measure the translocation of actin filaments sparsely labeled with single molecules of rhodamine [30]. These researchers also highlight the importance of optimizing the excitation light path and minimizing stray light that scatters in the microscope in order to achieve single molecule sensitivity.

In addition to imaging the position of single molecules, quantitative distance measurements between two molecules can be obtained by using Förster Resonance Energy Transfer (FRET), which entails the nonradiative transfer of energy between two different fluorophores that are spatially separated by only a few nanometers (i.e., the Förster radius, $R_0$). With this close configuration, excitation of the shorter wavelength fluorophore does not result in its fluorescence emission; instead, the energy is "transferred" to the longer wavelength fluorophore, which does emit its fluorescence. In a typical experiment, emission from the shorter wavelength fluorophore indicates that the two probes are more than the $R_0$ apart, whereas emission of the longer wavelength fluorophore indicates that the two probes are less than the $R_0$ apart; thus providing a quantitative distance measurement. FRET has been studied since the late

40's, and has been applied routinely to determine intermolecular distances in ensemble measurements [43]. The first demonstration of single molecule FRET was in 1996 [44], using near-field SOM to simultaneously measure the position and spectra of two closely spaced fluorophores. Since then it has become a standard single molecule tool for measuring short distances between two fluorophores, a "spectroscopic ruler" [45]. Advances in single molecule FRET are reviewed in Reference [46].

Recently, there has been a large increase in single molecule fluorescence experiments that exploit a loophole in the "diffraction limit" in order to image single fluorophores with nanometer accuracy. (The diffraction limit stipulates the minimum resolvable distance between two objects, not the localization of a single object.) One of the earliest examples of such nanometer localization were recordings of the hand-over-hand motion of a myosin V molecule "walking" on actin with steps several times smaller than the wavelength of light [47]. Combining nanometer localization with either controlled [48, 49] or random [50] fluorophore excitation and quenching has resulted in "super-resolution" images constructed by superimposing the precise location of thousands of fluorophores to build up an entire image with resolution below the diffraction limit of light. Such images promise to unlock numerous biological secrets that lie just beyond the limits of traditional light microscopy.

Other single molecule fluorescence strategies are being combined with nanometer localization including labeling molecules with inorganic fluorescent probes called quantum dots [51], which results in a slightly larger probe but a much brighter fluorescence signal. Three dimensional imaging of fluorophores has been achieved by introducing an asymmetry in the detected light path by, for example, splitting half of the image on to two focal planes [52] or introduc-

ing a cylindrical lens [53]. Lastly, a major development has been live cell imaging of single fluorescent molecules [54–56], where previous *in vitro* single molecule results can be tested in the more authentic environment of a cell. Next, a the sub-field of *polarized* single molecule fluorescence will be discussed.

### 1.0.3 Single molecule fluorescence polarization

A fluorescent molecule absorbs and emits light according to the electromagnetic properties of an oscillating dipole [43]. Consequently, it is excited preferentially by light that is polarized along its dipole axis, and its fluorescence emission is also polarized along its dipole axis. Utilizing these polarization properties of fluorescence at the ensemble level is a mature field [43]. In 1996, Ha et al., was the first to use polarized illumination in an epifluorescence microscope to measure the orientation of the in-plane component of a single fluorophore adhered to a surface in air with $0.2°$ accuracty [57]. In a follow-up study 2 years later the rotational dynamics of single fluorophores tethered to the surface by single-stranded DNA in an aqueous environment were investigated [58]. Molecules could be seen repeatedly adsorbing and releasing from the glass substrate, sometimes at a preferred orientation.

Sase et al. [59], added polarized detection to the sparsely-labeled gliding filament assay mentioned previously, and they were able to discern rotation of the actin filament about its axis as it translocated along myosin. The pitch of this twirling motion was much longer than the intrinsic pitch of the actin helix, supporting other results that showed that myosin only interacts with actin for a small fraction of the ATPase cycle. Warshaw et al. [60] exchanged rhodamine-labeled light chains onto smooth muscle myosin, and detected angle changes via

the polarized emission using a confocal fluorescence microscope. The fast time resolution in these experiments (1-10 ms) allowed them to measure a highly mobile state of the light chain when the myosin was detached from actin.

Forkey et al. [61] extended single molecule fluorescence polarization to TIRF microscopy (polTIRF), and determined the 3D orientation of the probe, not just its projection in the $x$-$y$ plane. Bifunctional-rhodamine labeled calmodulin were exchanged onto the myosin V lever arm, and angle changes were observed during translocation along actin. Quinlan et al. [62] used polTIRF to study the orientation of bifunctional-rhodamine labeled light chains on heavy meromyosin (HMM) and myosin subfragment-1 bound to actin in rigor. They confirmed that both heads of HMM are bound to adjacent actin monomers and under strain, similar to predictions from ensemble measurements. Forkey et al. [63] compared the orientation of fluorophores on sparsely labeled actin filaments with measurements of densely labeled filaments, and verified that the single molecule and ensemble approaches were consistent. They determined that the uncertainty of the angular estimates for $\theta$ and $\phi$ are $\sim 10°$ at 40 ms time resolution. Single molecule fluorescence polarization is reviewed in References [64, 65].

### 1.0.4  Overview

The following chapters in this thesis describe two new analysis tools for analyzing single molecule experiments and improvements to a polarized TIRF setup that were used to investigate acto-myosin translocation. Specifically, Chapter 2 develops a specialized hidden Markov method for determining the kinetics of DNA loop formation and breakdown in TPM experiments, without requiring any filtering of the raw data. Chapter 3 describes modifications to

the polTIRF apparatus described in References [61–63] that increase the range of discernable angles 4-fold, and then use it to determine the handedness of actin filament twirling in the gliding assay mentioned previously [59]. Chapter 4 describes a new analysis technique based on finding intensity change points in data where each photon's arrival time and polarization state is measured. In chapter 5, modifications to the polTIRF setup that increase the time resolution 50-fold compared to the experiments in Reference [61] are discussed, and the analysis from chapter 4 is used to identify substeps within the myosin V cycle as it translocates on actin. At the end is a glossary of some abbreviations encountered throughout the text.

# Chapter 2

# Diffusive Hidden Markov Method

## 2.1 Introduction

This chapter discusses a new technique (the Diffusive Hidden Markov Method, DHMM) for analyzing data from Tethered Particle Motion (TPM) experiments. The purpose of the method is to determine the kinetics of DNA loop formation and breakdown from the raw data with no additional binning or filtering nor any imposed thresholds or other external parameters. First background on DNA looping and TPM experiments are discussed, followed by a review of the existing TPM analysis methods. After showing that the standard HMM applied to the TPM raw data fails, the new DHMM approach is described, tested on simulated data, and applied to experimental looping data.

### 2.1.1 Biological motivation for DNA looping

Loops of DNA are an important feature in gene regulation. For example, in both eukaryotic and prokaryotic cells transcription factors bind DNA many base pairs away from the site of transcription initiation, yet they can influence transcription directly if a loop in the intervening DNA forms thereby bringing the two sites into physical contact [66]. Schleif [67] was the first to show DNA looping in the E. coli gene regulation of *ara*, but the phenomena is common in several of the classic networks including *gal*, *lac* and the *lambda* bacteriophage. The physical properties of the DNA and its helical structure are clearly important to the level of gene expression in some cases. For example, by varying the length of the DNA loop in the *lac* system over a wide range, Müller [68] showed a periodic 11-12 base pair phasing (the pitch of the DNA helix is 12.5 base pairs) in the levels of repression of *lac* promoter in E. coli when the DNA is in the looped state. Recently, Choi [69] showed that the kinetics of loop formation has a direct impact on gene expression and cell fate.

The role of looping in the lytic-lysogenic decision in *lambda* phage is a classic gene regulation system that has been extensively studied by TPM [70]. *lambda* is distinguished from other systems by a complex kinetic scheme involving 2 groups of 3 binding bites for the cI repressor protein. During lysogeny the phage is silently incorporated into the bacteria's DNA with cI repressor bound to each site, thereby preventing expression of genes required for mass virus replication and subsequent lysis of the bacteria. In this state the unlooped DNA results in continual expression of cI protein from a gene in the middle of the loop. In order to avoid this presumably wasteful expenditure of energy, at high cI concentrations a stable loop is formed between the two operators with as many as 12 cI repressor proteins in a single dodecamer

14

complex. In this work, data from tethered particle experiments (courtesy of the Finzi lab) using *lambda* DNA and cI repressor protein was used to develop and test the diffusive hidden Markov method.

## 2.1.2 Physical motivation for DNA looping

Since DNA is a semi-flexible polymer, its physical properties, such as elasticity and structure, play an important role in gene regulation. A simple but powerful model of DNA ignores the sequence information and treats the polymer as a linear elastic worm-like chain whose properties can be summarized by a single parameter, the persistence length. The persistence length is the maximum distance between two points along a polymer where the motion between the two points is coupled together by the elasticity of the polymer [71]. Loop formation is reduced at small lengths by a bending energy penalty and at long lengths by an entropic penalty for the two ends to find each other in space. Loop formation is energetically favorable due to the binding energy of repressor proteins [72] that stabilize the loop. More detailed models that include the 3D anisotropic elasticity due to the helical structure of DNA are required for some experiments that twist the DNA [73] or are sensitive to the orientation of a protein along the DNA [29]. Non-linear elastic models [27] have been proposed that may explain the high incidence of loop formation of DNA at short length scales where they are expected to be strongly suppressed by the large elastic bending energy. In some cases, incorporating the precise sequence dependence of the elasticity may be important [74]. Finally, more complex loop topologies due to DNA supercoiling may also play a role [75].

## 2.2 Tethered particle experiments

### 2.2.1 Overview of the experiments

Tethered particle motion (TPM) is an *in vitro* assay where single segments of a polymer, typically DNA, hundreds to thousands of base pairs long can be investigated with minimal external force. One end of the DNA is attached to a small particle such as a plastic bead or a small particle of gold and the other end is tethered to the surface of a microscope coverslip (Fig. 2.1). The 2D projected position of the particle is imaged through a microscope onto a CCD camera, and the restricted Brownian motion of multiple particles in a single field of view can be recorded for long periods of time (e.g., 30–60 minutes). Short camera exposure times minimize blurring in bead position and allow single particle tracking software to precisely localize the $(x, y)$ coordinate of the particle during each exposure. Some of the current implementations track multiple particles with 20–50 ms time and $\sim$10 nm spatial resolution, allowing rather precise determination of effective tether length from data [76–78]. Other current work observes a time-averaged image instead of using single particle tracking [79]. Even for short-timescale transitions, the long observations possible with TPM give an advantage, because the hidden Markov analysis discussed here can extract reliable information from long time series, even when it has low signal to noise ratio.

By using DNA from known gene regulatory systems (e.g., *lac, gal, ara* and *lambda* phage), loops in the DNA between specific sites form and break, in the presence of the appropriate DNA binding protein (i.e., LacI, GalR, AraC, cI). TPM experiments provide a relatively simple platform for studying how physical parameters such as loop length, protein concentration,
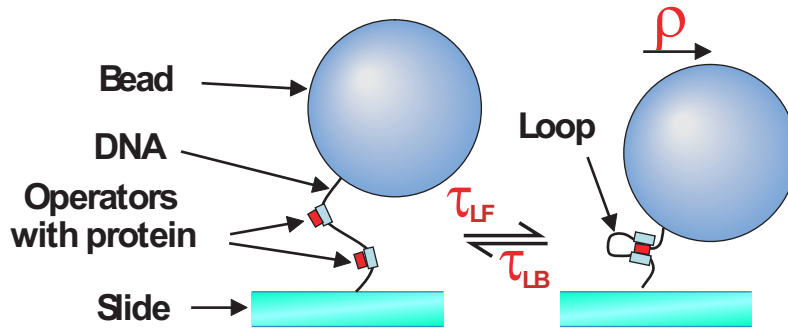
Figure 2.1: In tethered particle experiments a DNA molecule flexibly links a bead to a surface. The motion of the bead's center is observed and tracked in each video frame, and the position vector, projected to the $xy$ plane, is found. Typically, the DNA studied has two sets of binding sites ("operators") that bind a specific repressor protein. The scheme shown here is simplified; in reality, each operator can at a given moment be occupied or unoccupied. Abrupt changes in the motion of the particle indicate looping, where the time constants $\tau_{LF}$ and $\tau_{LB}$ determine the rates to form and break loops, respectively.

DNA elasticity, and binding site location influence DNA looping and thus gene regulation in a carefully controlled *in vitro* environment. Equilibrium properties of the loop formation are informative, but like other single molecule methods, a big advantage of TPM is that the kinetics of loop formation and breakdown can be determined directly from recordings of bead position. Typically, experiments assume two state kinetic schemes for the unlooped and looped tether, but more complex topologies are also possible [28, 70, 79]. Reliably obtaining these rates is thus a major goal of TPM.

## 2.2.2   Background on DNA looping

Tethered particle experiments were initially developed to study the transcription kinetics of RNA polymerase attached to a glass surface [80]. Using video-enhanced light microscopy, the motion of a 40 nm gold particle attached to the DNA template was recorded as it was transcribed by the polymerase. TPM was first used to visualize DNA looping in the *lac* system

by Finzi and Gelles in 1995 [26]. Recent TPM experiments with *lac* have focused on how the conformational flexibility of the repressor [79, 81] effects looping kinetics. TPM experiments that systematically vary the concentration of repressor and loop length have teased apart the chemical (i.e., protein binding energy) and physical (i.e., entropic and elastic energy) contributions to looping [28]. By varying the loop length in one base pair increments over a full helical repeat of the DNA, the effect of the repressor orientation on looping is measured.

Several theoretical papers have also carefully examined TPM experiments. Qian and Elson proposed using TPM to study conformational dynamics of the DNA molecule (independent of looping) and provided a useful analysis combining fundamental polymer physics with single particle tracking [78]. Segall *et al.*, propose a theory to quantify the small force exerted on the DNA due to the excluded volume between the particle and the microscope slide [77]. They verify the theory with an equilibrium Monte Carlo simulation of a worm-like chain DNA with only known experimental parameters including the length of the DNA, particle diameter, and DNA persistence length. Nelson *et al.* [76], apply a similar Monte Carlo simulation to non-looping (i.e., no repressor protein) TPM experiments of *lambda* DNA in order to reproduce the observed distributions of particle excursion with no free fit parameters. Towles *et al.* [29], further extend the Monte Carlo approach to looped DNA by incorporating the binding orientation, position and size of the lacI repressor protein from its crystal structure bound to the DNA [82]. With no free fit parameters, they determine the equilibrium looping probability as a function of operator spacing along the DNA in good agreement with experimental data [28].

Other applications of TPM include monitoring single molecule translation by a ribosome [83]. TPM also provides an attractive assay for studying the formation of DNA loops by

protein complexes that bind to multiple sites along the DNA such as the restriction enzymes NaeI and NarI [84]. The 3D position of the particle has also been obtained by measuring the relative intensity of a fluorescent bead in the evanescent decay of a TIRF beam, while simultaneously imaging its position [85].

### 2.2.3 Experimental details of looping by *lambda* phage DNA

TPM experiments [70, 76, 86] in which the projected $(x, y)$ positions of up to 6 beads are simultaneously imaged using differential interference contrast microscopy and recorded along with a time stamp for up to 45 minutes are analyzed. Images are recorded from alternate rows of pixels every 20 ms from a CCD operating in interlaced mode. Due to the difficulty in obtaining precise alignment of the two rows of pixels, each time series is treated as two separate sets with 40 ms time resolution. Rejection of anomalous beads (e.g., double tethers, surface adhesion, etc.) and correction for microscope drift are described in [76]. Simultaneous tracking of multiple beads allows microscope drift to be estimated from the collective motion of all the beads and then subtracted from each bead separately [76]. The long–time drift is determined by first finding the average $(x, y)$ position of each bead in a 20 s and then a spatial average over all the beads is calculated by summing over each of the 20 s time averages. An interpolating function that passes through these points is fitted and subtracted from each measurement [76]. This second average over the beads results in a smoother interpolation that minimizes any inadvertent removal of true bead motion. Rarely (2 points in Fig. 2.2), an anomalous outlying point or a missing frame is replaced with an interpolation of the neighboring points. All subsequent references to $x$ and $y$ are to the drift-corrected time series.
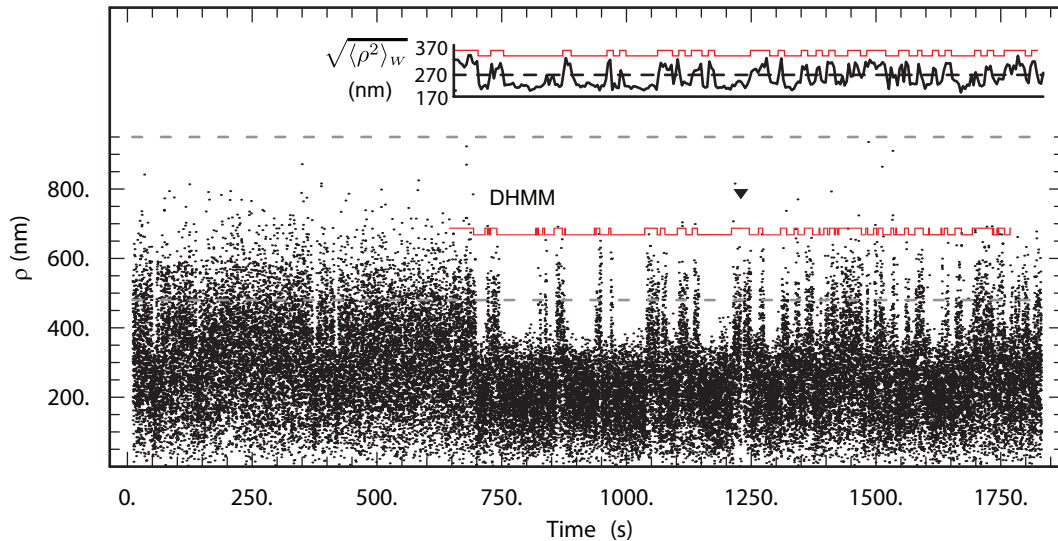
Figure 2.2: Typical time series of bead positions. DNA constructs of total length 3477 bp were attached at one end to a glass coverslip and at the other to a 480 nm diameter bead. The vertical axis gives the actual distance of the bead center from its attachment point, after drift subtraction. The DNA construct contained two sets of three operator sites. The two sets of operators were separated by 2317 bp. The system contained cI repressor protein at concentration 200 nM (where 200 nM refers to the concentration of cI dimers since monomers do not bind to DNA); repressor proteins bind to the operator sites on the DNA, and to each other, looping the DNA as in Fig. 2.1. A sharp transition can be seen from a regime of no loop formation to one of dynamical loop formation at $\sim$ 650 s. Later Sect. 2.5.3 will argue that the latter regime itself consists of two kinetically distinct subregimes. The dashed lines represent the two values of $\rho_{max}$ corresponding respectively to the looped and unlooped states; control data in these two states was observed never to exceed these values. A brief sticking event, indicated by the inverted triangle, was excised from the data prior to analysis. Section 2.4.3 uses these observed values of $\rho_{max}$ to create truncated Gaussian step distributions for the models of the looped and unlooped Brownian motion. (Experimental data for this and subsequent figures from [86], kindly supplied by C. Zurla and L. Finzi.)

Adding 200 nM of cI repressor protein converts the homogeneous tethered Brownian motion of the particle to a regime characterized by abrupt, dynamic transitions in bead motion (Figs. 2.2–2.4), a fraction of which have long enough dwell times ($\sim$1–100 sec) to be visible by eye in the raw data. Data from two kinds of control experiments is also used: *(1)* tethered beads with no protein and thus no looping, and *(2)* a small subset of beads with cI present that remain in a permanently looped configuration for many minutes (data not shown, see [86]). The first of these controls is obtained with every experiment from a preliminary 20 minute
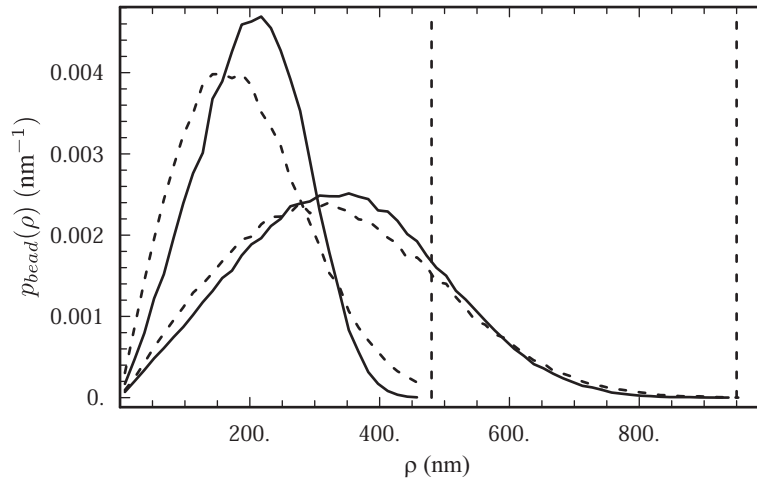
Figure 2.3: *Left solid curve:* Normalized probability distribution function (pdf) of bead center location for experimental control data corresponding to a permanently looped tether (about 65 000 video frames). *Right solid curve:* Corresponding pdf for unlooped control data (about 200 000 video frames). *Dashed curves:* Corresponding pdfs for simulated bead motion, computed using the step distribution functions found in Sect. 2.4.3, with similar numbers of simulated steps. Although the agreement with the experimental data is not perfect, it is quite nontrivial: The step distribution functions were not chosen to make these distributions agree, but rather to match the observed distributions of steps between pairs of adjacent video frames. (Data from [86].)
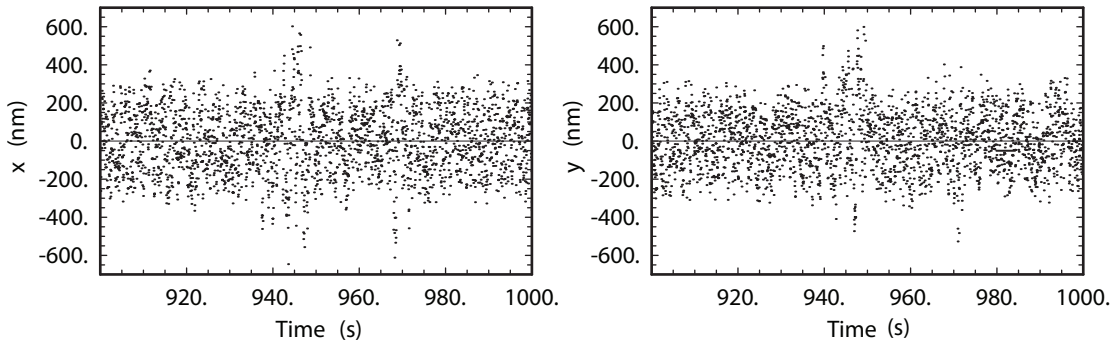


Figure 2.4: Time series for $x$ and $y$ corresponding to Fig. 2.2. The graphs show that the drift subtraction scheme leads to visually similar traces for $x$ and $y$.

recording with no repressor present. Figs. 2.3–2.5 show the histogram and autocorrelation of the experimental data (solid curves), along with simulation results to be discussed in later sections. The probability of a given $x$-$y$ pair belonging to a particular length tether is known because it can be obtained from calibration data of non-looping DNA of known length.

21
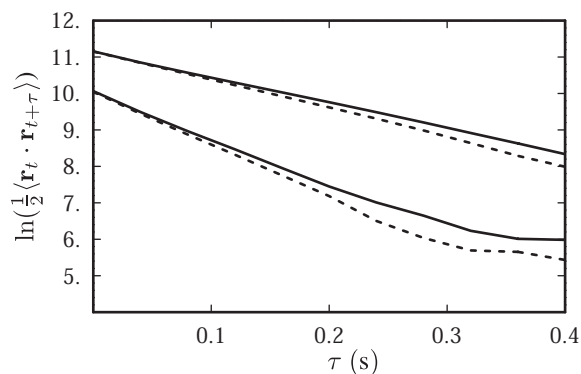
Figure 2.5: *Upper solid curve:* Semilog plot of the time autocorrelation function, $^1/_2\langle\mathbf{r}_t \cdot \mathbf{r}_{t+\tau}\rangle$ for unlooped experimental control data used in Fig. 2.3. *Lower solid curve:* Analogous function for permanently looped control data. *Dashed curves:* Analogous functions for simulated control data, computed using the step distribution functions found in Sect. 2.4.3. As in Fig. 2.3, the agreement is nontrivial: The simulation was based on pairs of data points differing by just one video frame, so the approximate agreement supports the assumption that the tethered bead motion is Markovian.

## 2.3 Prior methods for determining kinetic rate constants

### 2.3.1 Threshold method

The traditional method for determining transition rates in a single molecule experiment is to record the signal over many transitions, histogram the dwell times between transitions for each state, and then fit to an exponential (or multi-exponential) distribution. The parameters of the fits are the state lifetimes and their inverses are the transition rates. Transition events are defined when the signal crosses some threshold value. In data with high signal to noise, determining the threshold is easy and the results are independent of the exact threshold value. In data with low signal to noise, however, the threshold is often chosen arbitrarily despite strongly influencing the results.

TPM experiments present some additional difficulties for this straightforward approach. First, the observed signal (bead center position) is only indirectly related to the desired DNA

looping state. For example, in the unlooped state the bead will spend an appreciable fraction of its time close to the attachment point, mimicking the looped state, see Fig. 2.3. Additionally, the height coordinate $z$ of bead position is either not measured (e.g. in [70, 76]) or is measured to less precision than $x, y$ (e.g. in [85]), increasing further the overlap between the probability density functions (pdfs) (Fig. 2.3). Thus looping states of a majority of the individual data points in the time series can be in either looped state; e.g., measurements with $\rho_t$ less than $\sim 450\,\text{nm}$.

To overcome this difficulty, the raw data are often filtered using a sliding time window of width $W$, whose value is chosen to make clearly visible steps emerge in the data (inset in Fig. 2.2). Often this filtering step is a calculation of the signal's variance in the window, which has the additional advantage of being insensitive to instrumental drift over time scales slower than $W$. Next, a threshold is chosen that separates the high- and low-variance states, which now appear more clearly in the filtered data. Dwell times are then defined between those threshold crossings of the filtered data whose durations exceed the filter dead time (see [81, 87]). If the window $W$ contains many independent measurements, then the variance is accurately measured, and there are few spurious reported threshold crossings between the high- and low-variance states.

Unfortunately, any filter based on a finite-sample estimate of bead position variance converges slowly as $W$ is increased. For a time series of *uncorrelated* samples, the variance of the estimated variance is proportional to $1/(\text{number of samples in the window } W)$ [88, 89]. This observation may make it seem that recording data at a high enough frame rate $\gamma$ would make $1/(W\gamma)$ sufficiently small. But successive snapshots of bead position are *not* uncorrelated.
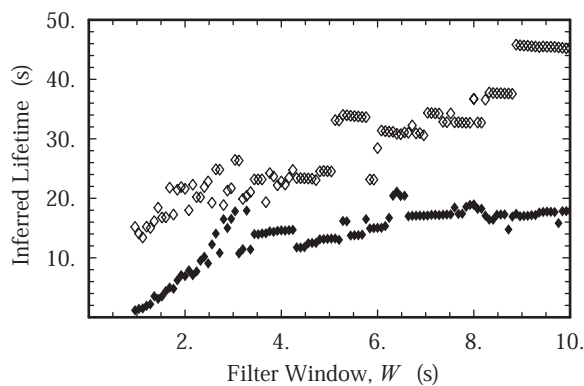
Figure 2.6: *Black dots:* Lifetime results for the windowing/threshold method for DNA loop formation lifetime (points), as a function of filter window size $W$. These results are based on the segment of data between 650–1750 seconds in Fig. 2.2 (total of 27 500 video frames). For each value of $W$, dwell times longer than twice the filter dead time (i.e. $W$) were histogrammed and fit to single exponentials to determine $\tau_{\mathrm{LF}}$. No attempt was made to correct for missed events. *Open dots:* Similar results for loop breakdown time scale $\tau_{\mathrm{LB}}$. The dependence of the inferred lifetime on the filter can complicate the "best" choice of $W$. The DHMM method developed in this chapter uses no window.

The appropriate prefactor is not $1/(W\gamma)$ but rather $\tau_{\mathrm{diff}}/W$, where $\tau_{\mathrm{diff}}$ is the diffusion time for the bead to traverse its range of motion. For TPM experiments with $\sim\mu$m length DNA fragment and $\sim 0.5\,\mu$m diameter beads, $\tau_{\mathrm{diff}} \approx 140\,$ms is estimated from the $1/e$ decay of the position autocorrelation function.

Consequently, the fractional statistical noise in the estimate of bead variance, $\sqrt{\tau_{\mathrm{diff}}/W}$, decreases slowly with increasing $W$; $W$ must therefore be taken large to obtain sufficient noise rejection (sufficiently rare spurious threshold crossings). For example, $W$ less than 1–2 seconds introduces spurious looping events in the unlooped control data where there should be none. On the other hand, $W$ must be taken smaller than the shortest state lifetime ($\sim$ 1 second); otherwise too many genuine state transitions are missed. These two constraints set a fundamental limit on the accuracy of the windowing/threshold method. Applying the threshold-crossing method to experimental data of reasonable duration resulted in reported lifetimes that depend on the choice of $W$ (see Fig. 2.6) [86].

### 2.3.2 Application of hidden Markov methods to tethered particle experiments

This section briefly reviews the standard hidden Markov method, considers its possible application to tethered particle experiments, and points out a serious limitation in its applicability. The purpose is to motivate the modifications to standard HMM in Sect. 2.4, and to establish some mathematical notation to be used there.

Hidden Markov Methods (HMM) were first described by mathematicians in the 1960s [90] and applied to speech recognition in the 1970s [91]. A classic tutorial [91] from the speech recognition field provides simple examples and a detailed procedure on how to perform the analysis. A common example of HMM in biophysics is inferring the number of open/closed ion channels in a membrane from the measured ion current across the membrane [92, 93]. Other single molecule applications of HMM include determining:*(1)* the step size of processive myosin motors labeled with fluorescent dyes [94, 95], *(2)* stroke size of non-processive myosin in optical trap experiments [89], and *(3)* the folding dynamics of an DNA Holliday Junction using single molecule FRET [96].

Classic HMM [91] involves a sequence of observations $\mathcal{O} = \{O_1, O_2, \dots\}$ that are related to an underlying kinetic process $\mathcal{Q} = \{q_1, q_2, \dots\}$ that is not directly observable but is assumed to be described by a model. Markov statistics arise because the state of the system at time $t$ depends only on its value at time $t-1$. The typical tasks of an HMM analysis are to (1) determine the probability of observing the sequence $\mathcal{O}$ given the model $P(\mathcal{O})$; (2) find the most likely sequence of hidden states $\mathcal{Q}^{\star}$ corresponding to the observations $\mathcal{O}$ and the model; and (3) to determine the parameters of the model that maximize $P(\mathcal{O})$. It is important to real-

ize that the resulting probabilities and parameters depend on the assumed model, and they do not prove its validity. Some authors retain the model (e.g., $\lambda$) in their notation to emphasize that the probability $P(\mathcal{O})$ is conditional on the model $P(\mathcal{O}|\lambda)$.

DNA looping experiments are natural candidates for application of hidden Markov methods, because the probability distribution functions (pdfs) for the bead position (called $p_{\text{bead}}(\mathbf{r}|q)$) can be calculated *a priori* [76,77] or measured directly [70,76]. To model dynamical looping data, an underlying (hidden) 2-state Markov process describing loop formation and breakdown is proposed and then in each of the two states the observed quantity (bead position) is drawn from the pdf appropriate to the current looping state. The overlap between the two unlooped and looped pdfs "hides" the true state of the tether. The underlying process has two unknown parameters, the rate constants $1/\tau_{\text{LF}}$ for loop formation and $1/\tau_{\text{LB}}$ for loop breakdown. Using assumed values for these parameters, and the known pdfs for bead position, the likelihood that any given time series of bead positions would be observed is calculated. Substituting an actual observed time series and maximizing the likelihood over $\tau_{\text{LF}}$ and $\tau_{\text{LB}}$ then yields the best estimates for the lifetimes, which are the quantities of interest.

In TPM, the *x-y* position of the bead center location is the observed signal $\mathcal{O} = \{(x_t, y_t)\} = \{\mathbf{r}_t\}$, and it reports, with a known probability, on the state of the invisible tether in either the looped or the unlooped configuration. Underlying this observed signal is the desired sequence $\mathcal{Q} = \{q_t\}$ of the DNA conformational state (e.g., in a 2-state system, $q = 1$ means unlooped, and $q = 2$ looped, at each time point). In principle, the probability distribution $P(\mathbf{r}_t, q_t)$ for the bead position and looping state at time $t$ could depend on the entire prior history of the system, that is, on $\mathbf{r}_{t-1}, q_{t-1}, \mathbf{r}_{t-2}, q_{t-2} \ldots \mathbf{r}_1, q_1$. Standard hidden Markov modeling [91] as-

sumes that the observed signal is uncorrelated, depending only on the current hidden state via a distribution $p_{\text{bead}}(\mathbf{r}_t|q_t)$, and that this hidden state in turn depends only on the previous one, via a transition matrix $T(q_t|q_{t-1})$:

$$P_{\text{HMM}}(\mathbf{r}_t, q_t) = p_{\text{bead}}(\mathbf{r}_t|q_t)T(q_t|q_{t-1}) \tag{2.3.1}$$

This assumption, however does not apply to TPM experiments, in part because of correlations in position due to the diffusive character of the bead's motion. Essentially, DHMM replaces the above assumption with a slightly more general version, in which $P(\mathbf{r}_t, q_t)$ depends on *both* $\mathbf{r}_{t-1}$ and $q_{t-1}$.

Before critiquing the HMM approach, the technique will be explicitly stated. The standard HMM [91] supposes that an observed signal reflects two processes: An autonomous Markov process (here, loop formation and breakdown) generates a time series $\mathcal{Q} = \{q_t\}$ at a discrete set of times $t = 1, \dots M$, using a $2 \times 2$ matrix of transition probabilities to represent $T(q|q')$, where the $t$ subscripts are dropped and the prime denotes the preceding measurement. $\mathcal{Q}$ is not directly observable, but it influences an observable signal $\mathcal{O} = \{\rho_t\}$: At each time, $\rho_t$ is drawn from a probability distribution $p_{\text{bead}}(\rho_t|q_t)$, which depends only on the current value of $q_t$. In particular, there is assumed to be no "back reaction" from the observed value of $\rho$ onto the underlying Markov process, and no "memory" in the process that generates $\mathcal{O} = \{\rho_t\}$.

The overall likelihood of observing a time series $\mathcal{O}$ is then taken to be a sum over all possible hidden trajectories $\mathcal{Q}$:

$$P_{\text{tot,HMM}}(\mathcal{O}) = \sum_{\mathcal{Q}} \left[ \prod_{t=2}^{M} p_{\text{bead}}(\rho_t|q_t)T(q_t|q_{t-1}) \right] \pi(\rho_1, q_1) \tag{2.3.2}$$

This is the equation for solving task (1), where the product is initialized with the probabilities

$\pi(\rho_1, q_1)$, and $\rho$ is the radial distance $\rho = \sqrt{x^2 + y^2}$ from the projected bead center to the tether attachment point (because $p_{\text{bead}}$ is circularly symmetric).

The evaluation of Eq. (2.3.2) may at first seem prohibitively difficult: Typically there can be $M = 70\,000$ video frames, and hence $2^M$ terms in the sum over $\mathcal{Q}$. But closer inspection shows that Eq. (2.3.2) is the product of $M$ $2 \times 2$ matrices, which can be evaluated in order-$M$ steps. Namely, Eq. (2.3.2) can be rewritten as

$$P_{\text{tot,HMM}}(\mathcal{O}) = (1,1) \cdot \mathsf{T}_{\text{HMM}}(\rho_M) \cdots \mathsf{T}_{\text{HMM}}(\rho_2)\Pi(\rho_1) \tag{2.3.3}$$

where

$$\mathsf{T}_{\text{HMM}}(\rho) = \begin{pmatrix} 1 - (\Delta t/\tau_{\text{LF}}) & (\Delta t/\tau_{\text{LB}}) \\ (\Delta t/\tau_{\text{LF}}) & 1 - (\Delta t/\tau_{\text{LB}}) \end{pmatrix} \begin{pmatrix} p_{\text{bead}}(\rho|q = 1) & 0 \\ 0 & p_{\text{bead}}(\rho|q = 2) \end{pmatrix} \tag{2.3.4}$$

The row vector $(1, 1)$ is used in Eq. (2.3.3) to obtain a scalar probability, and $\Pi(\rho)_q = \pi(\rho, q)$ is regarded as a column vector. The first factor in Eq. (2.3.4) is just $T(q|q')$ regarded as a matrix; $\Delta t$ is a time step that is much smaller than $\tau_{\text{LF}}$ or $\tau_{\text{LB}}$.

Evaluating the expression and optimizing it over the parameters $\tau_{\text{LF}}$ and $\tau_{\text{LB}}$ is not so prohibitive; however, in larger, more complex systems efficient optimization (task (3)) is one of the biggest challenges for implementing a practical HMM. Iterative procedures such as the popular Baum-Welch method (a form of the Expectation-Modification method in statistics) are often employed. In the simple two-state looping system discussed here for TPM experiments, merely calculating Eq. (2.3.3) over a range of guesses of $\tau_{\text{LF}}$ and $\tau_{\text{LB}}$ requires only a few minutes of computation time.

After determining the optimum parameters for the model, the most likely sequence of

hidden states $\mathcal{Q}^\star$ (task 2) corresponds to the best estimate of the looped state at every time point, and is determined from a final pass through the data using the Viterbi algorithm. $\mathcal{Q}^\star$ is a useful consistency check since the dwell times of these states can be histogrammed, fit to the proper distribution, and the parameters compared to those obtained directly from the HMM. The algorithm maintains a list of the most likely transition and its likelihood for each state at every observation. At the end of the data set, the state with the highest likelihood is the most likely. The sequence $\mathcal{Q}^\star$ is built up by working backwards through the list, each time choosing the current state's most likely predecessor.

A numerical issue does arise when dealing with long time traces, in that the value of $P_{\text{tot}}$ becomes very small. To handle this, a normalization procedure is performed after each time step [91] in the calculation of Eq. (2.3.3). For example, after the first $t$ multiplications, the two entries in the matrix are divided by their sum $s_t$, thus keeping all of the terms in the multiplication close to unity. A running tally $S_t$ of the normalizing factors $\ln s_t$ is maintained so that by the end of the calculation of Eq. (2.3.3), the final value $S_M$ is the logarithm of the desired $P_{\text{tot}}(\mathcal{O})$.

### *ad hoc* fix for Hidden Markov methods

One problem with the procedure outlined above, as mentioned in Sect. 2.3.2, is that it neglects correlations in observed bead position due to the Brownian character of tethered particle motion. Equation Eq. (2.3.2) assumes that the "noise" (bead motion) has no memory. Although this may be a valid assumption for the noise in ion channels, it is certainly not the case for tethered particle motion if the sample times are separated by less than the bead's diffusion time.

And indeed, HMM in this form was not able to determine reasonable lifetimes in experimental data.

Applying the standard hidden Markov analysis (Eq. (2.3.2)) to tethered particle experiments resulted in unrealistically short lifetimes for loop formation and breakdown that are on the same order as $\tau_{\text{diff}}$. These lifetimes are inconsistent with obvious looping events visible in the data, depend on the sampling rate of the measurement, and are present in data from control experiments with no looping. The most probable looping sequence for $\mathcal{Q}^\star$ corresponding to these fast lifetimes can be calculated, and is consistent with the bead moving diffusively between regions of large and small $\rho$, effectively masquerading as very fast looping events. That is, the spurious reported transitions reflect the fact that successive video frames are not really independent measurements of the underlying tether state.

This problem can be reduced by thinning the data, thereby decreasing the influence of diffusion and making successive points more independent of each other. Repeating the HMM analysis on the thinned data results in an increase in the reported lifetimes. If this thinning process is repeated, the calculated lifetimes eventually plateau to a value roughly consistent with the time scale of the looping events as identified by eye (Fig. 2.7). The looping sequence corresponding to these longer lifetimes also agrees with the looping events observed by eye in the raw data.

While this *ad hoc* approach for addressing bead diffusion may be acceptable in some circumstances, a better approach is to modify the HMM procedure itself to include bead diffusion directly. Section 2.4 will show that the required modification is simple, and computationally no more difficult than the calculations sketched in this section.
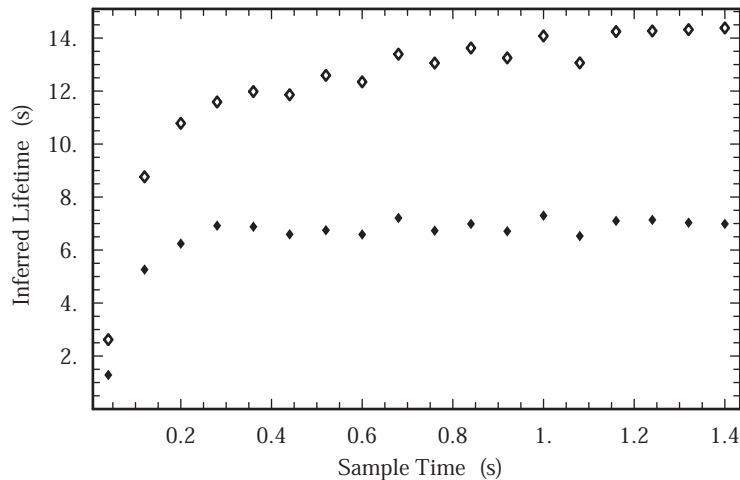
Figure 2.7: Hidden Markov analysis of the data from Fig. 2.2 illustrate how the diffusive time scale of the bead and tether dominate the inferred lifetimes when the measurement sampling interval is faster than the time scale for bead/tether diffusion. If the sampling time is artificially slowed down by thinning the data then the inferred lifetimes plateau approximately to the values obtained by DHMM (*solid/open* symbols refer to the inferred lifetimes for loop formation/breakdwon). For a thinning of '2' all of the odd points are separated from the even and then these two data sets are concatenated to reconstitute the original length trace. An analogous process was applied for higher order thinning. The HMM analysis of the concatenated recording gives results approximately equal to the average of the results if each thinned trace was considered individually (data not shown).

## 2.4 Diffusive hidden Markov method

### 2.4.1 Overview

The previous section argued that the standard HMM approach cannot be applied to tethered particle motion because its starting point, Eq. (2.3.2), is not valid. First, even if the rate of loop formation is zero (as it is in the absence of any cI protein), there will still be correlations in the observed bead positions that the algorithm interprets as spurious transitions. In fact, the time series of bead positions itself has a Markov character: Each position $\mathbf{r}_t$ is drawn from a probability distribution $T_{\mathrm{unl}}(\mathbf{r}_t|\mathbf{r}_{t-1})$ depending only on $\mathbf{r}_{t-1}$, independent of the positions at prior times [97].

The HMM assumption in Eq. (2.3.2) that the loop formation/breakdown process is inde-

pendent of the observed bead positions is also not valid. As an extreme example, if at some time the bead position is observed to be so far from the attachment point that the tether is stretched nearly straight, then it is geometrically impossible for a loop to form and the momentary rate of loop formation must equal zero.

In short, the dynamics of the bead/tether system must be regarded as a single, extended Markov process, with a joint conditional probability $\mathsf{T}_{\text{DHMM}}(\mathbf{r}_t|\mathbf{r}_{t-1})_{q_t,q_{t-1}}$; Eq. (2.3.3) is replaced by

$$P_{\text{tot,DHMM}}(\mathcal{O}) = (1,1) \cdot \mathsf{T}_{\text{DHMM}}(\mathbf{r}_M|\mathbf{r}_{M-1}) \cdots \mathsf{T}_{\text{DHMM}}(\mathbf{r}_2|\mathbf{r}_1)\Pi(\mathbf{r}_1) \qquad (2.4.1)$$

From this point on, $P_{\text{tot,DHMM}}$ is abbreviated as $P_{\text{tot}}$. (The transition matrix $\mathsf{T}_{\text{DHMM}}$ matrix will be defined in Eq. (2.4.2))

Note that since the goal is to capture the dynamics of the bead motion, simplifying the description of the bead center as the length $\rho$ from the full position vector $\mathbf{r}$ is no longer valid because there are pairs of points with the same $\rho$ that are nevertheless spatially distant. Replacing $\mathbf{r}$ by $\rho$ would therefore discard some valuable, observed, information. Since the $z$ position is not observed, the full 3-dimensional position is replaced by its 2D projection $\mathbf{r}$.

It may seem that the most desirable feature of HMM is lost, namely that the transition matrix is fully determined by the two fit parameters $\tau_{\text{LF}}$ and $\tau_{\text{LB}}$, along with functions known *a priori* (the two empirically observed pdfs $p_{\text{bead}}(\rho|q)$). To address this concern we next propose a correspondingly simple DHMM transition matrix $\mathsf{T}_{\text{DHMM}}(\mathbf{r}|\mathbf{r}')_{q,q'}$, which depends on two continuous quantities $\mathbf{r}, \mathbf{r}'$. Although not rigorously justified, it retains the properties of depending on empirically determined functions and two fit parameters $\tau_{\text{LF}}, \tau_{\text{LB}}$; also, it incorporates the diffusive character of bead motion, which is not included in Eq. (2.3.2). The

empirical functions describing the tethered motion of the bead are $T_{\text{unl}}(\mathbf{r}|\mathbf{r}')$ and $T_{\text{loop}}(\mathbf{r}|\mathbf{r}')$ for the unlooped and looped states, respectively. First the form $T$ is stated, and then its meaning is discussed. Subsequent sections will show how to extract the empirical functions from control data, then how to apply the model to data on dynamic looping.

The proposal is to assume that the matrix $\mathsf{T}_{\text{DHMM}}$ takes the form

$$
\mathsf{T}_{\text{DHMM}}(\mathbf{r}|\mathbf{r}') =
\begin{pmatrix}
1 - (\Delta t/\tau_{\text{LF}})\Theta & (\Delta t/\tau_{\text{LB}}) \\[2mm]
(\Delta t/\tau_{\text{LF}})\Theta & 1 - (\Delta t/\tau_{\text{LB}})
\end{pmatrix}
\begin{pmatrix}
T_{\text{unl}}(\mathbf{r}|\mathbf{r}') & 0 \\[2mm]
0 & T_{\text{loop}}(\mathbf{r}|\mathbf{r}')
\end{pmatrix}
\tag{2.4.2}
$$

In this formula, $\Theta \equiv 1 - \Theta(\rho - \rho_{\text{max}})$ is a step function, equal to 1 if looping is geometrically permitted, and 0 otherwise. The value of $\rho_{\text{max}}$ is to be obtained from experimental data, as described in Sect. 2.4.3.

When looping is either forbidden or obligatory, Eq. (2.4.2) reduces to tethered Brownian motion in either the unlooped or looped states respectively (no dynamic looping). In other cases, the formula can be thought of as describing an alternating series of transitions. First, the bead takes a diffusive step based on its current looping state (second matrix factor in Eq. (2.4.2)). Next, the tether updates its looping state, using probabilities that depend in a simple way on its current position (first matrix factor in Eq. (2.4.2)). Then the process repeats. If $\Delta t$ is much smaller than either the diffusion time or the loop formation/breakdown times, then no significant error is made by decomposing the process in this way. Note that Eq. (2.4.2) is properly normalized, as verified by summing it over all final states $\mathbf{r}, q$.

## 2.4.2 Critique of approach

Although it is reasonable, the DHMM proposal does make some strong and perhaps naive assumptions about the looping process. Before turning to the implementation of the method, these assumptions are made explicit, and future experiments that would help justify them are suggested.

DNA loop formation involves the motion of the molecule through a high-dimensional space of shapes, driven by thermal motion, subject to a free energy landscape determined by the molecule's elasticity. When binding sites on the proteins encounter each other, or the DNA's operator sequences, binding may ensue depending on the precision of their alignment and the relevant binding constants. Phrased in this way, it's clear that the calculation of DNA loop formation kinetics is very complicated. However, such *ab initio* calculations are not the goal.

The goal is to develop a simple characterization for the looping behavior seen in TPM experiments, in a way that is also relevant for looping behavior *in vivo*, and that is sensitive to differences in behavior as system parameters are changed. For a free DNA chain, polymer dynamics repeatedly brings binding sites into juxtaposition at some rate, with a certain probability that any such encounter leads to formation of a bound state. The product of the attempt rate and the probability per encounter is an average loop formation rate. If each encounter's probability for binding is small, then it is reasonable to expect that overall loop formation (and breakdown) processes should be monomolecular reactions describable with simple exponential kinetics.

Turning from free DNA to the case of DNA tethering a large reporter bead, it is noted that

the presence of the bead does not by itself alter the thermal force fluctuations on the looping part of the DNA; these equilibrium fluctuations are determined by equipartition applied to the entropic elasticity of the semi-flexible polymer chain. It is true that bead-surface repulsion can tend to stretch the DNA, altering the equilibrium constant for loop formation [77]. However, this entropic force falls off rapidly when the distance from the polymer's endpoint to the surface exceeds the bead diameter; it can be minimized by choosing small enough beads (or by replacing the bead by a functionalized colloidal gold particle [80, 98]).

Notwithstanding the above remarks about equilibrium, the large, sluggish bead is expected to significantly alter looping *kinetics*. But precisely because the bead is slowly diffusing, whenever it is close to the attachment point of the DNA to the wall, it is likely to stay close for many milliseconds. During this time, the bead offers no significant obstacle to the same thermally-driven chain rearrangements that bring the operator sites of free DNA into juxtaposition. Hence, when the bead is close to the wall attachment point, it is expected that DNA loop formation will proceed as if the DNA were free in solution (or part of a larger bacterial genome). More precisely, the time required for the polymer tether to explore its available conformations is assumed to be much less than the time for the bead to diffuse a significant fraction of its total range of motion. In the contrary case (the bead is far from the attachment point), loop formation is geometrically forbidden. A similar argument suggests that loop breakdown kinetics should not be altered by the presence of the reporter bead.

Eq. (2.4.2) embodies the above ideas, together with the idea that the bead wanders in and out of the range allowed for looping, subject to distributions $T_{\text{loop}}$ and $T_{\text{unl}}$ that themselves can be found from the observed behavior of permanently looped or unlooped tethers. Thus

the parameters $\tau_{\mathrm{LF}}$ and $\tau_{\mathrm{LB}}$ appearing in Eq. (2.4.2) are expected, when the model is fit to TPM data, to give a good guide to looping rates for DNA free in solution. In contrast, simply applying the windowing/threshold method to data does not correct for the expected slowing-down of loop formation due to the presence of the bead. Indeed, applying that method to the data considered here leads to inferred $\tau_{\mathrm{LF}}$ values significantly slower than the one that will be obtained in Sect. 2.5 below.

Although the preceding paragraphs have argued that the DHMM approach is reasonable, it is crude in some respects. For example, once the bead center is observed to be at a certain distance from the attachment point, this distance amounts to a stretching of the DNA chain. The expected rate for loop formation will be some decreasing function of this stretching, but not of course a step function, as assumed in Eq. (2.4.2).

Another simplification is to ignore the unobserved height variable $z$, in effect treating the bead motion as diffusion in two dimensions. Although in *free* Brownian motion all three coordinates perform independent random walks, in TPM the presence of the wall and tether couple $x, y,$ and $z$. To some extent, the technique of obtaining $T_{\mathrm{unl}}$ and $T_{\mathrm{loop}}$ in Eq. (2.4.2) directly from control data will correct for this effect, but the criterion for loop formation to be possible really depends on the full 3D separation $\sqrt{x^2 + y^2 + z^2}$, not on $\rho = \sqrt{x^2 + y^2}$ as assumed in Eq. (2.4.2). A more detailed analysis might treat $z$ as another hidden (unobserved) variable.

Rotatory Brownian motion of the bead is also ignored. The ability of the tether to form loops actually depends on the distance between the two DNA end points. One endpoint, where the DNA attaches to the microscope slide, is fixed. The bead center location is a proxy for the

other endpoint, but really the point where the DNA attaches to the bead also depends on the angular orientation of the bead. Again, a more detailed analysis might treat this orientation as another hidden variable.

The justifications for all three of the above simplifications are simply that *(a)* although the pdfs for projected bead position in the looped and unlooped states overlap partially, they are nevertheless fairly distinct, allowing reliable state identification even with the simplified model; *(b)* the projected-step distribution functions $T_{unl}$ and $T_{loop}$ that are extracted from control-experiment data do have the qualitative form expected for two-dimensional diffusion in an effective spring trap [97] (see Sect. 2.4.3); and *(c)* changing the cutoff $\rho_{max}$ in the analysis does not significantly change the inferred values of the rate constants (data not shown). Despite these encouraging observations, however, other experimental tests of the method would certainly be desirable, for example, analyzing the kinetics of loop formation in identical tethers attached to different-sized beads, to check that similar values of $\tau_{LF}$ and $\tau_{LB}$ emerge.

## 2.4.3   Implementation

**Obtaining step distribution functions**

It would be a daunting task to determine the appropriate step distribution functions $T_{unl}$ and $T_{loop}$ appearing in Eq. (2.4.2) *a priori* directly from theory. For example, bead–wall hydrodynamic interactions depend on the bead's height, which is not observed; the tether couples the unobserved bead orientational fluctuations to the observed position fluctuations; and so on. These difficulties are circumvented by empirically determining the $T_{unl}$ and $T_{loop}$ from experimental control data for the two states. After these functions are obtained, the simple

model of tethered-particle dynamics constructed from them is confirmed to reproduce some nontrivial features of the real control data (Figs. 2.3 and 2.5). Finally, dynamic-looping data are examined, and the two remaining free parameters $\tau_{\mathrm{LB}}$ and $\tau_{\mathrm{LF}}$ in Eq. (2.4.2) are adjusted until the log-likelihood, $\ln[P_{\mathrm{tot}}(\mathcal{O})]$, is a maximum.

In order to obtain $T_{\mathrm{unl}}(\mathbf{r}|\mathbf{r}')$ from the unlooped control data, note that this function must be symmetric under rotations of both $\mathbf{r}$ and $\mathbf{r}'$ about the attachment point by a common angle. Thus this function for $\mathbf{r}'$ only needs to be determined on the $\hat{\mathbf{x}}$-axis, at some radial distance $\rho'$. Starting from a time series for unlooped DNA (no repressor protein present), all of the points in the time series for which the bead center's distance from the anchor point, $\rho'$, lies in a particular range are selected. Next, the rotation in the plane that brings $\mathbf{r}'$ to the $\hat{\mathbf{x}}$-axis is determined, and also applied to $\Delta\mathbf{r} = \mathbf{r} - \mathbf{r}'$, the bead's vector displacement to its position on the following video frame. Finally, a 2-dimensional histogram of the observed displacements $\Delta\mathbf{r}$ is constructed, and normalized to obtain $T_{\mathrm{unl}}(\mathbf{r}|\mathbf{r}')$. The process is repeated, producing histograms for all observed initial distances $\rho'$. Using data obtained from about 30 minutes of bead observation, the observed range of $\rho'$ could be divided into 30 intervals and still have reasonable statistics in the histograms; Figs. 2.8–2.9 shows typical examples for two values of $\rho'$. A similar procedure is applied to the permanently-looped control data to obtain $T_{\mathrm{loop}}(\mathbf{r}|\mathbf{r}')$.

The step-probability distributions (Fig. 2.9) obtained in this way show that at small $\rho'$ there is no preferred direction for the next time step; for larger $\rho'$, the tether is stretched and exerts a restoring force on the bead, so the step distribution shows a bias to diffuse toward the attachment point (the $-\hat{\mathbf{x}}$ direction). Next, a convenient analytical representation of these
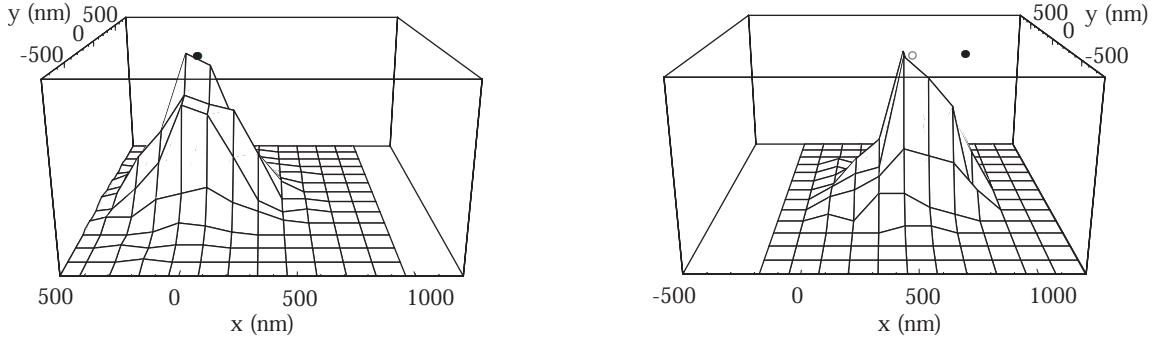
Figure 2.8: 2D histograms of unlooped control data at two values of $\rho'$ near (*left*) and far (*right*) from the anchor point (0,0) after rotation onto the $\hat{\mathbf{x}}$ and $\hat{\mathbf{y}}$ axes (see text). The dots on the upper x-y plane indicate the initial position $\rho'$ (*full circle*) and the mean midpoint of the final position $\mu(\rho')$ (*open circle*). For $\rho'$ near the anchor point the two dots coincide.
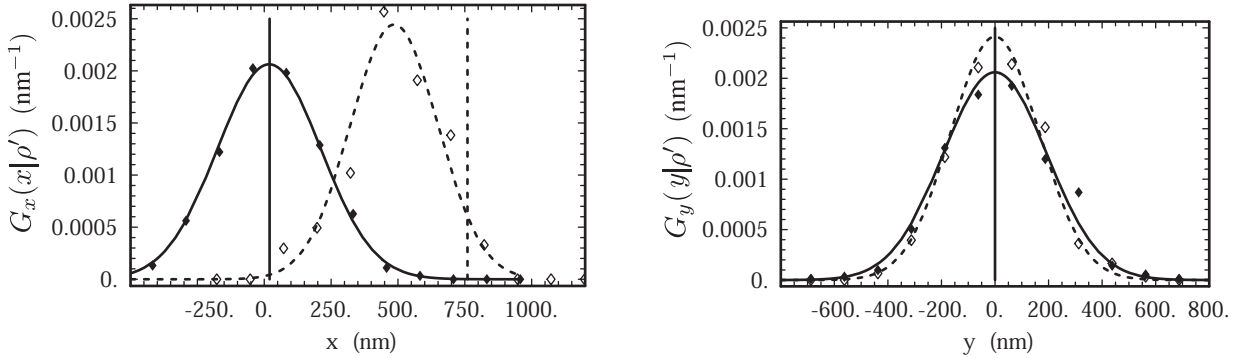


Figure 2.9: Projections of the two distributions in Fig. 2.8 onto the $\hat{\mathbf{x}}$ and $\hat{\mathbf{y}}$ axes, together with Gaussian distributions chosen to idealize them. *Left:* the *vertical lines* represent two choices for the initial bead position; *dots* represent the corresponding distributions of bead positions on the next video frame. Note the shift in the mean $\hat{\mathbf{x}}$ at larger $\rho'$ (*open*) compared to shorter $\rho'$ (*full*). *Right:* No such shift is observed in the $\hat{\mathbf{y}}$ direction.

distributions, both for computing the likelihood function $P_{\text{tot}}(\mathcal{O})$, and also for simulation purposes is described.

Each distribution is seen to be roughly a 2D Gaussian, with one principal axis along the radial direction to the attachment point. After rotating $\mathbf{r}'$ to lie along the $\hat{\mathbf{x}}$ axis as described above, the principal axes of the distribution are the $\hat{\mathbf{x}}$- and $\hat{\mathbf{y}}$-axes. The center point also lies
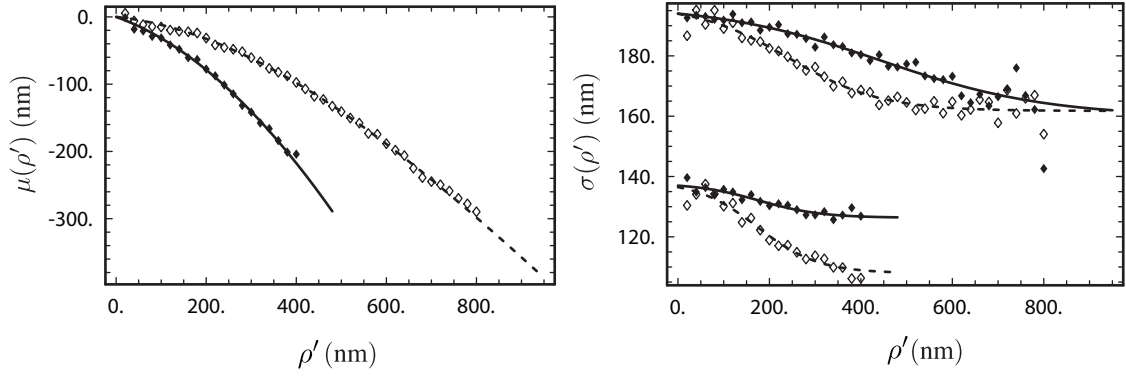
Figure 2.10: Empirical fit functions for the mean (*left*) and variance (*right*) of the 2D histograms (see e.g. Fig. 2.8) for experimental control data corresponding to unlooped (*solid* symbols) and looped (*open* symbols) tether states. Corresponding fit parameters for the functions of Eq. (2.4.3) are located in Sect. 2.4.3.

on the $\hat{\mathbf{x}}$-axis, and is increasingly shifted from $\rho'\hat{\mathbf{x}}$ toward the attachment point $(0,0)$ as $\rho'$ increases due to the tether's entropic elasticity. Accordingly, $T_{\mathrm{unl}}(\mathbf{r}|\mathbf{r}')$ is characterized for each fixed $\mathbf{r}' = (\rho',0)$ by finding its mean $\langle x \rangle$ and the variances in the $x$ and $y$ directions. The mean $\langle y \rangle$ equals zero (see for example Fig. 2.9), as it must by rotational invariance. Thus three functions of $\rho'$ that characterize the histograms are required: a 3rd-order polynomial for the mean $\mu(\rho') \equiv \langle x \rangle_{\rho'}$, and sigmoids for the variances $\sigma_x^2(\rho')$ and $\sigma_y^2(\rho')$ (see Fig. 2.10):

$$\mu_x(\rho) = a_0 + a_1\rho + a_2\rho^2 + a_3\rho^3$$

$$\sigma_x^2(\rho) = b_0/(1 + e^{(\rho-b_1)/b_2}) + b_3 \qquad (2.4.3)$$

$$\sigma_y^2(\rho) = c_0/(1 + e^{(\rho-c_1)/c_2}) + c_3$$

Using these fit functions, the observed step probabilities are represented as the product of 1D

Gaussian distributions in $x$ and $y$ starting from the point $\mathbf{r}' = (\rho', 0)$:

$$T_{\text{unl}}(\mathbf{r}|\mathbf{r}') \;=\; G_x(x|\rho') \cdot G_y(y|\rho') \;\; \text{where} \tag{2.4.4}$$

$$G_x(x|\rho') \;=\; (2\pi\sigma_x^2(\rho'))^{-1/2} \exp\left( \frac{-(x - \mu(\rho'))^2}{2\sigma_x^2(\rho')} \right) \tag{2.4.5}$$

$$G_y(y|\rho') \;=\; (2\pi\sigma_y^2(\rho'))^{-1/2} \exp\left( \frac{-y^2}{2\sigma_y^2(\rho')} \right) \tag{2.4.6}$$

Examples of these functions for illustrative values of $\rho'$ appear in Fig. 2.10. For arbitrary $\mathbf{r}'$ (not necessarily on the $\hat{\mathbf{x}}$ axis), the probability is evaluated by rotating $\mathbf{r}'$ to the $\hat{\mathbf{x}}$-axis, rotating $\mathbf{r}$ by the same amount, and evaluating Eq. (2.4.4) on the components of the rotated $\mathbf{r}$.

**Truncated Gaussian approximation**

The procedure summarized in Eqs. (2.4.4–2.4.6) is conceptually simple. The accuracy of the calculations, however, can be improved with a small elaboration. Like any Gaussian, the distribution defined above is nonzero for any $x$ and $y$. In reality, however, the DNA tether sets an absolute limit on $\rho$ beyond which the probability must be exactly zero. Not surprisingly, following the procedure outlined above yielded simulated time series that occasionally violated this limit. Although the effect of this error may be minor for the unlooped step distribution, for the looped distribution it could interfere with looping state identification.

Accordingly, formula for $T_{\text{unl}}(\mathbf{r}|\mathbf{r}')$ is modified to account for the limit in an approximate (and computationally inexpensive) way: Eq. (2.4.5) is replaced by a truncated Gaussian function. That is, $G_x(x|\rho')$ is set to zero for $x > \rho_{\max}$, and a Gaussian with modified parameters for $x < \rho_{\max}$. The modified parameters were chosen in such a way that the truncated Gaussian would again have the mean $\mu(\rho')$ and variance $\sigma_x^2(\rho')$ shown in Fig. 2.10. That is, for each value of $\rho'$, the $\mu$ and $\sigma_x^2$ determined empirically from the data were not used directly; instead

a new Gaussian, with modified parameters $\tilde{\mu}$ and $\tilde{\sigma}_x^2$ is found, which has mean $\mu$ and variance $\sigma_x^2$ when the probability of values greater than $\rho_{\max}$ is set to zero.

Ideally $G$ should be chosen to be a function that vanishes when $x^2 + y^2$ exceeds $(\rho_{\max})^2$, and falls smoothly to zero as that boundary is approached. To make the calculations tractable, $G$ is taken to be the product of a cutoff, shifted, 1D-Gaussian in $x$ times an ordinary Gaussian in $y$. Examination of many graphs like Fig. 2.8 indicate that this simplification adequately represents the empirical histograms. Moreover, since the axes are rotated to make the initial position lie along the $x$-axis, an extra excursion along $x$ is more likely to violate the tether condition than one along $y$. Small changes in the choice of the empirical function $G$ have little effect (see Sect. 2.6) on the final results.

To implement efficient calculation of the truncated Gaussian $G_x(x|\rho')$, a look–up table for the Gaussian with mean, variance, and normalization $(\tilde{\mu}(\rho'), \tilde{\sigma}^2(\rho')$ and $\tilde{N})$ is evaluated such that when $\rho > \rho_{\max}$ this Gaussian is zero and satisfies the mean and variance $(\mu(\rho')$ and $\sigma_x^2(\rho'))$ determined empirically from data in [86]:

$$\int_{-\infty}^{\rho_{\max}} dx \frac{1}{\tilde{N}} e^{-(x-\tilde{\mu})^2/(2\tilde{\sigma}^2)} = 1, \quad \int_{-\infty}^{\rho_{\max}} dx \frac{x}{\tilde{N}} e^{-(x-\tilde{\mu})^2/(2\tilde{\sigma}^2)} = \mu(\rho') \qquad (2.4.7)$$

$$\int_{-\infty}^{\rho_{\max}} dx \frac{x^2}{\tilde{N}} e^{-(x-\tilde{\mu})^2/(2\tilde{\sigma}^2)} = \sigma_x^2(\rho') \qquad (2.4.8)$$

Such look-up tables were evaluated at 100 values of $\rho'$ for both (unlooped, looped) tether states using Eq. (2.4.3) and parameters: a0=(0,0), a1= (-0.068, -0.238), a2= (-5.0e-4, -7.9e-4), a3 = (1.52e-7, 6.30e-8), b0= (35.1, 30.6), b1=(161.75, 107.95), b2=(242.3, 173.8), b3=(100.16, 66.42), c0=(37.11, 11.43), c1=(159.8, 126.3), c2=(444.88, 177.06), c3=(180.72, 67.86), where $\rho$ is measured in nm.
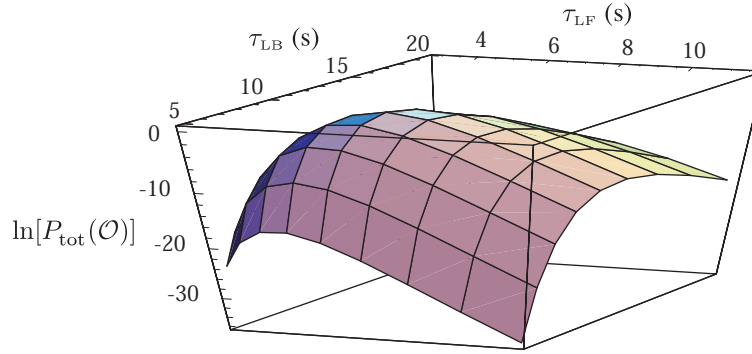
Figure 2.11: Evaluation of $\ln[P_{\text{tot}}^*(\mathcal{O})]$ on a logarithmically-spaced grid of $\tau_{\text{LF}}, \tau_{\text{LB}}$ lifetimes corresponding to data from Fig. 2.2.

**Optimization**

The optimum lifetimes are found by evaluating $P_{\text{tot}}(\mathcal{O})$ on an evenly-spaced logarithmic grid of values for $\tau_{\text{LF}}$ and $\tau_{\text{LB}}$, and the location of the maximum $P_{\text{tot}}^*(\mathcal{O})$ determined. The resulting likelihood surface is smooth (Fig. 2.11), so the peak likelihood can be determined more precisely by fitting a 2D quadratic in the neighborhood of the optimum lifetimes. The uncertainty of the optimum lifetimes corresponding to $\ln[P_{\text{tot}}^*(\mathcal{O})] - 2$, i.e., enclosing 97% of the probability, were estimated along the principal axes of this 2D quadratic to account for any correlation between the estimated lifetimes. In order to facilitate this iterative process, an automated simplex solver routine was implemented to find the maximum [99].

**Simulation strategy**

Simulations of bead motion, with and without dynamic looping, were performed in *Mathematica* to test the DHMM model. Each step of the simulation (*a*) first determined whether or not to remain in the current looped state, and then (*b*) the next spatial position was determined appropriate for the particular loop state. In more detail, (*a*) If the initial state was looped, a pseudorandom number was used to determine whether to transition to the unlooped state with

probability $\frac{\Delta t}{\tau_{\mathrm{LB}}}$. If the initial state was unlooped, and if $\rho < \rho_{\max}$, then a transition to the looped state was allowed with probability $\frac{\Delta t}{\tau_{\mathrm{LF}}}$. Next (*b*) a $(\Delta x, \Delta y)$ pair was drawn from the appropriate distribution obtained in Sect. 2.4.3. That is, $\Delta y$ was Gaussian distributed, and similarly for $\Delta x$ except that steps resulting in $\rho > \rho_{\max}$ were discarded and the step repeated in order to achieve a truncated Gaussian as discussed earlier.

## 2.5   Results and discussion

Section 2.4.3 outlined how to determine $T_{\mathrm{unl}}(\mathbf{r}|\mathbf{r}')$ and $T_{\mathrm{loop}}(\mathbf{r}|\mathbf{r}')$ from the control data, then used these functions to simulate tethered particle motion. In this section one-state simulations are compared with control data and two-state simulations with dynamic looping data. Also, a change in looping dynamics, possibly indicating a change in protein occupancy of one or both of the *lambda* operators is determined using DHMM.

### 2.5.1   One-state modeling

To validate the assumptions used to model the equilibrium, tethered Brownian motion, a simple simulation using the step-distribution functions obtained from adjacent video frames (Sect. 2.4.3) is performed and compared to the resulting trajectories with the experimental control data. The resulting simulated time series $\{\rho_t\}$ are difficult to distinguish from actual data by inspection (not shown), so the equilibrium properties of the motion are compared using the radial probability distributions (Fig. 2.3) and the dynamic properties using the autocorrelation function (Fig. 2.5). Both of these non-trivial checks agree fairly well with the actual data, although for unknown reasons the equilibrium distribution of the longer tether is

captured better by the model than the shorter tether.

The two-state DHMM approach is also applied to permanently-unlooped experimental control data to see if the algorithm would incorrectly report any looping transitions. Instead, the algorithm correctly reported loop-formation times that were proportional to the length of the data set (that is, consistent with infinity), and loop-breakdown times approaching the sampling interval (that is, consistent with zero). Simulations of unlooped motion behaved similarly. As expected, DHMM applied to permanently-looped experimental control data and simulations did not detect any false loop breakdown events with the trends for loop breakdown and formation lifetimes exchanged from the unlooped case. Another consistency check was to verify that the step distribution functions originally calculated from the experimental control data Sect. 2.4.3 were the same for the simulations.

Finally, the maximum likelihood transition sequence corresponding to the optimal lifetime values $\mathcal{Q}^\star$ is determined. No false looping transitions were reported for either of the control data sets, indicating that the rate for false positives for loop formation and breakdown is low.

### 2.5.2 Dynamic looping

The two-state DHMM algorithm is applied to the part of the time series in Fig. 2.2 that displays dynamic looping (the region between 650 and 1750 seconds). The algorithm reported $\tau_{LF} = 5.8\,\text{s} \pm 25\%$ and $\tau_{LB} = 9.9\,\text{s} \pm 25\%$; it also determined the most-likely sequence of state transitions. To see whether the model is really detecting dynamic transitions between the two tether lengths in this parameter regime, DHMM is applied to a 20-minute simulation of dynamic looping generated using the same lifetime values. In addition to comparing the re-

|          | # Events | $\tau_{\text{LF}}$ | $\tau_{\text{LB}}$ | $\ln[P_{\text{tot}}(\mathcal{O})]$ | $\frac{1}{M}\ln[P_{\text{tot}}(\mathcal{O})]$ |
|----------|----------|------|------|-----------|----------|
| Data | 50 | 5.8 | 9.9 | $-374\,089$ | $-12.714$ |
| Sim. #1 | 68/75 | 4.9 | 9.2 | $-376\,951$ | $-12.811$ |
| Sim. #2 | 57/64 | 6.4 | 9.3 | $-378\,173$ | $-12.853$ |
| Sim. #3 | 62/77 | 5.6 | 8.3 | $-378\,228$ | $-12.855$ |
| Average Sim. | 62.3/72 | 5.6 | 9.0 | $-377\,784$ | $-12.840$ |

Table 2.1: Comparison of results for three simulations, their average, and data (from Fig. 2.2). The inferred lifetimes for the data were used as input for the simulations. All trials had a total number of points $M = 29\,424$. The second number in the event column is the (known) number of events. Lifetimes are in seconds and other terms are nondimensional.

ported lifetimes, each of the transitions in the simulated data are known and can be compared with the reconstructed sequence from the algorithm. The lifetimes for the simulation and the experiment agree within uncertainty ($\sim 20\%$, see Table 2.1), and the state sequence successfully detects $\sim 85$–90% of the known transitions, with missing events usually less than $\sim 1\,\text{s}$ in duration. Like any Hidden Markov method, a benefit of DHMM is that it is not specifically sensitive to missing events, since event identification is performed *after* the lifetimes are determined. Instead of binning identified events and fitting the resulting histogram, DHMM directly maximizes the likelihood that a function describes the entire data set. If the time scale of events is too short compared to other time scales in the problem, DHMM reports that fact via its estimates of uncertainty in the fit parameters.

Simulations of looping with lifetimes different from those seen in the experimental data were also performed. A $5 \times 5$ log-spaced grid of different combinations of lifetimes centered on the optimum lifetimes obtained from the experimental data was defined. DHMM was
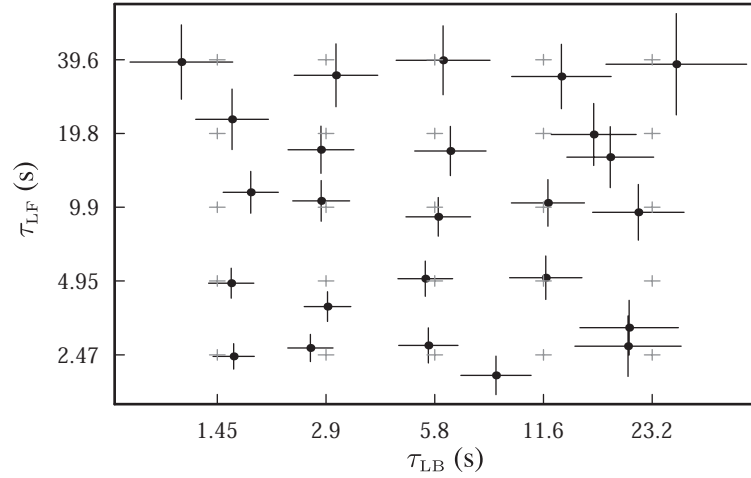
Figure 2.12: 25 simulations were performed with input lifetimes $\tau_{LF}$ and $\tau_{LB}$ distributed on a log-spaced grid *(gray crosses)* centered at the optimum lifetimes obtained from experimental data. Each simulated data set had length $M$ equal to that of the experimental data. Next, DHMM was performed for each simulated data set, to determine the most-likely lifetimes *(black symbols)*.

applied to simulations generated using those assumed lifetimes to see how well it could extract them (Fig. 2.12). The agreement over the range ($1/4\times$ to $4\times$) was good to within the error bars estimated by the curvature of the log-likelihood function (Fig. 2.11). These error bars in part reflect the finite sample size $M$, which is often limited by experimental considerations. To check that last assertion, 10 additional simulated data sets were generated all with the same "true" lifetimes and number of data points $M$ as the experimental data discussed previously. The variation in lifetimes deduced from the known transition times represents the minimal variation due to finite sample size. Indeed, the scatter in the best-fit lifetimes determined by DHMM is no worse than this minimum amount. Simulations with longer lifetimes $\tau_{LF} = \tau_{LB} = 20\,\text{s}$ and a total time of $\approx 60\,\text{minutes}$ to give more transitions were similarly successful (agreement of lifetimes within 10% and 92% success in detecting events, data not shown).

As discussed in Sect. 2.3, in both the threshold method and traditional HMM the time resolution depends on how the data are analyzed (i.e., window size and degree of thinning

respectively). To demonstrate the robustness of the DHMM method, the data set is subdivided (taken at a frame rate of $(20\,\text{ms})^{-1}$) into two subsets with $\Delta t = 40\,\text{ms}$, and also into four subsets with $\Delta t = 80\,\text{ms}$ and lifetimes for all of these subsets are computed. All lifetimes agree within the uncertainty of the method (data not shown; note that Eqs. (2.4.3–2.4.6) must be re-calculated for different $\Delta t$).

### 2.5.3   Detection of very long-lived state transitions

So far, the peak of the likelihood function $P_{\text{tot}}(\mathcal{O})$ and its vicinity have been used to determine the optimum looping lifetimes and their uncertainty. The likelihood function can be further utilized to assess the uniformity of the dynamics. This is a useful scenario because in a real DNA-looping system there are certainly more than two discrete states: e.g., individual repressor proteins can bind and unbind to their operator sites [79]. Indeed, the data studied here came from a system with two sets of three operators, leading to a large set of potential occupancy patterns. Presumably the obvious change in behavior in Fig. 2.2 at $t = 700\,\text{s}$ reflects the arrival of another repressor at an operator site, enabling loop formation. But there seems also to be a less obvious transition in the data around $t = 1250\,\text{s}$, from one looping regime to another one with different kinetics. Can DHMM locate such changes objectively?

If the data had uniform, two-state looping behavior for the entire recording, then the log-likelihood of the whole would be equal to the sum of the log-likelihoods of its parts, and also the best-fit lifetimes should come out roughly equal for each part separately as for the whole. To test this, a procedure used by Ref. [100] is adapted: the data in Fig. 2.2 is restricted to the region after $650\,\text{s}$, but this time the data is divided into two regions, $A$ from 1 to $M'$
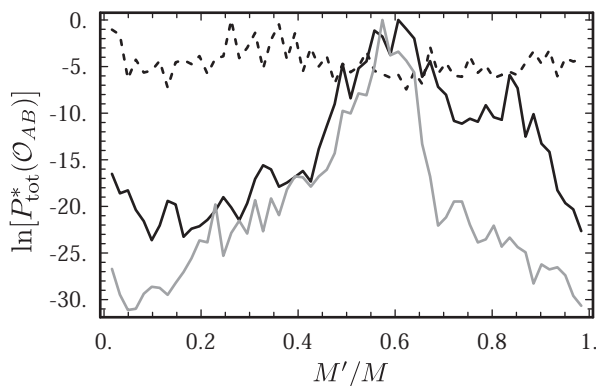
Figure 2.13: See text. The peak in $\ln P_{\text{tot}}(\mathcal{O}_{AB})$ (*solid line*) suggests that the data from Fig. 2.2 is composed of two regions at $M' \simeq 61\%M$ with different kinetics. The *gray/dotted* lines are the results from simulated data with/without a transition at $M' \simeq 61\%M$, respectively. For comparison purposes, each likelihood has had its peak vertically shifted to 0 by subtracting a constant.

and $B$ from $M'$ to $M$, and then separately applied DHMM on the two regions to determine $\ln P_{\text{tot}}(\mathcal{O}_{AB}) \equiv \ln P_{\text{tot}}(\mathcal{O}_A) + \ln P_{\text{tot}}(\mathcal{O}_B)$. The resulting $\ln P_{\text{tot}}(\mathcal{O}_{AB})$ has a single, very sharp peak at a particular value of $M'$ (Fig. 2.13). In agreement with visual inspection, the optimal value of $M'$ is roughly two-thirds of the way through the retained data, that is, around $t = 1300\,\text{s}$ in Fig. 2.2. Moreover the reported optimal lifetime values in the two subsets are quite different: $(\tau_{\text{LF}}, \tau_{\text{LB}})_A \simeq (10\,\text{s}, 20\,\text{s})$ and $(\tau_{\text{LF}}, \tau_{\text{LB}})_B \simeq (3\,\text{s}, 4\,\text{s})$. When the procedure is repeated with simulated data including a transition at $M' = 0.6M$ where looping kinetics changes from $(\tau_{\text{LF}}, \tau_{\text{LB}})_A$ to $(\tau_{\text{LF}}, \tau_{\text{LB}})_B$ values, a peak in $\ln P_{\text{tot}}(\mathcal{O}_{AB})$ very similar to the one in the experimental data is found (Fig. 2.13). In contrast, when the procedure was applied to simulated constant, two-state dynamics, $\ln P_{\text{tot}}(\mathcal{O}_{AB})$ was insensitive to $M'$ as expected.

## 2.6   Conclusions

The purpose of DHMM is to enhance the ability of tethered particle experiments to study DNA looping kinetics *in vitro*. For illustration, a simplified 2-state model that includes the

one looped and one unlooped tether state is used, i.e., the various possible occupancies of the repressor protein on the DNA binding sites is ignored, but the method can readily be extended to include such details. Since publication, DHMM has been used to study the kinetics of DNA looping by the Type II restriction enzyme SfiI [101].

Previously, threshold methods were applied to the data to quantify the kinetic rates between various looped and unlooped states. This method involves filtering the data to extract the transitions from the noisy diffusive motion of the bead, then fitting a (single or double) exponential to the tail of a histogram of the dwell times. Both filtering and histogramming discard potentially useful information; moreover, at least in the *lambda* phage system studied here, the choice of filter window can influence the reported results. The DHMM method avoids any such steps.

Hidden Markov modeling is a useful tool to learn about the hidden conformation of the DNA tether from the observed motion of the bead, because the observed motion can be statistically quantified and simple models used to describe the unobserved state of the tether. The uninteresting diffusive motion is determined empirically from control experiments, and then the looping is assumed to follow exponential kinetics with unknown parameters corresponding to the loop formation and breakdown lifetimes. Then the likelihood that the experimental data (or a simulation) came from the proposed model is maximized. The method is implemented in a computationally efficient code in *Mathematica*. Since there is no filtering and no binning of the data in DHMM, the kinetic parameters can be determined unambiguously. If desired, the most-likely transition state sequence can also be determined.

It is easy to obtain unlooped control data to train the DHMM algorithm by omitting re-

pressor protein during the experiment; however looped control data can be more challenging. For the *lambda* system considered here, infrequent yet long-lived looped states made this a relatively simple task. In other systems alternatives exist, including separate experiments on constructs with shorter length tethers corresponding to the expected looped length or, if available, mutant repressor proteins with stronger affinity for DNA that result in permanently looped tethers. In the *lambda* system, the robustness of DHMM to the model of the looped state is verified by varying the fit parameters in Eq. (2.4.3) by $\pm 10\%$ and noting that $\tau_{\mathrm{LB}}$ and $\tau_{\mathrm{LF}}$ remained unchanged (data not shown).

Another advantage of DHMM is its ability to, at least partially, compensate an experimental bias inherent in the tethered particle method: Loops cannot form between successive measurements if the DNA is in an extended conformation due to the time for the bead to diffuse to a location closer to the anchor point. This effect inflates the observed loop formation times relative to the case of interest (free DNA in solution); indeed, in simulations where the lifetimes are known *a priori*, this effect inflates $\tau_{\mathrm{LF}}$ by $\sim 30\%$. The DHMM model compensates for this by allowing loops to form only when $\rho < \rho_{\mathrm{max}}$.

The recent incorporation of single–particle tracking into the TPM method was essential, because it allows rapid and precise measurements of bead position that are required for DHMM. In particular, the ability to simultaneously track *multiple* tethered beads is helpful for removing instrumental drift [76]. Future experiments could in principle remove drift from the data entirely by simultaneously tracking a fixed, fiducial marker object.

DHMM is applied to one illustrative experimental dataset of *lambda* DNA with 200 nM cI, and it determined loop formation and breakdown lifetimes of $\sim 6$ and 10 s respectively.

One surprisingly biologically relevant application of this work is that, at physiological [cI] corresponding to the lysogenic state, the loop is not permanently closed. It is interesting that these lifetimes are neither representative of all the beads that were observed in [86] (data not shown), nor even for the entire observation time of any single bead (see Fig. 2.2). Prior to adding cI, most beads have nearly identical tethered diffusive motion; however, after addition of cI, the kinetics of looping varied widely. Some beads were mostly unlooped with occasional looping events, some beads were the inverse of this, others showed long periods of dynamic looping, and some like Fig. 2.2 seemed to show very sharply-defined changes between long-lived (often $> 10\,\text{min}$) regimes of homogeneous behavior. One hypothesis to explain these long-time looping trends is that the occupancy of cI protein among the 6 *lambda* binding sites changes, resulting in periods with more or less stable loops. For example, when all 6 sites are occupied a very stable loop might form, whereas 4-sites occupancy could result in a less stable, but still detectable, loop. Future experiments with fewer operators, or perhaps fluorescent cI protein, could be used to test this hypothesis directly.

One technique for considering such complex kinetic scenarios is to use a more elaborate state diagram; however, a different approach might be appropriate if cI proteins are binding and unbinding on a time scale much slower than loop formation, as observed. In this case, DNA looping data could be adequately represented by a concatenation of 2-state models, each with different kinetics, rather than by a far more elaborate model with many states. There appear to be three such regions in the data shown in Fig. 2.2. First, the mostly unlooped region was removed to focus on the faster dynamics of the later region, which was split in all possible ways into two subregions. Each subregion was analyzed separately using DHMM,

and the partition that resulted in the highest total likelihood, which was also much higher than if the two regions were assumed to be one homogeneous kinetic regime, was chosen. The sharp peak in Fig. 2.13 indicates that DHMM is a sensitive tool to localize such subtle transitions in time.

# Chapter 3

# Twirling of actin by myosin II observed via polarized TIRF in a modified gliding assay

## 3.1  Introduction

The swinging lever arm model [102, 103] explains force production and movement between actin and myosin II in muscle contraction [104] and also applies to non-muscle myosins [105]. Separate crystal structures of myosin and actin docked into cyro-EM maps of actomyosin [106] indicate that the lever arm swing is nearly parallel to the axis of the actin filament, thereby efficiently converting the free energy released from ATP hydrolysis into motion along the filament. Even small torque components around the filament axis, however, may have biological roles in muscle contraction (Ref. [107], and references therein) or regulation [108].

For processive non-muscle motors, a torque may be desirable for navigating cargo around obstacles present in the crowded environment of the cell [109–111].

Several studies have suggested off-axis components to the relative motion between actin and myosin. For example, decreased lateral spacing of the filaments of frog skeletal muscle in rigor compared with relaxation was attributed to radial forces between the thick and thin filaments [112]. In a modified gliding assay, actin filaments that were selectively immobilized onto the slide at their pointed ends formed superhelices that suggested a right-handed component of torque generated by myosin II [113]. In standard gliding assays where the filaments are free to translocate, a torque component of the cross-bridge force could result in rotation of the filament about its longitudinal axis, i.e., "twirling." Actin filaments with marker beads attached at their ends showed no twirling on HMM-coated slides [114] while gliding, but when the filaments were marked sparsely with fluorescently labeled actin monomers, simultaneous twirling and gliding of the filaments was observed by polarized fluorescence microscopy [59, 65]. Symmetries in the fluorescence polarization technique prevented both of those studies from determining the handedness of the twirling motion.

A separate way of gauging sideways motions and possible components of torque between actin and processive myosins is to suspend the actin filament above the surface of the microscope slide and record the path of a bead being transported by myosin along the suspended filament [115, 116]. Off-axis force causes the bead to travel in a helical path. In the suspended filament assay, myosins V [115] and VI [116] exhibited left-handed and right-handed helical paths, respectively.

Polarized epifluorescence microscopy [59] and polarized total internal reflection fluores-

cence (polTIRF) microscopy [62,63,65] typically use incident and/or detected light polarized along the $x$, $y$ and $z$ axes of the microscope. In such configurations, rotation of the fluorophore, but not the handedness of its helical motion, can be observed because orientations of the fluorophore reflected across any of the Cartesian planes give the same fluorescence intensities and thus are not distinguishable. Intermediate excitation or emission polarizations that break these symmetries enable the handedness to be recovered [117].

In the present work, extra linear polarizations are added to the previously reported polTIRF technique [2,61–63,65] that are intermediate between those aligned along the Cartesian directions. As a result, there is a four-fold increase in the range of unambiguously detected probe orientations. The orientation is then estimated within a hemisphere, the remaining two-fold ambiguity being an unavoidable property of dipolar absorption and emission of light.

This chapter reports on twirling and its handedness from gliding actin filaments that are translocated by whole myosin II. The twirling motion is nearly always left-handed with an average pitch, i.e. the distance that the filament translocates during one complete rotation, of approximately 0.5 $\mu$m that is not strongly influenced by myosin concentration, Mg·ATP concentration or filament length in the range studied here. These values for the twirling pitch are much longer and opposite in handedness to the intrinsic pitch of the actin filament. Several mechanical effects are discussed that could give rise to filament twirling.

## 3.2 Methods

### 3.2.1 Biological samples

Proteins, buffers, and slides were prepared as in [2, 63] with minor modifications. Briefly, whole myosin II was purified from rabbit fast skeletal muscle and stored in 300 mM KCl, 5 mM Hepes, pH 7.0, 5 mM NaN$_3$ and 50% glycerol at -20°C [118]. Actin was prepared from rabbit muscle in G-buffer (2 mM Tris, pH 8.0, 0.2 mM CaCl$_2$, 0.2 mM ATP, 0.5 mM DTT), frozen in liquid N$_2$, and stored at -80°C [119]. G-actin monomers were labeled [120] at Cys374 with 5-iodoacetamido-tetramethylrhodamine (a gift from J. E. T. Corrie, National Institute for Medical Research, Mill Hill, London). Filaments, sparsely-labeled ($\sim$ 0.05%) with rhodamine-actin, were polymerized by mixing labeled and unlabeled monomers, at 1 $\mu$M total actin concentration, in F-buffer (50 mM KCl, 2 mM MgCl2, 1 mM EGTA, 10 mM Hepes, pH 7.4) and stabilized with 1.1$\mu$M Alexa 647 labeled phalloidin (Invitrogen A22287).

In order to remove "dead" myosin heads that do not release actin upon binding ATP, a 12 mg/ml myosin stock was diluted in high salt buffer (500 mM KCl, 10 mM Hepes, pH 7.0, 5 mM MgCl$_2$) and combined with a molar excess of actin filaments, 2.5 mM ATP and 5 mM DTT and then centrifuged at $200\,000 \times g$ for 30 min on the day of each experiment. The concentration of protein retained in the supernatant was then determined by Bradford assay.

A $\sim$ 20 $\mu$l flow cell was created using a clean quartz microscope slide, glass cover slip, and two pieces of double-sided tape. For myosin II, a 1 mg/ml solution of poly-L-lysine was flowed into the cell and incubated for 1 min. Excess polylysine was rinsed out with 20 $\mu$l of high salt buffer, and then the myosin, diluted from stock in high salt buffer, was flowed into

the cell and incubated for 2 min. The following solutions were made in wash buffer (WB: 25 mM KCl, 20 mM Hepes pH 7.4, 5 mM MgCl$_2$) and flowed through the cell. $2\times$ 0.5 mg/ml BSA, $2\times$ 5 $\mu$M unlabeled sheared actin filaments to block any remaining dead myosin heads, 2 mM ATP to dissociate actin from the active heads, and $2\times$ WB to wash out the free actin and excess ATP. Finally, 5 nM 0.05% rhodamine-labeled Alexa 647 phalloidin-stabilized actin filaments and motility buffer with 5-20 $\mu$M ATP, 50 mM DTT, 5 mM phosphocreatine and 0.4 mg/ml creatinephosphokinase were flowed into the cell. All experiments were performed at 22-23°C.

The concentration of myosin II flowed into the cell was equal to 0.03, 0.1, 1, or 3 mg/ml. Mg·ATP concentration was varied between 5 and 20 $\mu$M which resulted in filament velocities of 0.1-0.5 $\mu$m/s. For low myosin concentrations ($\leq$0.1 mg/ml), 0.1% methylcellulose was added to the motility solution to increase filament run length. Twirling of filaments with variable lengths in the range 1-50 $\mu$m was determined at concentrations of 0.03 and 0.1 mg/ml myosin.

### 3.2.2 Experimental Setup

The polarized total internal reflection fluorescence (polTIRF) setup has been described in detail previously [2, 63]. Here a brief explanation is provided followed by a description of the modifications that enable linear polarizations of the incident laser illumination to be polarized in between the $s$- and $p$- polarization directions, see Fig. 3.1.

Two alternating beams from a 532 nm Nd:YAG laser are focused onto a prism such that the incident angle (with respect to the $z$ axis, normal to the quartz slide/water interface) is $\sim 68°$
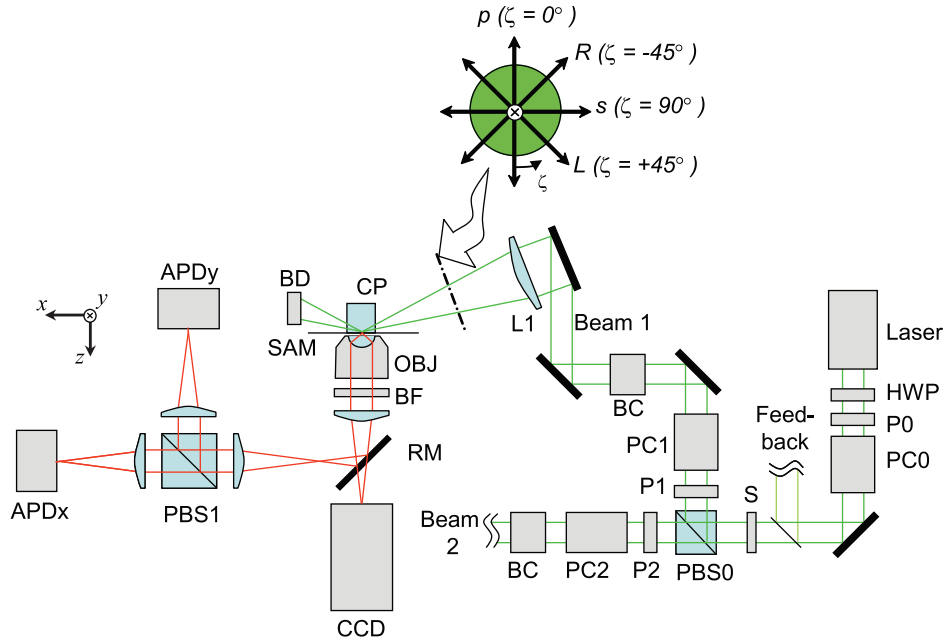
Figure 3.1: At the sample plane, the two incident laser beams alternately propagate nearly along the $x$ (Beam 1) and $y$ (Beam 2) axes, illuminating the sample with one of four linear polarizations: $s$, $p$, $L$, or $R$ for each path (see inset). For clarity, a portion of Beam 2 is omitted. It reflects from the sample interface similar to Beam 1, but propagates in the $y$-$z$ plane perpendicular to the page. Beam 1 is focused by a lens ($L1$) at a glancing angle through a coupling prism ($CP$) onto the sample ($SAM$) and terminated in a beam dump ($BD$). Reflecting mirrors are shown as thick black lines. The laser intensity is controlled by a rotatable half wave plate ($HWP$) and vertical polarizer ($P0$). The polarization of the beam is switched between vertical and horizontal polarizations by a Pockels cell ($PC0$), passed through a shutter ($S$) and directed along paths 1 and 2 by a polarizing beam splitter ($PBS0$) and clean-up polarizers ($P1$ and $P2$). The polarization in each path is controlled by a Berek compensator ($BC1$ or $BC2$) and a second Pockels cell ($PC1$ or $PC2$), which change the polarization every 10 ms to $p$, $s$, $L$ and $R$. The emitted fluorescence intensity is collected by a microscope objective lens, passed through a barrier filter ($BF$) and directed onto either a CCD camera or reflected by a removable mirror ($RM$) onto two avalanche photodiodes (APDx and APDy) that measure the fluorescent intensity polarized along the $x$ and $y$ axes by $PBS1$. A small fraction of the beam prior to the shutter ($S$) is directed into a feedback circuit [63] that controls the polarization from $PC0$ in order to maintain high extinction between Beams 1 and 2.

. Fluorescent emission is collected by a $100\times$ 1.2 NA water immersion lens, passed through a long pass blocking filter and either imaged onto an intensified CCD camera or passed through a polarizing beam-splitter onto two avalanche photodiodes (APDs). Using a Pockels cell (PC0 in Fig. 3.1) and a polarizing beam splitting cube ($PBS0$), the incident illumination is cycled between two paths that are aligned predominantly along the $x$ and $y$ directions and intersect at

59

the sample. Four linear polarizations in each beam path (termed $s$, $p$, $R$, and $L$) are obtained by applying different voltages to additional Pockels cell ($PC1$ and $PC2$, ConOptics M370) and then passing the beam through a Berek variable compensator ($BC1$, $BC2$, New Focus Inc) in each path. With $45°$ between the crystal axis of the PC and the linearly polarized incident light, the PCs produce vertical, horizontal or elliptically polarized light depending on the input voltage. The Berek compensator acts essentially as a $^1/_4$-wave plate to convert the elliptically polarized light to beams linearly polarized at any arbitrary azimuth. The bending mirrors used to project the excitation onto the sample re-introduce phase shifts and resulting ellipticity into the intermediately polarized ($L$ and $R$) beams. The Berek compensator is adjusted in angle and retardation slightly away from the $^1/_4$-wave setting to correct for these extra phase shifts. The $L$ and $R$ linearly polarized beams are obtained by adjusting the PC voltages and the Berek compensators until the beams are linearly polarized at angles intermediate (approximately $\pm45°$) between $s$ and $p$ at the entry to the coupling prism ($CP$). Polarizations are verified with a crossed linear polarizer, which extinguishes the beam immediately prior to the final focusing lens ($L1$).

Each polarization alternately illuminates the sample for $10\,\text{ms}$ in the sequence: $s1, p1, p2,$ $s2, R1, L1, L2,$ and $R2$. The fluorescence emission from a selected rhodamine fluorophore is directed through a polarizing beam splitter ($PBS1$) that separates its $x$ and $y$ components onto two APDs (APDx and APDy) for a total of 16 measured intensities $_{s1}I_x$, $_{s1}I_y$, $_{p1}I_x$, $_{p1}I_y$, etc..., see Fig. 3.2A. For imaging of the field, a mirror ($RM$) is removed so that the fluorescence is projected onto the intensified CCD camera.

The evanescent field generated by the incident $p$ polarized light has a slight ($\sim 5\%$) el-

lipticity in the $x$-$z$ and $y$-$z$ planes for Beams 1 and 2, respectively, due to the component of incident radiation parallel to the reflecting surface. In addition to this $x$-$z$ ellipticity under $p$-polarized illumination, the $L$- and $R$- polarizations in Beam 1 have additional ellipticity in the $y$-$z$ plane due to the different phase shifts in the evanescent wave from the $s$ and $p$ components ($\delta_s$ and $\delta_p$, see Appendix 3.5.1). A similar phase shift holds for elliptical polarizations from $R2$ and $L2$. As done before with ellipticity induced by $p$-polarization [2, 63], the ellipticity of $L$ and $R$ excitation are included in the analytical equations used to determine the probe orientation.
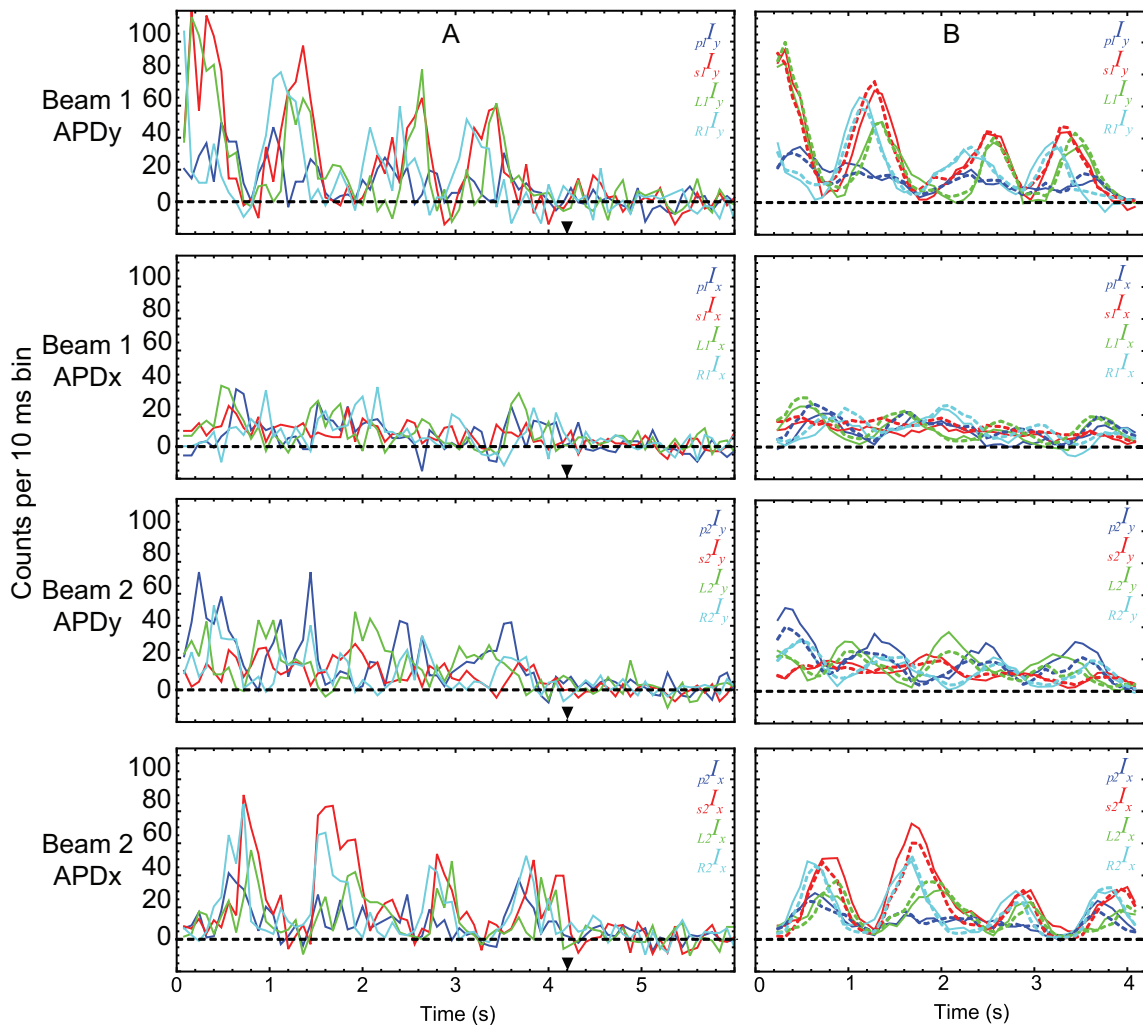
Figure 3.2: Typical polarized fluorescence intensity data for a single molecule of rhodamine attached to a twirling actin filament with 0.1 mg/ml myosin loading concentration, 10 $\mu$M Mg·ATP, and velocity of 0.24 $\mu$m/s. The filament translocated at an angle of -95°(i.e, $\phi_{\text{actin}}$) relative to the positive $x$-axis. ($A$) Calibration factors for the 16 recorded intensities have been applied to the raw data and the background of each has been subtracted. ($B$) The data prior to the bleach at $\sim$ 3.6 s ($\blacktriangledown$, see Fig. 3.4 for the total fluorescence intensity) is passed through a 5-point (0.4 s) mean filter before maximum likelihood analysis for extracting angles. The resulting intensity calculated from the probe model is in good agreement ($dotted$) with the filtered data ($solid$). Peak intensities occur when the probe is aligned with the detector and the incident polarization. Consequently, evidence for twirling of the probe can be directly seen in the data as sets of oscillating intensity curves that are out of phase with one another. For example, in this case the data recorded for Beam 1 by APDy shows a pattern of sequential peak intensities $_{R1}I_y$, $_{s1}I_y$, $_{L1}I_y$ that repeats with each rotation of the probe (see also Fig. 3.6).

## 3.2.3   Single molecule position and average filament velocity

After mounting the sample slide and adding motility buffer, a 30 s movie of a field of $\sim$20-40

single rhodamine fluorophores was recorded by the CCD camera to determine the average

filament speed. Mg·ATP concentration was limited to 5-20 $\mu$M so that the filaments moved slowly enough (0.1-0.5 $\mu$m/s) to enable 2-7 s recording of the fluorophore as it passed across the 1.8 $\mu$m diameter projected spot size of the APDs before photo-bleaching. A second movie was recorded after a series of polarization measurements to verify consistent speeds at the beginning and end of the experiment. Occasionally, the first movie was omitted in order to obtain measurements of long filaments, which become shorter due to shearing at high concentrations of myosin. The $(x, y)$ coordinates of the filament were tracked automatically by fitting a $2D$ Gaussian intensity distribution to the image of the fluorophore for each frame. The $x$-$y$ path of the fluorophore was smoothed using a 5-point Savitsky-Golay filter [99], and the filament velocity was determined from the path length of 15-30 measurements. Average filament velocity for each slide was obtained from 7-10 filaments.

### 3.2.4   Single molecule orientation and filament twirling

Prior to recording each polarization trace, two images of the field of candidate fluorophores were recorded with the CCD camera, superimposed and displayed on a monitor. These images were used to calculate a filament-specific velocity for each fluorophore, which could be used as an alternative to the average velocity mentioned above. A molecule was then selected for polarization analysis, and centered above the objective by a computer-controlled piezoelectric stage. The collected fluorescent emission was directed away from the CCD and onto the photodiodes by replacing the removable mirror ($RM$ in Fig. 3.1). Thus, during polarization recording, spatial information from the fluorophores was not available.

After a moving rhodamine molecule was selected and centered over the APDs, 125 cycles

of 16 polarized fluorescent intensities were recorded for 10 s. Typically, the fluorescence signal photobleached to the background level in a single step during this 10 s period. For recordings with the occasional double bleach, presumably arising from two nearby labeled monomers, only the single fluorophore region before the final bleach was used for analysis.

The orientation of the probe was estimated by fitting analytical equations that predict the polarized fluorescence intensities during each complete illumination cycle as described in [63] and expanded here to include the $L$- and $R$- incident polarizations. Briefly, the raw intensity traces are corrected for instrument factors using a calibration procedure (see Reference [63] with additional terms in Appendix 3.5.2) and the background is subtracted. Sixteen intensities (one complete 80 ms cycle) are combined in a mathematical model of the probe that describes its 3D orientation and rotational motions (see Fig. 3.3A) by approximating it as an electromagnetic dipole that absorbs and emits photons preferentially polarized along its dipole axis; see Appendix 3.5.1 for details. Corrections for partial mixing of the components of polarized fluorescent emission due to refraction by the high NA objective are included in the model; see References [2, 63] for details.

The maximum likelihood values for the probe's 3D orientation and rotational wobble $(\theta, \phi, \delta, \kappa)$ are determined for each 80 ms cycle using a Levenberg-Marquardt C algorithm that matches the predicted and measured intensities. $\kappa$ is an amplitude factor that scales the total intensity of the probe to the number of photons collected during each cycle. $\delta$ describes wobble motions on a time scale faster than measurement time ($\sim 10$ ms) but slower than the fluorescent lifetime of the probe ($\sim 4$ ns). The parameter describing rotational wobble on time scales faster than the fluorescent lifetime, $\delta_f$, was fixed during the analysis at $22.5°$ [65].
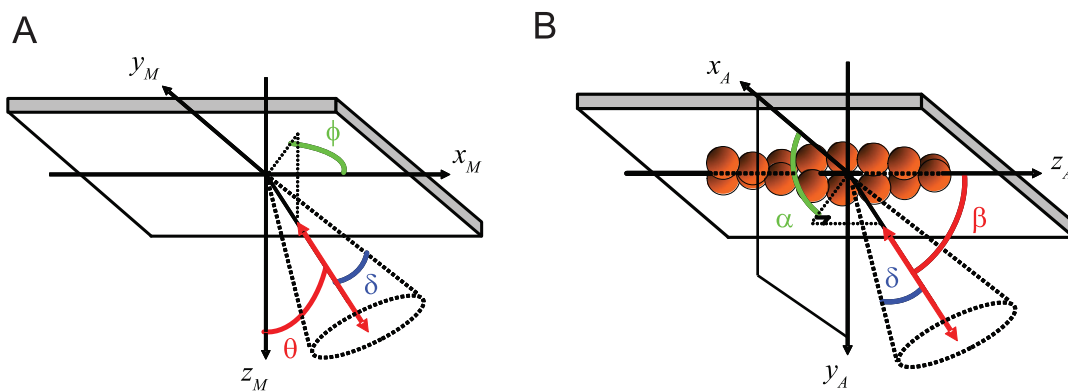
Figure 3.3: Calculations are performed in the microscope coordinate frame $(A)$, where the $+z$ axis is the optical axis, pointing toward the microscope objective, and the $+x$ and $+y$ axes are in the plane of the quartz/water interface and aligned with the plane of propagation of Beams 1 and 2, respectively. The evanescent TIRF field decays in the $+z$ direction. $\theta$ is the polar angle of the probe with respect to the $+z$ axis and $+\phi$ is the azimuthal angle of the probe around $z$ defined positively from the $+x$ axis towards the $+y$ axis. The extent of fast ($\delta_f$, not shown) and slow wobble ($\delta$) motions are included in the analysis model to account for mixing between the polarizations due to motions of the probe on two time scales, both much faster than the twirling rate. Twirling is quantified in a frame of reference relative to the actin filament $(B)$ where $\beta$ is the polar angle of the probe with respect to the forward moving end of the actin filament axis and $\alpha$ is the azimuthal angle around the filament axis.

The angular values $(\theta, \phi)$ in the microscope coordinate frame were rotated into the coordinate frame of the actin filament $(\beta, \alpha)$ using the direction of probe motion from the preceding pair of video frames as the polar axis in the actin frame of reference (see Fig. 3.3B, Appendix 3.5.3, and [2] for more details).

## 3.2.5 Filament length

In order to estimate the length of the actin filament, the sample was briefly illuminated with a HeNe laser to excite the Alexa 647 labeled phalloidin. The fluorescent emission was passed through a band pass filter (Omega 670DF40) and captured in a single image by the CCD. The Alexa 647 image of the filaments was overlaid with two subsequently acquired images of the rhodamine fluorophores to aid in molecule selection. Switching lasers required approximately 1-2 s so that matching the rhodamine actin with its filament was unambiguous. Filament

lengths were measurable for the first 20 min of data recording. The length of the filament was estimated in ImageJ [121] by summing short line segments manually selected along the filament contour. Filament length could only be determined at low (0.03 and 0.1 mg/ml) myosin concentration due to shearing of the filaments, which for high (1 and 3 mg/ml) concentrations occurred within the first 1-2 min of adding motility buffer to the flow cell.

## 3.3   Results

Polarized fluorescence intensities from a filament twirling about its axis during translocation show prominent oscillations (e.g., Fig. 3.2A). When all of the separate polarized fluorescence intensities are summed together the resulting total is a constant intensity that bleaches to background in a single step (see Fig. 3.4). Strong variation of the polarized fluorescence intensities with constant total intensity is an indicator of probe rotation. The intensities of the different channels oscillate with different phases as the rotating probe temporarily comes into alignment with the polarization direction of the incident illumination. Prior to maximum likelihood analysis, a 5-point running average is applied to the data (solid lines in Fig. 3.2B) in order to remove some high-frequency noise. The traces and their oscillations due to changes in $\alpha$ as the filament translocates are reproduced by the predictions of the fitted model (dotted lines in Fig. 3.2B).

In a plot of $(\theta \text{ vs. } \phi)$ actin filaments translocating uniformly (i.e., with constant velocity and direction within the $x$-$y$ plane) that are also twirling with a constant angular velocity show a circular pattern that is centered at $(90°, \phi_{actin})$, see Fig. 3.5A,B. $\phi_{actin}$ is the direction in the $x$-$y$ plane of the filament trajectory with respect to the $+x$ axis. $\theta$ oscillates about $90°$ because

66
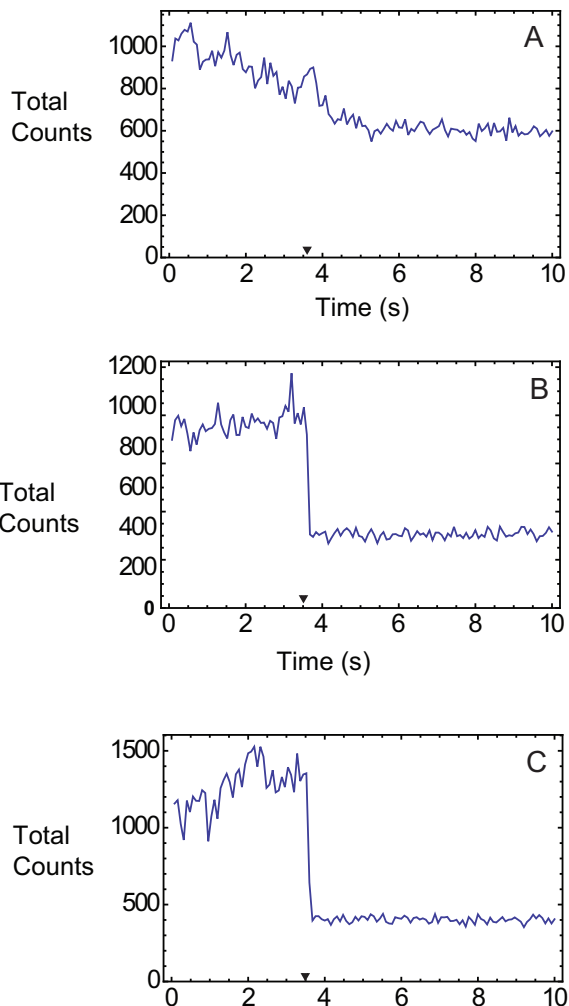
Figure 3.4: Total intensity for each 80 ms cycle of the 16 raw, uncorrected polarized fluorescence intensities for (A) the molecule shown in Fig. 3.2, (B) a typical molecule with constant intensity prior to bleaching (indicated by ▼), and (C) the molecule shown in Fig. 3.7. Twirling motion is accompanied by strong undulations in individual polarized fluorescence intensities (see Fig. 3.2) that when summed together during a complete polarization cycle are relatively flat, apart from photon noise fluctuations, prior to bleaching. Bleaching to background in a single step is indicative of a single fluorophore recording. Occasionally, molecules decrease in intensity during the recording despite clear twirling motions (e.g., A). Two possible mechanisms for this decrease in signal include the molecules being translocated away from the small spot detected by the APDs, or the filament moving away from the surface (and thus out of the evanescent field).

a probe that is fixed in a twirling filament will spend half of each rotation pointing above the x-y plane and the other half pointing below it.

For a filament that is uniformly twirling about its axis, $\beta$ is approximately constant between $0°$ and $90°$ (Fig. 3.5C), and $\alpha$ increases (right-handed pitch) or decreases (left-handed pitch)
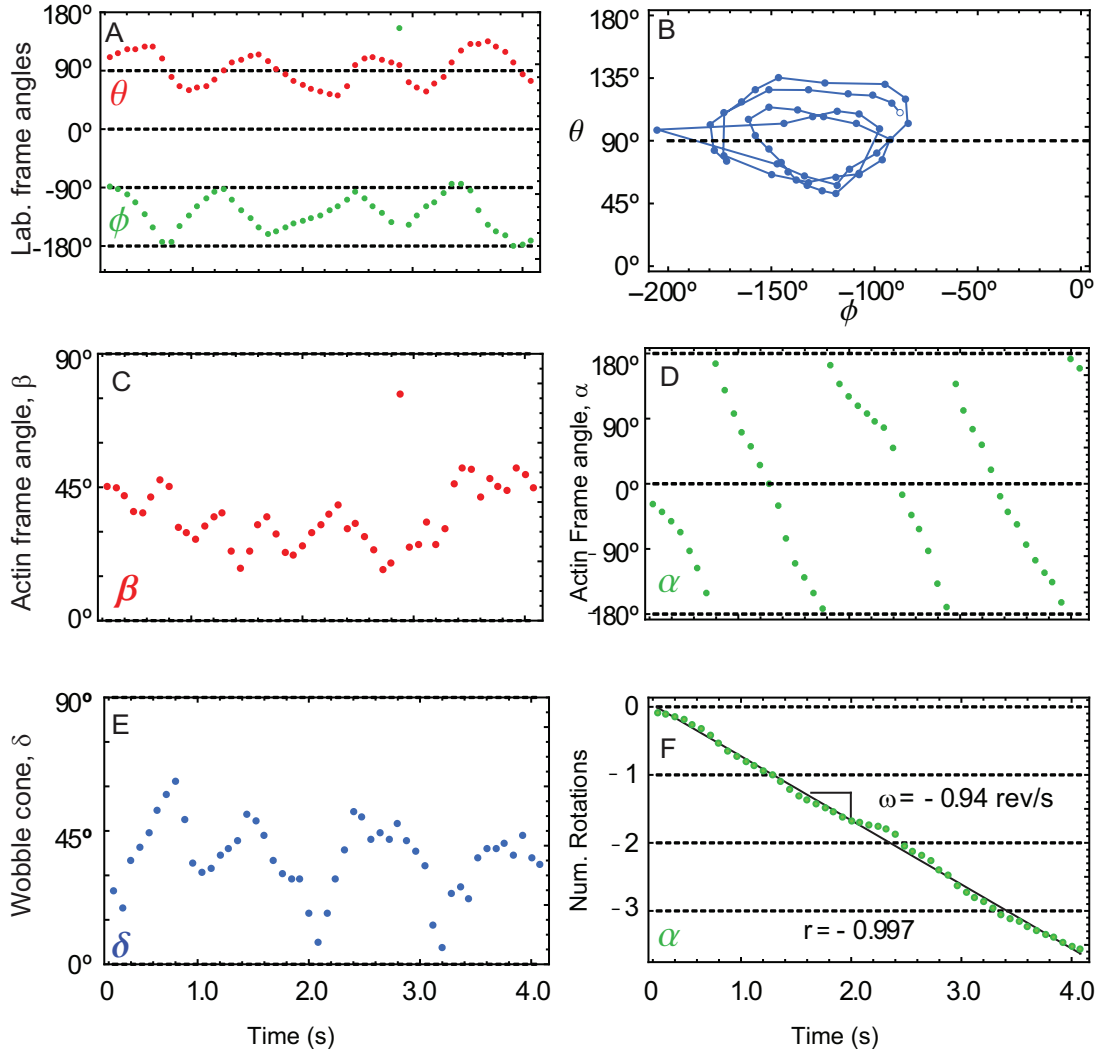
Figure 3.5: For each complete cycle of the polarization data in Fig. 3.2, the maximum likelihood angle in the microscope frame $(\theta, \phi)$ and actin frame $(\beta, \alpha)$ are plotted. Twirling is seen in the microscope frame either $(A)$ as oscillations in time of $\theta$ and $\phi$ or $(B)$ as a circle when plotted as $\theta$ vs. $\phi$ (open circle is $t = 0$s). In the actin frame twirling is indicated by $(C)$ a relatively constant $\beta$, here equal to $\sim 40°$, and $(D)$ saw-tooth shape for $\alpha(t)$. $(F)$ When $\alpha(t)$ is shifted by $360°$ after each rotation, the saw-tooth becomes a straight line with slope $\omega$ equal to the twirling frequency, here $\approx -0.94$rev/s. The direction of translocation (along the $+x$-axis) is required for determining the handedness of the twirling motion; left- and right-handed are depicted here by a negative and positive slope for $\alpha(t)$, respectively. The slow wobble cone $(\delta)$ of the probe is $\sim 45°$. Approximately half of the twirling filaments have traces similar to the quality shown here.

linearly in the range $-180° < \alpha < 180°$ (Fig. 3.5D). The wobble, $\delta$, of the probe attached to actin is noisy (Fig. 3.5E), similar to results from [65], but it neither exhibits systematic variation with $\alpha$ and $\beta$, nor prevents determination of the probe orientation, as would be the
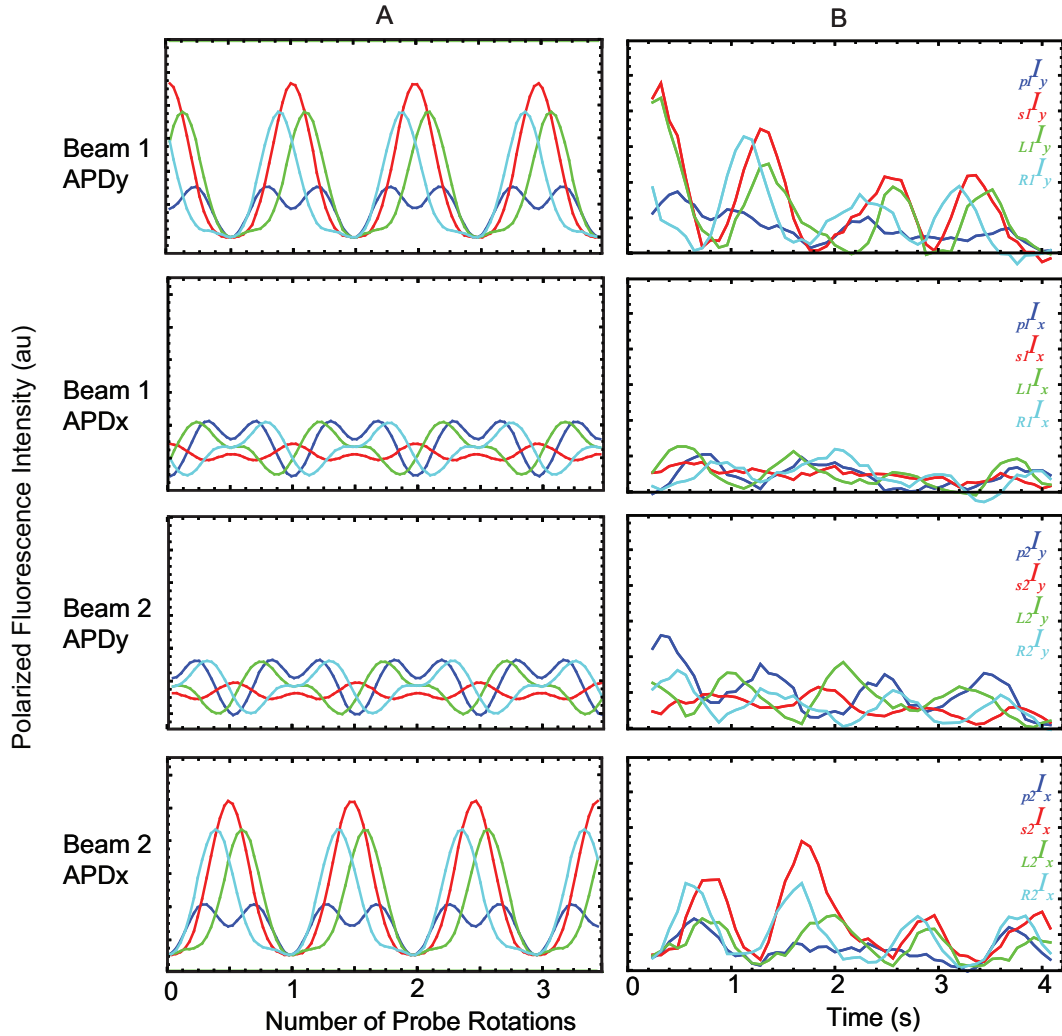
Figure 3.6: Relative phasing amongst the different polarized fluorescence intensities *(colors)* is in good agreement between a simplified simulation $(A)$ and the data from Fig. 3.2 in the text reproduced in $(B)$. The simulation assumes a uniformly twirling probe undergoing -3.5 rotations (i.e., $\Delta\alpha = -1260°$) with $\beta = 45°$, $\delta = 45°$, and $\phi_{actin} = -135°$. The simulated trace does not display the decrease in intensity found in the actual data (see Fig. 3.2 for details and complete maximum likelihood solution).

case if the probe could freely rotate about its attachment point, i.e., $\delta = 90°$. A continuous line for $\alpha$ can then be obtained by shifting the values after each full rotation (Fig. 3.5F) by $360°$.

The angular frequency $\omega$ of filament twirling is calculated from the slope of the line fit to $\alpha$ vs. time. For the filament in Fig. 3.2, $\omega$ was 0.94 rev/s and its linear velocity was 0.24 $\mu$m/s. The direction of rotation for $\alpha$ combined with the direction of motion of the filament, allows

for determination of the handedness of actin twirling. To be sure of this handedness, the 3D orientation of the fluorescence signals was carefully checked with polarizers that extinguish the various polarized incident beams and the sign of the $x$-$y$ coordinates of the camera images by physically moving the stage while observing the video output. The value of the twirling motion pitch is given by the ratio of the linear velocity to angular frequency $v/\omega$, which for the filament of Fig. 3.2 is 0.25 $\mu$m. Simulated polarization intensities of a uniformly twirling filament with parameters similar to those in Fig. 3.5 ($\beta = \delta = 45°$ and $\Delta\alpha = 3$ rotations) are shown for comparison to the data in Fig. 3.6. The traces in Fig. 3.2 agree quite well with the prediction of the simulations despite the simplifications of constant $\beta$ and $\delta$.

Twirling assays were performed over a range of myosin and Mg·ATP concentrations; however, most data were collected at 10 $\mu$M Mg·ATP and 0.1 mg/ml myosin, where filament length was also determined. Recordings were selected for orientation analysis when the total intensity (i.e., the sum over both APD signals for each complete cycle plotted as a function of time, e.g., Fig. 3.4) prior to irreversible fluorophore photo-bleaching was 1.5 - 2× the total background intensity (711 out of 3 528 recordings). For further analysis, the filaments were required to meet several other criteria: (i) approximately constant rotational velocity (i.e., linear fit of $\alpha(t)$ vs. time with |correlation coefficient| $> 0.9$), (ii) a minimum total rotation about the filament axis of 180°, and (iii) a recorded signal duration before bleaching of at least 1.6 s. 144 filaments satisfied these criteria. After checking the 3D orientation results and fitted lines for these filaments, an additional 47 filaments were rejected due to apparent large, abrupt changes in $\theta, \phi,$ or $\delta$ that were inconsistent with a smoothly twirling filament (see Fig. 3.7 and Fig. 3.8 for examples and more detail on the selection process). Of the remaining 97
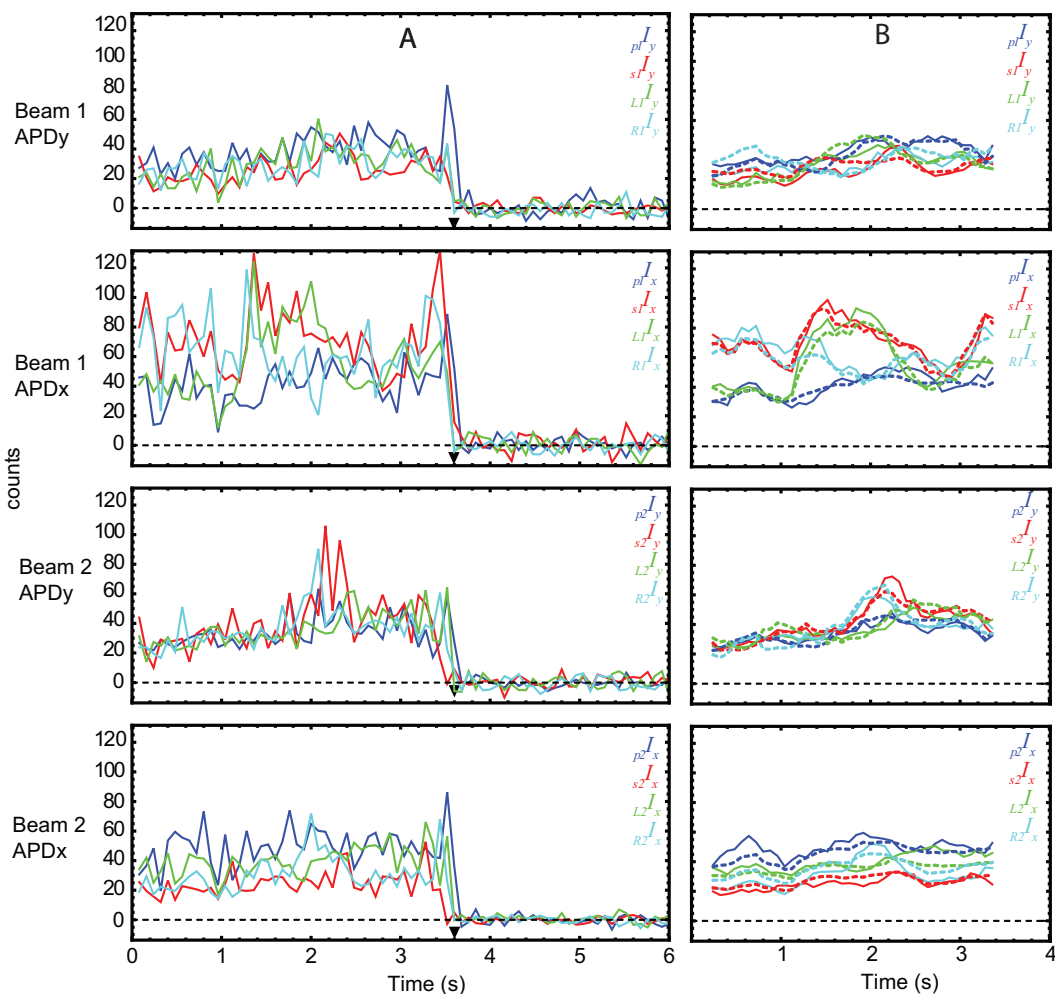
Figure 3.7: Measured polarized fluorescence intensities $(A)$ for a rejected filament. The agreement between the filtered data *(B, solid)* and the maximum likelihood intensity *(B, dashed)* is good despite its rejection. The initial rejection of 2817 molecules was due to missed recording of the molecule (e.g., recording only background), recording of contamination (unreasonably high intensity or irregular intensity), double molecules, etc. These molecules were never analyzed. Of the remaining 711 after the first cut, 567 were rejected because the total rotation was less than $180°$, the bleach duration was less than 1.6 s, or the magnitude of the correlation coefficient $r$ of the linear fit to $\alpha(t)$ was less than 0.9. Of the remaining 144 molecules after the second cut, 47 were rejected due to abrupt change in $\beta$, $\theta$, or $\phi$. Abrupt changes did not occur in $\alpha$ (i.e., they didn't twirl one way and then the other nor did they simply stop twirling), but rather there was a large change in some other angle that was inconsistent with a continuously translocating/twirling filament (see Fig. 3.8).

filaments, 94 and 3 of the filaments twirled with left- and right- handed pitches, respectively.

There was no apparent trend or additional defining characteristic of the rejected filaments.

Approximately 450-550 of the filaments had sufficient duration and signal quality but did not

twirl, thus resulting in a twirling fraction of $\sim 20\%$. Nearly all $(\sim 95\%)$ of the filaments that
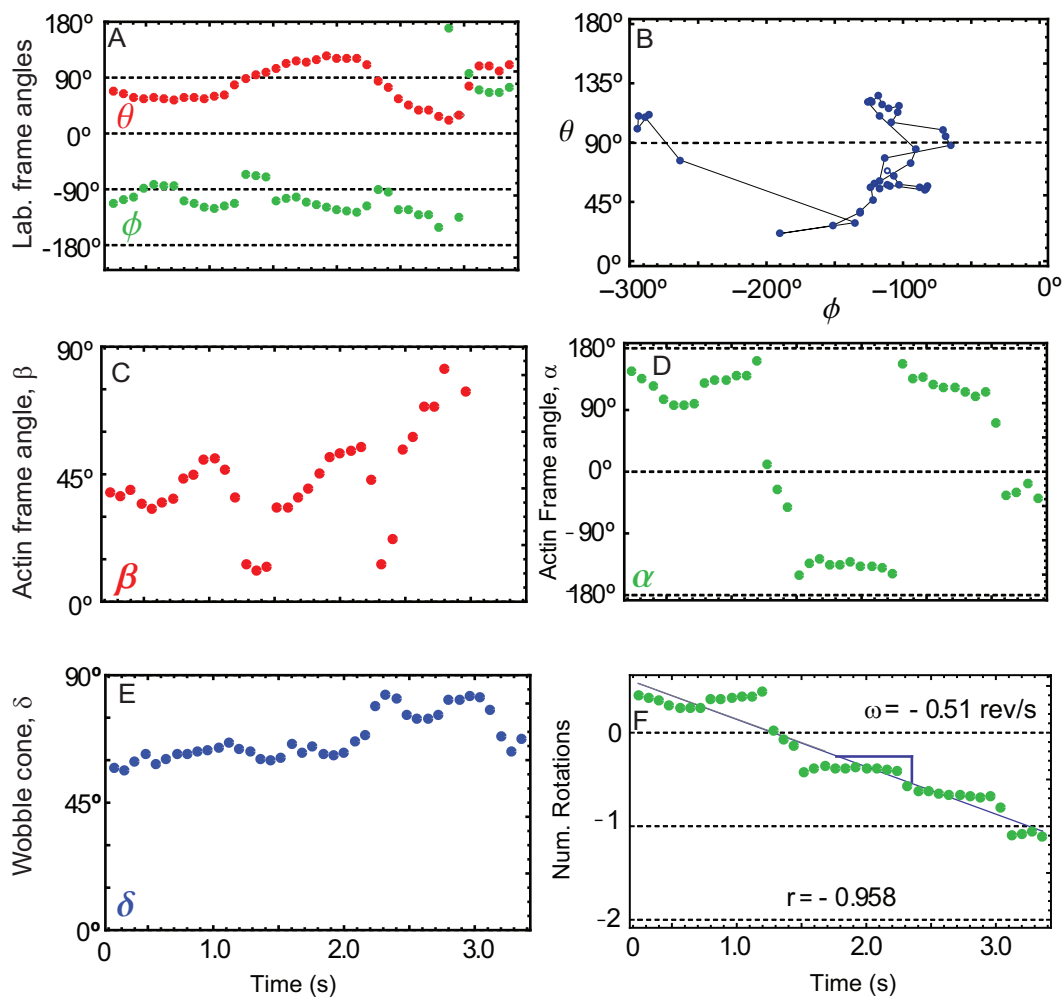
Figure 3.8: Maximum likelihood results for the recording shown in Fig. 3.7. Refer to Fig. 3.5 for detailed descriptions of the parameters in *A-F*. This molecule had a high quality bleach to background (Fig. 3.4) and $|r| > 0.9$, but was rejected because of the abrupt change in $\theta$ and $\phi$ at $\sim 3$ s.

twirled did so with a left-handed pitch, which is opposite to the intrinsic right-handed pitch of actin.

Excluding as outliers the three filaments that seemingly twirled with opposite pitch, the average twirling pitch of $-0.47 \pm 0.2\,\mu$m (mean $\pm$ SD, $n = 94$) is quite long compared to that of the long-pitch actin strands (74-76 nm). The angular velocity of the filaments was correlated with the linear velocity (Fig. 3.9). If the path of a twirling filament was dictated by structural considerations, then the linear and angular velocities would be coupled together in
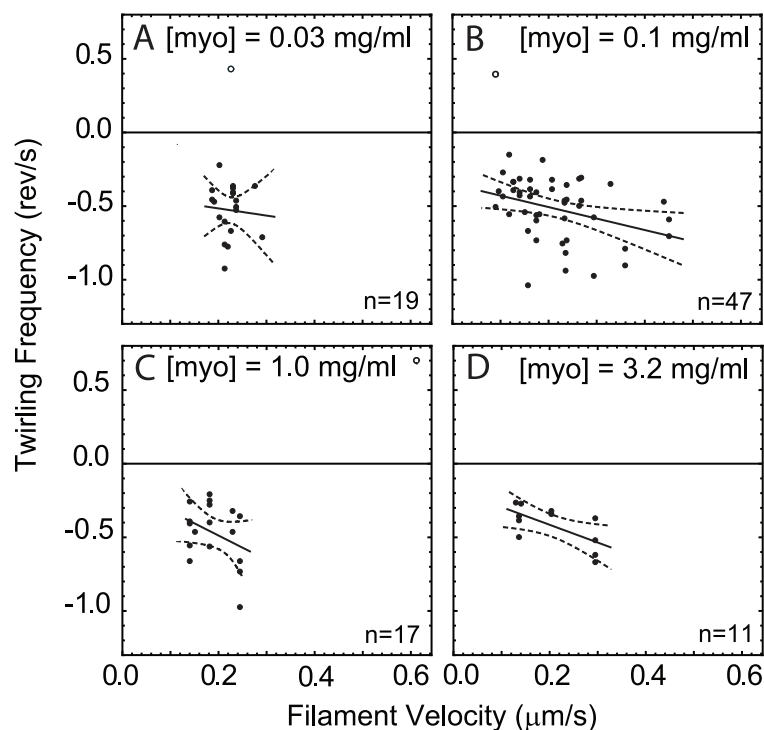
Figure 3.9:   Angular frequency versus average filament velocity with linear fits (*solid*) and 95% confidence interval (*dashed*) for the fitted lines for $(A)0.03, (B)0.1, (C), 1.0, (D)3.2$ mg/ml myosin II loading concentration. Solid points correspond to left-handed twirlers (negative angular frequency). Open points, which are not included in the fit, correspond to right-handed twirlers (positive angular frequency).

direct proportion. The lines fitted to the data at each myosin concentration, however, do not go through zero (angular and linear velocity are not directly proportional), suggesting that kinetic aspects (such as the rate of myosin binding and/or detaching from actin) determine the pitch as well as structural ones.

As myosin concentration loaded into the flow cell increased from 0.03 to 3.2 mg/ml, the velocity of the filaments increased for a fixed Mg·ATP concentration (see Fig. 3.10). Obtaining polarization data from filaments moving faster than $\sim0.25$ $\mu$m/s (corresponding to $> 15$ $\mu$M Mg·ATP and $\gtrsim 1$ mg/ml myosin concentration), however, was difficult using the present polTIRF setup. In order to maximize the time traversing the relatively small APDs,
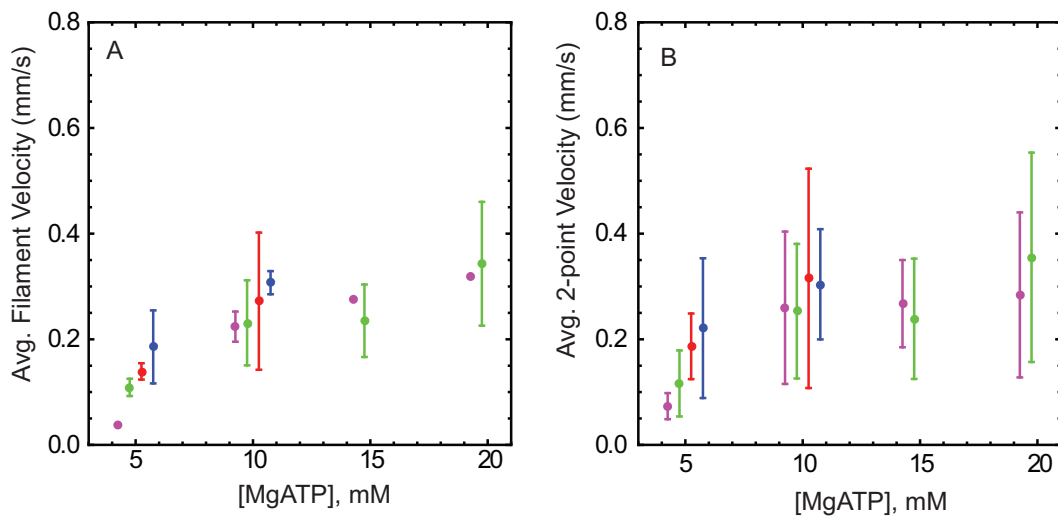
Figure 3.10: Average filament velocities and standard deviations at 5, 10, 15, and 20 $\mu$M Mg·ATP concentrations for the four myosin loading concentrations 0.03 (*magenta*), 0.1 (*green*), 1.0 (*red*), 3.2 mg/ml (*blue*). As discussed in the text, the average in $(A)$ is from 5-7 filaments each recorded for $\sim 30$ frames, and in $(B)$ the average is of all the two-point velocities for each molecule measured from the two CCD images obtained just before the polTIRF recording. The two trends are similar, but the standard deviation of the average in $(B)$ is greater than in $(A)$ since two-point velocity estimates were more variable than the velocity obtained from a longer recording.
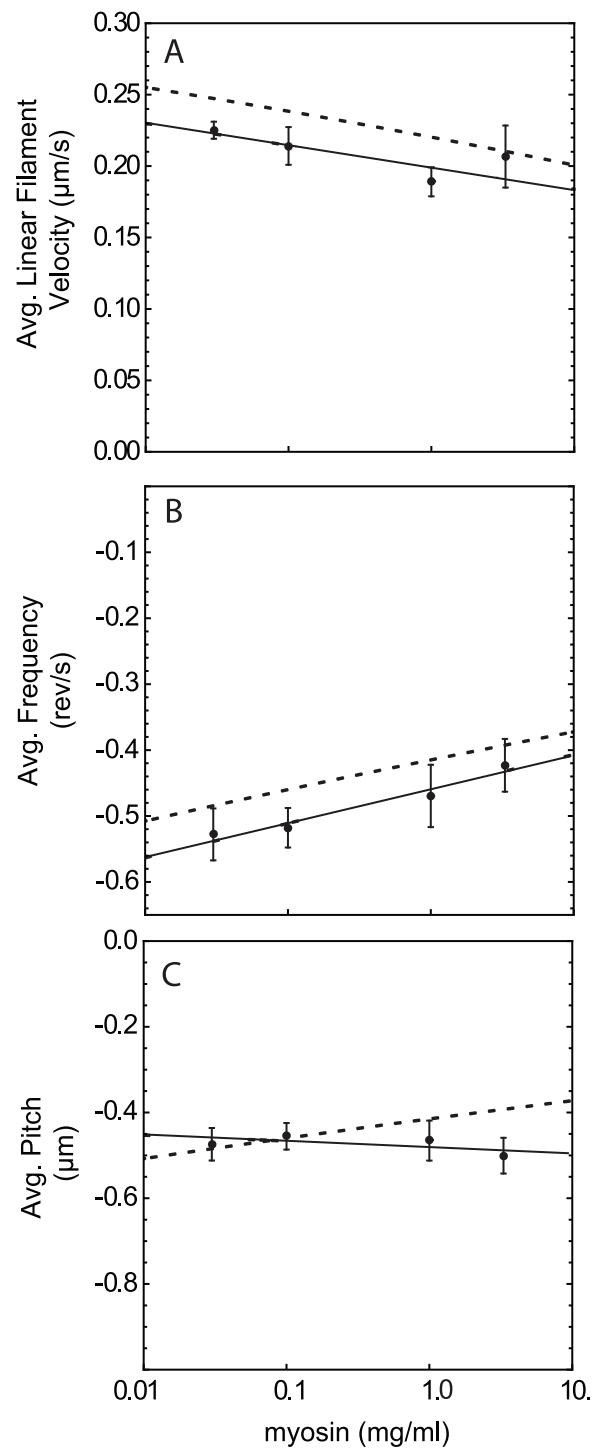
Figure 3.11: Average values and linear fits (*solid*) for (*A*) velocity, (*B*) angular frequency, and (*C*) pitch computed at each myosin concentration (from the data in Fig. 3.9) with error bars determined by the bootstrap method [99]. Negative values of angular frequency indicate left-handed rotation in the actin reference frame. The magnitude of the twirling frequency decreased with increasing myosin concentration while the velocity of the filaments was relatively constant. Predictions (*dashed*) in each panel are calculated from the fits of the other two panels using the relation pitch $= v/\omega$ and are in approximate agreement with their respective fits.

lower Mg·ATP concentrations were used at the higher myosin concentrations in most of the experiments. As a result, when the data from Fig. 3.9 were averaged and considered versus myosin concentration, the linear velocity (Fig. 3.11A) and pitch were fairly constant (Fig. 3.11C). A slight decrease of the magnitude of the (negative) angular frequency over this range (Fig. 3.11B) is not statistically significantly.

At 0.03 and 0.1 mg/ml myosin concentrations, filament velocity is independent of filament length, see Fig. 3.13, as reported previously [122]. The twirling frequency and pitch are also insensitive to filament lengths longer than $\sim 1\,\mu$m (Fig. 3.12). Filament twirling by myosins II is summarized in Table 3.1 and also compared with myosin V [123] and VI [124] data.

## 3.4   Discussion

### 3.4.1   Angular scope of polTIRF measurements

Several previous reports [59, 65, 113, 115, 116] have indicated that under various conditions, myosin isoforms produce a torque either in conjunction with axial force production, or while stepping along actin in a helical path. Previous work using polarized total internal fluorescence (polTIRF) microscopy [65] indicated filament twirling; however, symmetries in the measurement of the probe orientation resulted in an ambiguous sign for the azimuthal angle and thus did not report the handedness. These symmetries were broken here by incorporating incident polarizations ($L$ and $R$) that are intermediate between $p$ and $s$ into the polTIRF method [117]. The only remaining ambiguity of probe orientation is unavoidable due to its inherent dipole symmetry: $(\theta, \phi)$ is equivalent to $(\pi - \theta, \pi + \phi)$.
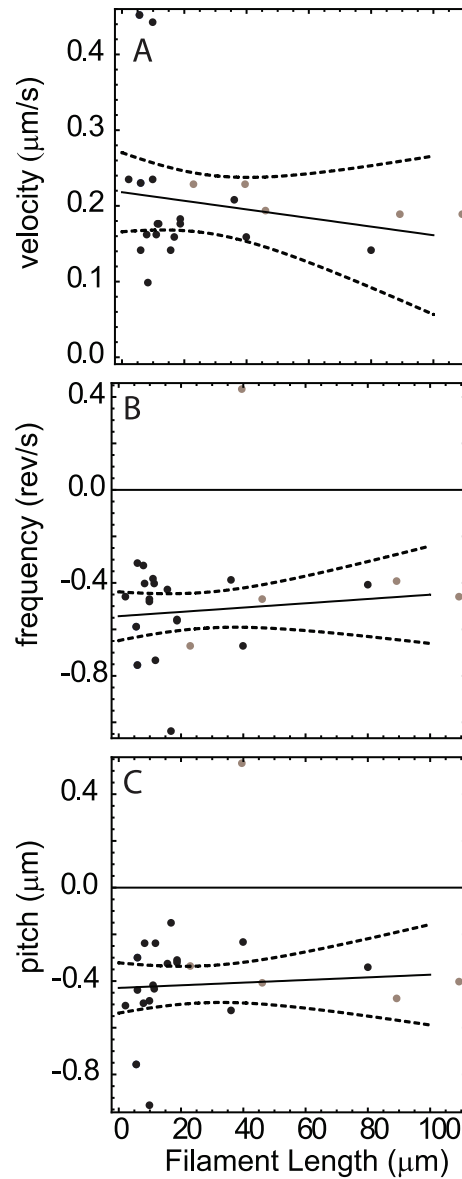
Figure 3.12: Average ($A$) velocity, ($B$) angular frequency, and ($C$) pitch as a function of filament length at 0.03 ($gray$) and 0.1 mg/ml($black$) loading concentration of myosin with linear fits ($solid$) and 95% confidence interval of the fit ($dashed$).

Recordings of actin filaments, labeled with rhodamine at Cys374, and gliding under the propulsion of myosin isoforms II, V [123], or VI [124] corresponded to oscillations of the probe orientation $(\theta, \phi)$, which in the actin frame of reference were consistent with a fairly constant axial angle $\beta$ and linearly increasing or decreasing azimuthal angle $\alpha$. This angular response of the probe during motility shows that the filament often twirls about its axis during

77
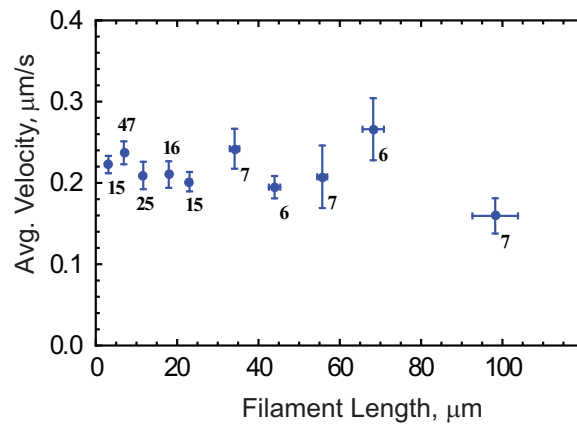
Figure 3.13: Average filament velocity (including twirling and non-twirling filaments) at myosin loading concentrations of 0.03 and 0.1 mg/ml is independent of filament lengths between 1-100 $\mu$m.

translocation, and also confirms that the method, with the additional input polarizations and the attendant analysis, resolves the probe orientation within a hemisphere as expected. Twirling generated by myosin II and V has a strong left-handed bias while twirling by myosin VI was strongly right-handed, arguing against a dominating experimental artifact, which would likely result in twirling with either handedness independent of the myosin isoform.

### 3.4.2   Non-twirling filaments

Similar to earlier reports [115], only $\sim$ 20% of the filaments translocated by myosin V showed clear twirling rotations. In the twirling assay with myosin II most of the filaments translocated, but only 20% clearly twirled, thus indicating that azimuthal rotation is not necessary for gliding. In this work, probe orientation and location were not measured simultaneously; consequently the initial direction of gliding was assumed to be maintained during the polarization analysis. If a filament were to undergo large, unobserved changes in this motion, such as stopping or turning, it would likely be rejected during screening of the filaments. Such motions, however, are unlikely to account for all of the non-twirling filaments since U-turns and stopping events were observed for only 10-20% of filaments during a 30 s observation, which is much less than the 80% of filaments that did not twirl. Non-twirling filaments were difficult to characterize, but they rarely exhibited steady $\alpha$ and $\beta$ orientations, which would be expected if the filament slides perfectly straight or stops moving completely, as is seen when ATP is omitted [65].

The suspended-filament bead assay reported earlier for myosin V [115] and VI [116] showed that often the motors stepped straight along the filament, rather than in a helical path.

Thus, both twirling and non-twirling motions are observed in experiments with single motors and in gliding assays where multiple motors are involved.

### 3.4.3 Handedness of twirling

Measuring the probe orientation unambiguously for half of a rotation or more allows the direction of angular rotation to be determined. Combining this angular direction with the direction of filament sliding indicates the handedness of actin filament twirling; a feature not obtained in previous experiments using single molecule polarized fluorescence [59, 65]. When filaments twirl by fast skeletal whole myosin II and native myosin V from chick brain, they consistently have a left-handed pitch, opposite to the intrinsic right-handed long pitch of actin. Filaments twirled with a relatively long pitch of 0.47 and 1.7 $\mu$m for myosin II and V, respectively, see Table 3.1. Myosin VI twirls filaments with the opposite, right-handed pitch [124]. Right-handed twirling by myosin VI is not simply due to its "backward" pointed-end directed motility, as can be realized by considering a nut twirling on a machine screw, where the handedness is the same for tightening and loosening. Preliminary twirling experiments using myosin V with a truncated lever arm, having only 4 calmodulin-binding IQ motifs, twirls a higher fraction of filaments to the right than full-length myosin V with 6 IQ-motifs per head (J. H. Lewis, personal communication). The truncated lever arm results suggest that the handedness is related to the step distance of these molecules.

Single and multiple molecules of myosin V move a proportion (20%) of bead duplexes in a helical path around a suspended actin filament [115] with the same left-handedness and a similar pitch (2.2-2.5 $\mu$m) as twirling filaments in the gliding assay, pitch $\sim 1.7\,\mu$m. Similar

| Myosin Isoform | II | V [123] | VI [124] |
|---|---|---|---|
| Myosin, mg/ml | 0.1-3.3 | 0.26 | 0.26 |
| Ave. Velocity,$\mu$m/s | 0.091-0.61 | 0.07-0.27 | 0.09 - 0.21 |
| ATP, $\mu$M | 5 - 20 | 10 - 2000 | 500 - 1000 |
| Handedness | Left | Left | Right |
| Number$^\star$ | 94 | 42 | 23 |
| Frequency, rev/s | -0.50$\pm$0.19 | -0.12$\pm$0.12 | 0.14$\pm$0.05 |
| Total Rotation $\Delta\alpha$ , rev | -1.4$\pm$0.7 | -0.6$\pm$0.4 | 0.7 $\pm$0.4 |
| Pitch, $\mu$m | -0.47$\pm$0.19 | -1.7$\pm$0.6 | 1.3 $\pm$0.5 |
| Probe Angle $\beta$, $^\circ$ | 49$\pm$19 | 55$\pm$12 | 54 $\pm$9 |
| Slow Wobble $\delta$,$^\circ$ | 48$\pm$17 | 30$\pm$13 | 30 $\pm$11 |

Table 3.1: Summary of actin filament twirling by myosins II, V and VI (mean $\pm$ SD). The range of angular rotations ($\Delta\alpha$) for myosins II, V and VI are -0.5 to -4.4, -0.09 to -1.8, and +0.2 to +2.0 rotations, respectively. 'Number' indicates those molecules twirling with the dominant handedness, which are the basis for the other average values in the table (see text for details). $^\star$A minority of filaments (3, 1, and 0 for myosins II, V, and VI, respectively) twirled with the opposite handedness, and are not included in the table averages.

experiments with myosin VI [116] gave a right handed pitch, in agreement with the polTIRF twirling assay [124], although the pitch of the bead-duplex path was longer (2.2-5.6 $\mu$m) than the twirling pitch ($1.3 \pm 0.1\,\mu$m) in the gliding assay. Regardless of whether multiple motors, fixed on a microscope slide, were translocating actin, or a single motor was stepping along a suspended filament, the rotational motion is similar. This agreement in handedness between the two different assays suggests that a similar mechanism underlies torque generation in these two geometries.

Formation of actin filament superhelices by HMM translocating filaments at 1 mM Mg·ATP [113] indicate a right-handed torque, opposite to that of the twirling actin filaments obtained here. This discrepancy might arise from the difference in Mg·ATP concentration, which was higher in the superhelix experiments and limited in the twirling experiments to produce velocities compatible with time resolution and size of the photodetector in the present setup. Another difference is that the supercoiling filaments [113] were specifically attached to the slide at their pointed ends and the remaining filament forced to buckle by a track of HMM, created by decorating the filament prior to surface attachment. Twirling filaments here were moved by myosin molecules randomly distributed on the surface.

### 3.4.4   Possible mechanisms of twirling

The mechanisms responsible for twirling filaments are not known, but the experiments presented here suggest several possible effects: a torque component to the myosin power stroke [113, 115], the step size of myosin relative to the actin filament helix [59, 115], or the drag force of rigor heads on the filament. A torque between myosin and actin could arise if the vec-

tor of the myosin working stroke is not parallel to the axis of the actin filament, thus resulting in a small angular component to the velocity in addition to the linear component. An estimate of the vectorial direction of the working stroke for myosin II can be obtained from crystal structures in the pre-power stroke position [125] and near the end of the power stroke [126] when both structures are docked into cryo-electron microscopy density maps of actin decorated with myosin subfragment-1 [106]. The flexible joint between the light chain domain and myosin rod is located near Lys843 of chicken skeletal myosin. Between the pre-power stroke and the near rigor state of the docked structures, Lys843 moves predominantly along the filament axis, but with a slight $(\sim 20^\circ)$ right-handed tilt relative to the actin axis. A tilt in the other direction would be required to induce the typical twirling pitch that was detected in myosin II and V. Thus the left-handed twirling that was observed is not explained by the path of the power stroke, unless the docked structures are misoriented by at least $20^\circ$. Also, if the torque is generated directly by the working stroke, then a strong coupling between linear and angular velocities would be expected in the twirling assay. The twirling measurements discussed here, however, show only weak coupling between these two quantities.

Alternatively, the handedness seen in processive bead assays [115, 116] could arise from the interaction between the stride length of myosin and the helical disposition of the actin monomers. Actin filaments are torsionally flexible, but often approximated as a 13/6 helix when interpreting the path of myosins on actin [115, 116]. The 13/6 index defines an actin filament with monomers disposed around the left-handed short-pitch 'genetic' helix rotating 6 full turns in 13 monomers. Starting from the zeroth actin monomer as the origin, the 13th monomer along this short pitch helix is located at the same azimuthal orientation around the

filament as the original one. Each monomer is $360° \cdot (-6/13) \approx -166°$ azimuthally around the short pitch helix (negative sign means to the left). The 2$^{nd}$ monomer is positioned at: $-166° \cdot 2 = -332° = 360° - 332° = 28°$ , i.e., on the right-handed long-pitch strand. On the 13/6 helix, a motor whose stride is 13 monomers ($\sim 36$ nm) would walk straight. Left-handed rotation would arise if the motor made more 11 monomer steps than 15, and vice versa for a right-handed helical path.

Electron micrograph data showing the spacing of myosin V rigor heads bound to actin [127] indicated a distribution of stride lengths spanning mostly 13 monomers, and significant amounts of 11 and 15 monomer spans. There were more 15s than 11s, which would imply a bias toward a right-handed helical path. Our twirling results and the experiments with suspended actin filaments [115, 116], however, show left-handed bias.

Reference [128] pointed out that this apparent discrepancy would be resolved if the filament structure is not a 13/6 helix. For instance a 28/13 helix, which has also been observed [129] has an azimuthal rotation of the left-handed genetic helix of $360° \times (-13/28) \approx -167°$ . The 13$^{th}$ and 15$^{th}$ actin monomers are positioned at 13° to the left and right of the axial (straight) direction, respectively. Then a motor, such as myosin V, which takes more 13-monomer steps than 15s (as shown in the EM distribution of spans [127]) would walk slightly left-handed, as we observe.

Myosin VI adopts a straight or slightly right-handed helical path [116, 124]. This was interpreted as indicating an even longer stride than myosin V [115], but it could also indicate the presence of much shorter steps, for instance the proper ratio of 6 and 7 monomer steps on a 13/6 helix (azimuthally oriented at 83° to the left and right, respectively) could also

result in a slight right-handed helical pitch. Myosin VI has a very wide distribution of step sizes [124, 130], making the azimuthal path of the individual molecules highly variable [124].

It is less clear how to extend the effect of stride-length to the smaller, non-processive steps of myosin II. If they followed the long-pitch actin helix, then myosin II would twirl actin with a short right-handed pitch (74 nm) and not the more gradual left-handed motion that is observed. The step-size idea also predicts a strong correlation between linear velocity and azimuthal twirling frequency, variables that are only weakly correlated in the data here Fig. 3.9).

Theoretical modeling [131] suggests that left-handed actin twirling by non-processive myosin in a gliding assay arises from myosin heads preferentially binding to actin monomers that approach at the correct azimuth. This preference arises because only a fraction of the monomers, which are helically distributed around the filament, lie within a range of azimuthal orientations suitable for binding of myosin ("target zone" [132]). These monomers are presented to the head at regular intervals as the filament translocates above it. In the 13/6 actin helix, if the myosin head binds to the 13 monomer, then the filament would glide straight (black arrow in Fig. 3.14A). If attachment is very fast, however, then monomers within the range of acceptable azimuths (e.g., the hatched area in Fig. 3.14A) and leading the center of the target zone (e.g., number 11) will become the preferred binding site. In a gliding assay the torque arises as the left-of-center monomer (monomer 11) is pulled in toward the filament axis during the stroke (red arrow) analogous to the mechanism proposed for the processive bead assays [115, 116]. A prediction of this model is that an experiment at higher ionic strength, which would weaken myosin binding to actin, might show straighter or even right-handed
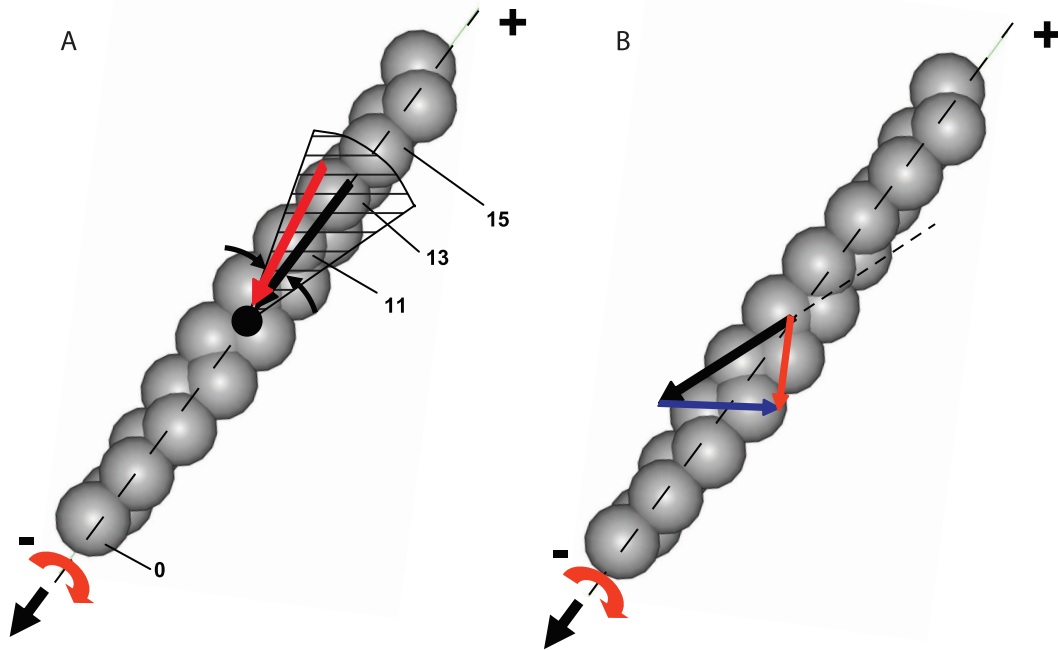
Figure 3.14: Two models for actin twirling: (*A*) Target zone model. Monomer 11 of the translocating actin filament (*gray helix*, pointed-end up) enters the target zone *(shaded)* of the myosin head *(black dot)* before monomer 13 and therefore binds more rapidly to myosin, despite lying slightly off the filament axis. Twirling of the filament occurs during the power stroke as monomer 11 is pulled predominantly along the direction of filament motion, but also in toward the filament axis *(red arrow)*. Myosin attachment to on-axis monomer 13, however, would translocate actin during the power stroke without twirling the filament *(black arrow)*. For convenience, monomers are labeled relative to a supposed previous binding site one helical repeat away at monomer 0 along the 13/6actin helix. (*B*) Rigor drag model: Hypothetical motions for myosin attached to actin are shown by arrows at a possible binding site along the actin helix. The motion due to the power stroke of the myosin heads attached to actin *(solid black)* is mostly along the *z*-direction, but may also apply a slightly right-handed torque [106, 113]. The drag due to the rigor heads attached to actin *(blue)* retards the linear motion, but instead of acting along the same direction as the power stroke *(dotted black)*, it is sufficiently skewed to cause the resultant motion *(red)* to be slightly left-handed.

twirling. Higher velocity filaments, due to higher Mg·ATP concentrations, might also affect the twirling pitch by altering which monomers within the target zone are the most likely binding sites.

Finally, the drag force of the rigor heads, which are bound tightly to actin, is considered since they are probably the dominant retarding force on a gliding actin filament at the low Mg·ATP concentrations used here. If forward motion of the filament is due to a nearly straight

or slightly right-handed power stroke [113], then left-handed twirling may result from a drag force due to rigor heads pulling backwards but also slightly laterally. Hopkins et al. [133] measured tilting and twisting of myosin regulatory light chains in muscle fibers. They reported a twisting motion of the myosin (i.e., the $\gamma$ angle) when a rigor muscle is allowed to shorten, but no twisting in an active muscle. The analogous drag force of rigor heads in a gliding assay would result in a left-handed torque to the gliding filament. In Fig. 3.14B, the resultant velocity (red arrow) on an actin filament is shown as the vector sum of velocities due to the power stroke (black arrow) from active heads and drag from strongly attached rigor heads (blue arrow). The rigor-drag hypothesis may explain the insensitivity of twirling to filament length and myosin concentration because twirling would instead be attributed to the ratio of active and rigor heads along the filament and not their absolute number. Unlike models that explain twirling via a direct structural coupling between linear and angular velocity, the rigor-drag hypothesis would predict a larger pitch at higher Mg·ATP concentrations because linear velocity would increase as angular velocity decreased (since there are fewer rigor heads bound to actin). This prediction has not been tested critically in this work or previous experiments [59] due to the limited range of Mg·ATP concentrations tested. Since the fraction of heads bound to a filament in the rigor state decreases at high Mg·ATP concentrations, the tendency to twirl with a left-handed pitch would be reduced, and thus possibly reconcile the difference between the left-handed twirling at low Mg·ATP concentrations measured in this work with the experiments by Nishizaka et al. [113] that showed a right-handed torque at high (2 mM) Mg·ATP concentration.

### 3.4.5 Conclusions

PolTIRF has been extended to enable measurement of probe angles within a hemisphere of solid angle. It has been used to determine the handedness of twirling actin filaments gliding over a surface containing myosin II. Approximately 20% of analyzable filaments, translocated by myosin II, twirled with left-handed pitch. The magnitude of the pitch depends on myosin isoform, but for myosin II is insensitive to filament velocity, filament length or myosin concentration in the range investigated. A torque component to the working stroke, the myosin stride length, the helical distribution actin monomers, and the drag of rigor myosin heads may contribute to the azimuthal force component in a gliding assay, but no single one of these influences adequately describes the rotational motions observed.

## 3.5 Appendix

### 3.5.1 $\pm 45°$ degree polarization terms

In order to determine the $3D$ orientation and rotational ('wobble') motions of a single fluorescent molecule, measured polarized fluorescence intensities are compared to intensities that are calculated from a theoretical model of the molecule. This model approximates the probe as an electromagnetic dipole $\hat{\mu}$ (see main text and [63]) that absorbs and emits photons polarized preferentially along its dipole axis. This appendix derives the equation for calculating the intensity $I$ of a probe oriented with respect to both the polarization direction of the detector and the linearly polarized electric field of the incident illumination:

$$_{\hat{\varepsilon}}I_{\hat{\alpha}} = \kappa \cdot P_a(\hat{\mu}_a, \hat{\varepsilon}) \cdot P_e(\hat{\mu}_e, \hat{\alpha}) \tag{3.5.1}$$

Where $I$ is the rate of photons collected from a static dipole $\hat{\mu}$ with probability $P$ of absorbing $(a)$ or emitting $(e)$ photons relative to the incident electric field polarization $(\hat{\varepsilon})$ or analyzer $(\hat{\alpha})$. $\kappa$ is an overall normalization factor. The complex quantity $(\hat{\varepsilon})$ describes the polarization of the electric field $\mathbf{E}$, but not its magnitude $E_0$:

$$\mathbf{E} = E_0 \hat{\varepsilon} e^{-z/d} e^{-i\omega t} \tag{3.5.2}$$

$\hat{\varepsilon}$ can be decomposed into its Cartesian components:

$$\hat{\varepsilon} = \left[ \hat{x}\varepsilon_x e^{-i\delta_x} + \hat{y}\varepsilon_y e^{-i\delta_y} + \hat{z}\varepsilon_z e^{-i\delta_z} \right] \tag{3.5.3}$$

This appendix is concerned with the new features of the model required for the off-axis incident polarizations $(L1, R1, L2, R2)$; thus only the terms describing the absorption proba-

bility, $P_a$, need to be modified:

$$P_a(\hat{\mu}_a, \hat{\varepsilon}) \equiv |\hat{\mu}_a \cdot \hat{\varepsilon}|^2 \tag{3.5.4}$$

$$\propto (\varepsilon_x^2 \mu_x^2 + \varepsilon_y^2 \mu_y^2 + \varepsilon_z^2 \mu_z^2 + 2\varepsilon_x \varepsilon_y \mu_x \mu_y \sin(\delta_s - \delta_p) \tag{3.5.5}$$

$$+ 2\varepsilon_y \varepsilon_z \mu_y \mu_z \cos(\delta_s - \delta_p))$$

Note that for Beam 2, $\varepsilon_x$ should be replaced with $\varepsilon_y$ and *vice versa* in Eq. (3.5.5). Similarly for $\mu_x$ and $\mu_y$.

Calculations are performed in the reference frame of the microscope; where $z$ points into the objective and the $x$-$y$ plane is parallel to the stage with the $x$ and $y$ axes along the direction of propagation of Beam 1 and 2, respectively, see Fig. 3.3. The orientation $(\theta, \phi)$ of the dipole in this frame is given by $\hat{\mu} = (\sin(\theta)\cos(\phi), \sin(\theta)\sin(\phi), \cos(\theta))$. The Cartesian components of $\hat{\varepsilon}$ in the microscope frame are determined from the magnitude of the $s$ and $p$ polarizations. The $s$ component of $\varepsilon$ is entirely in the $y(x)$ direction for Beam 1(2). Due to the shallow glancing angle $(\theta_i)$ of the incident beams, the $p$ component of $\varepsilon$ is predominantly normal to the reflection plane ($\varepsilon_{p,n} \sim \hat{z}$); however the small tangential component ($\varepsilon_{p,t} \sim \hat{x}$ and $\hat{y}$) in Beam 1 and 2, respectively, is also included in the analytical expressions. The cross terms ($4^{th}$ and $5^{th}$ terms of Eq. (3.5.5)) arise when the polarization of the electric field, given by angle $\zeta$, is intermediate between $p$ and $s$. The components of the evanescent field are given by:

$$\varepsilon_{p,t} = -2\cos(\zeta)\cos(\theta_i)\sin(\delta_p)$$

$$\varepsilon_{p,n} = 2\cos(\zeta)\sin(\theta_i)\cos(\delta_p)/\zeta^2$$

$$\varepsilon_s = 2\sin(\zeta)\cos(\delta_s) \tag{3.5.6}$$

90

Where $\tilde{\zeta}$ is the ratio of the indices of refraction in the aqueous solution to the higher index slide material at the reflecting surface, and $\zeta = +45°$ and $-45°$ for $\varepsilon_L$ and $\varepsilon_R$, respectively.

$$
\begin{aligned}
\cos^2(\delta_p) &= \frac{\tilde{\zeta}^4 \cos^2(\theta_i)}{\tilde{\zeta}^4 \cos^2(\theta_i) + \sin^2(\theta_i) - \tilde{\zeta}^2} \\
\sin^2(\delta_p) &= \frac{\sin^2(\theta_i) - \tilde{\zeta}^2}{\tilde{\zeta}^4 \cos^2(\theta_i) + \sin^2(\theta_i) - \tilde{\zeta}^2} \\
\cos^2(\delta_s) &= \frac{\cos^2(\theta_i)}{1 - \tilde{\zeta}^2}
\end{aligned}
\tag{3.5.7}
$$

The previous equations describe a static dipole. As described in more detail in [63], rotational motions of the dipole are separated into a fast and slow time scale. Rapid motions that re-orient the dipole on a time scale faster than the $\sim 4\,\text{ns}$ fluorescent lifetime are assumed to occur within a wobble cone of half-angle $\delta_f$. Rotational motion of the probe on time scales slower than $\sim 4\,\text{ns}$, yet faster than the $10\,\text{ms}$ illumination time are assumed to occur within a wobble cone of half-angle $\delta$. See Reference [2] for a complete derivation of these terms, which are used in a Levenberg-Marquardt C code to find the parameters $(\theta, \phi, \delta, \delta_f, \kappa)$ that maximize the likelihood of the measured intensities.

### 3.5.2 Calibration factors

Calibration factors are defined for the additional $L$ and $R$ excitation polarizations:

$$_{p1}I_y = {}_{p1}I_y^r$$

$$_{p1}I_x = {}_{p1}I_x^r/C_d$$

$$_{s1}I_y = {}_{s1}I_y^r/X_1$$

$$_{s1}I_x = {}_{s1}I_x^r/(X_1 \cdot C_d)$$

$$_{p2}I_y = {}_{p2}I_y^r/X_{12}$$

$$_{p2}I_x = {}_{p2}I_x^r/(X_{12} \cdot C_d)$$

$$_{s2}I_y = {}_{s2}I_y^r/(X_2 \cdot X_{12})$$

$$_{s2}I_x = {}_{s2}I_x^r/(X_2 \cdot C_d \cdot X_{12})$$

$$_{L1}I_y = {}_{L1}I_y^r/X_{L1}$$

$$_{L1}I_x = {}_{L1}I_x^r/(X_{L1} \cdot C_d)$$

$$_{R1}I_y = {}_{R1}I_y^r/X_{R1}$$

$$_{R1}I_x = {}_{R1}I_x^r/(X_{R1} \cdot C_d)$$

$$_{L2}I_y = {}_{L2}I_y^r/(X_{L2} \cdot X_{12})$$

$$_{L2}I_x = {}_{L2}I_x^r/(X_{L2} \cdot C_d \cdot X_{12})$$

$$_{R2}I_y = {}_{R2}I_y^r/(X_{R2} \cdot X_{12})$$

$$_{R2}I_x = {}_{R2}I_x^r/(X_{R2} \cdot C_d \cdot X_{12}) \tag{3.5.8}$$

Where $C_d$ and the various $X$'s represent the 8 calibration factors, and the $r$ superscript indicates a raw polarized fluorescence intensity. Calibration data is obtained by recording three

background measurements followed by three recordings of a 15 nM solution of Rhodamine B in 5% dimethylformamide that is flowed into the sample chamber (see Reference [63] for details). The calibration factors are obtained from a model similar to the one described in Appendix 3.5.1, but modified to accommodate multiple molecules free in solution by increasing the wobble cone to $\delta = 90°$.

### 3.5.3 Twirling analysis

The path traced out by a probe bound to an actin filament that is twirling about its longitudinal axis is evident in two different representations of the angular motion. First a plot of $\theta$ vs. $\phi$ for one rotation of the probe traces out a circle that is centered at $(90°, \phi_{actin})$ where $\phi_{actin}$ is the direction in the $x$-$y$ plane of the actin filament translocation. The reason that $\theta = 90°$ is because a probe that is attached to a filament, which is uniformly twirling about its axis in the $x$-$y$ plane, maps out a locus of points that lie along the surface of a cone with symmetry axis in the $x$-$y$ plane. Alternatively, the probe orientation can be represented in the $(\beta, \alpha)$ reference frame of the actin filament [65], where $\beta$ is the polar angle with respect to the actin axis toward the forward moving end of the actin filament and $\alpha$ is the azimuthal angle around the filament; for details, see Fig. 3.3. In the actin frame a uniformly left-hand twirling filament has a constant $\beta$ and a decreasing $\alpha$ with a constant rate equal to the angular velocity ($\omega$) of the twirling motion.

The inherent dipole symmetry implies two equally valid solutions to Eq. (3.5.1): $(\theta, \phi)$ and $(\theta', \phi') = (180° - \theta, \phi + 180°)$, either of which the numerical solver can obtain. Consequently, we need to determine one set of solutions that describes the trajectory of one end

of the dipole. This is relatively straight-forward for a uniformly twirling filament because subsequent orientations of the dipole should be nearby previous orientations. Prior to quantifying any twirling motions, we determine the minimum trajectory by choosing the orientation at time $t$ (either $(\theta, \phi)_t$ or $(\theta', \phi')_t$) that is closer to the orientation at $t - 1$ and then repeat for the entire trace. Mathematically, we accomplish this by choosing $\hat{\mu}_t$ that minimizes: $\psi_t = \arccos(\hat{\mu}_t \cdot \hat{\mu}_{t-1})$. We arbitrarily choose the initial probe orientation as the one that points closer to the direction of positive translocation.

In order to reduce the impact of a single spurious point on the entire trajectory, the process is repeated omitting the point with the largest $\psi$ to make sure the path of the minimum trajectory does not change. If $\phi_{t'}$ crosses the hemisphere from $+180°$ to $-180°$ then $360°$ is added to $\phi$ values with $t > t'$ in order to generate a continuous trajectory (similarly, $360°$ is subtracted for crossings in the opposite direction). Sometimes this automated detection fails and we manually shift the data onto a more confined trajectory in order to undo unrealistically large and sudden angle changes.

In order to transform angles into the actin frame, we rotate the twirling axis of the filament to align with the $x$-axis (i.e., $\phi' = \phi - \phi_{\text{actin}}$) and apply the transformation:

$$\alpha = \arctan2(\mu_y, \mu_z)$$

$$\beta = \arccos(\mu_x) \tag{3.5.9}$$

Where $\alpha = \arctan2(\mu_y, \mu_z)$ is similar to $\alpha = \arctan(\mu_y/\mu_z)$ but with a larger range of unique angles: $-180° < \alpha < 180°$. After this transformation, a uniformly rotating probe will exhibit a constant $\beta$ and a sawtooth pattern for $\alpha$, which repeats after every rotation. In order to determine the angular velocity, $\omega$, we fit a line to $\alpha$ after first shifting all $\alpha$'s after

each complete right (left) handed rotation by $+(-)360°$. Because $\phi_{actin}$ is determined from only two CCD frames, we sometimes manually adjust $\phi_{actin}$ to minimize the error of the fit, usually only within $\pm 30°$ and never by more than $90°$, which would change the handedness of rotation. Due to the probe's dipole symmetry, orientations that are aligned with $\alpha = 0°$ and $180°$ have identical intensities in all 16 polarizations. These points are manually adjusted by $\pm 180°$ prior to fitting the line to $\alpha$.

# Chapter 4

# Multiple Intensity Change Point

# Algorithm

## 4.1 Introduction

The goal of polarized TIRF (polTIRF) measurements is to determine the orientation and wobble of a single fluorescent molecule. The approach discussed in Sect. 3 accomplishes this by comparing the relative magnitudes of the different polarized fluorescence intensities (PFIs) measured in 10 ms width bins to those predicted by a dipole model of the probe. Incorporating single photon counting (SPC) technology into polTIRF (Sect. 5) allows the intensities to be determined in arbitrarily long or short regions of the data since there is no binning of the photons. The question becomes: When during the recording does the intensity change? Change point analysis provides a statistically rigorous way to answer this question by locating the point in the data where the intensity abruptly changes magnitude but is otherwise constant

in the two flanking regions. The advantages of this approach are that no artificial time base due to binning is imposed on the data, there is no need for user adjustable thresholds that separate the molecule into supposedly different states, and there is no assumed model or kinetic scheme. Instead, abrupt intensity changes in the raw data are identified assuming only that the photons arise from a random Poisson process, independent of any model.

PFIs that change magnitude in sudden discrete steps, but are otherwise constant would not be a good description of the continuously varying PFIs measured twirling experiments, but it would be a reasonable model for a myosin V molecule that takes steps along an actin filament. Section 5 describes polTIRF measurements of a bifunctional rhodamine labeled calmodulin attached to the myosin V lever arm. At low Mg·ATP concentrations, the molecule dwells for a relatively long time before binding ATP and rapidly stepping to the next actin binding site. The ultimate goal of the algorithm is to find change points in the PFIs recorded from a rhodamine probe undergoing these orientation changes. After locating the change point in the recording, the PFIs in the intervals between adjacent change points are input to the dipole model (see Sect. 3.2.4) to determine the molecule's orientation and wobble during the recording.

The single intensity case for detecting change points in SPC data was thoroughly developed by Watkins and Yang [100] and applied by them to single molecule FRET recordings to determine the intensity changes in each of the donor/acceptor fluorophores [134]. The multiple intensity change point (MICP) analysis presented here extends their work to single molecule polTIRF measurements where the change in intensity occurs simultaneously across multiple PFIs while the total intensity is constant. In a later paper, Xu and Yang [135] developed an affinity functional (an integral expression for comparing two probability distributions) for the

joint analysis of the change point information in each of the donor/acceptor FRET intensities. In this work, the polarization information is combined into a single likelihood function and the change points are identified simultaneously on all the PFIs.

In the following sections, a conventional approach for distinguishing different intensity regions in a binned intensity trace is reviewed and contrasted with the change point method. The change point analysis is then formulated from binomial statistics, and the analysis described in detail for the case of a single change point [100]. The method is then extended to multiple intensities suitable for polarized TIRF measurements and an algorithm for searching for multiple change points described. The MICP is tested on several types of simulated intensity changes, including the change in PFIs expected for a labeled myosin V molecule stepping along actin. In Sect. 5, it is applied to high time resolution polTIRF experiments of myosin V motility.

### 4.1.1 Conventional analysis of time binned data

Typically, intensity traces are obtained by counting the number of photons that are detected during a fixed interval of time. A meaningful change in intensity is claimed to have occurred when the signal crosses a user defined threshold. In noisy data, the bin width is increased or the data is filtered to increase the signal to noise ratio and minimize the number of false positive threshold crossing events. Issues with this approach, such as missing short-lived threshold crossing events, can effect the results and were discussed extensively in Sect. 2. An alternative, discussed in that section, was the hidden Markov method that detects events by incorporating the statistical noise of the raw observation into the kinetic model used to describe the system.

Alternatively, if little is known about the specific intensities and the underlying model, the size of the change could be compared using a statistical test, as is done in various step finding algorithms [136, 137].

Even if one of these approaches reliably identified the transitions, their time resolution would be limited by the width of the time bin, thus requiring corrections for any missed events. One improvement is to record the arrival time of each photon using single photon counting technology and then, after the experiment is complete, an optimum bin size can be chosen. The time resolution of the analysis is still limited by the bin size, and new complications arises as to choosing the proper bin width. As shown in Sect. 2, hidden Markov models can be designed for unbinned raw data including single photon counting data [138, 139]; however, a kinetic model must still be imposed on the analysis. Single photon counting data is amenable to change point analysis, which as mentioned in the introduction is well-suited for detecting the abrupt changes in the PFIs observed in polTIRF experiments of myosin V stepping.

Change point analysis exploits the time stamped data directly by modeling the statistics of the photon arrival times. The statistics of the photons that arrive before and after a putative change point at time $t_i$ are compared to the statistics if there were no change point. There are several mathematical descriptions for counting photons in the regions before and after $t_i$: (1) two different Poisson distributions for the number of photons emitted during the two intervals [100], (2) two different exponential distributions for the time intervals between photons, and (3) two different binomial distributions of the photons in either region. Each approach assumes that photons are emitted randomly at a constant rate, and each leads to a similar final expression for the likelihood of a change point occurring in the data.

## 4.2 Change point analysis

Before developing the MICP analysis, the single intensity case will be reviewed. Important

results include the basic likelihood equation, the threshold for false positives, and a correction

scheme that is required for minimizing bias in the change point location within the interval.

These same topics will then be extended to the case of two intensities, and the results pertinent

for polTIRF experiments, which typically include 8 or 16 PFIs, are included. In developing

the method, a single interval with only one change point is considered. Later in Sect. 4.2.3,

this assumption will be relaxed and the algorithm will be applied to data with multiple change

points.

### 4.2.1 One change point and one intensity

**Mathematical framework**

The goal of the change point analysis is to determine if the intensity of the fluorescence emis-

sion changed during an interval, and if so when in the interval did the change occur. Before

considering photons that are detected in multiple polarizations, the change in intensity of a

single stream of photons is considered; for example, a single fluorescence molecule that emits

at rate $\kappa_1$ and then photo-bleaches to the background rate $\kappa_2$ (e.g., Fig. 4.2A). In this scenario

$N$ photons are recorded during the interval $T$ where each photon $i = 1, 2, 3 \ldots N$ is tagged

with its arrival time $t_i$ using single photon counting technology (Fig. 4.1, and Sect. 5 for ex-

perimental details). During periods of high intensity the interval between adjacent photons

$\Delta$ is shorter than in periods of low intensity, which can be visualized by plotting the photon
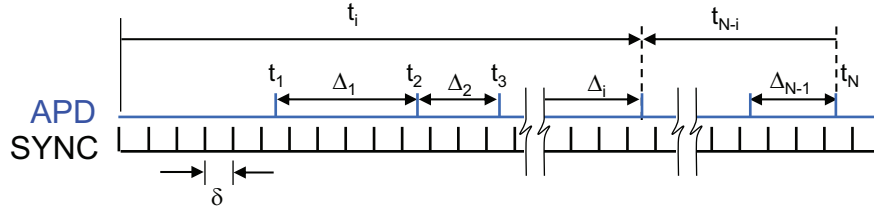
Figure 4.1: Diagram illustrating 10MHz sync pulses that discritize time into short bins $\delta = 100\,\mathrm{ns}$ such that the probability of detecting more than one photon by the APD (blue) in $\delta$ is very low. The "macrotime" $t_i$ indicate which bin the $i^{\mathrm{th}}$ photon arrived in. The "microtime" specifies the precise arrival time within $\delta$, and is not used here. In the case of a single change point at $t_i$, the time intervals between successive photons $\Delta_i = t_{i+1} - t_i$ that arrive before the change point are exponentially distributed with mean $1/\kappa_1$, after the change point the remaining $\Delta$'s are distributed with mean $1/\kappa_2$.

arrival times (Fig. 4.2B). For constant rate of emission the slope of the curve is the average

interval between detected photons $\langle \Delta \rangle$, which is equal to the inverse of the emission rate $1/\kappa$.

Changes in intensity are clearly identified by a kink in the curve (Fig. 4.2B). Locating the

position of these kinks is the heart of change point analysis. The challenge is distinguishing

changes in the slope that correspond to different emissive states of the molecule, especially in

short intervals, with the small changes in the slope due to the random photon arrival times.

The algorithm locates the intensity change by comparing two scenarios: Either the probe

emits $i$ photons with constant rate $\kappa_1$ until time $t_i$ and the remaining $N - i$ photons with rate $\kappa_2$

from $t_i$ to $T$, or the probe emits all $N$ photons with constant rate $\kappa_0$ during the entire interval.

The sync pulse in the SPC circuit (Fig. 4.1) discretizes time into bins that are very short (here

$\delta = 100\,\mathrm{ns}$) so that the probability of detecting a photon in any one bin is much less than unity

$(\kappa_0 \delta \ll 1)$, and therefore the probability of detecting two photons in one bin is negligible, i.e.,

$\sim (\kappa_0 \delta)^2$. The total number of bins is $\mathcal{N} = t_N / \delta$, where $N$ of the bins contain one photon

and the remaining $\mathcal{N} - N$ are empty. To make this comparison precise, the two scenarios are

formulated as hypotheses and the relative likelihood compared in a ratio test.

The first hypothesis is that the $i$ photons before change point at time $t_i$ are binomially
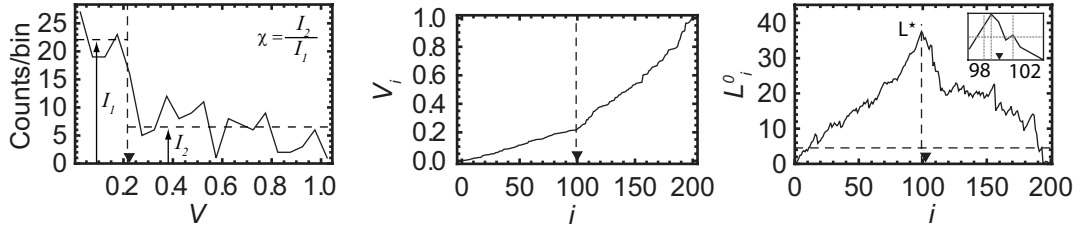
Figure 4.2: Example of a single change point at $N/2$ in a single-intensity simulation with $N = 200$ and a ratio between the high and low intensity of $\chi = 3$. A) The intensity is binned with 20 constant-width bins and shows a transition in the approximate location of the actual (▼) and inferred *(dotted line)* change point. B) The kink in the cumulative distribution of photons clearly indicates a change in intensity when $i \sim N/2$. C) The peak of the likelihood surface $\mathcal{L}^\star$ occurs at $i = 99$ (vertical dotted line) and the $\mathcal{L}^\star - 2$ confidence intervals at $i = 98$ and 102 enclose the actual change point (inset, horizontal lines)

distributed amongst $\mathcal{N}_i$ bins and after the change point the remaining $N - i$ photons are bino-

mially distributed amongst the $N - \mathcal{N}_i$ bins:

$$H_A = \left[ \binom{i}{\mathcal{N}_i} (p_1)^i (1 - p_1)^{\mathcal{N}_i - i} \right] \cdot \left[ \binom{N - i}{\mathcal{N} - \mathcal{N}_i} (p_2)^{N-i} (1 - p_2)^{\mathcal{N} - \mathcal{N}_i - (N-i)} \right] \quad (4.2.1)$$

where, $\mathcal{N}_i = t_i / \delta$ are the number of bins prior to the change point,

$p_1 = \kappa_1 \delta = \frac{i}{t_i} \delta$ is the probability of detecting a photon in a bin $\delta$ during the region before the

change point and,

$p_2 = \kappa_2 \delta = \frac{N-i}{t_N - t_i} \delta$ is the probability of detecting a photon in a bin $\delta$ after the change point.[1]

$H_A$ will be compared with the second (null) hypothesis that no change point occurred

during the same two intervals:

$$H_0 = \left[ \binom{i}{\mathcal{N}_i} (p_0)^i (1 - p_0)^{\mathcal{N}_i - i} \right] \cdot \left[ \binom{N - i}{\mathcal{N} - \mathcal{N}_i} (p_0)^{N-i} (1 - p_0)^{\mathcal{N} - \mathcal{N}_i - (N-i)} \right] \quad (4.2.2)$$

where, $p_0 = \kappa_0 \delta = \frac{N}{t_N} \delta$ is the probability of detecting photon in a bin $\delta$ during the entire

interval.

---

[1] The two probabilities can be left as unknown parameters in the likelihood function and then maximized to

find their optimum value. The result is that the probability for emission is equal to the mean rate of emission ($\kappa$

= total photons/time interval) multiplied by the time bin $\delta$ as expected for independent events

Note that maintaining the two regions in $H_0$ even though the emission probability is constant allows for the combinatorial terms to cancel when a likelihood ratio test, $\mathcal{L}^{\mathrm{o}}_i = \ln \frac{H_{A,i}}{H_{0,i}}$, is performed at each photon in the interval $[100, 140]$:

$$\mathcal{L}^{\mathrm{o}}_i = \ln \left[ \left( \frac{p_1}{p_0} \right)^i \left( \frac{1 - p_1}{1 - p_0} \right)^{\mathcal{N}_i - i} \cdot \left( \frac{p_2}{p_0} \right)^{N - i} \left( \frac{1 - p_2}{1 - p_0} \right)^{\mathcal{N} - \mathcal{N}_i - (N - i)} \right]$$

After substituting and rearranging terms, the ratio is the product of a function that depends on the arrival time of the $i^{\mathrm{th}}$ photon and a negligible correction term (with the underbrace), which approaches unity when the number of photons is much less than the number of bins (i.e., $N \ll \mathcal{N}$ or $\kappa_0 \delta \ll 1$).

$$\mathcal{L}^{\mathrm{o}}_i = \ln \left[ \left( \frac{i / t_i}{N / t_N} \right)^i \left( \frac{(N - i)/(t_N - t_i)}{N / t_N} \right)^{N - i} \cdot \underbrace{\left( \frac{1 - p_1}{1 - p_0} \right)^{\mathcal{N}_i - i} \left( \frac{1 - p_2}{1 - p_0} \right)^{\mathcal{N} - \mathcal{N}_i - (N - i)}} \right]$$

Dropping the correction term and normalizing the arrival time by the total time $V_i = t_i / T$ gives a very simple result [100]:

$$\mathcal{L}^{\mathrm{o}}_i = i \ln \left( \frac{i/N}{V_i} \right) + (N - i) \ln \left( \frac{1 - i/N}{1 - V_i} \right) \tag{4.2.3}$$

This equation converts the list of photon arrival times into a list of likelihoods that the two-intensity hypothesis fits the data better at each point than the one-intensity hypothesis. The index of the photon $i^\star$ with the peak likelihood

$$\mathcal{L}^{\mathrm{o}\star} = \max_{i=1...N} \mathcal{L}^{\mathrm{o}}_i$$

is the most likely location of the change point, in principle with single photon precision. The uncertainty in the location of the peak is quantified with 95% confidence intervals that include the photons with likelihoods within two log-units of the peak, i.e., $\mathcal{L}^{\mathrm{o}}_i \geq \mathcal{L}^{\mathrm{o}\star} - 2$ [88]. Since there will always be a maximum value in the list, merely finding the peak is not sufficient for

proving that a change point actually occurred. Next a process for determining the significance of the peak will be described.

**Example of single intensity change point**

A single intensity change point at $i = 100$ for $N = 200$ and $\chi = \kappa_1/\kappa_2 = 3$ is simulated (Fig. 4.2) in order to demonstrate the analysis. The approximate location of the intensity change is clear in the binned intensity plot (Fig. 4.2A), and with more precision in the graph of the photon arrival times (Fig. 4.2B). The likelihood surface (Fig. 4.2C) indicates that the change point is close to the expected location with a prominent peak that exceeds the false positive threshold (*horizontal dashed line* Fig. 4.2C) found in Fig. 4.3A. The uncertainty in the change point, determined from those photons with $\mathcal{L}^o_i \geq \mathcal{L}^\star - 2$, is $\pm 2$ photons and encloses the known location of the change point (Fig. 4.2C inset).

**Threshold for false positives detection**

The probability that $\mathcal{L}^{o\star}$ is a false positive can be determined if the distribution of $\mathcal{L}^{o\star}$ when *no* change point is known. A threshold for false positives $\rho^0$ can then be defined such that (for example) 95% of the $\mathcal{L}^{o\star}$ are below the threshold and correctly report no change, whereas the remaining 5% of the $\mathcal{L}^{o\star}$ exceed the threshold and report a false positive. In actual data, any $\mathcal{L}^{o\star}$ that exceeds the threshold is taken to be a valid change point with 95% confidence. If the fraction of acceptable false positives is referred to as $\alpha$ then the probability of a false-positive can be used to determine the unknown threshold $\rho^0$ according to:

$$Pr\left(\mathcal{L}^{o\star}_i \geq \rho^0_{1-\alpha}(N); i = 1, \ldots, N-1\right) = \alpha \qquad (4.2.4)$$
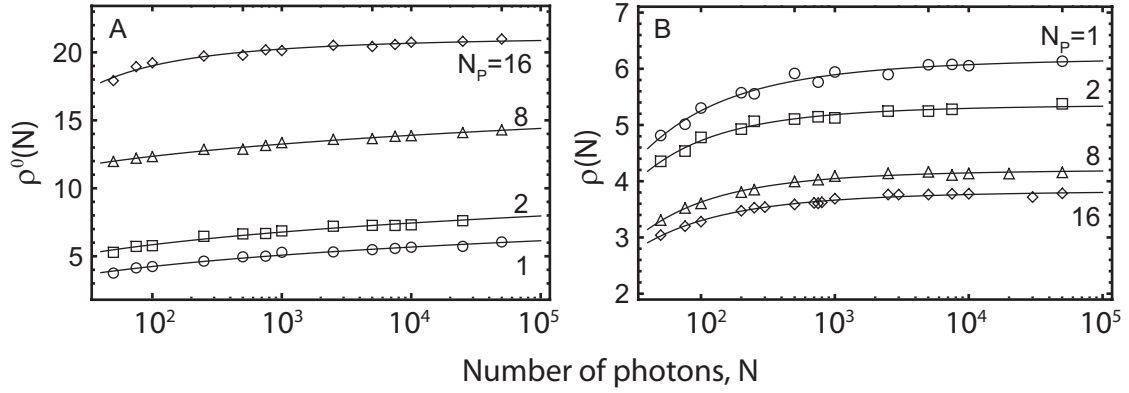
Figure 4.3: Values of the threshold $\rho$ for 5% false positive error rate for $N_P = 1, 2, 8$ and $16$ intensities as a function of the number of photons in the interval $N$. (A) Threshold for the uncorrected likelihood function defined in Eq. (4.2.6). (B) The threshold after correcting for the non-uniform false positive error rate.

Note that the threshold does not depend on the absolute rate of photon emission, but it does depend on the total number of photons in the interval; as expected since Eq. (4.2.3) increases with increasing $N$.

Impressively, Eq. (4.2.4) can be computed exactly for the single intensity case using an algorithm that was initially developed by Noé [141] for calculating probabilities of Kolmogorov-Smirnov statistics. Since the threshold is the unknown quantity and not $\alpha$, it is found by numerically solving Eq. (4.2.4) for the the desired false positive rate. The dependence of the threshold on $N$ is found by repeating the calculations over the range of photons that will be encountered experimentally [100, 142]. The threshold is also easy to compute via simulations, which will be necessary in multiple intensity data since Noé's algorithm only applies to the one intensity case. Thresholds corresponding to $\alpha = 0.05$ were simulated (see Sect. 4.3.1) over a wide range of $N$ and fit to a power law function (see Table 4.1) for use in the change point algorithm (see Fig. 4.3A).

**Non-uniform distribution of false positives**

Even though this technique successfully determines the number of false positives, the location of these false positives across the interval is highly non-uniform (e.g., *black line* for 16 intensities in Fig. 4.4). The probability of detecting a change point is $\sim 10\times$ higher in a region near the boundaries of the interval containing $\sim 1-5\%$ of the total photons than in the center of the interval. This problem has been addressed successfully for single change points and a two step solution proposed [143].

Qualitatively the phenomena is not unexpected: When testing for a change point near the edge of the interval, a random fluctuation in the region with a small number of photons is better fit with an intensity that differs from the intensity estimated in the larger region. Essentially, overfitting to these fluctuations results in change points being identified near the boundaries of the interval. When testing for a change point in the middle of the interval, however, there are enough photons in either region to prevent large fluctuations. Mathematically, this bias arises because photons in middle of the interval can arrive with a relatively wide distribution of times, all of which are centered about 0.5 (in normalized units of time), whereas photons near the boundaries of the interval have a relatively narrow distribution of times, either close to zero or close to unity. The result is that the likelihood function $\mathcal{L}^{o}{}_{i}$, which depends on these distributions in the different regions, is larger on average near the boundaries than in the middle.

In order to correct for this asymmetric likelihood function the distribution at each $i$ is normalized so that it has zero mean and unity standard deviation. This is accomplished by subtracting the mean likelihood $E[\mathcal{L}^{o}{}_{i}]$ and dividing by its standard deviation $\sigma_i$ at each value
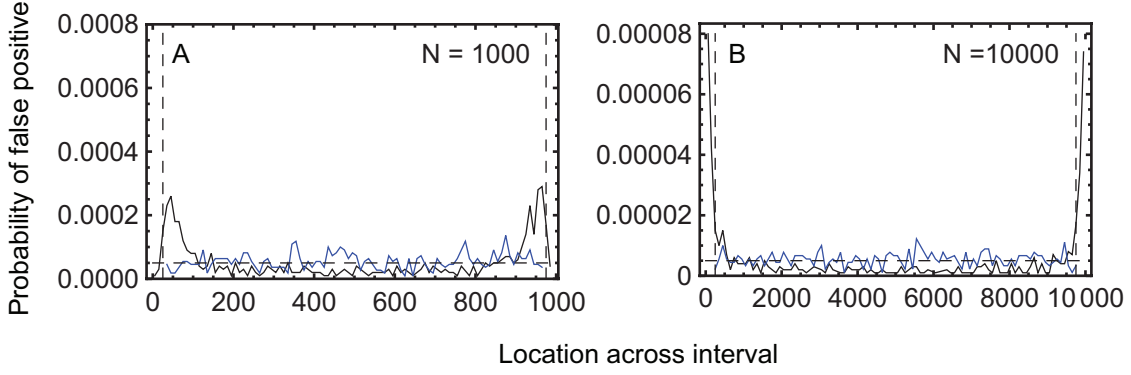
Figure 4.4: The distribution of false positives for $N_P = 16$ across an interval is strongly peaked near the edge of the interval for uncorrected likelihoods $\mathcal{L}^{\text{o}}_i$ *(black)*. The uncorrected distributions rise from zero immediately at the edge, increase rapidly before peaking and then decay slowly down to a minimum at the center. The distribution becomes increasingly peaked as $N$ is increased from $N = 1000$(A) to $10\,000$(B). The fraction of the total probability lying within the first and last 5% of each interval is 30% and 60% (instead of 10%) for $N = 1000$ and $10\,000$, respectively. Applying the correction factors (see Fig. 4.6) to the likelihood and excluding 2.5% of the photons from near the edges (vertical dashed lines, see Sect. 4.3.1) results in a nearly uniform distribution of false positives (blue), as expected for the 5% false positive rate used here (horizontal dashed line).

of $i$:

$$\overline{\mathcal{L}^{\text{o}}}_i = \frac{\mathcal{L}^{\text{o}}_i - E[\mathcal{L}^{\text{o}}_i]}{\sigma_i}$$

If the initial distributions of $\mathcal{L}^{\text{o}}_i$ at each $i$ were different size Gaussian distributions, then the distribution of false positives would now be uniform across the interval. Instead, the $\mathcal{L}^{\text{o}}_i$ are actually beta distributed random variables [143] and the normalization procedure is not sufficient. An *ad hoc* additional weighting function $W_i = 0.5 \ln \left(4i(N-i)/N^2\right)$ is applied to further penalize the likelihoods near the edge of the interval [143]. The final form of the corrected likelihood function $\mathcal{L}_i$ is:

$$\mathcal{L}_i = \frac{\mathcal{L}^{\text{o}}_i - E[\mathcal{L}^{\text{o}}_i]}{\sigma_i} + W_i = \overline{\mathcal{L}^{\text{o}}}_i + W_i \tag{4.2.5}$$

Amazingly, for the one intensity case the $E[\mathcal{L}^{\text{o}}_i]$ and $\sigma_i$ can be evaluated analytically [143], and thus the threshold for false positives (using Eq. (4.2.4) with $\rho$ in place of $\rho^0$) can still be calculated using Noé's algorithm [100]. These analytic solutions, however, are not readily

extended to multiple intensities and so are not repeated here. As will be discussed in Sect. 4.3, the $E[\mathcal{L}^o{}_i]$ and $\sigma_i$ can be obtained from simulations for any number of intensities. Determining these correction factors requires numerous simulations over the desired range of photons $N$ and number of intensities $N_P$ (see Sect. 4.3.1), but they only need to be performed once and then the results referenced by the algorithm.

## 4.2.2 Theory for one change point and multiple intensities

**Mathematical framework**

Polarized TIRF data consists of multiple polarized fluorescence intensities (PFIs) that report on the orientation of a fluorescent molecule. When the molecule suddenly changes orientation, for example during the step of a labeled myosin V, the magnitude of the PFIs change abruptly and simultaneously. Depending on the orientation of the probe in the two states, some PFIs will change greatly and others very little. If the probe is illuminated from multiple directions such that it is always well-excited, then the total intensity remains approximately constant even though the underlying PFIs can change dramatically.

Just as the binomial distribution was used to describe the statistics of $N$ photons in $\mathcal{N}$ bins, a multinomial distribution for multiple intensities can be used to describe the probability of detecting $N_p$ different "types" of photons. Here the different "types" of photon are detected under different polarization conditions but could also be different wavelengths, as in FRET for example. The probability of $n_1$ photons being detected in channel 1 and $n_2$ in channel 2

and so on, each with individual detection probabilities $p_1, p_2 \ldots$ is:

$$Pr(n_1, n_2, \ldots n_j | p_1, p_2, \ldots p_j) =$$

$$\frac{N!}{n_1! n_2! \ldots n_j!} p_1^{n_1} p_2^{n_2} \cdots p_j^{n_j} \underbrace{\left[ 1 - (p_1 + p_2 + \ldots p_j) \right]^{N - (n_1 + n_2 \ldots n_j)}}$$

If the hypothesis of a change point after $i$ photons is compared with the null hypothesis of no change point at point $i$, then the multinomial coefficients drop out, similar to the binomial case discussed for a single change point (Sect. 4.2.1). Also, the last term quantifying the probability of detecting no photons in any of the channels (underbrace in the above equation) is close to unity as long as the number of photons is much less than the number of available bins $(N \ll \mathcal{N})$. These assumptions allow Eq. (4.2.3) to be rewritten as a sum over each of the independent channels (since the log of a product equals the sum of their log's):

$$\mathcal{L}^{\mathrm{o}}{}_i = \sum_{j=1}^{N_p} \left( n_{j,i} \ln \left( \frac{n_{j,i} / N_j}{V_i} \right) + (N_j - n_{j,i}) \ln \left( \frac{1 - n_{j,i} / N_j}{1 - V_i} \right) \right) \qquad (4.2.6)$$

where $N_j$ is the total number of photons in the $j^{\mathrm{th}}$ intensity such that $\sum N_j = N$. $n_{j,i}$ is a set of $j$ vectors (one for each intensity) each containing $N$ elements that starts with 0 and increments after a photon is detected in that channel up to $N_j$. $V_i$ is the same vector of the photon arrival times normalized by the total time $T$ as for the single intensity case. Defining the set of vectors $n_{j,i}$ allows each PFI to contribute its photons to the likelihood function in the order in which they were detected. As with the single intensity case, $\mathcal{L}^{\mathrm{o}}{}_i$ for the multiple intensity case also suffers from a non-uniform of distribution false positives, which is corrected in the same way by subtracting off the mean likelihood $E[\mathcal{L}^{\mathrm{o}}{}_i]$, dividing by the standard deviation $\sigma_i$ and applying a weighting factor, $W$, see Sect. 4.2.1. These correction factors and the weighting function are different from the single intensity case and remove most of the bias except for a

small peak very close to the boundary. In order to avoid any residual bias, the MICP algorithm only considers change points that occur within the center 95% of the interval. That is, change points are neglected if they occur within a $0.025N$ buffer on either end of the interval (see for example Fig. 4.4 *vertical dashed lines* for the 16 intensity case).

The procedure for locating the peak, finding its confidence interval, and testing for its significance are the same as for the one intensity case, except that a new threshold for false positives must be computed for the multiple intensity case.

**Threshold for false positive detection**

As mentioned in Sect. 4.2.1, the threshold for false positive detection depends on $N$, but as shown in Eq. (4.2.6) it also depends upon the number of intensities $N_p$ among which the photons are divided. The new threshold values with and without the correction factors $E[\mathcal{L}^o{}_i]$ and $\sigma_i$, are determined from simulations as described for the one intensity case but with the photons divided amongst the different intensities. The details of the simulations will be discussed in Sect. 4.3.1, but the thresholds for 1, 2, 8 and 16 PFIs and $\alpha = 0.05$ are shown in Fig. 4.3. Least-squares fits to the simulated values were determined using the functions $\rho^0(N) = A + B\left(\log_{10} N\right)^C$ for the uncorrected likelihoods and $\rho(N) = a/\left(1 + b\left(\log_{10} N\right)^c\right)$ for the corrected likelihoods. The se functions were empirically chosen because they appeared to fit the data well, see Table 4.1 for the values of the parameters.

**Example of multiple intensity change point**

In order to demonstrate the technique for locating a change point with multiple intensities, photon arrival times for two-intensity channels with a change point at the $100^{\text{th}}$ photons are

| $N_P$ | $A$ | $B$ | $C$ | $a$ | $b$ | $c$ |
|---|---|---|---|---|---|---|
| 1 | -85.07 | 87.91 | 0.0229 | 6.207 | 1.481 | -3.029 |
| 2 | -120.0 | 124.2 | 0.0182 | 5.369 | 1.360 | -3.314 |
| 8 | -50.25 | 61.09 | 0.0352 | 4.212 | 1.671 | -3.377 |
| 16 | 21.22 | 8.857 | -2.004 | 3.839 | 1.338 | -3.032 |

Table 4.1: Fitting parameters used to determine the 5% false positive threshold $\rho(N)$ for different number of intensities $N_P$ using the uncorrected likelihood $\rho^0(N) = A + B \left(\log_{10} N\right)^C$ and corrected likelihood $\rho(N) = a / \left(1 + b \left(\log_{10} N\right)^c\right)$

simulated for $N = 200$ total photons (▼ Fig. 4.5). One intensity increases by a factor of $\chi = 3$ (*red line* Fig. 4.5) while the other decreases by $1/\chi$ (*blue line*) such that the total intensity remains constant (*black line*). Intensity traces constructed from 20 equal time bins across the interval indicate the approximate location of the actual change point (Fig. 4.5A). The distribution of arrival times (*black line* Fig. 4.5B) has a constant slope with no significant kinks; however the relative arrivals in each of the separate intensities (i.e., $n_{j,i}/N_j$, the *blue and red lines* in Fig. 4.5B) indicate a clear kink at $i = N/2$. The peak of the likelihood surface (Fig. 4.5C) exceeds the false positive threshold for 2 polarizations *(horizontal dashed line)*. The uncertainty in the change point, determined from those photons with $\mathcal{L}^0{}_i \geq \mathcal{L}^\star - 2$, includes photons $97 - 101$ thus bracketing the known location of the change point at $N = 100$ (Fig. 4.2C inset).
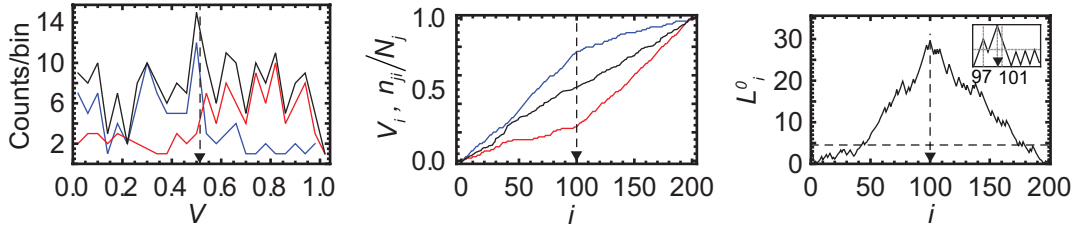
Figure 4.5: Example of a single change point in a two-intensity simulation with $N = 200$ where one intensity changes by $\chi = 3$ and the other by $1/\chi$ at $i = N/2$.(A) The individual (red,blue) intensities are binned with 20 constant-width bins and show a transition in the approximate location of the actual (▼) and inferred (dotted line) change point, whereas the total intensity (black) is constant across the interval. (B) The kink in the cumulative distribution of photons $n_{j,i}/N_j$ clearly indicates a simultaneous change in in both intensities when $i = N/2$. (C) The peak of the likelihood surface $\mathcal{L}^{o\star}$ occurs at $i = 100$ (vertical dotted line) and the $\mathcal{L}^{o\star} - 2$ confidence intervals at $i = 97$ and $101$ enclose the actual change point (inset, horizontal line)

## 4.2.3 MICP algorithm

In experimental data, a processive myosin V is recorded for multiple translocation steps and consequently multiple changes in orientation of the attached fluorophore are contained within the data, not just a single change point flanked by constant intensities as has been discussed so far. Fortunately, the method can be applied directly to the entire data set [100] and each change point found in an iterative process. For the first few change points that are found, the flanking regions are clearly not constant since they contain the other change points. After the change points are found in this rough manner, however, they are optimized one at a time in order to eliminate the influence of neighboring change points. More precisely:

1. For a single recording, which includes $N$ photons, $N_P$ PFIs and multiple change points, the MICP algorithm is applied as follows: (1) calculate $\mathcal{L}^o{}_i$ for each photon in the interval with Eq. (4.2.3), (2) apply the correction and weighting factors $E[\mathcal{L}^o{}_i]$, $\sigma_i$, and $W_i$ to each value of $\mathcal{L}^o{}_i$ to obtain the corrected likelihood function for each photon in the interval $\mathcal{L}_i$, (3) within the interval 0.025$N$-0.0975$N$ find the most likely change

point as the location $i^\star$ of the likelihood peak, (4) test the candidate change point for significance by comparing it with the false positive threshold $\mathcal{L}^\star > \rho_\alpha$, (5) if the peak exceeds the threshold, record its location as a change point and determine its confidence interval from those photons with likelihoods greater than $\mathcal{L}^\star - 2$.

2. On the next iteration, the data prior to the peak at $i^\star$ is analyzed and the location of its largest peak above the threshold is determined. Similarly, the largest peak in the region between $i^\star$ and the end of the data set is determined. This process is repeated on each sub-region of the data until none of the peaks exceed their respective thresholds.

3. After determining the approximate location of the change points, the location of each one is re-evaluated over the range limited by its neighbors. If the change point no longer exceeds the threshold over this smaller range, then the region is combined with its neighbor and then that neighbor is evaluated. Regions containing less than 50 photons are automatically combined with the neighboring region.

4. After refining the location of each change point, the intervals between all adjacent change points are tested for additional change points.

5. Steps *2- 4* are repeated 4 times to optimize the location and number of change points. In these iterations the interval between change points is determined from the confidence intervals and not the location of the change points.

6. The final list of change points with their confidence intervals are stored for subsequent analysis.

After the change points are determined, the intensities in each interval are used to estimate the maximum likelihood orientation and wobble of the fluorophore, as described in Sect. 3.2.4. In order to assess the sensitivity of the inferred orientation to the precise location of the change point, four additional sets of intensities are determined for each interval by using the edges of the confidence intervals as the boundary instead of the change point. For example, consider two change points at $t_i$ and $t_{i+1}$, the first with confidence intervals $(\tau_i^-, \tau_i^+)$ and the second with $(\tau_{i+1}^-, \tau_{i+1}^+)$. Five sets of orientations are determined for the $i^{\text{th}}$ interval:

$$\left\{ (t_i, t_{i+1}), (t_i - \tau_i^-, t_{i+1} - \tau_{i+1}^-), (t_i - \tau_i^-, t_{i+1} + \tau_{i+1}^+), \ldots \right.$$
$$\left. \ldots (t_i + \tau_i^+, t_{i+1} - \tau_{i+1}^-), (t_i + \tau_i^+, t_{i+1} + \tau_{i+1}^+) \right\}$$

When applied to myosin V motility experiments, each set of these PFIs is input into the dipole model in order to determine the sensitivity of the estimated probe parameters to the uncertainty in the change point location.

### 4.2.4   Critique of MICP

The MICP algorithm makes several simplifying assumptions that will be listed here before discussing the simulations.

For single molecule experiments, the time fluorophore's emission rate limits the achievable time resolution. Typical count rates are $20 - 50$ photons/ms.

The statistical model that underlies the multiple intensity likelihood function (Eq. (4.2.6)), assumes that photons in each intensity channel can be emitted independent of one another and detected simultaneously. In practice, however, polTIRF experiments alternately illuminate the sample so that only one excitation polarization state is measured at a time. Artifacts may arise

if the motions of the molecule are comparable to the cycle frequency, but this is not typically the case for biological molecules and $>10$ kHz cycling frequencies.

The threshold for false positives is clearly a crucial parameter as it determines the validity of a particular change point. An advantage of the change point analysis is that this threshold is not a user-defined value, but is instead determined by the desired limit $\alpha$ on false positives. The analytic method used to calculate the single change point threshold is fast, but is not readily applied to multiple intensities. Determining the false positive rate from simulations is easily performed on a personal computer. Furthermore, the threshold is a smooth function of the number of photons in the interval, so only a few values of $N$ need to be calculated and the rest can be obtained from a equation fit to the results of the simulations.

In Sect. 4.2.2, the threshold for false positives was determined assuming that the intensity of the separate PFIs were equal. For applications specific to polTIRF experiments, a better assumption might be that each PFI is consistent with the intensity emitted from an isotropic distribution of fluorophores. Because the likelihood function Eq. (4.2.6) depends on the number of photons in each state, the false-positive threshold in these two scenarios would not be the same. Distributing the photons equally, however, results in the largest magnitude likelihood (on average) so the threshold determined in this way is a conservative estimate of whether or not a false positive occurred. Also, assuming an equal distribution of photons is advantageous because it is independent of the model used to represent the molecule's fluorescence emission and detection.

The weighting function $W$ and the 2.5% buffer zone used to remove the remaining bias, are easy to apply to the change point analysis with minimal additional computation. The

115

origin of the weighting function appears to be somewhat *ad hoc* [143]; however, it is effective in simulated data and has been used successfully by other groups [100]. A key feature of the weighting function is that although it suppresses detection of change points near the edge of the interval, it does not preclude them entirely; a legitimate change point will be detected if its likelihood is large enough. The additional buffer zone on either end of the interval, however, precludes the detection of change points in this small region. Short duration events that precede or follow a long duration event may be missed, but in typical experiments events longer than $10\,000$ photons are not common, and the resulting dead time of 250 photons is near the limit of detection. In cases where this trade-off is not desirable, the MICP algorithm would be useful for identifying the long duration dwells, which could then be subjected to a local analysis at the two ends to test for additional change points.

Estimating the 95% confidence intervals from the likelihood surface is a common statistical practice [88, 140]; however, more rigorous confidence intervals can also be defined [100]. For example, all photons adjacent to a change point for which the alternate hypothesis is at least 5% likely to be true would be included in the 95% confidence interval. In the single intensity case, Watkins and Yang [100] found that the fraction of change points that fell within the confidence interval depended on the magnitude of the change point. Simulations to determine the confidence interval in the multiple rate case would be more expensive than those used to determine the false positive threshold, because both the magnitude of the change point and the number of photons in the interval would need to be varied. Given these limitations, simply estimating the 95% confidence interval from $-2$ offset on the likelihood surface (i.e., all photons $i$ with $\mathcal{L} \geq \mathcal{L}^{\star} - 2$) is a practical approach.

The MICP algorithm can be used to detect multiple change points in a trace one at a time on progressively smaller subsets of the data until no change points remain. Each change point is then tested again for significance independent from its neighbors. This piece-wise approach is in contrast to a single likelihood function that includes all of the change points, whose optimal positions are found simultaneously. Occasionally, evidence that the assumption of independent change points breaks down can be seen in a group of 3 change points that never settle on precise locations. For example, the intervals defined by two change points support the inclusion of a third change point in between them, but if that change point is included then one of the initial two loses its significance. The occurrence of this is rare, but could be addressed by incorporating the three change points into a single function and optimizing all three at once for the most likely configuration. In fact, all of the change points detected via the sequence of independent 1D searches suffer a similar problem: a more likely configuration might be attained by moving the two change points relative to one another in a 2D search. The issue is mitigated somewhat by iteratively passing through the data multiple times, but nonetheless it is never completely resolved. The computational cost of simultaneously varying two change points is relatively high since each interval of $N$ photons would require $N^2/2$ calculations; considering some intervals have thousands of photons a full 2D search is prohibitive. A compromise may be desirable in some situations such as when two nearby change points are subjected to a 2D search over a limited region of the interval.

In single molecule polTIRF experiments, change points are expected to occur when the probe changes orientation, but change points will also be detected when the total intensity changes magnitude, similar to the scenario in single-intensity change point analysis. Typ-

117

ically re-orientations are associated with constant intensity, but some fluctuations in steady state intensity are also detectable. For example, the change point algorithm easily detects the step decrease in intensity when the single molecule bleaches to background, as well as the occasional double bleach and blinking events where the fluorophore turns off and then back on again.

## 4.3   Simulation results

Three types of simulations were performed to test the algorithm: (1) no change point simulations tested the null hypothesis and were used to determine the correction factors $E[\mathcal{L}^{o}_{i}]$ and $\sigma_i$ and the threshold for false positives; (2) single change point simulations assessed the false-negative rate of the algorithm over a range of change point magnitudes and duration; (3) double change point simulations of a large transition followed by a short-lived state with a second transition tests the algorithm's sensitivity to detect substeps within the myosin V cycle. The various intensities for a simulation are generated either arbitrarily to give intuition on the detection algorithm or by calculating the PFIs that correspond to actual fluorophore orientations using the dipole model (see Sect. 3.2.4 for details). A fourth set of simulations, independent of the change point algorithm, was used to determine the minimum number of photons required for the dipole model to reliably detect orientations relevant to myosin V processivity experiments in shot-noise limited data.

The simulations of the MICP analysis rely on generating a specified number of inter-photon arrival times from an exponential distribution. Each photon is randomly assigned to one of the independent polarization channels (usually $N_P = 8$ or 16, which correspond to the

typical number of channels in experimental data) with a probability that is weighted according to its relative intensity. For example, if the probe model assigns rate $\kappa$ to 6 PFIs, and rate $2\kappa$ to the remaining 2, then the photon arrival times are generated with $\kappa_{tot} = 10\kappa$, and each photon is randomly assigned to one of the six low rate channels with probability 0.1 and to one of the two high rate channels with probability 0.2. This two-step process ensures that the total intensity is constant, and that each of the individual PFIs has the proper relative rate with exponentially distributed arrival times.

Most simulations were performed in *Mathematica 7.0* on a standard PC with two Intel 2.5 GHz processors. A particularly useful command for achieving the proper intensity and arrival time of the photons in each PFI is *RandomChoice* [{weights}, {values}], which randomly picks a number from a set of values according to a user-defined list of weights for each number. As just discussed, these weights $w$ are defined consistent with the intensity in each PFI, $w_j = \frac{\kappa_j}{\kappa_{tot}}$. A simulation thus consists of generating $N$ exponentially distributed inter-photon arrival times from a distribution with rate $\kappa_{tot}$, each of which is randomly assigned a value $j = 1..N_P$ according to the weights $w_j$. A change point is introduced after the $i^{\text{th}}$ photon by using one set of weights from $1 \ldots i$ and second set of weights from $i \ldots N$. The MICP algorithm (Sect. 4.2.3) is then applied to the simulated data, and any statistically significant change points are recorded. This process is repeated $M$ times (typically $500 - 10\,000$ depending on the simulation) to minimize statistical fluctuations.

### 4.3.1 No change point simulations

The peak likelihood $\mathcal{L}^\star$ calculated from Eq. (4.2.6) must exceed a threshold to be considered a valid change point (with false positive rate $\alpha$). The threshold is determined from simulations over a range of photons $N$ and intensities $N_P$ for $\alpha = 0.05$. Before calculating the threshold, however, the correction factors $E[\mathcal{L}^o{}_i]$ and $\sigma_i$ are determined since they will affect its magnitude.

**Correction factors**

As discussed in Sect. 4.2.1, the distribution of peak likelihoods simulated under conditions of the null hypothesis (i.e., no change point) is not uniform across the interval and results in a bias for detecting false-positive change points preferentially near the boundaries of the search interval. The distribution of $\mathcal{L}^o{}_i$ can be empirically determined by repeatedly applying Eq. (4.2.6) to a constant intensity simulation. The mean and standard deviation of $\mathcal{L}^o$ at each point across the interval is then used to normalize the likelihood. Specifically, the first and second moments at each point $i$ are tallied for $M \geq 10\,000$ simulations so that $E[\mathcal{L}^o{}_i] = \langle \mathcal{L}^o{}_i \rangle_M$ and $\sigma_i^2 = \left\langle (\mathcal{L}^o{}_i)^2 \right\rangle_M - \langle \mathcal{L}^o{}_i \rangle_M^2$. The process is repeated over a range of $N = \{50, 76, 100, 200, 300, 500, 700, 800, 1000, 2000, 3000, 5000, 7500, 9000, 10000,$ $30000, 40000, 50000\}$ to generate a look-up table for the two correction factors. Values of $N$ not in the look up table are linearly interpolated between the two nearest values.

The resulting correction factors $E[\mathcal{L}^o{}_x]$ and $\sigma_x$ for $N = \{50, 100, 500, 1000, 5000, 10000,$ $50000\}$ follow a similar pattern across the interval as $N$ is increased for both 8 and 16 intensities (Fig. 4.6). In order to compare simulations with different numbers of photons on the

same graph, the photon index $i$ is normalized by the total number $x = i/N$ and plotted on a logarithmic scale to emphasize the region close to the boundary of the interval. Since the correction factors are symmetric about $x = 0.5$ the counting statistics are improved 2 fold by superimposing the results from the two halves of the interval. As the number of polarizations increase from 8 to 16 the magnitude of both $E[\mathcal{L}^o{}_x]$ and $\sigma_x$ increase, as expected since the number of ln terms in Eq. (4.2.6) doubles.

When $N \gtrsim 500$, all of the correction factors show a plateau in the center of the interval that increases as the edge of the interval is approached and then falls abruptly immediately at the edge. The increase in both the mean and the standard deviation near the edge of the interval reflect the observed increase in the rate of false positives. Unlike the correction factors for change points with multiple intensities, the correction factors in the single intensity case (not shown) increase monotonically at the edge of the boundary. The reason that multiple intensity correction factors experience a sharp decrease immediately at the boundary is that the magnitude of the $\mathcal{L}^o$ depends on the number of logarithm terms in Eq. (4.2.6) that contribute to the sum. If enough photons are present in each region (before and after a change point) then every term can contribute to the sum. But, as the algorithm tests points that are closer to the boundary, eventually the number of photons in some of the intensity channels will drop to zero and the corresponding terms will drop out of the sum (since $0 \ln 0 = 0$). This will lower $\mathcal{L}^o$ proportionally until the minimum at $i = 1$ where half of the terms in Eq. (4.2.6) are zero.

An additional weighting function $W_i$ and a buffer consisting of 2.5% of the photons is applied to the interval to penalize change points from occurring at the edges. The omitted photons are included in the estimate of the average emission rate but only values in the range

121
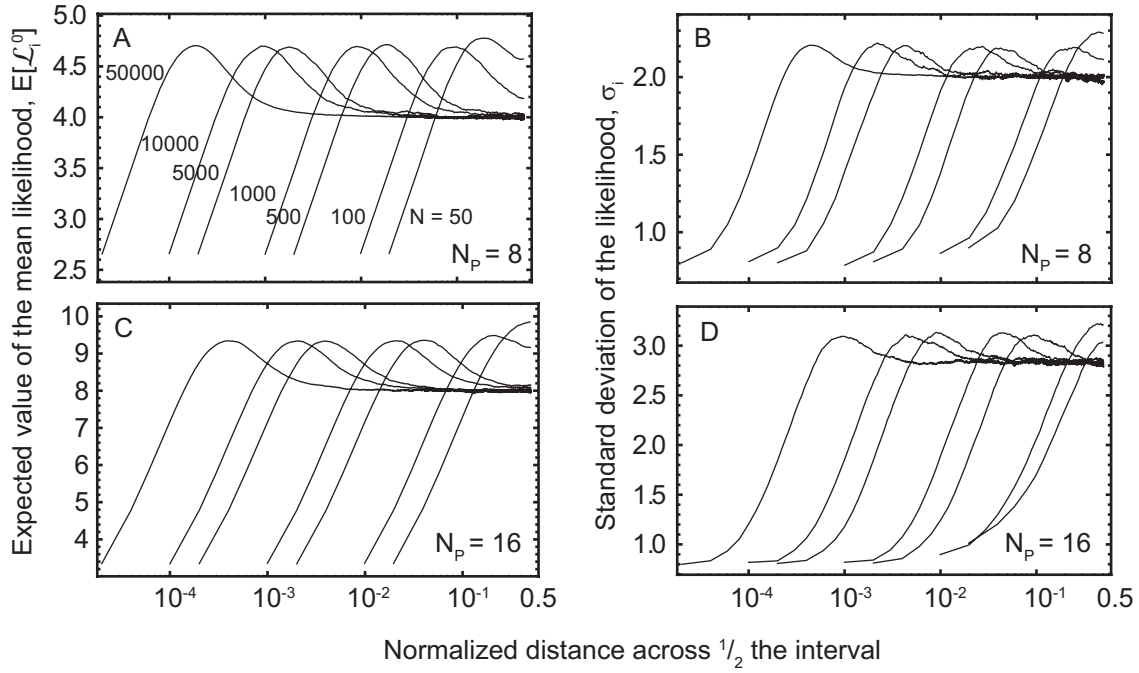
Figure 4.6: MICP correction factors for the expected value $E[\mathcal{L}^o{}_x]$(A,C) and the standard deviation $\sigma_x$ (B,D) of the likelihood function $\mathcal{L}^o$ (Eq. (4.2.3)) for $N = \{50, 100, 500, 1000, 5000, 50000\}$ and $N_P = 8$(top) and $N_P = 16$ (bottom). The horizontal axis $x = i/N$ indicates the position of the $i^{\text{th}}$ photon across the interval normalized to the total number of photons. For clarity, only half the distribution is shown since the correction factors are symmetric about $x = 0.5$. The correction factors are applied to each photon $i$ in the interval so that the resulting likelihood of each $\overline{\mathcal{L}^o}_i = \left(\mathcal{L}^o{}_i - E[\mathcal{L}^o{}_i]\right)/\sigma_i$ is approximately normally distributed with mean zero and variance one.

$0.025N < i < 97.5N$ are considered for change points. The final result including the correction factors, weighting function and buffer is a uniform distribution of false positives, at least in the range considered here $N = 50 - 50\,000$ and $N_P = 8$ and $16$ (*blue line* Fig. 4.4).

**False positive threshold**

Determining the threshold for false positives is similar to the set of constant intensity simulations just described. Instead of recording the first and second moments of $\mathcal{L}^o$, however, the peak likelihood $\mathcal{L}^\star$ and its location $i^\star$ is recorded for each of the $M$ simulations. This list of $\mathcal{L}^\star$ is sorted and the value that separates the largest $M \cdot \alpha$ from the remaining $M \cdot (1 - \alpha)$ is

the desired threshold. The functional dependence on $N$ is obtained by repeating the calcula-tion over a range, typically $N = \{50, 75, 100, 250, 500, 750, 1000, 2500, 5000, 7500, 10000,$ $25000, 50000\}$. Because actual data can have any value of $N$, the simulated values of $\rho$ are fit to the interpolating function $\rho(N) = a/(1 + b(\log_{10} N)^c)$ to determine $a, b$ and $c$. Finally the entire process is repeated for different numbers of intensities. The results for $N_p = 1, 2, 8, 16$ are shown in Fig. 4.3B and the corresponding values of $a, b$ and $c$ for each fit are summarized in Table 4.1. All thresholds used here correspond to a 5% false positive rate $(\alpha = 0.05)$.

For comparison purposes, the same set of simulations can be used to determine the thresh-old for uncorrected likelihood function $\mathcal{L}^{o\star}$ Fig. 4.3A. The simulations over a range of $N$ are fit to the expression $\rho^0(N) = A + B \left(\log_{10} N\right)^C$ to determine $A, B$ and $C$, see Table 4.1.

The threshold for uncorrected likelihoods $\rho^0$ increases slowly with $N$ (Fig. 4.3A), unlike the threshold for corrected likelihoods $\rho$ which increases abruptly and then is fairly constant as $N$ is increased. The dependence of the $\rho$ on the number of intensities is the opposite as for $\rho^0$, presumably because of the larger magnitude correction factors for $N_P = 16$ compared with $N_P = 8$ (Fig. 4.6).

### 4.3.2 Single change point detection

**Power of MICP for detecting arbitrary intensity change**

A low false positive rate is important for confidence in the results; however a low rate of false-negatives (i.e., the power of a test) is also crucial in order to detect a majority of the change points.

The power of the MICP algorithm is determined from simulations performed with 8 and

16 intensities over a range of photons $N$ and change point magnitudes $\chi$. The intensities were not based on any assumed orientation of the probe; half of the intensities changed from 1 to $\chi$ and the other half change from $\chi$ to 1 thus ensuring a constant total intensity. Change points were simulated at the midpoint of the interval $(N/2)$ and the MICP was successful if the $\mathcal{L}^\star - 2$ confidence interval enclosed the true location.

Simulations were performed over a range of change point magnitudes $\chi = \{1, 1.1, 1.2, 1.3,$ 1.4, 1.5, 2, 2.5, 3\}$ and photon intervals $N = \{100, 500, 1000, 5000\}$ for $N_P = 8$ (Fig. 4.7A) and $N_P = 16$ (Fig. 4.7B). 5000 simulations for each combination of $\{N, \chi, N_P\}$ were run and the fraction of trials with a detected change point are recorded (*solid lines*), as well as, the fraction of change points whose confidence interval includes the true location *(dotted line)*. As expected, simulations with a large $N$ and $\chi$ resulted in a higher fraction of detected change points, and larger intensity changes required fewer photons to identify the change point. At the larger $\chi$ and $N$ nearly 100% of the change points are detected. Even though an interval corresponding to the 95% confidence interval was chosen, the actual accuracy of the method exceeded 98% depending on $N$ and $\chi$ (data not shown). The non-zero fraction of detected events at $\chi = 1$ indicates the false positive error rate.

Increasing the number of PFIs from 8 to 16 decreases the power of the test slightly due to the increase in the photon counting noise that occurs when $N$ photons are divided into twice as many intensity channels. The sensitivity to additional intensities is mitigated in the arbitrary intensity model used here because all of the intensities contribute equally to the change point. This is not true when the intensity change arises from probe re-orientations, since some PFIs respond more strongly to a particular change then others. Consequently, in
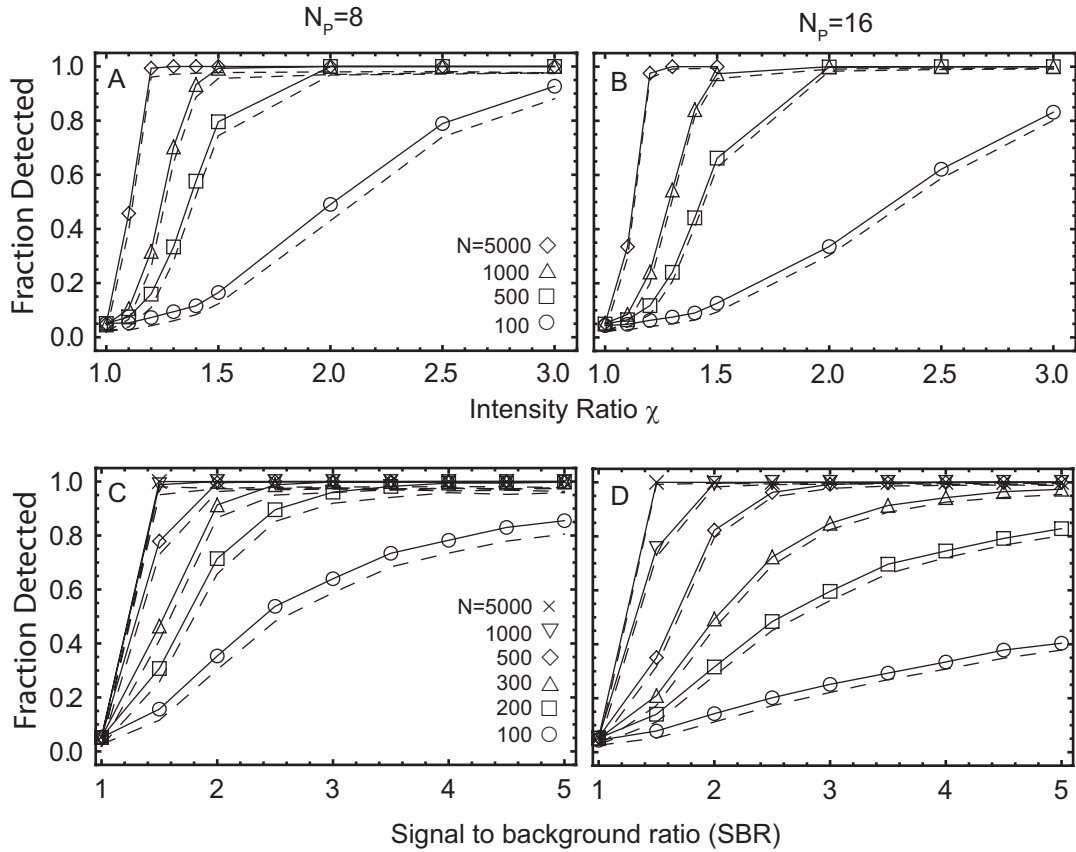
Figure 4.7: Power of the MICP algorithm to detect change points of different magnitudes depending on the number of intensities $N_P = 8(A, C)$ and $N_P = 16(B, D)$ and the number of photons in the interval.*Top row* The fraction of change points detected versus an arbitrary intensity change of $\chi$ (see Fig. 4.2 for the definition of $\chi$) and $N = \{100, 500, 1000, 5000\}$.*Bottom row:* The fraction of change points detected for an angle change corresponding to the tilting motion of a probe attached to the myosin V lever as it steps (see Table 4.2) as a function of signal-to-background ratios (SBR) for $N = \{100, 200, 300, 500, 1000, 5000\}$. More than 95% of the actual change point falls within the $\mathcal{L}^\star - 2$ confidence interval indicating that these confidence intervals are conservative (dotted).

polTIRF experiments there is a trade-off between accuracy, which requires more PFIs, and time resolution, which requires fewer PFIs.

**Power for detecting myosin lever arm change**

In order to determine the power of the MICP in experiments of myosin V stepping, simulations of the probe angle before and after a step (see Table 4.2) are performed using the dipole model to determine the PFIs. Instead of an arbitrary factor $\chi$, the simulations were performed at

| State | $\{\theta, \phi\}$ | $\{\beta, \alpha\}$ | $\delta$ |
|---|---|---|---|
| Pre-step | $\{96.7, 168.8\}$ | $\{20, -20\}$ | 40 |
| Detached | - | - | 90 |
| Post-step | $\{18.9, 23.3\}$ | $\{80, -85\}$ | 40 |

Table 4.2: Orientation and wobble ($\delta$) used in the simulations of myosin V stepping. The orientations are represented in the microscope ($\theta, \phi$) and actin ($\beta, \alpha$) frames. All angles are in degrees.

different signal-to-background ratios (SBR) by varying the intensity of the fluorophore in the dipole model with a constant background. Otherwise, the simulation conditions were similar as in the previous section.

As in the arbitrary intensity case, the power of the algorithm to detect change points increases with increasing SBR and number of photons (Fig. 4.7). The reduction in sensitivity when the number of PFIs is increased from 8 (Fig. 4.7C) to 16 (Fig. 4.7D) is larger than in the arbitrary intensity case because some of the additional PFIs are not sensitive to the angle change yet still contain a fraction of the total number of photons. Experiments with SBR's of 3 require $\sim 200$ and $\sim 400$ photons for $\sim 90\%$ detection in the 8 and 16 PFI configurations, respectively. If the fluorophore emits with a rate of $\sim 30/\text{ms}$ then the corresponding time resolution in the two cases would be 7-10 ms and 13-25 ms. The shortest detectable events will be tested directly in the next section.

### 4.3.3 Two change point detection

Substeps in the myosin V ATPase cycle are predicted to occur in a short period of time immediately before or after a step is taken; that is, a second, short duration interval adjacent to the

long interval that accompanies the tilting motion of a step. Simulations are used to determined the sensitivity of the MICP algorithm to detecting these short-lived states over a range of photons in the transient state $N_t = 1 - 1000$ and signal-to-background ratios SBR= $1.5, 2, 3,$ and 4.

The simulation consists of a long-lived state with a well-defined orientation, followed by a short-lived state with large wobble (no well-defined orientation), and ends in a long-lived state also with a well-defined orientation, see Table 4.2. The number of photons in the post-step and leading head states is held fixed at 2000 each and the number of photons in the transient state is varied. Each combination of $N_t$ and SBR is simulated 500 times and the fraction of trials resulting in single, double and triple change points is recorded for the 8 (Fig. 4.8A,B,C) and 16 (Fig. 4.8D,E,F) PFI configurations.

The simulations are generated as outlined in Sect. 4.3.2. To find the change points in each trial, the algorithm is applied 3 times: first to the entire interval of $N_t$ photons, and if the peak likelihood exceeds the threshold, the regions to the left and right of the peak are interrogated for change points in these shorter regions. In the event that three change points are detected, the middle one is re-evaluated on the interval between the other two and only retained if its peak exceeds the required threshold.

As the number of photons in the transient state increases, the fraction of trials with single change points decreases (Fig. 4.8A,D), while the fraction with two change points increases to $\sim 90\%$ (Fig. 4.8B,E). The fraction of trials with a spurious third change point is relatively constant at $\sim 10\%$. When there is no transient state, the fraction of trials with single change points is $\sim 90\%$, indicating a $\sim 10\%$ false positive rate (Fig. 4.8C,F).
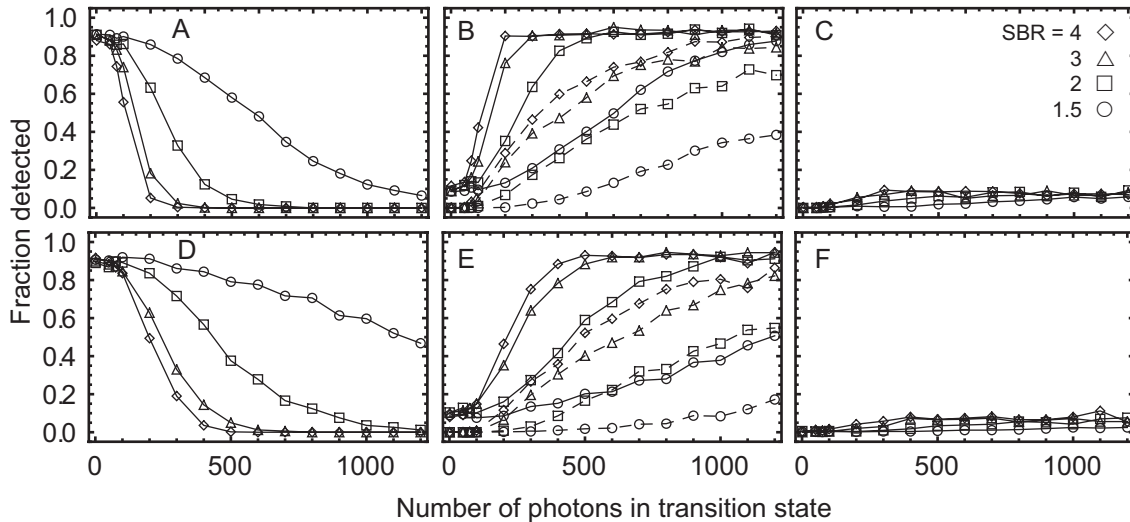
Figure 4.8: The power of the MICP algorithm to detect short duration states in the Myosin V ATPase cycle, specifically the short-lived detached state after the trailing head (pre-step state) releases from actin but before it re-binds to as the new leading head (post-step state) is determined from intensities simulated using the angles in Table 4.2. Simulations with $N_P = 8$ (top) and $N_P = 16$ (bottom) indicate one (left), two (middle) or three (right) detected change points as the number of photons in the transient state is increased from 0 to 1200 for different signal-to-background ratios SBR = $\{1.5, 2, 3, 4\}$ (symbols). Requiring that the interval be detected with at least 10% accuracy (dashed, middle) significantly increases the number of photons needed to identify the state.

If the known locations of the simulated change points are used to determine the accuracy of the detected change points then fewer of the trials will be considered successes. For example, if the overlap between the detected and the actual interval of the transition is required to be between $90 - 110\%$ then 2-3× more photons in the transient state are required to detect the same fraction of events. If a fluorophore emits $\sim 30$ photons/ms then only 300 photons will be recorded during a 10 ms transient state. If the signal-to-background ratio is assumed to be 3 then $\sim 500$ photons are required to detect 50% of the events in the 8 PFI configuration and $\sim 700$ photons in the 16 PFI configuration, approximately twice as many as was required in the single change point simulations.

128

### 4.3.4 Number of photons required to measure large probe wobble

The interval between change points indicates the orientation, wobble and/or brightness of the molecule, and are determined by using the dipole model. This analysis is used to identify myosin V stepping events, since the orientation of the probe on either side of the change point should change. Variability in the results for a given state is expected due to the low signal to background ratio and finite number of photons. Simulations that include these statistical fluctuations are performed to determine the minimum number of photons required to identify a particular state.

Simulations of the orientation and wobble before (Fig. 4.9A,D), during (B,E) and after (C,F) a step are performed over a range of photons ($N = 50\text{-}1000$) and signal-to-background ratios (SBR $= 1.5, 2, 3, 4, \infty$) for the 8 (A-C) and 16 (D-F) polTIRF configurations. The orientation and wobble during the three states, denoted $(\theta^\star, \phi^\star, \delta^\star)$, are the same as used previously (Table 4.2). Each combination of $N$ and SBR is simulated 500 times and the PFIs used as input in the orientation analysis to determine the most likely set of parameters $(\theta', \phi', \delta')$ for the dipole orientation and wobble. The fraction of trials with parameters that fall within $15°$ of the simulated values are reported as successes in Fig. 4.9. For the simulation during the step, $\delta^\star = 90°$ and the orientation is not well defined, so a successful trial is defined as $\delta' \geq 75°$. For the pre- and post-step states, a successful trial requires that $32.5 \leq \delta' \leq 47.5°$ (i.e., the range of acceptable $\delta$ is $15°$) and the absolute angular displacement $\zeta$ between $(\theta', \phi')$ and $(\theta^\star, \phi^\star)$ be less than $15°$. That is, $\zeta \leq 15°$, where $\zeta = \arccos\left(\overrightarrow{\mathcal{O}}^\star \cdot \overrightarrow{\mathcal{O}'}\right)$ and $\overrightarrow{\mathcal{O}}^\star$ is the vector pointing in the direction of the simulated value and $\overrightarrow{\mathcal{O}'}$ is the vector pointing in the direction estimated from the analysis.

Perhaps most informative are the simulations with zero background (SBR $= \infty$) since they represent the best case scenario for detection of a photon-limited polTIRF signal. For example, approximately 500 photons are required to measure a large wobble cone with 90% accuracy, whereas actual experiments have $SBR \lesssim 3$ and would only detect 50% of these duration events.

A striking feature of the 8 PFI simulations is that a large wobble cone cannot be reliably measured, even with zero background and large numbers of photons. The reason for this is that there is a symmetry that arises from exciting and detecting the fluorophores along the 3 orthogonal axes; the diagonal polarizations in the 16 PFI data break this symmetry. The probe model predicts the same 8 intensities for $\delta = 90°$ as for an orientation $\{\theta, \phi\} = \{54.7°, 45°\}$. $54.7° = arctan\left(\sqrt{2}\right)$ is the "magic" angle in ensemble polarization experiments and corresponds to the angle of the analyzer (with respect to the excitation polarization) required for equal detection of the polarized fluorescence.

## 4.4   Discussion

Fluorescence experiments that utilize single photon counting technology can achieve very high time resolution by recording the arrival time of each detected photon. There is no binning of the raw data; afterward the experimentalist can choose any bin size to analyze the data. This chapter describes an alternate approach that never imposes a bin size on the data and uses the photon arrival times directly. Change point detection algorithms meet both of these requirements and are particularly powerful because they do not require any user-defined thresholds (e.g., a threshold that separates high and low intensity states [100]). All parameters within
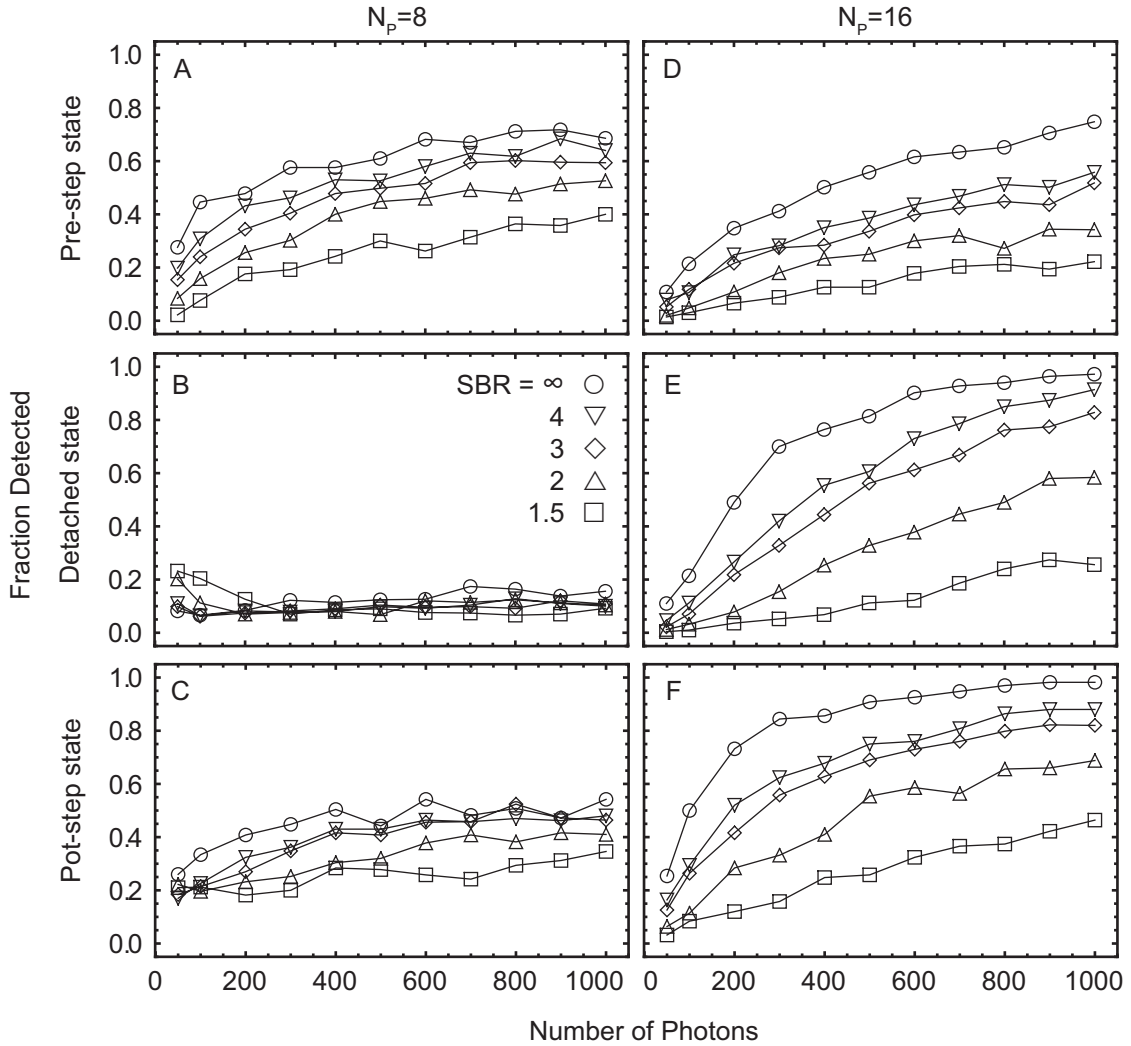
Figure 4.9: Sensitivity of the orientation analysis (i.e., no change points) to optimize to large wobble cones $(75° \leq \delta \leq 90°)$ in simulations representing polarized TIRF experiments with $\delta = 90°$ in the 8 PFI (A) and 16 PFI (B) configurations. In the range of low to moderate numbers of photons $(N = 50 - 1000)$ with the signal to background ratios (SBR= $1.5, 2, 3, 4, \inf$), the case of $N_P = 8$ nearly orthogonal PFIs is insufficient for determining large probe wobble, but the off-axis PFIs in the $N_P = 16$ case break a symmetry which allows large wobbles to be determined. Each point represents the fraction of successful trials in 500 simulations.

the change point algorithm are statistically defined, once an acceptable false positive rate is

chosen.

The high time resolution polTIRF experiments discussed in Sect. 5 are an example of

fluorescence experiments that implement SPC technology. In addition to recording photon

arrival times, the polarization state (either 8 or 16) of the detected photons is also recorded. In these experiments, the majority of change points do not involve any change in the overall intensity; instead the time when the PFIs change relative to one another is determined. Because of this distinction, a new multiple-intensity change point (MICP) analysis was developed to analyze the high time resolution polTIRF data.

The basic idea of the change point method is to test if two adjacent regions of the data are better described by two intensities or one constant intensity. Because three free parameters (i.e., two rates and the location of the change point) will fit the data better than one, a threshold consistent with a specified false positive rate is defined that requires the two-intensities to be significantly better than the one-intensity. If that condition is met, the location in the interval with the largest likelihood above this threshold is identified as an intensity change point. All of the change points in the data can be determined by applying this test recursively to the intervals between previously determined change points.

The two pieces of information recorded in polTIRF experiments can be viewed as separate terms in Eq. (4.2.6):

$$\mathcal{L}^{\mathrm{o}}{}_i = \sum_{j=1}^{N_p} \left[ n_{j,i} \ln \left( n_{j,i}/N_j \right) + \left( 1 - n_{j,i}/N_j \right) \ln \left( 1 - n_{j,i}/N_j \right) \right] \cdot$$
$$- \left[ i \ln V_i + (N - i) \ln \left( 1 - V_i \right) \right] \qquad (4.4.1)$$

The time stamp information reports on the overall intensity of the fluorophore and is contained in the second term, which depends only on the arrival time of each photon and not its polarization. The polarization information, which only consists of a number ($j = \{1, 2 \ldots N_P\}$) for each photon, is contained in the first term, where the $n_{j,i}$'s are the accumulated number of photons in each polarization channel.

In recordings with only one channel, the likelihood simplifies to the previously derived expression [100]; changes in the total intensity (Fig. 4.2*A*) can be located within a few photons of the actual change (Fig. 4.2*C*). Qualitatively, this precision is consistent with the abrupt change in intensity when the arrival times are plotted in the order that they were measured(Fig. 4.2*B*).

In recordings with two intensities, which are analogous to a simplified polarization measurement, the location of the change point is determined predominately by the first set of terms in Eq. (4.4.1) since the total intensity is constant (e.g., *black curve* Fig. 4.5*A*) and the individual PFIs change abruptly (e.g., *blue/red curve* Fig. 4.5A). Despite the relative coarseness of the polarization information, change points can still be accurately identified (Fig. 4.5C). In practice both pieces of information are useful since the orientation of the fluorophore can change in addition to the total intensity; for example, due to a bleaching event or fluctuation in laser intensity.

One disadvantage of the likelihood function Eq. (4.2.3), is that its magnitude is not uniform across the interval and is higher on average near the boundary even if no change point exists. The peaks in the likelihood function (and thus the change points) are therefore biased near the edge of the interval especially for large numbers of photons (*black line*, Fig. 4.4). Physically, this is not surprising as regions near the edge have fewer photons and are thus susceptible to relatively large fluctuations in apparent intensity. Fitting these fluctuations with an intensity that is different from the remainder of the interval, where fluctuations are smaller, falsely appears to be a significant improvement. Analytical corrections for this effect have been derived [143] for the one intensity case and successfully applied to fluorescence data [100]. Analogous correction factors were determined here from simulations (Fig. 4.6) for the multi-

ple intensity case and used in the MICP algorithm. Modifying the likelihood function using the correction factors, a weighting function, and a narrow exclusion region that prohibits change points from occurring within the first and last 2.5% of the data, nearly eliminates the bias across a wide range of photons (*blue line*, Fig. 4.4). Correcting for this effect is particularly relevant for finding substeps in myosin V polTIRF experiments since the intervals of interest are expected to follow shortly after a prominent change point, which is the same region that is sensitive to a false positive.

For intervals with a sufficient number of photons $N \gtrsim 500$, the shape of the correction factors across the interval follows a pattern as $N$ is increased. Their average values are relatively constant in the center region, peak near the edge, and then drop precipitously at the boundary. The reason for this drop is that the likelihood (Eq. (4.2.6)) is proportional to the number of polarization terms; if there are too few photons in a region then some of the terms drop out and the likelihood function decreases. This effect is clearly seen when comparing the distribution of correction factors for various number of intensities (not shown), where in the single intensity case there is no decrease at the edge and it becomes more pronounced as the number of intensities increases. The total number of terms in the likelihood function is also directly proportional to the magnitude of the correction factors. For example, the plateau of $E[\mathcal{L}^o{}_i]$ doubles from 4 to 8 as the number of intensities doubles from 8 to 16. A similar trend can be seen for $N \lesssim 500$ where the correction factors slowly increase in magnitude as the number of photons increase.

The false positive thresholds with ($\rho^0$) and without ($\rho$) the correction factors are similar but differ in significant ways (Fig. 4.3). Both increase as the number of photons in the interval

increases, but $\rho$ remains fairly constant after $N \sim 1000$ whereas $\rho^0$ continues to increase (albeit a small increase in absolute terms considering the log scale for $N$ in Fig. 4.3). As a result $\rho$ is fit by a hyperbolic equation and $\rho^0$ by a power law (see Table 4.1). The magnitude of $\rho$ and $\rho^0$ for the $N_P = 1$ case are similar, but they trend in opposite directions with increasing $N_P$. $\rho^0$ increases as the number of intensities increases because the number of logarithmic terms in Eq. (4.2.6) increases with each additional intensity. In contrast, $\rho$ decreases with additional intensities, presumably because the correction factors more than compensate for the additional number of logarithmic terms.

Single change point simulations with 8 and 16 intensities were accurately identified over a range of photons $N$ and signal-to-background ratios (SBR, Fig. 4.7). The number of photons required to detect an event was inversely proportional to the size of the transition, i.e, large magnitude change points events were easier to detect. Simulations that assume that each of the intensities participate equally in the change point are used to compare the 8 and 16 (Fig. 4.7A,B) PFI cases. For a given $N$ and SBR there is a small reduction in the sensitivity when the number of intensities is increased, but often this is a useful trade off because the orientation of the probe is better defined with 16 polarizations.

The accuracy the algorithm can also be determined by comparing the change point with its known location. The confidence limits are expected to bracket the known location for 95% of the trials. The actual accuracy depended on the number of photons and SBR, but was often greater than 98% for most of the conditions (*dashed lines*, Fig. 4.7).

If the dipole model for the probe is used instead of distributing photons equally according to $\chi$, then the sensitivity of the analysis for experimental data can be assessed. Because the

experiment entails a single molecule of myosin V translocating along actin, the orientation of the probe before and after the myosin steps is simulated (see Table 4.2). The detection of events improves as the number of photons and the SBR increases, however the decrease in performance upon increasing from 8 to 16 PFIs is more significant (Fig. 4.7C,D). An optimistic value of the SBR in polTIRF experiments is $\sim 3$ indicating that $\sim 200$ photons are required to detect 95% of the change points in the 8 PFI case. This number approximately doubles when the number of PFIs increases to 16. The reason for this is that only a few of the PFIs may be sensitive to a change in orientation, thus the number of photons contributing to the change point can be fewer than expected based on the SBR. For example, a probe that rotates $90°$ from being aligned along the $x$-axis to the $z$-axis would be obvious if the polarizations were aligned along those two directions, but would be invisible to polarizations aligned at $45°$ to those directions.

A more interesting scenario is the ability to detect a relatively short duration interval immediately adjacent to a long duration interval. Such a pattern is expected during a step of myosin V where the long interval corresponds to the tilting of the lever arm before and/or after a step and the short duration interval change point is the short lived substep of the detached head before it rebinds to actin. Simulations emulate this scenario by modeling 3 states: (1) a long-lived state (with 2000 photons) corresponding to the post-step head orientation with relatively little wobble since both heads are attached to actin, (2) a variable duration substep (0-1200 photons) of large probe wobble due to the detached head rapidly diffusing towards the next binding site, and (3) a long-lived state (also with 2000 photons) in the leading head orientation with relatively little wobble.

When there is no substep, the algorithm detects 90% of the single change points (Fig. 4.8A,D) representing the step, similar to Fig. 4.7C,D. As the number of photons in the substep increases the probability to detect it also increases (Fig. 4.8B,E) but plateaus at $\sim$ 90% due to a relatively constant $\sim$ 10% probability to detect a spurious third change point (Fig. 4.8C,F). For large $N$ the 3-change point cases almost always involve a correct determination of the substep plus an additional false positive somewhere else in the interval. Detecting the substep requires more photons in the 16 PFI case (Fig. 4.8E) compared with the 8 PFI case (Fig. 4.8B), similar to the results discussed for single change point detection. If the detected substep must be at least 90% accurate compared to its known location, then the fraction of successful events decreases markedly (*dashed*, Fig. 4.8B,E). For an SBR $= 3$, approximately 750 and 1100 photons are required to detect 80% of the intervals with 90% accuracy in the 8 and 16 PFI cases, respectively.

It is important to realize that these simulations are useful estimate of the experiments, but the actual sensitivity may be different for particular orientations. Furthermore, the simulations of myosin stepping assume that the dipole model of the probe intensities is accurate; however, this is not a necessary assumption when experimental data is analyzed since the MICP algorithm is model-independent.

Determining the probe orientation and wobble in the interval between change points (see Sect. 4.2.3) can be used to validate wether a particular change point is physically relevant. In polTIRF experiments, for example, a small change in overall intensity may result in a statistically significant change point, but if the corresponding orientation does not also change then its not likely to be biologically relevant. The usefulness of this approach, however, is

compromised by spurious changes in the orientation that arise from over-fitting to photon counting noise. The MICP algorithm minimizes this by ensuring that the maximum number of photons are included in each dwell, but the effect still remains for short duration dwells.

In order to quantify this effect for myosin V polTIRF experiments, intensities corresponding to the orientations in the post-step / detached / pre-step head states were simulated for fixed numbers of photons and signal-to-background ratios. The intensities were used as input in orientation analysis and those trials with orientations and angles within $15°$ of the simulated value were considered successful. The fraction of successful events depended on the actual orientation, but in general the ability to accurately determine the angle was better in the 16 PFI case than with 8. The detached state with a high-wobble cone was particularly improved with the addition of polarizations (Fig. 4.9B,E), due to the symmetry in the 8 PFI case between $\delta = 90°$ and $(\theta, \phi) = (54.7°, 45°)$ which result in identical polarized fluorescence intensities.

With 8 PFIs, the fraction of successful trials was comparable in the pre- and post- step states (Fig. 4.9A,C), with plateaus at 70% and 50% respectively. These relatively low rates occurred even with the maximum possible SBR with zero background counts. The reason for this low success is that PFIs with similar magnitudes can correspond to different angles. This is particularly true for values close to $\theta = 0°$ and $\theta = 90°$. In the pre-step state where $\theta \sim 97°$, increasing the number of photons $N$ eventually results in a high success rate (data not shown), but for the post-step state where $\theta \sim 19°$, $\phi$ is not well resolved close to pole resulting in a lower number of successful trials.

With 16 PFIs, the fraction of successful trials was higher for the post-step orientation than for the pre-step. The reason for this is that a "success" requires both $\theta, \phi$ and $\delta$ to be within

the 15° tolerance. Orientations that are related by symmetries in the setup may only be broken by a few of the PFIs thus making it susceptible to fluctuations in intensity that cause the inferred orientation to switch between the two symmetric states. In the pre-state the symmetry between $\phi$ and $-\phi$ is still significant for $N = 1000$ resulting in a lower success rate even though $\phi$ is well determined. In order to identify the increase in the wobble parameter during the substep with $\sim 80\%$ accuracy approximately 700 photons are required, comparable with what is required to detect the state using the MICP algorithm.

## 4.5 Conclusions

A change point analysis used for single intensity fluorescence experiments [100], was extended to multiple intensity polTIRF data. Simulations to test its accuracy and power to detect change points was determined over a range of photons and signal-to-background ratios. Simulations indicate that approximately 700 and 1100 photons are required to detect the detached state between myosin V steps in 8 and 16 polTIRF configurations. With 8 PFIs fewer photon are required to locate the short-lived state; however, 16 PFIs are required to accurately identify the increase in wobble cone. In the the next chapter, the algorithm will be applied to high time resolution polTIRF measurements of a myosin V molecule translocating along an actin filament. Change points, corresponding to abrupt orientation changes of a probe attached to the myosin lever arm, are expected with each step of the molecule. The algorithm will also be used as an impartial tool for detecting potential substeps in the cycle that occur before or after the main stepping event.

# Chapter 5

# Detection of substeps in the myosin V ATPase cycle using high time resolution polarized TIRF

## 5.1 Introduction

### 5.1.1 Motivation

Myosin V is molecular motor found in numerous eukaryotic cell types from yeast to humans and has been one of the most extensively studied myosins. Like muscle myosin, myosin V is a two-headed dimer of two catalytic domains that coordinates actin binding and ATP hydrolysis in order to perform mechanical work against a load. Unlike muscle myosin, myosin V remains bound to actin for a large fraction of its ATPase cycle and can "walk" processively for approximately 2 $\mu$m, taking $\sim$ 50 steps before dissociating [47, 144]. A central question is

how the two heads of myosin coordinate their ATP hydrolysis with stepping in order to achieve these long run lengths; a process termed "gating". In order to study gating mechanisms that are coupled to angular changes of the myosin V lever arm, the maximum time resolution of the polarized TIRF setup described in Sect. 3 is increased 100-fold using a modified time-correlated single photon counting (TCSPC) circuit. Change points in the single photon data corresponding to angle changes of the lever arm are determined using an automated algorithm, the Multiple Intensity Change Point (MICP) analysis described in Sect. 4.

## 5.1.2 Myosin V

**Biological role of myosin V**

Depending on the cell type, Myosin V acts as both a transporter and a tether for cellular components. For example, in yeast the myosin V homolog Myo4p from the mother cell controls the fate of the daughter cell by transporting an mRNA that encodes a protein which is responsible for preventing the cell from switching mating types [145]. In melanocytes, pigment granules called melanosomes are transported to the cell periphery along microtubules, while myosin V localizes the pigment in the actin rich dendrites of the cell [146]. In humans, patients with the neurological disorder Griscelli syndrome often have mutations in the myosin V gene; a discovery that was prompted by a similar phenotype in *dilute* mice, which also have impaired melanosome trafficking [147]. In Drosophila photoreceptors, light induces the release of free calcium, which triggers myosin V to carry pigment granules toward the rhabdomere (a structure in a compound eye analogous to a pupil), thereby attenuating the light that reaches the receptor [148]. The motor function of myosin V has been made famous by numerous single

molecule in vivo tracking experiments (e.g., Yildiz et al. [47]); however, other work (summarized in reference [149]) emphasizes the non-transport role of non-muscle myosins, which for myosin V includes roles as a dynamic tether of endosomes [150], binding to microtubules, localization to the centrosome, and localization within the nucleus.

**Structure and function of myosin V**

Myosin V is a homodimer (see Fig. 5.1) with structure and sequence similarity to muscle myosin with the notable exception of a $3\times$ longer lever arm containing 6 IQ motifs (IQXXXRGXXXR) that bind calmodulin or calmodulin-like light chains, and a long C-terminus alpha helical domain that dimerizes and contains a globular cargo binding tail. Native myosin V ($\sim 600$ kDa) was first isolated from from chick brain [151, 152], but today recombinant constructs, often expressed using the baculovirus system in SF9 insect cells, are widely used because the sequence can be directly manipulated and the protein expressed in large quantities. In single molecule motility measurements along actin, the tail domain is often removed in order to avoid spurious sticking to the surface and also to prevent inactivation of the myosin via head-tail binding (believed to be an autoinhibitory feature *in vivo* [153, 154]).

Kinetic measurements of a truncated single-headed 1-IQ myosin V construct indicated that myosin V spends most of its ATPase cycle attached to actin, even in the presence of ATP, and that the ADP release rate at $\left(\sim 12/\mathrm{s}\right)$ is the rate-limiting step [156], see Fig. 5.2. The fraction of the cycle that myosin is bound to actin is termed the duty ratio, and was determined to be $> 70\%$ for this single-headed construct at low actin and ADP concentrations [156]. Electron micrographs of myosin V and actin in the presence of low ATP concentrations indicate a
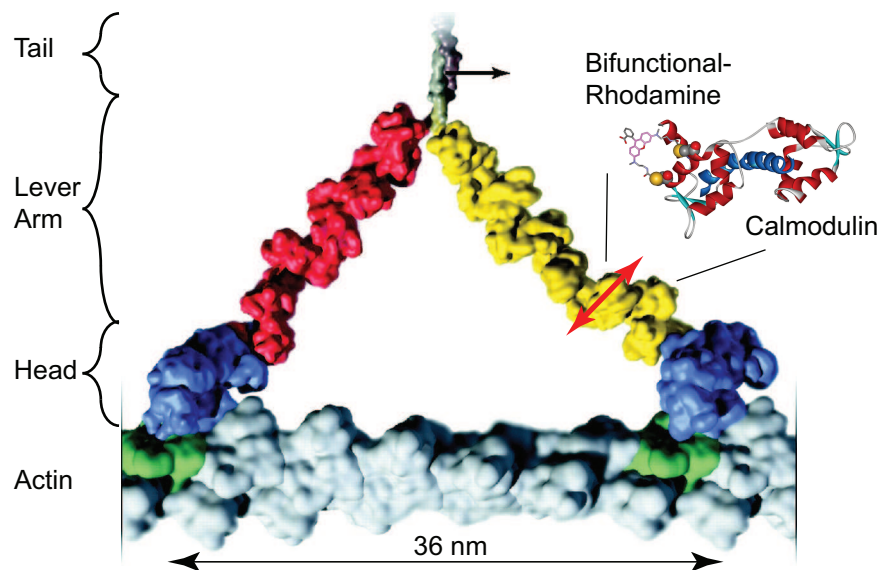
Figure 5.1: Schematic showing Myosin V bound to an actin filament [155] with bifunctional-rhodamine labeled calmodulin (BR-CaM) . One of the calmodulins (there are six on each lever arm) is labeled with bifunctional- rhodamine *(inset)* fluorophore that connects two Cysteines at amino acids 66 and 73, with a dipole axis represented by the red double-headed arrow. The molecule "walks" to the right towards the "barbed" end of the actin filament, typically taking 36 nm steps so that binding occurs on an actin monomer that is favorably oriented on the pseudo-repeat of the actin helix *(green)*. Under physiological conditions, the two head bound state is likely to have ADP bound to both motor domains *(blue)*. The symmetry in the chemical state of the two heads is broken by the mechanical asymmetry since the lead head lever arm *(yellow)* is tilted backwards in the pre-power stroke configuration and the trailing lever arm *red* is tilted forward in the post-power stroke configuration. The preference for forward steps (i.e., gating) is believed to arise–at least in part–from intramolecular strain due to rearward force on the lead head and forward force on the trail head that results in ADP releasing preferentially from the rear head so that ATP can bind, freeing it to bind to the next actin binding site. Detecting substeps in this cycle, such as tilting of the lead head lever arm before the trailing head detaches (the "telemark" state) or the highly- mobile detached state that occurs when the trailing head steps forward, are the goal of the work described here.

large fraction ($\sim$ 50%) of doubly attached myosin V molecules spanning the 36 nm half-helical repeat of actin [127]. These results are markedly different from myosin II, which typically binds to adjacent actin monomers in the absence of ATP, and provide support for a processive motor. Most of the attached molecules were in a state similar to the one in Fig. 5.1, however a minority of molecules showed a kink in the lever arm of the lead head, as if the power stroke occurred, yet could not be completed since the trail head was still attached to actin; the so-called "telemark" state. Evidence for this state has been elusive as

weak binding

attached: M.A $\xrightarrow{\text{T}}$ M.A.T     M.A.D.P$_i$ $\xrightarrow{\text{P}_i}$ M.A.D $\xrightarrow{\text{D}}$ M.A

dettached: M.T $\longleftrightarrow$ M.D.P$_i$
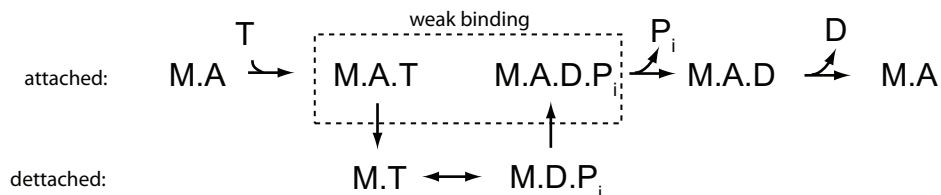
Figure 5.2: Simplified ATPase cycle of myosin illustrating the dominant pathway for force production of a single head (some states are omitted for clarity). Myosin (M) is attached to actin (A) and detaches upon binding ATP (T), which is then hydrolyzed into ADP (D) and inorganic phosphate (Pi) while myosin is detached from actin. Force is produced in the strong binding state after the hydrolysis products are released upon re-binding actin and the cycle repeats. Potential substeps in the cycle that would accompany a large angle change of the dipole and thus be detected by polTIRF include tilting motion of the lever arm in the M.A. state before ATP binds or diffusion of the free head in the period when myosin is detached *(bottom row)* or in the weak binding state *(dashed)*.

a followup study indicated that molecules in this kinked configuration were more rare than initially believed [157], however a third more recent study claims that they occur in 5–10% of molecules [158].

Direct evidence for the processive nature of myosin V was first demonstrated in two ways [18]: (1) gliding assays of actin along lower surface densities of myosin than is possible with muscle myosin and (2) optical trap measurements of multiple 36 nm displacements of an actin filament suspended above a fixed myosin V molecule. This second approach is known as a "3-bead assay" because each end of the actin is attached to a ∼micron sized bead, and then positioned above the myosin, which is attached to a third bead that is fixed to the cover slip surface. Load-dependent stepping was also observed in these optical trap experiments, culminating in ∼ 3 pN stall force and backward steps, suggesting a coupling within the molecule between force generation and the biochemical transitions.

Labeling single molecules of myosin V with fluorescent calmodulins and observing long run lengths confirmed the processivity of single myosins along an actin filament [159]. "Hand-over-hand" stepping, where one head remains bound while the other is released and swings

forward to find the next actin binding site, was supported by polarized TIRF measurements of the tilting lever arm [61]. Successive images of myosin V "walking" were soon confirmed with fluorescence imaging at one nanometer accuracy (FIONA) measurements where asymmetries in the step sizes of the fluorescent calmodulin attached to lever arm were consistent with hand-over-hand motion [47]. ADP release from the rear head prior to stepping was confirmed by simultaneously imaging the positions of a translocating GFP-tagged myosin and two fluorescent ATPs (deac-AminoATP) that were bound to either head [144].

At low ($< 50 \ \mu$M) Mg·ATP concentrations, where many single molecule experiments are performed, myosin V is often in a two heads bound state. The trailing head is likely in the nucleotide-free (apo) state with its lever arm titled forward in the post-power stroke configuration making $\sim 40°$ angle with the actin filament [127] (*red* lever arm in Fig. 5.1). The lead head most likely has ADP bound with its lever arm tilted backwards in the pre-power stroke state, making an angle of $\sim 115°$ to the actin filament [127] (*yellow* lever arm in Fig. 5.1). Upon binding ATP, the rear head releases actin and the lever arm of the front head tilts forward (the power stroke) positioning the free head in a position that is favorable to bind to the next actin binding site. As the detached head undergoes tethered Brownian diffusion in search of the next binding site [98, 160], its lever arm reverses its conformation (the recovery stroke) into the pre-power stroke state and ATP is hydrolyzed to ADP.Pi. Both products remain bound to the myosin in a state that is weakly bound to actin (Fig. 5.2), but upon locating the next binding site, the inorganic phosphate (Pi) is released, which locks the myosin into a strongly bound state with actin [156]. Some form of intramolecular gating mechanism maintains this nearly symmetric state until ADP is preferentially released from

the rear head [144] allowing the cycle to repeat.

Gating is thought to include one or more of the following mechanisms [161–168]: (1) accelerating the release of ADP on the rear head (2) retarding its release on the front head, (3) impeding ATP binding to the front head, or (4) favoring ATP binding to the rear head. Additionally, the angle change between the lever arm and head during the recovery stroke may also preferentially bias the detached head for the forward actin binding site, thus minimizing the number of back-steps [169]. The steps in ATP cycle are believed to be the same at high ATP concentrations, except that ATP binding to the apo trailing head is very rapid so that ADP release from this head becomes rate limiting.

**Prior evidence for gating and substeps**

Veigel et al. [170] measured substeps of 20 and 5 nm during the power stroke of single-headed myosin V as it pulled on a suspended actin filament in a 3-bead assay. Since binding sites were distributed every 36 nm along the filament, they hypothesized that the remaining 11 nm of the step size was the result of a random search by the head for the next binding site (i.e., the "diffusive search"). Using a Kramer's first passage calculation along with their measured single head stiffness and 1 $\mu$s diffusion time of a trapped bead, they estimated the diffusive search to be 0.1 ms. Kinetic experiments [166] of two headed constructs indicated the rapid release of phosphate from both heads but a slower ADP release rate from the leading head, further supporting the role for ADP in the gating mechanism.

Using high spatiotemporal optical trapping nanometry of a 200 nm diameter bead attached to myosin V, Uemura et al. [171], measured 12 and 24 nm substeps during some of the steps of

a myosin V translocating along actin. According to their model, the 12 nm step occurs when the trailing head binds ATP and releases actin before the lead head has undergone its power stroke. The 24 nm step follows after the lead head power stroke positions the detached head in a forward position suitable for binding to the next actin binding site. If the power stroke occurs before the trail head is released (resulting in a strained "telemark" state on the lead head) then re-binding to the next actin site occurs in one rapid 36 nm step and no substeps are detected. Their optical trap experiments of myosin V translocating along actin were preformed at saturating ATP concentration with 0.5–2.5 pN of backward load, which presumably helped maintain the detached head in a rearward position until the lead head stroke occurred. The duration of substeps were exponentially distributed with time constant of $\sim$6 ms at 1 mM Mg·ATP. The substep duration increased with increasing trap force and also in the presence of 100 mM 2,3-butanedione monoxime (BDM, traditionally a myosin II inhibitor [172]), which slowed the substeps to $\sim$40 ms. Either lowering the concentration of Mg·ATP to 10 $\mu$M or including 200 $\mu$M ADP slowed the release of the trailing head, which did not effect the duration or size of the substeps, but it did decrease the probability of a substep being detected. These results are consistent with their assay missing substeps when the lead head undergoes a power stroke before the trailing head binds.

Simultaneous measurements of orientation and position of bifunctional-rhodamine labeled calmodulin (BR-CaM, see Fig. 5.1) attached to myosin V using polTIRF with FIONA [109] determined that the lever arm usually tilts as a single straight element and does not bend or kink as suggested by telemarking molecules seen in EM images [127,158]. Even fluorophores bound to the calmodulin located closest to the head at IQ-1 or IQ-2, which didn't seem to move

147

forward with every step in previous studies [47], were also found to tilt and move forward by a small, previously unresolved amount. Sometimes large polarization changes were detected but with only a small $\pm 5$ nm change in position with no preference for leading or trailing head. At the low Mg·ATP concentrations used (0.15 and 0.5 $\mu$M), the fraction of the substeps per 37 nm increased from 10 to 25% in the presence of 100 mM BDM. Noting that the actin monomers are $\sim 5$ nm apart, these small shifts in the lever arm were proposed to be a the myosin testing its vicinity, possibly by hopping to adjacent actin monomers, before taking a full step.

By attaching a 40 nm gold particle to the myosin V lever arm and imaging the scattered light, Dunn et al. [98] were able to directly measure the bead position with nanometer accuracy and sub-millisecond temporal resolution. Increased variance in the position of the gold particle after each step of the labeled head provided strong evidence for the diffusive search. The durations of the searches were exponentially distributed with lifetime $\sim 15$ ms, and were slowed $\sim 50\%$ upon addition of 100 mM BDM but unchanged in the presence of 50 mM inorganic phosphate. The diffusive search was also measured by attaching a relatively long microtubule to the myosin V lever arm and recording its position and orientation during motility experiments [160]. They observed large variation in the microtubule orientation after the labeled head steps, and a long duration search that is exaggerated by the large diffusive drag of the microtubule.

Cappello et al. [173] measured the position of a 200 nm plastic bead attached to a single myosin molecule with subnanometer precision and microsecond time resolution using a modified optical trap-TIRF setup that also determined the $z$ position of the bead. They observed 3

substeps within the power stroke, and modeled the results as a small 5 nm longitudinal change in bead position as the molecule rocks back and forth into a telemark state, which occurs after ADP is released but before ATP binds. ATP binding releases the rear head allowing the power stroke to pull the bead forward 25 nm with a concomitant increase in $z$ and in the variance of the bead position before re-binding of the free-head to the next binding site. They estimate several time scales: the transition into the pre-step telemark state as 0.3-5 ms, depending on ATP concentration; the power stroke as $\sim 0.1$ ms; and the diffusive search to be in the millisecond time range. Some of the results are in contrast to those of Uemura et al. [171], who measured 12 and 24 nm substeps and no dependence of the substep on ATP concentration.

Several theoretical estimates for the duration of the diffusive search have been calculated. The first-passage calculation by Veigel et al. [170] already mentioned determined a diffusive search of $\sim 0.1$ ms. Using a simple model for the probability of a myosin head rebinding, the length of processive runs, and the detachment rate due to ADP release, Smith [174] estimated the rebinding rate to be $> 900/s$ (corresponding to $\sim 1.1$ ms between attachments). Craig and Linke [175] simulated gating in the molecule as intramolecular strain transmitted along the lever arms between the two heads that modified the ADP release rate. They also simulated the dynamics of the tethered head during its search for the next binding site, and determined that the diffusion time scale is between 0.1 and 1 ms. They conclude that rebinding of the free head is limited by ATP hydrolysis and not the diffusion time required to find the next actin binding site. Biochemical estimates of ATP hydrolysis rate are $> 700/s$ and phosphate release is $175 - 250/s$ (corresponding to mean intervals of 1.5 ms and 4-5 ms, respectively) [156, 166].

In summary, substeps in the myosin V ATPase cycle have been measured by several groups

and typically involve resolving portions of the power stroke of the attached head or the diffu-sive search of the free head for the next binding site. Some discrepancies exist in the results as to the exact magnitudes and dependency on ATP, ADP, and BDM, although factoring in tech-nical differences between the techniques such as the concentration of ATP, size of reporter particle, and the spatial and temporal time resolution may resolve many of these apparent differences.

It is interesting to note that the diffusive search of the free head of kinesin for the next binding site is relatively easy to measure since the ATPase cycle is shifted relative to myosin. In kinesin ATP binding triggers neck-linker docking along the microtubule-bound head [176], which positions the detached head in proximity to the next binding site. Simply reducing Mg·ATP lengthens the period when the detached head is free from the microtubule. The detached state has been measured by single molecule polarized fluorescence [177] and optical trap [178].

### 5.1.3   High time resolution fluorescence measurements

Single molecule fluorescence experiments of molecular motors typically implement a high-sensitivity CCD camera in order to image many molecules simultaneously across a large field of view. The time resolution of such experiments is usually limited to video rates (30 frames/second) although faster rates are possible (e.g., [98, 179]). In single molecule fluores-cence measurements, the frame interval is increased to 100's of milliseconds (e.g., [47, 109]) in order to collect sufficient photons. Avalanche photodiodes (APDs) are an alternative pho-ton detector with higher maximum count rates ($> 10^5/s$), but are restricted to a much

smaller field of view. APDs are frequently used to record bursts in fluorescence correlation experiments as the molecule of interest diffuses into the imaging volume [180]. A particularly powerful technique involves combining APD detection with a TCSPC device that maximizes the time resolution of the measurement by recording the arrival time of each photon [100, 139, 181]. Such experiments with immobilized single biomolecules has also been achieved [182], including on the molecular motor kinesin [183].

## 5.2 Single photon counting technology

Time-correlated single photon counting (TCSPC) technology has its origin in nuclear instrumentation used to measure the decay of radioactive elements, but it has been continuously developed and improved for use in measuring the nanosecond lifetime of fluorescence molecules. An entire branch of microscopy known as fluorescence lifetime imaging (FLIM) is based on reconstructing images based on how the fluorescence lifetime changes across a sample [184].

The technique involves periodically illuminating a fluorescent sample with a short laser pulse and then measuring the time elapsed from the excitation pulse to the detected fluorescent photon. Extremely fast and precise electrical circuits are required to measure these nanosecond arrival times with picosecond accuracy, record the answer, and then reset the circuit, all before the next laser pulse excites the sample [185]. In ensemble measurements, the laser power is reduced such that most of the laser pulses do not result in any detected photons. This strategy reduces the number of photons that are detected but not recorded during the instrument dead time, which can result in artifacts. The nanosecond time between excitation and fluorescence emission is called the "microtime" and represents the time-correlated part of TCSPC. The

arrival time of each photon from the beginning of the experiment (termed the "macrotime") is also recorded.

Experiments with continuous laser illumination, such as the polTIRF experiments described here, utilize only the single photon counting macrotime and not the microtime. The technical challenge in developing millisecond-time resolution polTIRF is synchronizing the rapid switching of the excitation polarizations with the photons detected during each interval. A more practical challenge is collecting enough photons from the fluorophore in the short period of time that a substep occurs. Increasing the laser intensity will increase the rate of fluorescence emission, however, the rate of photo-bleaching (irreversible quenching of the fluorophore) also increases,thus limiting the recording time of each molecule. Next, the details of single photon counting are summarized, and then their implementation in the polarized TIRF setup described in Sect. 3 will be discussed in Sect. 5.2.2.

## 5.2.1 Hardware

Single photon counting consists of a fast timing circuit that measures the time interval between two pulses: the sync pulse, normally corresponding to the rapidly ($\sim 10 - 50$ MHz) pulsed laser excitation in a conventional TCSPC configuration, and the detector pulse, corresponding to the fluorescence emission (see Fig. 4.1). The major components of an SPC circuit that are required to perform this calculation include a constant fraction discriminator (CFD), time-to-amplitude converter (TAC), and analog-to-digital conversion (ADC), see Fig. 5.3.

The purpose of the constant fraction discriminator is to distinguish between detector events that are generated by fluorescence photons from those that are generated by background noise.
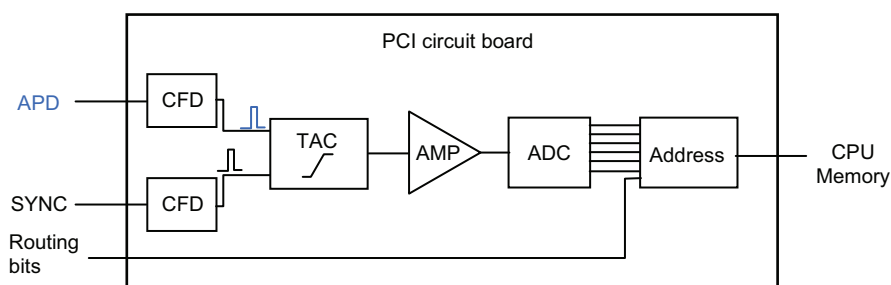
Figure 5.3: Diagram of a single photon counting circuit. The APD and sync pulses pass through a constant fraction discriminator (CFD), which rejects anomalous pulses. The APD pules starts a voltage ramp in the time-to-amplitude converter (TAC) that is stopped by the subsequent sync pulse. The voltage ramp is amplified (AMP) and converted to a digital signal (ADC) that is stored in memory along with the 3 bits of routing information which indicate the detector and polarization state when the photon was detected.

This step is important when photomultiplier tubes are used to convert the fluorescence emission into an electrical pulse because there is considerable variability in the pulse width and height. With single photon counting APDs, however, an internal circuit performs this task and the output is a uniform 5 V pulse that is 40 ns in duration, and is unambiguously detected by the SPC circuit. The quantum efficiency of the APDs is $\sim 55\%$ at the emission peak of rhodamine with linear detection efficiency up to $10^6$ counts/s. Thus, discrimination of APD pulses from the background is not an issue.

The TAC is the heart of the timing circuit. The sync pulse starts a linear voltage ramp and the APD pulse stops the ramp so that the voltage is directly proportional to the arrival time between the two pulses. This time interval is the microtime used to measure the nanosecond lifetime of fluorescence molecules. In order to minimize the dead time associated with resetting the ramp during intervals when no photons are detected (which is most of them), the circuit is operated in a "reverse stop-start" configuration. The ramp is only started when a photon is detected, and then the following sync pulse stops the ramp. The desired arrival time is then the sync pulse interval minus the ramp time.

With the continuous laser source used here the microtime feature is not meaningful, but a sync pulse is still required to reset the TAC. There are two ways to obtain this sync pulse: an external pulse from a signal generator can be used to mimic the pulsed laser, or an internal 20 MHz clock can be used in conjunction with a dummy sync pulse. The dummy pulse is basically an "echo" of the APD signal that is obtained by splitting the APD signal so that one end goes to the detector input, and the other end is passed through a long ($\sim$10 m) length of cable in order to generate a delay before going into the sync input. This delay mimics the excited state lifetime, and results in a constant microtime for each detected photon, but its actual purpose is to reset the timing circuit so that another fluorescence photon can be measured.

An analog to digital converter (ADC) converts the voltage from the TAC into a memory address that encodes the micro- and macrotimes. If multiple detectors are used, an additional 3 routing bits of the memory address can be used to encode which detector measured the photon. Because SPC experiments are performed at low fluorescence intensities, especially when measuring single molecules, multiple detectors (up to 8) can be routed into a single SPC board. As will be discussed, in this work one bit is used to represent the two detectors and the other two bits are used to encode the polarization state of the setup when the photon was recorded.

Numerous software modes exist for visualizing the data in real time, however for the single molecule motility experiments the SPC circuit is operated in FIFO mode (first in-first out) and the data consists of a text file containing a long list of photon arrival times measured in units of the sync pulse. If the internal clock is used then the sync pulses arrive every 50 ns, but here

154
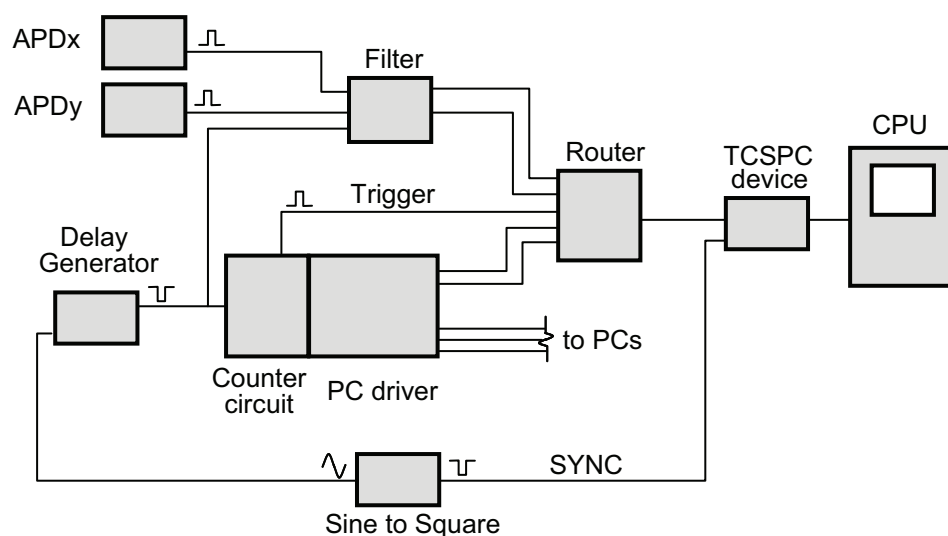
Figure 5.4: SPC modifications to the polTIRF setup shown in Fig. 3.1. A delay generator provides a 10 kHz gate pulse that consists of a short negative pulse (typically, 3 $\mu$s at 0 V followed by 97 $\mu$s at 5 V) that provides the timing signal for a counter circuit, which changes the voltage on the Pockels cells to preset magnitudes corresponding to the desired $s$, $p$, $L$, and $R$ polarizations every 100 $\mu$s. The gate pules is also combined with the APD signals to filter out photons that arrive during the 3 $\mu$s that the Pockels cells undergo the voltage change, see Fig. 5.7. The filtered APD signals, experiment trigger, and 2 bits representing the polarization state of the setup are combined in a router before input to the TCSPC device where the arrival time of the photon pulse is measured and stored in memory on the computer. In order to synchronize the TCSPC clock with the delay generator, the 10 MHz oscillator signal from the delay generator is converted to a negative pulse using a custom circuit (Sine to Square) that is then used as the SYNC signal in the TCSPC device, see Fig. 5.8.

an external signal is used to generate a sync pulse every 100 ns.

## 5.2.2   Modifications to polarized TIRF setup

In order to measure substeps in the myosin cycle, the polTIRF setup from Sect. 3 is modified

by increasing the frequency at which the polarized laser illuminates the sample and also by

recording the individual photon arrival times and their polarization state using a modified

TCSPC device (Fig. 5.4). The optics in the polTIRF setup (Fig. 3.1) remain unchanged, but

significant modifications to the detection hardware and software were required.

A digital delay generator (DG645, Stanford Research Systems) is used to generate a timing

gate pulse at the desired frequency of 10 kHz for cycling the Pockels cell voltages, which control the polarization state of the illumination laser. These voltages are controlled by a custom built circuit that is synched to the DG645 gate pulse [63]. Fluorescence emission is detected on two APDs (Perkin Elmer, SPCM-AQR-16) whose signals are combined into a single channel using a specialized router (HRT-82, Becker and Hickl) and then input into the SPC circuit (SPC-130, Becker and Hickl). A single SPC circuit is adequate for two detectors because the photons emitted from a single fluorescence molecule are much lower than the maximum count rate of the circuit. Here, the dead time of the SPC circuit is $\sim$200 ns and corresponds to a maximum detection rate of $5 \times 10^6$ photons/s, which is $\sim 50\times$ the count rate emitted from the molecules. Since only two detectors are used, the polarization state of the system (up to 4 polarizations) is output from the counter circuit and substituted for the 2 unused routing bits. A trigger signal that synchronizes the beginning of the recording with the first polarization in the cycle is also routed into the TCSPC device.

The resulting data file consists of a list of the photon arrival times, each with a tag (0-7) that corresponds to the detector (APDx or APDy) and polarization (*s1, p1, p2, s2*) of the excitation laser when the photon was detected. Plotting the polarization tag versus the arrival time results in a staircase-like plot of the photons detected in each APD during the gate interval (*points and dashed vertical lines*, respectively, in Fig. 5.5A). There are 1000 sync pulses during each 0.1 ms gate and thus 1000 potential photon arrival times, although typically only 0-5 photons are measured during each gate.

A high-sensitivity CCD camera (Cascade II, Photometrics) replaced the V/ICCD camera that was used to collect data for twirling experiments in Sect. 3. Due to the integral nature of
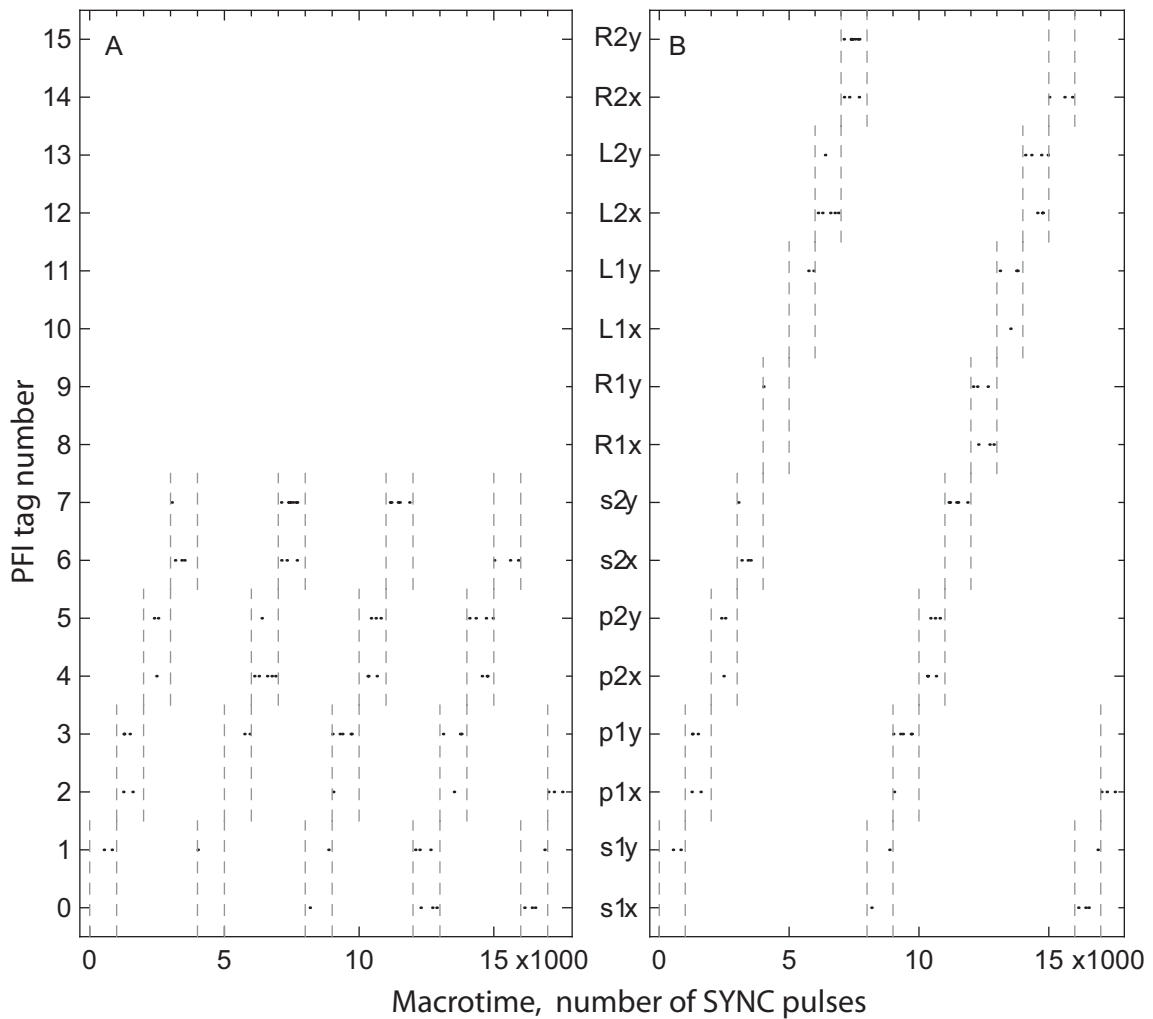
Figure 5.5: SPC photons with polarization tags. (A) Detected photons *(points)* are tagged with a number (0-7) indicating their polarization state while their macrotime, measured in units of the number of sync pulses that have elapsed, is also recorded. One sync interval is 100 ns so that a macrotime of 10 000 equals 1 ms. Photons arrive randomly during each gate interval of 100 $\mu$s with a probability that is proportional to the intensity of the corresponding polarized fluorescence intensity (PFI) in either APDx (odd tags) or APDy (even tags). After the gate is complete the polarization tags increases resulting in a staircase-like distribution of arrival times that repeats after 1 cycle of four polarizations. (B) The number of routing bits limits the number of unique polarization tags so that experiments with 8 input polarizations (16 PFIs) need to have their tags shifted in software by 8 during every other half-cycle.

the camera in coordinating the experiment and the significant difference in camera technology,

a new software interface was written in LabView (National Instruments, (Austin, TX)) to

replace the previous interface written in C code (Sect. 3). The functionality of the new program

157

is basically the same: dual shutter controls for the 633 nm (HeNe) and 532 nm (Nd:YAG) lasers; real-time control, acquisition and display of camera images; selection of a pixel and its subsequent alignment above the APDs via a nanostage for polarization analysis; turning the microscope mirror turret to direct fluorescent emission collected by the objective away from the camera and towards the APDs; simultaneous triggering the hardware and software to begin recording during the 1$^{st}$ polarization of the cycle; and control, acquisition and display of the photons recorded by the SPC circuit. A major advantage of the LabView software is that different camera triggering and shutter schemes can be easily implemented, resulting in a more flexible and user-friendly interface than with the C code interface.

Another key difference with the twirling experiments is that higher laser powers are required to measure the short duration substeps within the myosin ATPase cycle. Typically, the laser power was $\sim$15 mW incident on the sample plane for each beam, approximately 3$\times$ times higher than for the twirling experiments in Sect. 3.

**Pockels cell voltage decay**

The low voltage signals used to set the Pockels cell voltage change rapidly ($\sim$10 ns), however the high voltage amplifiers needed to drive the Pockels cells change much more slowly, in approximately 1-5 $\mu$s, see Fig. 5.6A. This response is problematic for polTIRF measurements because the polarization state of the illumination during this transient is ambiguous and results in detected photons that cannot be attributed to any of the polarized fluorescence intensities (PFIs). The slow voltage change also decreases the signal to background ratio since the initial Pockels cell (PC0 in Fig. 5.4) directs the laser between the two beam paths. Thus, leakage of
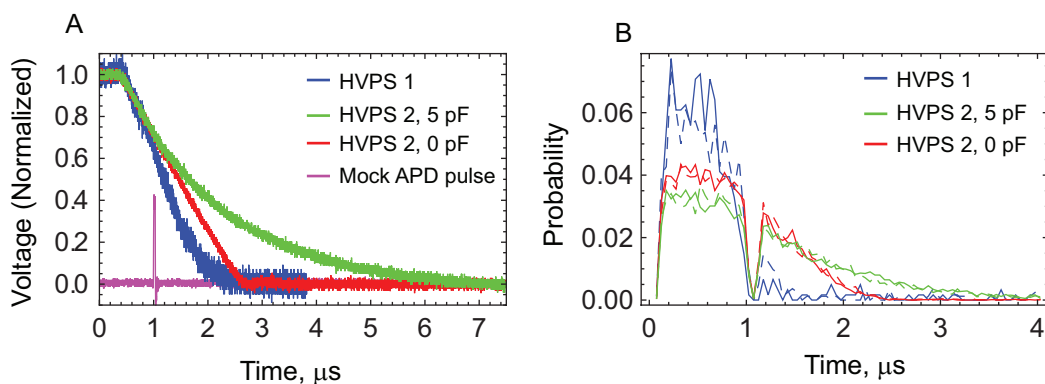
Figure 5.6: Pockels cell high-voltage transient. (A) The voltage transient across the Pockels cell during the change between two polarization states is shorter when the capacitance across the output terminal of the high voltage amplifier is reduced from 5 *(green)* to 0 pF *(red)* in a custom built high-voltage power supply (HVPS2). The voltage transient using a commercial power supply (*blue* HVPS1 (ConOptics, Danbury CT)) is slightly faster. A mock-APD pulse is generated on the rising edge of the the gate pulse for synchronization purposes *(magenta)*. (B) Probability of detecting a photon in APDy during a polarized fluorescence measurement of the decay due to high voltage transient slowly changing the polarization state from high to low fluorescence in Beams 1 *(solid)* and 2 *(dashed)*. The dip in intensity at 1 $\mu$s is due to the mock pulse in APDx, which prevents any photons from being detected in APDy (see text for details).

Beam 1 photons into Beam 2 (and vice versa) directly increases the background counts during the recording.

The voltage transient of the custom-built high-voltage power supplies is improved by removing the capacitor across the power amplifier output terminal (*green and red lines* Fig. 5.6A), and the resulting transient is almost as sharp as for a commercial high-voltage power supply (ConOptics, (Danbury, CT), *blue line* Fig. 5.6A). In order to assess the impact of this voltage transient on a typical measurement, a 100 nM rhodamine solution is excited by one beam while the other is blocked with an opaque object. The fluorescence emission is collected on one of the APDs and a mock photon is generated in the other APD on the rising edge of the gate pulse in order to ensure that the collected fluorescence is precisely synchronized with the electrical signal (*magenta line* Fig. 5.6A). The fluorescence detected when the beam is in the blocked path should be very low, however since the high voltage requires ∼1 $\mu$s to change, the

beam is not immediately directed into the blocked path, and a decay in the fluorescence signal down to the low background level can be seen at the beginning of the gate interval (Fig. 5.6B). The decay of the fluorescence for the different power supplies is in rough agreement with the corresponding voltage decay. The dip in the distributions at $\sim$1 $\mu$s is because the SPC circuit is busy detecting the mock photon pulse when the fluorescence photon was detected.

The influence of the remaining Pockels cell voltage transient is eliminated by omitting the photons recorded immediately after the gate pulse. In order to accomplish this filtering in hardware, the pulses from the APDs are compared with the gate pulse (using an 'AND' logic gate) so that photons that arrive during low voltage region of the gate pulse are rejected and photons that arrive during the high voltage region between gate pulses are passed on to the router (Fig. 5.7A). Using the delay generator, the duration of the gate pulse can be set independently from its period of 0.1 ms. Fluorescence measurements similar to those described for Fig. 5.6B were performed with gate durations of 0, 1, 2 and 3 $\mu$s to filter out the effects of the voltage transient (Fig. 5.7B). Subsequent experiments all used 3 $\mu$s gate pulses so that the filter rejects photons detected during the first 3% of the gate interval.

**Sine to sync conversion circuit**

The SPC circuit board measures the arrival time in intervals defined by an internal 20 MHz clock. Deviations as small as 1 part in $10^6$ between this internal clock and the external gate pulse from the delay generator result in 1 $\mu$s of drift per second of recording. In order to avoid any issues arising from this mismatch, the internal clock of the SPC board is bypassed with the 10 MHz oscillator signal from the delay generator, thus ensuring that the polarization of
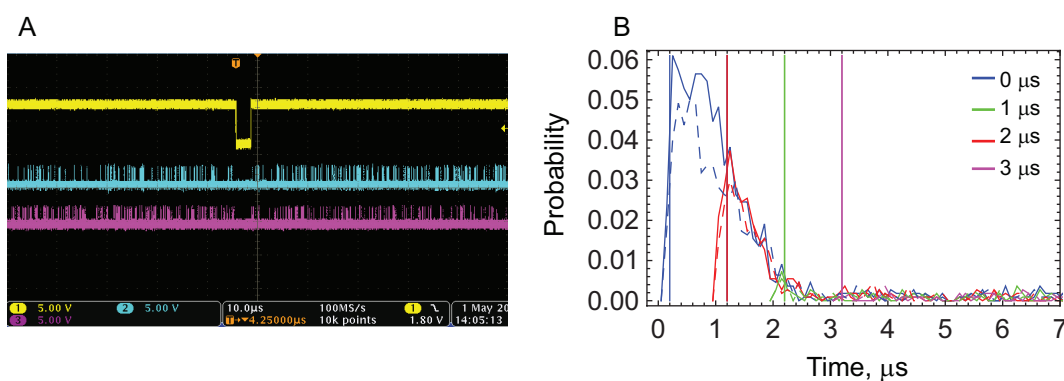
Figure 5.7: APD and gate pulse filter. (A) the APD pulses in APDx (cyan) and APDy (magenta) are AND-ed with the gate pulse (yellow) so that only photons that arrive after the short gate pulse are recorded. (B) Experiments similar to Fig. 5.6B using HVPS2 with 0 pF capacitance with a varying duration gate pulses (0-3 $\mu$s) to exclude photons that arrive within that interval immediately after the Pockels cell changes voltage. Subsequent experiments were performed with a 3 $\mu$s gate pulse.

the laser changes synchronously with SPC circuit. As a result, the SPC circuit measurement interval is longer (100 ns instead of 50 ns), but any concerns with drift between the two clocks is eliminated. The 10 MHz sine wave from the delay generator must be converted to very short duration 10 MHz negative pulses in order to mimic a typical sync signal from a photomultiplier tube. This conversion was accomplished in a custom built external circuit before passing the sync signal into the SPC circuit (Fig. 5.8).

# 5.3 Myosin V experiments

Single molecule processivity experiments were performed on recombinant mouse myosin V with the cargo-binding tail domain removed. The myosin is visualized by labeling one of the 12 calmodulins with a bifunctional rhodamine that crosslinks two specific sites on the calmodulin, see Fig. 5.1. During the processivity assay, the orientation of the bifunctional rhodamine is measured using polarized TIRF as the myosin translocates along actin in the

Figure 5.8: Sine wave to square pulse circuit. The delay generator 2 V peak-to-peak 10 MHz sine wave is converted to a short duration negative pulse of the same frequency for use as the SYNC pulse in the SPC circuit. The initial PNP bipolar junction transistor (BJT) rectifies the negative part of the input sine wave and the totem pole arrangement of the two PNP and NPN BJTs amplifies this small signal into a sharp negative going pulse suitable for input into the SPC circuit.

presence of Mg·ATP. Protocols for the purification of myosin V, exchanging a BR-CaM onto its lever arm, and performing a processivity assay are discussed in Appendix 5.7 since they have been discussed elsewhere in the literature [2, 61, 63, 186, 187].

The most relevant details of the processivity assay are briefly summarized. Low concentrations of BR-CaM myosin V present in solution such that single molecules were observed to occasionally land and translocate on actin filaments. Phalloidin-stabilized actin filaments were polymerized in a ratio of 1:5:20 monomers of biotin-actin : Alexa-647 actin : unlabeled actin, and attached to a PMMA-coated quartz slide using either the biotin-BSA/streptaividn system or NEM-myosin. BSA was used to block myosin V molecules from non-specifically sticking to the surface. Imaging buffer contained 100 mM DTT, 5-40 $\mu$M Mg·ATP, and sometimes 100 mM BDM, a myosin II inhibitor. See Appendix 5.7.3 for further details. Next, novel details of a modified polTIRF analysis are described.

### 5.3.1 Data collection and calibration

Polarization data is collected similar to the twirling experiments, except that the images of a moving rhodamine molecule (i.e., BR-CaM attached to myosin V) are superimposed on a background image of the stationary Alexa-647 labeled actin filament. Only molecules moving along an actin filament are selected for polarization recording. The data collected for each molecule consists of three CCD images of the sample plane (one of the stationary Alexa-647 actin filaments and two of the moving rhodamine molecules), the pixel coordinates of the selected molecule so that it can be located during analysis, and a text file containing the photon arrival times and corresponding polarization tags. The tags indicate the detector and polarization state of the excitation laser.

Calibration and alignment is performed as discussed for the twirling experiments (Appendix 3.5.2), except that the rhodamine B calibration solution adheres to the PMMA so a separate calibration sample without PMMA is required.

### 5.3.2 Data analysis

In general, the determination of fluorophore orientation and wobble from the measured polarized fluorescence intensities (PFIs) using the dipole model is very similar to the procedure in the twirling experiments (Appendix 3.5.3), however some differences arise due to the format of the SPC data and the discontinuous angle changes of a tilting myosin V compared to a smoothly twirling actin filament. Intensity traces of the binned data are calculated for visualization purposes and are not used in the main analysis. Instead, the MICP analysis developed in Sect. 4 is used to find change points in the unbinned SPC data, and then intensities are

defined during each interval between adjacent change points for input to the dipole model. Another difference is that in order to consistently choose a hemisphere for representing the dipole orientation, a new approach based on defining the principle axis of the distribution of orientations (i.e., the director) is developed.

After data collection is complete, the raw SPC data for each photon must be converted to arrival time and assigned to the proper PFI. Conversion of the macrotime from units of sync pulse to units of seconds requires a scale factor, in this case 100 ns per sync pulse. With 4 input polarizations (8 PFIs), identifying the proper PFI is trivial since there are an equal number of tags, however, in the event of 8 input polarizations (16 PFIs) an additional step is required. The polarization tags in Fig. 5.6A are represented in chronological order to give the staircase shape, but in the raw data the tags are assigned according to Table 5.1. For data with 16 PFIs, there are not enough tags to uniquely identify each one, so every other half-cycle of 8 polarizations (corresponding to the off-axis polarizations $L1, R1, L2$ and $R2$) must be assigned to tags 8-15. Since the trigger starts the experiment at the beginning of the polarization cycle, the macrotime can be used to shift the polarization tag by 8 after every other half cycle (one half-cycle equals 4000 sync pulses, see Fig. 5.5B). The time for one complete cycle of the 16 PFIs is 0.8 ms.

After converting the raw SPC data to arrival times and the proper PFIs, the total intensity during the recording in 10 ms bins is determined so that molecules emitting for at least $\sim$ 0.5 s before photo-bleaching could be manually selected for further analysis. Occasionally, the intensity indicates either rapid blinking events or slow variations, presumably due to a contaminant entering the recording volume; both of these types of recordings were omitted

164

| SPC tag | PFI | SPC tag | PFI |
|---------|-----|---------|-----|
| 0 | $_{s2}I_x$ | 4 | $_{p2}I_x$ |
| 1 | $_{s2}I_y$ | 5 | $_{p2}I_y$ |
| 2 | $_{p1}I_x$ | 6 | $_{s1}I_x$ |
| 3 | $_{p1}I_y$ | 7 | $_{s1}I_y$ |

Table 5.1: Conversion between 8 SPC tags and 8 polarized fluorescence intensities, 16 PFIs requires additional modification (see text for details).

from further consideration. Each recording was analyzed using the MICP algorithm developed in Sect. 4 to locate the statistically significant change points and their uncertainty (with 5% false positive error rate). Afterwards, a region of the recording containing the fluorescence emission prior to photo-bleaching (i.e., the 'signal') and a region afterwards that is free of large fluctuations (i.e., the 'background') are chosen manually for further orientation analysis.

The dipole model used to determine the maximum likelihood orientation and wobble of the probe from the measured PFIs is the same as for twirling (see Sect. 3.2.4). The magnitude of the PFIs input into the model, however, are calculated from the number of photons that arrive between two adjacent change points, thereby determining the most likely orientation and wobble of the probe during the entire interval. One detail is that the dipole model assumes Poisson statistics so that the input is actually the number of photon counts for each PFI, not its intensity (i.e., counts/time). This distinction allows the proper weighting between the PFIs with different numbers of photons; however, the number of background counts, which is also an input for the model, must be separately assigned for each dwell. To accomplish this, the average background intensity for each PFI is determined from a region of the recording after

the bleach. For a given interval, the number of background counts in each PFI is calculated by multiplying the dwell duration by the average background intensity of each PFI.

The uncertainty in the orientation and wobble during each dwell is estimated from the uncertainty in the precise location of each change point. By varying the beginning and ending time of each dwell consistent with the high and low confidence intervals of the two change points, the uncertainty in the PFIs during each dwell can be estimated (see Sect. 4.2.3 for details). As a result, five estimates of the probe's orientation ($\theta$ and $\phi$ in the microscope reference frame), wobble $\delta$, and intensity $\kappa$ are determined for each dwell. For comparison purposes, the dipole model is also used to analyze the data binned with 8 ms bins per cycle, analogous to the twirling analysis but with $10\times$ smaller bins. Of course, many more estimates of the orientation and wobble are obtained for the binned PFIs, but each one is noisier due to the relatively low number of photons that arrive within each 8 ms bin.

**Director-defined hemisphere**

The dipole model determines the maximum likelihood orientation $(\theta, \phi)$ of the probe, but the vector pointing in the opposite direction $(180° - \theta, \phi + 180°)$ is equally valid due to its dipole symmetry. Unambiguously distinguishing between these two is impossible, however it is convenient to represent the orientation of the probe by referring to one of the two ends in a consistent manner. When the opposite end of the dipole is reported, spurious 180° jumps in orientation appear to occur, even for a stationary dipole. Thus, it is desirable to define a hemisphere and refer to only the end of the dipole contained within it. As long as the change in angle between the different orientations is less than 90°, a single hemisphere can contain

166

the same end of the dipole, however if the angle changes are greater than $90°$, then reporting the opposite end of the dipole will occur. This procedure is relatively straightforward for molecules attached to twirling actin filaments since the motion was continuous with no large angle changes. For a translocating myosin V, however, the issue is more complex due to the large, discontinuous angle changes that accompany each step.

In order to choose a hemisphere that is optimum for each molecule, the polar axis of a hemisphere is calculated from the set of dipole orientations for that molecule. This axis is defined as the director of the nematic liquid crystal order parameter $\Xi$ [188]:

$$\Xi_{i,j} = \frac{1}{n_D} \sum_{k=1}^{n_D} \left( \mathcal{O}_{k,i} \mathcal{O}_{k,j} - \frac{1}{3} \hat{\delta}_{i,j} \right) \tag{5.3.1}$$

where $n_D$ is the total number of dwells in the recording, $\overrightarrow{\mathcal{O}}_k = \langle \sin(\theta_k) \cos(\phi_k),$ $\sin(\theta_k) \sin(\phi_k), \cos(\theta_k) \rangle$ is the $k^{\text{th}}$ orientation of either end of the dipole represented as a unit vector in cartesian coordinates; $i, j = \{1, 2, 3\}$ are indices representing the $x, y$ and $z$ coordinates; and $\hat{\delta}_{i,j}$ is the Kronecker delta equal to 1 when $i = j$ and zero otherwise. Note that regardless of whether $\langle \mathcal{O}_{k,x}, \mathcal{O}_{k,y}, \mathcal{O}_{k,z} \rangle$ or its dipole symmetry $\langle -\mathcal{O}_{k,x}, -\mathcal{O}_{k,y}, -\mathcal{O}_{k,z} \rangle$ is used in Eq. (5.3.1), the directions of the eigenvectors are unchanged since the matrix is symmetric. Since $\Xi$ is a $3 \times 3$ matrix, there are 3 orthogonal eigenvectors, and the polar axis of the hemisphere is assigned to be the dominant eigenvector (i.e., the eigenvector with the largest eigenvalue).

The advantage of this approach is that the director can point in any direction, and a hemisphere that is aligned along it will contain only one end of the probe dipole for each estimate of the orientation during the recording. One still has to choose which end of the director axis

to align with the hemisphere; here the end closest to the direction of motion of the molecule is chosen arbitrarily and termed $\hat{n}$. In motility experiments the direction of motion is along the actin filament, where the angle $\phi_{\text{actin}}$ is determined from the molecule's location in the CCD images that were obtained prior to the polarization recording (see Appendix 3.5.3 for details). After defining the director and restricting the orientation of the probe to be in a hemisphere centered about $\hat{n}$, the orientation in the microscope frame $(\theta, \phi)$ is rotated into the actin frame $(\beta, \alpha)$, where $\beta$ is the polar angle with respect to the actin filament and $\alpha$ is the azimuthal angle around the filament, as was described in Sect. 3.

The dipole symmetry for the set of orientations determined for the binned data calculations $\{\theta_B, \phi_B\}$ is resolved by choosing whichever end of the dipole has the smaller polar angle, i.e., if $(\theta_B - \theta) < (180° - \theta_B - \theta)$ then $\{\theta_B, \phi_B\}$ is chosen but if not then $\{180° - \theta_B, 180° + \phi_B\}$. This definition forces most of the discrepancies between the change point and binned results into the azimuthal coordinate $\phi$, where they can be compared more easily. In the microscope frame, the analogous algorithm for distinguishing between $(\beta_B, \alpha_B)$ and $(180° - \beta_B, 180° + \alpha_B)$ was less successful so the end of the dipole which minimized the total deviation with $(\beta, \alpha)$ was chosen.

Lastly, the absolute angular displacement between adjacent dwells (which includes contributions from both $\alpha$ and $\beta$) is defined as $\zeta = \arccos\left(\overrightarrow{\mathcal{O}}_k \cdot \overrightarrow{\mathcal{O}}_{k+1}\right)$. $\zeta$ can be used to gauge the size of an angle change independent of a particular reference frame, however, it still depends on the choice of hemisphere used to describe the dipole.

### 5.3.3 Analysis assumptions

The MICP algorithm assumes that the fluorescence emission from the probe can be divided into regions where each PFI is described by a constant rate Poisson process, and that the transitions between regions are abrupt. The algorithm locates change points at each statistically significant transition and different states of the molecule are represented during the intervals between adjacent change points. Each state is characterized by the magnitude of the PFIs using the dipole model to determine the maximum likelihood orientation and wobble of the probe during the interval.

Specific assumptions for the dipole model are described in Appendix 3.5.3, but the wobble parameter requires further consideration as it assumes that the probe has had sufficient time to explore the available orientations during the time of the measurement. Despite increasing the polarization cycle 100-fold such that each polarized illumination excites the sample for 100 $\mu$s, this short duration is still relatively long compared to the rotational diffusion time. For example, the rotational correlation time measured by fluorescence anisotropy experiments for a large protein such as the 840 kDa chaperonin protein GroEL is $\sim$ 350 ns [43], almost 300 times faster than the polarization time scale in polTIRF. The detached myosin V head including the 6 calmodulins is over 3 times smaller than this. Thus, the variability of the probe orientation on the microsecond time scale can still be represented as rapid wobble in a cone of half angle $\delta$ centered along the orientation $(\theta, \phi)$.

It is assumed that the orientation of the probe during each interval reports on the orientation of the lever arm since the calmodulins are firmly attached under the low calcium conditions used during the motility assay. A crystal structure of calmodulin bound to a region of the

lever arm containing the first IQ motif (pdb 1aji, [189]) suggests that the BR-CaM attached between residues 66 and 73 makes a 40° angle with the lever arm [61]. The exact angle of the fluorophore around the lever arm is unknown because there are 6 different calmodulin binding sites, although it seems that only a subset of 3-4 are readily exchanged [47, 109]. Because of this uncertainty in orientation between the lever arm and the probe, the measured rotation of the probe $(\Delta\beta, \Delta\alpha)$ does not directly describe the power stroke. As an extreme example, if the probe is aligned in the same direction as the axis of the lever arm rotation, then the probe orientation will not appear to change at all. Empirically this is not the case as orientations are clearly visible in most of the traces.

In the simplest interpretation of the power stroke, where the myosin translocates along the actin filament [115], the lever arm can be considered to swing mostly along the direction of the actin filament with a smaller component around the actin filament (i.e., $\Delta\beta_L > \Delta\alpha_L$, where the '$L$' denotes angles of the lever arm with respect to the actin filament, which are not directly measured, but are related to the $(\beta, \alpha)$ by a fixed angle). Angle changes corresponding to twisting of the lever arm would also cause the probe angle to change, and further complicate the interpretation of $(\beta, \alpha)$. Twisting motions do not seem necessary for the typical 36 nm (13 actin monomer) step, but myosin V is known to also step to monomer-11 and -15 [127], which would result in additional azimuthal rotation in $\alpha$ of $-28°$ and $+28°$, respectively, and possibly a twisting component due to the helical geometry of the filament.

The hemisphere assumption can also introduce angular ambiguity when the angle between the two orientations is greater than 90° (i.e., $\arccos\left(\vec{\mathcal{O}}_k \cdot \vec{\mathcal{O}}_{k+1}\right) > 90°$). In this case the hemisphere contains opposite ends of the dipole and the reported angle changes will not reflect

the physical angle change of the lever arm. Not only does $\zeta$ appear to be smaller than it should be, but the relative magnitudes of $\beta$ and $\alpha$ will each be shifted to $(180° - \beta, 180° + \beta)$.

## 5.4  Results

Using the high time resolution polTIRF setup, single molecules of BR-CaM labeled myosin V translocating along actin were measured over a range of Mg·ATP and BDM concentrations. Changes in intensity, primarily due to molecular reorientations (e.g., steps and substeps) but also bleaching events, are visible in raw PFIs, but were rigorously located–without binning the data –using the Multiple Intensity Change Point (MICP) algorithm (see Sect. 4 for details). Each molecule exhibits distinct features making it difficult to choose a single representative molecule for discussion here. Instead, a candidate molecule is chosen which illustrates several key features that are seen throughout a sub-population of molecules, but not typically seen in the same molecule. The orientation and wobble during the intervals between change points are determined using the dipole model, and used to confirm a physically meaningful change in the molecule.

396 of the molecules recorded were manually chosen for change point and orientation analysis based on the duration $(> 0.5\,\text{s})$ and quality of the molecule's fluorescence before photo-bleaching to background. Due to the high laser power, many recordings showed either no bleach or only a very brief recording prior to photobleaching. 53 of these "good bleaches" were performed with zero Mg·ATP in solution. Other molecules were recorded under a range of Mg·ATP and BDM concentrations (see Table 5.2 for details). Of the remaining molecules with Mg·ATP present, 149 were manually selected that showed at least 4 clear changes in

| All analyzed molecules (N=396) | | | | | |
| --- | --- | --- | --- | --- | --- |
| BDM, mM | Mg·ATP, $\mu$M | | | | |
| | 0 | 5 | 10 | 20 | 40 |
| 0 | 31 | 17 | 124 | 24 | 18 |
| 100 | 22 | 3 | 150 | 7 | 0 |
| Subset of molecules (N=149) | | | | | |
| 0 | 0 | 9 | 49 | 14 | 13 |
| 100 | 0 | 3 | 57 | 4 | 0 |

Table 5.2: Breakdown of the number of analyzed molecules at different Mg·ATP and BDM concentrations for the entire set of analyzed molecules and the subset of molecules that show at least 4 changes in orientation and/or wobble (see text for details).

orientation and/or wobble, and were chosen as a subset of molecules most likely to represent the distribution of a translocating myosin V.

### 5.4.1 Translocating myosin V

Modifications to the polTIRF setup in Sect. 3, including single photon counting of the fluorescence emission and faster cycling of the excitation polarizations, increased the time resolution 100 fold. Since each polarization illuminates the sample for 0.1 ms and most experiments were performed with 8 polarizations, the maximum time resolution is 0.8 ms. At the fastest time resolution (*first column* in Fig. 5.9) only a few photons are measured in each PFI per cycle, resulting in a signal that is difficult to interpret visually since it is dominated by Poisson noise. Increasing the bin size 10 and 100 fold (*middle* and *last column*, respectively, in
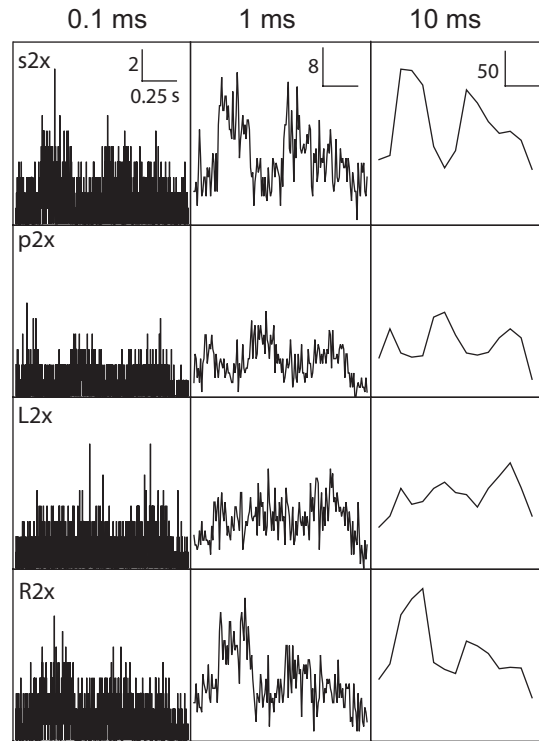
Figure 5.9: Binned polarized fluorescence intensities (PFIs). 4 of the 16 PFIs are shown binned at 0.1, 1 and 10 ms time resolution for a single BR-CaM myosin V processing along actin for $\sim 1.2$ s. The 0.1 ms bin corresponds to the photons recorded during a single gate and the 10 ms corresponds to the time resolution of the twirling experiments in Sect. 3. Changes in intensity are most evident with the largest bin size, but at the expense of lower time resolution. Choosing an optimum bin size is useful for visualizing the intensities, however, it is irrelevant for the automated change point analysis, see Sect. 4.

Fig. 5.9) improves the signal to noise ratio, but reduces the time resolution commensurately. In the presence of Mg·ATP, changes in orientation of the probe with each step of a BR-CaM labeled myosin V molecule [61, 109, 124] are clearly seen as alternating intensities in the different PFIs. The same trend occurs at high time resolutions, although the signal can be less obvious due to the low photon counts. For visualization purposes, the PFIs are typically represented by averaging the counts in 10 consecutive cycles, i.e., 8 ms. Note that each PFI is only active for $1/8$ of the cycle time (see Fig. 5.5).

The entire 5 s recording for the candidate molecule indicates a double bleach event in

the total intensity trace, which is binned at the cycle time (*gray*) and 10-point mean filtered (*black* Fig. 5.10A). Presumably, this is due to a myosin V molecule that happened to have two exchanged BR-CaM molecules attached. Only the region containing one molecule is considered for orientation analysis (*blue* Fig. 5.10A). An estimate of the background intensity after the second bleach (*black horizontal line* Fig. 5.10A) is chosen during a region of constant intensity with no sustained increases in intensity. The total intensity of the PFIs during the period between the two bleaching events (Fig. 5.10B) is constant with magnitude 15 counts per 0.8 ms cycle ($\sim$19 counts/ms) despite the large undulations of the underlying PFIs (Fig. 5.10C-J). There are obvious changes in intensity that occur simultaneously across several PFIs, for example at 0.2, 0.4, 0.65 and 1.1 s, potentially corresponding to orientation changes as the myosin steps along actin in the presence of 5 $\mu$M Mg·ATP. The precise location of these change points and any others is statistically determined using the un-binned photon data with the MICP algorithm (see Sect. 4 for details).

During the region between photo-bleaching events for the molecule in Fig. 5.10A, the MICP algorithm finds 8 statistically significant change points, each corresponding to a peak in the log-likelihood function that exceed the threshold for 5% false positives (*colored lines* Fig. 5.11). As expected, the last peak at $\sim$1.1 s is the largest since it corresponds to the time when all of the PFIs decrease due to photo-bleaching. Other peaks are smaller; in part because shorter duration events have fewer photons, but also because some polarization changes are larger than others. For example, the likelihood of change point (CP) #4, which is flanked by almost 3400 photons, is approximately 90 log units larger than CP#7, which contains a comparable number of photons ($\sim$3200), due in part to the large polarization changes in $_{s1}I_x$
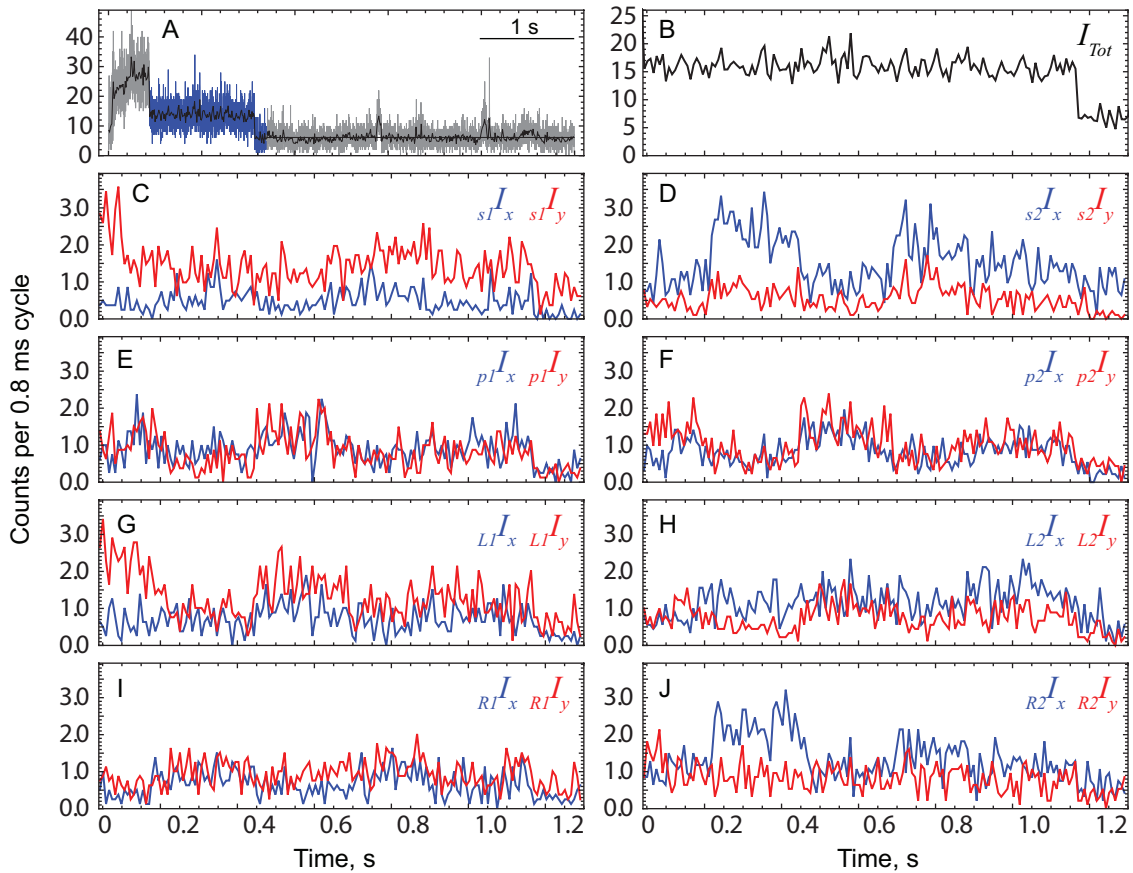
Figure 5.10: Total intensity and individual PFIs for a translocating BR-CaM myosin V in the presence of Mg·ATP. (A) Total intensity for the entire 5 s recording for the molecule shown in Fig. 5.9 summed over each complete cycle of the 16 PFIs with 0.8 ms time resolution *(gray)* and averaged over 10 cycles *(black)*. The single fluorophore region *(blue)* is selected for analysis. (B) Zoomed-in view of the average intensity from A. (C-J) Large alternating intensities in the different PFIs (binned at 0.1 ms and averaged over 10 bins) with constant total intensity suggests titling motion of the probe. The velocity for this myosin V molecule (see text) is estimated to be 250 nm/s in the presence of 5 $\mu$M Mg·ATP along an actin filament oriented at $\phi_{\text{actin}} = 20.6°$ with respect to the $x$-axis.

and $_{R2}I_x$ at CP#4. The 95% confidence interval (CI) for each change point is determined by those photons with likelihoods that are within 2 log-units of the peak. The arrival time and index of the photon closest to the change point, its confidence interval and the duration of the dwell are summarized in Table 5.3 for all of the change points .

Superimposing the MICP change points and confidence intervals (*dotted black lines* and *shaded gray rectangles*, respectively in Fig. 5.12) on the binned PFI data confirms the changes
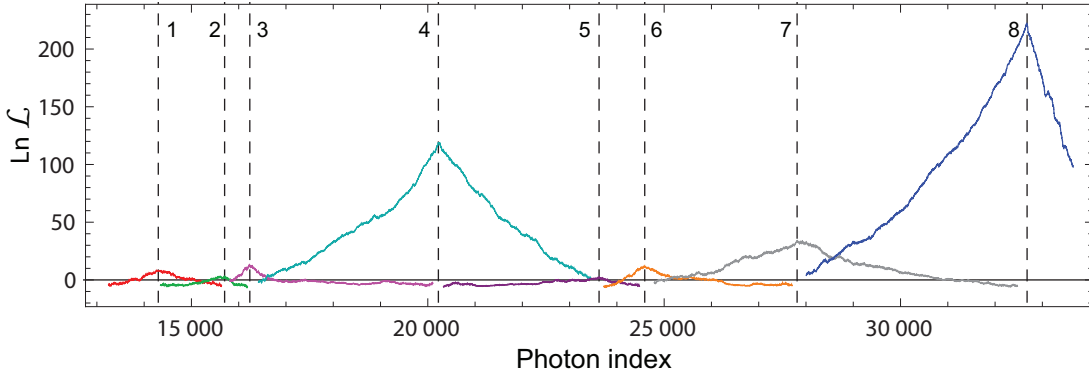
Figure 5.11: Results of the Multiple Intensity Change Point (MICP) algorithm. Peaks *(vertical dashed line)* in the likelihood surfaces *(colored)* above the threshold *(horizontal line)* indicate the location of statistically significant (i.e., 5% false positive error rate) intensity change points for the data shown in Fig. 5.10. For comparison purposes, the likelihood surfaces were shifted so that their false-positive thresholds all coincided with zero.

| Summary of change points and 95% confidence intervals | | | | | | | | |
|---|---|---|---|---|---|---|---|---|
| Index | 0 | 1 | 2 | 3 | 4 | 5 | 6 | 7 | 8 |
| CP (ph) | 13 186 | 14 298 | 15 701 | 16 234 | 20 223 | 23 622 | 24 588 | 27 811 | 32 676 |
| CI (ph) | 0 | 305 | 338 | 98 | 49 | 416 | 177 | 243 | 28 |
| CP (ms) | 0 | 64.022 | 145.936 | 177.822 | 407.23 | 593.829 | 651.359 | 837.149 | 1127.36 |
| CI (ms) | 0 | 19.2381 | 17.7005 | 5.0539 | 2.2789 | 22.8257 | 11.3408 | 12.3041 | 2.1702 |
| Interval | {0,1} | | {1,2} | {2,3} | {3,4} | {4,5} | {5,6} | {6,7} | {7,8} |
| dwell (ph) | 1112 | | 1403 | 533 | 3989 | 3399 | 966 | 3223 | 4865 |
| dwell (ms) | 64.0221 | | 81.8963 | 31.9032 | 229.408 | 186.598 | 57.5344 | 185.79 | 290.209 |

Table 5.3: Change point parameters corresponding to the molecule in Fig. 5.12 indicating the location of the change point (CP) and its 95% confidence interval (CI) either by the photon index (ph) or its arrival time (ms). The initial time has been shifted to the beginning of the analyzed region (*blue* in Fig. 5.10).

in intensity that are expected by eye at $\sim$0.2, 0.4, 0.65 and 1.1 s. The longer duration dwells

between change points: 3-4, 4-5, and 6-7 of 229.4, 186.6 and 185.8 ms, respectively, are

in agreement with the average stepping interval of 200 ms, estimated from the second order

ATP binding rate $\sim 1\,\mu\text{M}^{-1}\text{s}^{-1}$ [156] and the 5 $\mu$M concentration of Mg·ATP. In order to

confirm that the change points correspond to meaningful orientation and/or wobble changes,

the intensities between adjacent change points, including an estimate of their uncertainty from

the confidence intervals (see Sect. 5.3.2), is determined and used as input for the dipole model
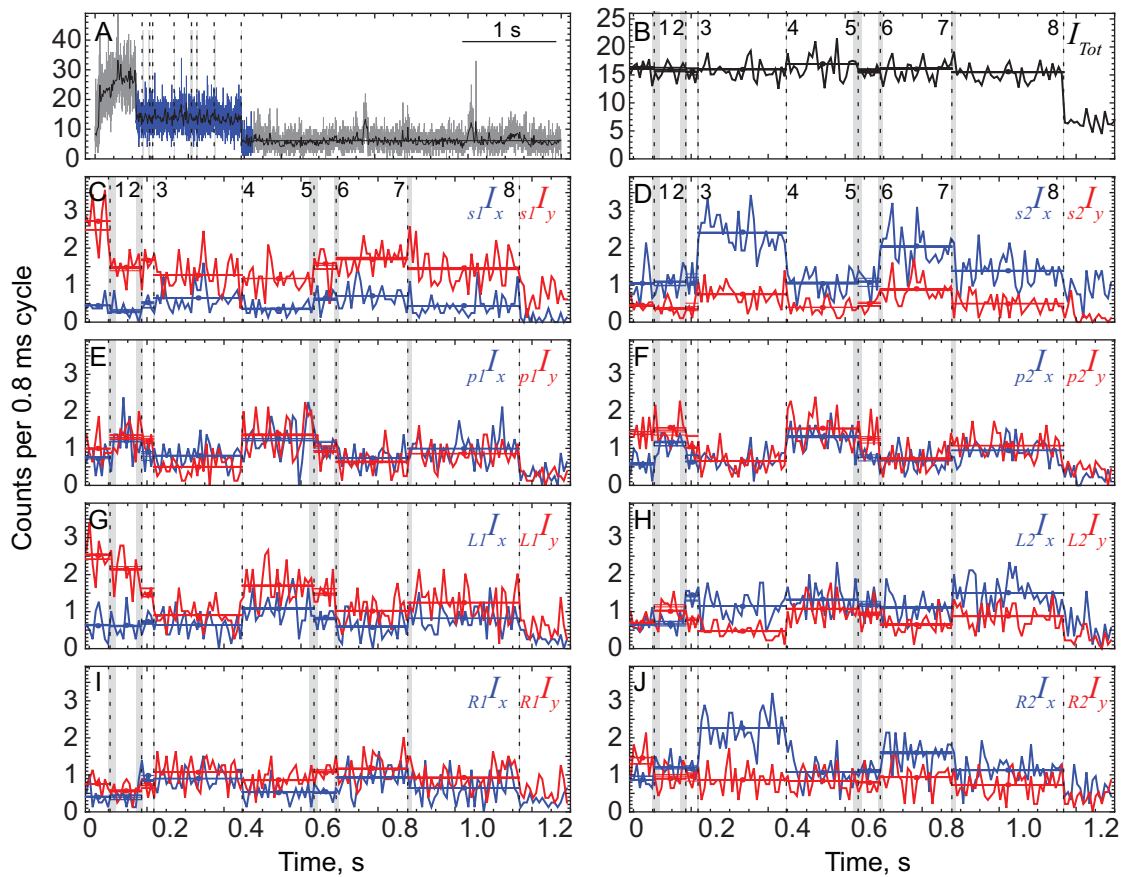
Figure 5.12: Intensity change points for a translocating BR-CaM myosin V in the presence of Mg·ATP. The change points from Fig. 5.11 are superimposed on the data from Fig. 5.10 to indicate the location of the change points *(dashed)* and their 95% confidence interval *(gray)*. A horizontal line between adjacent change points with a small dot in the center of the line indicates the most likely intensity during the interval. Four additional estimates (horizontal lines with no dot) are determined from the intervals defined by the different combinations of the adjacent confidence intervals (see Sect. 4.2.3 for details). Typically the confidence intervals are relatively narrow so that the 5 lines appear to overlap completely.

(*horizontal lines* in Fig. 5.12). Two putative substeps at CP#2 and CP#5 do not correspond to intensity changes in some of the PFIs (e.g., $_{s2}I_x$ and $_{s2}I_y$), but there are changes in others that clearly precede the larger changes at CP#3 and CP#6 (e.g., $_{L2}I_x$ for CP#2 and $_{p2}I_x$ for CP#5). Furthermore, theses putative substeps do not correspond to changes in total intensity, which is relatively constant for each dwell (Fig. 5.12B).

The orientation analysis is performed on both the change point intensities and the binned

intensities for each 8 ms cycle. The fit parameters $(\theta, \phi, \delta, \kappa)$ for each interval/bin are shown in Fig. 5.13. The scale factor $\kappa$ indicates that the signal to background ratio (SBR) is $\sim$ 2.25$\times$ above background (Fig. 5.13A), which is typical for the molecules analyzed under these illumination conditions. $\chi_\nu^2$ is defined as $\chi^2/(\nu - 1)$, where the number of degrees of freedom equals $\nu = 16 - 5 - 1 = 10$, and is $\sim$1 for the results corresponding to the binned intensities, but varies above and below unity for the results evaluated during the change point intervals (Fig. 5.13B). While not the case for this molecule, many of the other molecules that were analyzed show a strong correlation between dwell duration and $\chi_\nu^2$, see Fig. 5.19.

The probe changes between two relatively well-defined orientations. In the microscope frame, $\theta$ for the binned data is in good agreement with the change point data, and many but not all of the $\phi$ values are in good agreement (Fig. 5.13C,D). The large fluctuations in $\phi$ for the binned data often occur between symmetry points that are not robustly broken by the $L$ and $R$ polarizations, either due to the low number of photon counts or due to a probe orientation that is parallel to the $x$-$y$ plane (i.e., when $\theta = 90°$). The reason for this breakdown is that effective excitation by $L$ and $R$ polarizations (and thus effective symmetry breaking) requires the probe to have a $z$ component of its dipole, which is missing when it is oriented parallel to the $x$-$y$ plane. During the dwell between CP#3 and #4, most of the changes in $\phi$ occur across $\phi = 180°$ (the $y$-$z$ plane), and would be removed by replacing $\phi$ with $180° - \phi$. Orientations based on the change point intervals are less sensitive to this symmetry hopping because of the larger number of photons used in the estimate.

In the actin frame of reference, $\beta$ predominately changes between $85°$ and $125°$ and $\alpha$ changes between $-20°$ and $65°$ (Fig. 5.13E,F). The fluctuations in orientation seen in $(\theta, \phi)$
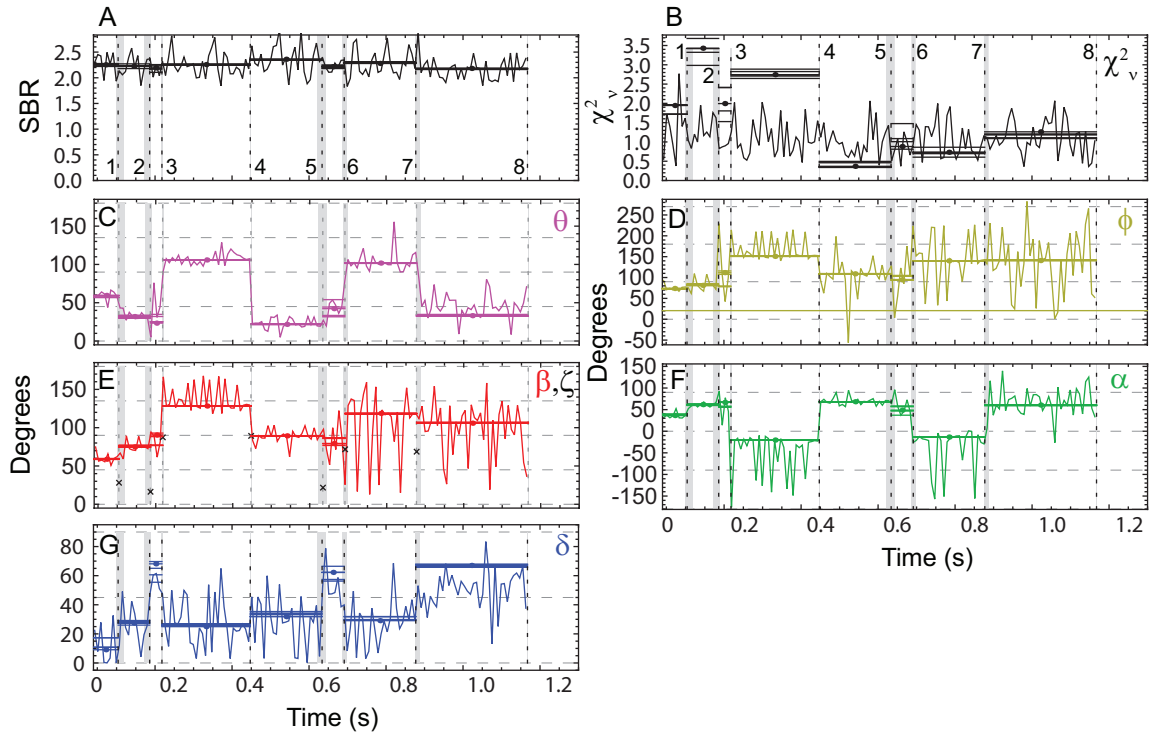
Figure 5.13: Fit parameters from the dipole model for a translocating BR-CaM myosin V in the presence of 10 $\mu$M Mg·ATP. The binned *(lines)* and MICP intensities *(horizontal lines)* from Fig. 5.12 were input to the dipole model to determine the orientation and wobble of the probe during translocation of the myosin on actin. (A) Signal to background ratio. (B) Reduced $\chi^2$. (C) $\theta$ and (D) $\phi$ for the orientation in the microscope frame of reference. $\phi_{\mathrm{actin}}$ for this molecule is 20.6°*(solid line)*. (E) The change in absolute angular displacement $\zeta$ (×'s), and the polar angle $\beta$ and (F) azimuthal angle $\alpha$ for the orientation in the actin frame of reference. (G) Slow wobble cone $\delta$. Large changes in angle for the 1 ms binned data typically occur between angles related by symmetries in the setup (e.g., $\phi$ and $-\phi$, see text for details). The hemisphere for these molecules is centered about the director axis pointing in the direction $\{\beta, \alpha\} = \{85.8°, 53.5°\}$ or equivalently $\{\theta, \phi\} = \{36.7°, 83.0°\}$.

are present in $(\beta, \alpha)$, but can be more or less pronounced depending on where the symmetry points lie relative the actin filament.

Another source of large angle fluctuations occurs when either polar angle ($\beta$ or $\theta$) is close to zero. For example, small changes in orientation of a probe about an actin filament the is aligned along the $x$-axis corresponds to small variations in ($\theta, \phi$, and $\beta$), but a large change in $\alpha$ since it is defined around the $x$-axis. Similar fluctuations occur in $\phi$ when $\theta$ is close to 0°. Another caveat is that the probe orientation is not well-defined during the periods of large

wobble. When $\delta = 90°$, the orientation from the dipole model arises entirely from fluctuations and can randomly appear to favor certain directions.

The absolute angular displacement $\zeta$ between each dwell is independent of the reference frame and contains contributions from both $\beta$ and $\alpha$ ($\times$, Fig. 5.13E). $\zeta$ changes by $\sim 90°$ prior to the longer dwells and less ($20° - 30°$) between the shorter dwells.

The reported orientations are confined to a hemisphere centered about the director axis in the direction $\{\beta, \alpha\} = \{85.8°, 53.5°\}$ or equivalently $\{\theta, \phi\} = \{36.7°, 83.0°\}$. The choice of hemisphere determines which end of the dipole is reported, so that any pair of angles $(\theta, \phi)$ or $(\beta, \alpha)$ that have been discussed could be replaced by its symmetric pair $(180° - \theta, \phi + 180°)$ or $(180° - \beta, \alpha + 180°)$.

The wobble for this molecule (Fig. 5.13G) is perhaps the most interesting. Prior to 0.8 s, it is restricted to relatively low values ($\sim 35°$) during the longer dwells and increases to $\sim 65°$ during the putative substeps at 0.15 and 0.6 s. During the last dwell after 0.8 s, the wobble also increases to $\sim 65°$ before photo-bleaching or dissociating from actin.

The orientation and wobble parameters in Fig. 5.13C-G, correspond to a set of predicted PFIs in the dipole model (*dashed lines* Fig. 5.14), and are in good agreement with the data (*solid lines*) despite the increase in $\chi_\nu^2$ for some of the dwells (Fig. 5.13B). There is no obvious correlation between $\chi_\nu^2$ and the dwell duration for the molecule in Fig. 5.13 (*black points* in Fig. 5.19A), although several estimates of $\chi_\nu^2$ are significantly larger than for the binned data (*gray point* in Fig. 5.19A).
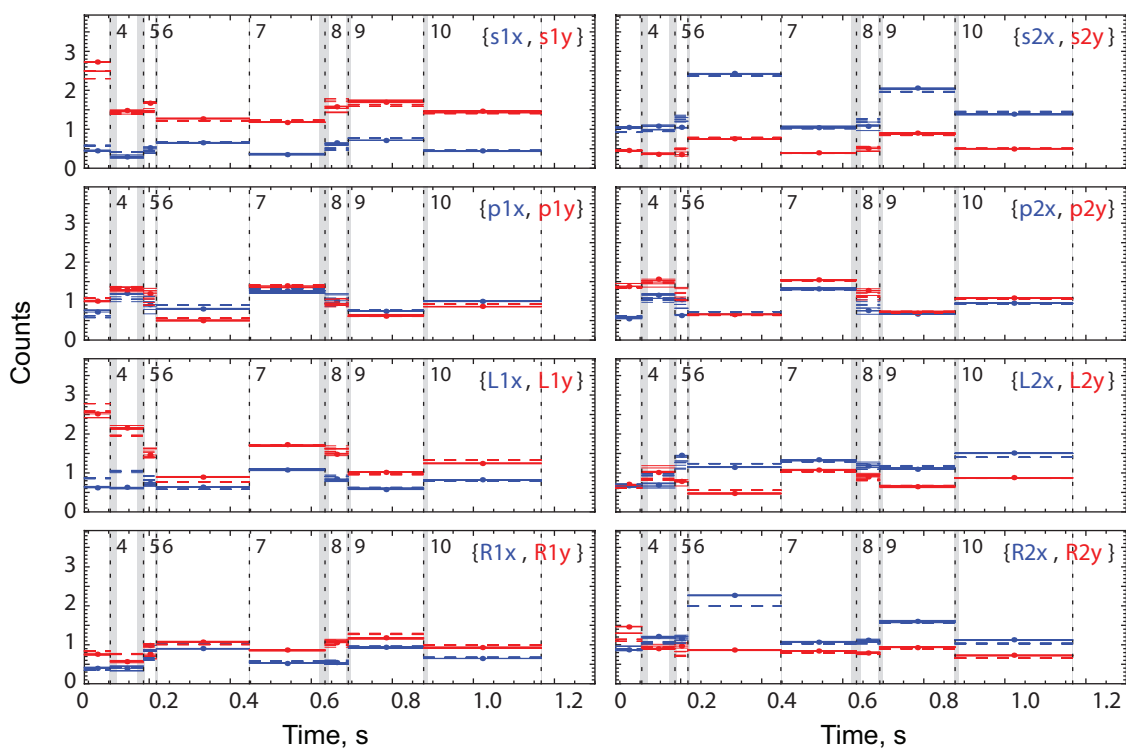
Figure 5.14: Comparison of measured intensities *(solid horizontal lines)* with those predicted by the orientation model *(dashed horizontal lines)* using the parameters from Fig. 5.13. In general, the agreement between the model and the data is good, although small differences can lead to large differences in $\chi^2$ for long duration intervals, see Fig. 5.19.

## 5.4.2 Myosin V translocation in the presence of BDM

The velocity of BR-CaM myosin V translocating along actin is determined by tracking several translocating molecules during a 60-100 s recording (see Sect. 3.2.3). At 10 $\mu$M Mg·ATP the average velocity is 206 nm/s and is slowed to 136 nm/s in the presence of 100 mM BDM. Assuming 36 nm steps, these velocities correspond to an average stepping interval of 175 ms and 265 ms, respectively, indicating that BDM increases the dwell interval by $\sim$50%.

An alternate estimate of the stepping rate can be obtained from the intervals between change points in the polarization recordings. These intervals are collected for all molecules in the presence of 10 $\mu$M Mg·ATP (*black dots* Fig. 5.15) and with additional 100 mM BDM in so-
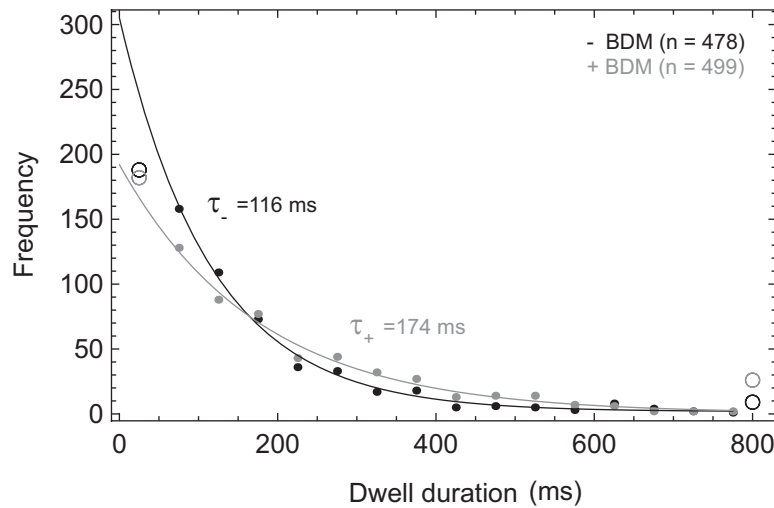
181

Figure 5.15: Histogram and single exponential fits to dwell times with and without BDM. Single exponential fits to the intervals between change points of BR-CaM myosin V translocating on actin in the presence of 10 $\mu$M Mg·ATP *(black)* and with additional 100 mM BDM *(gray)* results in time constants of 116 ms and 174 ms, respectively, indicating that BDM increases the dwell by ~50%. These fit parameters were sensitive to the bin size and the number of photons in the first bin *(open circles)*, yet fits with two exponentials did not describe the data better (data not shown). Average velocities determined from 60-90 s recordings result in velocities of 206 and 136 nm/s without and with BDM. Assuming 36 nm steps, these velocities correspond to 175 and 265 ms between steps, also indicating that BDM slows the dwell duration by ~ 50%. Fits to the dwells between intensity change points, however are ~ 35% shorter than expected from the velocity measurement. 478 and 499 dwells without and with BDM were restricted between 0.05 and 0.8 s and histogrammed with bin size = 50 ms omitting the first bin from the fit *(open circles)*.

lution (*gray dots*), histogrammed, and fit with single exponentials. The mean dwell times from the fits are 116 ms and 174 ms without and with BDM, respectively. BDM increases the dwell duration in nearly the same ratio as predicted by the velocities; however, the magnitudes of the fit parameters are faster suggesting additional changes in dipole orientation/wobble beyond what is expected for a single angle change with each step of the myosin molecule. Further indication of a substeps in the polarization data, is that the exponential fits to the histogram are sensitive to bin size and also whether or not the first bin is included in the fit. Despite this apparent instability in the single exponential fits, two exponential fits did not support the existence of a second population of dwell events.

Orientation and wobble distributions for translocating molecules in the presence of 10

$\mu$M Mg·ATP (*black curves* Fig. 5.16A-C) are similar to the distributions with additional 100

mM BDM present in solution (*gray curves*). The polar angle $\beta$ is predominately between $0°$

and $100°$ with or without BDM, with a slight increase at $\beta \approx 20°$ in the presence of BDM

(Fig. 5.16A). The distribution of azimuthal angles $\alpha$ are also similar (Fig. 5.16B), with a slight

preference for the fluorophore to be oriented parallel to the $x$-$y$ plane (i.e., $\alpha = 0°$ and $\pm 180°$).

Both of these distributions are influenced by the choice of hemisphere used to represent the

dipole. Probe wobble $\delta$ is distributed about $45°$ nearly identically for both sets of molecules

(Fig. 5.16C).

In order to investigate the change in angle at each potential step/substep in the record-

ing, estimates of probe orientation and wobble in adjacent intervals are subtracted and his-

togrammed. As with the distributions of orientation/wobble, the distributions of the change

in orientation/wobble (i.e., $\Delta\beta$, $\Delta\alpha$, and $\Delta\delta$) for translocating molecules are similar with and

without BDM (Fig. 5.17A-C). Without BDM, the change in polar angle $\beta$ has 3 peaks at $0°$ and

$\pm 50°$, two of which are maintained in the presence of BDM whereas the third peak at $+50°$

is less pronounced, if not eliminated (Fig. 5.17A). The distribution of change in azimuthal

angles around the actin filament are nearly identical in the two cases. The average values of

both are within $3°$ of zero indicating little average rotation of the molecule about the actin

filament, even though some individual azimuthal changes can be relatively large (Fig. 5.17B).

The change in wobble during an event is centered at zero with most of the changes in wobble

falling within $\pm 20°$ (Fig. 5.17C). In the presence of BDM the distributions of $\zeta$ are similar

except for a small, but statistically significant, increase in the number of small angle changes
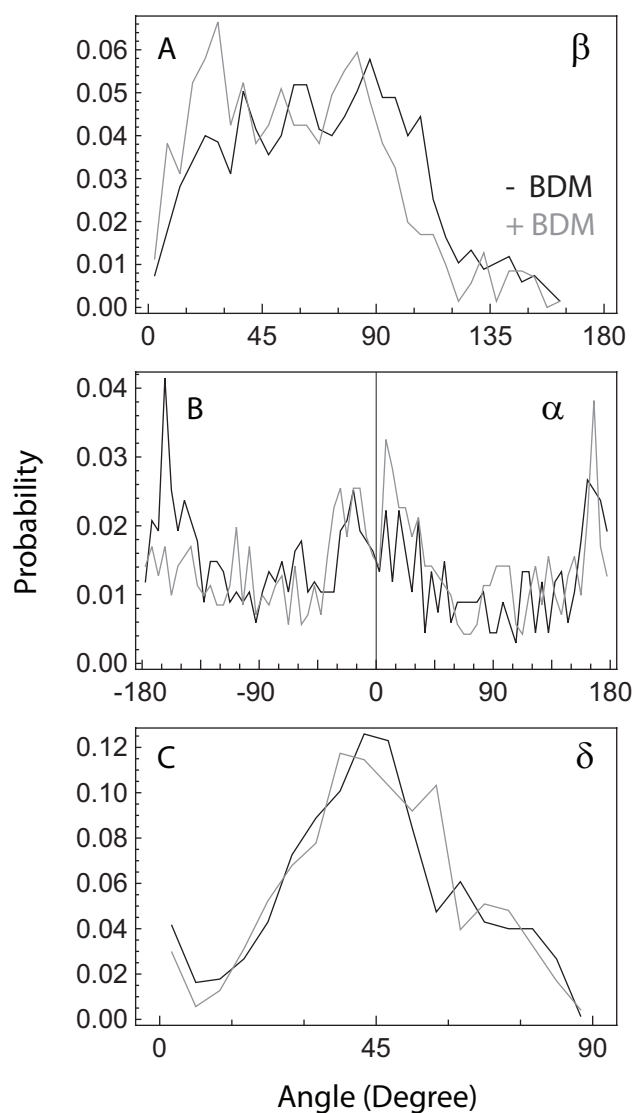
Figure 5.16: Distributions of orientation and wobble determined between adjacent change points for translocating BR-CaM myosin V in the presence of 10 $\mu$M Mg·ATP *(black)* and with additional 100 mM BDM *(gray)*. (A) In both distributions $\beta$ is predominately less than 90° and neither illustrate tilting between two peaks that is typically seen in individual traces. The broad range of $\beta$ is partly attributed to the choice of hemisphere which may represent a fraction of the $\beta \sim 130°$ dwells as $\beta \sim 50°$, and *vice versa*. (B) Azimuthal orientations $\alpha$ are distributed between -180° and 180°, with a slight preference to be oriented parallel to the *x-y* plane ($\alpha = 0°$ and $\pm 180°$). (C) Wobble parameters $\delta$ are peaked at $\sim 45°$. Note that the orientation distributions $(\beta, \alpha)$ also contain the poorly-defined angles at large wobble, but they do not change appreciably when these values are omitted.

at $\zeta \approx 20°$ (Fig. 5.17D).

The peak at $\sim 90°$ and shoulder at small $\zeta$ is consistent with the tendency of small increases in $\zeta$ to precede big changes (e.g., Fig. 5.13). Correlations between changes in $\zeta$ and
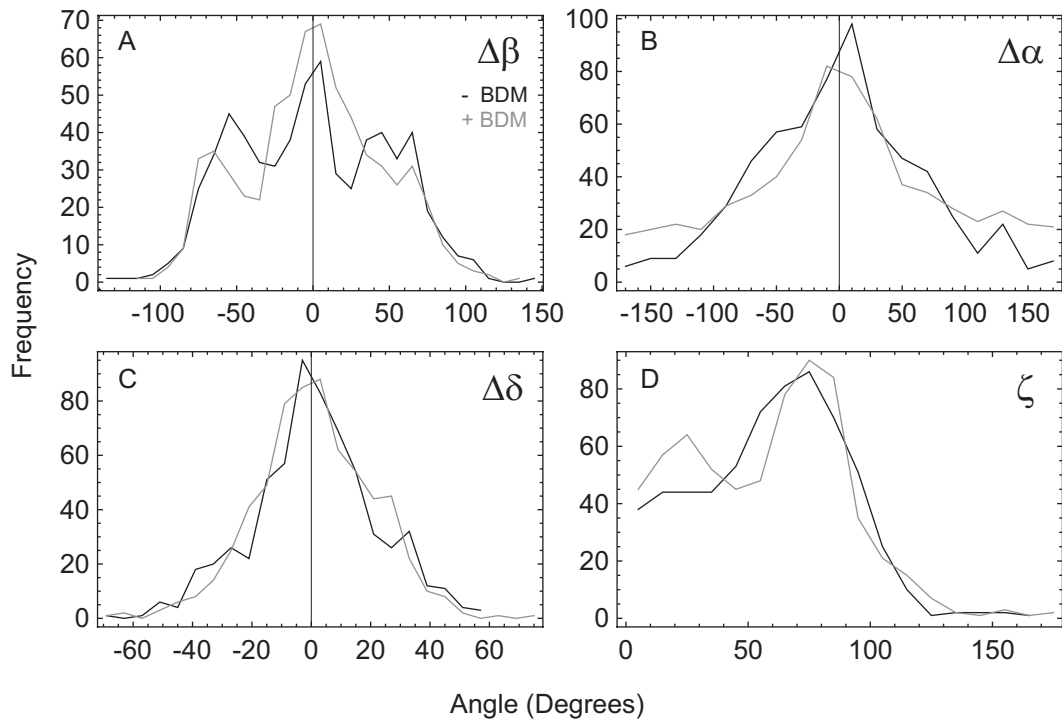
Figure 5.17: Distribution of changes in orientation and wobble for translocating BR-CaM myosin V in the presence of 10 $\mu$M Mg·ATP *(black)* and with additional 100 mM BDM *(gray)*. (A) Without BDM, the changes in polar angle ($\Delta\beta$) are peaked at $0°$ and $\pm 50°$. With BDM, the peak at $+50°$ is reduced, but otherwise the distributions are similar. (B) The distribution of changes in azimuthal angle ($\Delta\alpha$) are similar with and without BDM present in solution. Despite the presence of some large azimuthal changes around the actin filament, the average of either distribution is within $3°$ indicating relatively little net motion around the actin filament. (C) The distribution of changes in wobble parameter ($\Delta\delta$) with and without BDM is peaked at zero with no significant side lobes. (D) The distribution of total orientation changes ($\zeta$) is similar with and without BDM, except for a noticeable peak at small $\zeta$ in the presence of BDM. Except for $\zeta$, which is calculated as described in the text, the changes in orientation are determined by subtracting values in successive intervals in each recording and combining the results for multiple molecules.

the duration of the dwell before and after the change were explored, but no clear trends were

observed (e.g., in a scatter plot of the two parameters, data not shown). Instead, all dwells after

a large change in orientation, (i.e., $\zeta > 50°$, Fig. 5.18A) were histogrammed and compared to

the dwells after a small change in orientation (i.e., $\zeta < 50°$, Fig. 5.18B). Single exponential

fits to the histograms indicate that the dwells after small $\zeta$ are approximately 25% shorter than

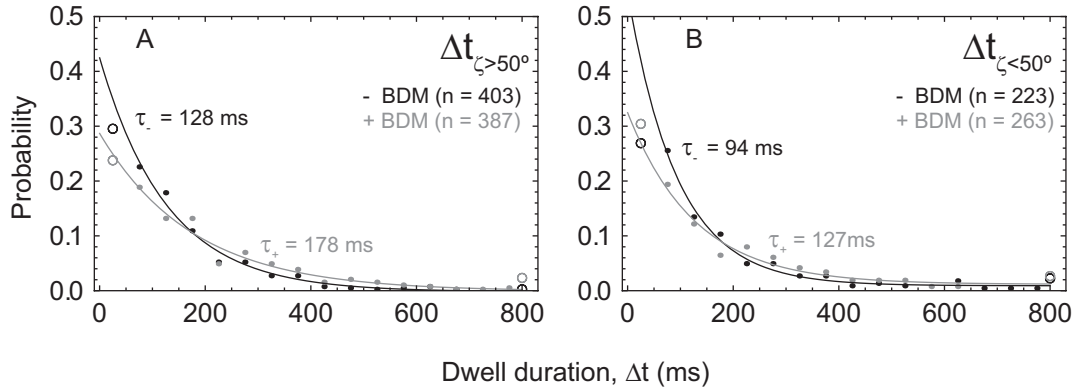those after large $\zeta$. In both cases the molecules translocating in the presence of 100 mM BDM

Figure 5.18: Distribution of dwells and single exponential fits for small and large $\zeta$ for for translocating BR-CaM myosin V in the presence of 10 $\mu$M Mg·ATP *(black)* and with additional 100 mM BDM *(gray)*. (A) The dwell following a large change in total angle ($\zeta > 50°$, chosen to separate the peaks in Fig. 5.17D) for all molecules without and with BDM were combined, histogrammed and fit to single exponentials with time constants of 128 ms ($n = 403$) and 178 ms ($n = 387$), respectively. (B) Similarly, dwells following a small change in total angle ($\zeta < 50°$) for all molecules without and with BDM were fit to single exponentials with time constants of 94 ms ($n = 223$) and 127 ms ($n = 263$), respectively. In both cases BDM increases the dwell duration by $\sim 35\%$, but the dwells for small $\zeta$ are 40% shorter than for large $\zeta$. The trend of these results does not depend on the value of the cutoff or bin size used in the histogram, but the magnitudes of the time constants vary by $\sim 20\%$. Results for a similar analysis for dwells *preceding* the change in $\zeta$ varied widely with no clear pattern, and depended on the choice of cutoff and bin size (data not shown). For comparison purposes, the distributions were normalized by the total number of counts in each. The fit was restricted to dwells in the range of 0.05 and 0.8 s and histogrammed with bin size = 50 ms omitting the first bin from the fit *(open circles)*.

*(gray curves* in Fig. 5.18) result in 35-40% longer dwells.

## 5.4.3 $\chi_\nu^2$ of all translocating molecules

The subset of myosin V molecules with at least 4 state changes (Table 5.2), shows a strong correlation between dwell duration and $\chi_\nu^2$. If all of the dwells and their respective $\chi_\nu^2$ are pooled together *(black dots* Fig. 5.19B), then the correlation is clear from the large value of the slope in the fit line *(gray line* Fig. 5.19B), as well as its moderately high correlation coefficient of $\sim 0.505$. The correlation between $\chi_\nu^2$ and dwell duration is also determined separately for each molecule. The fraction of molecules with correlation coefficients greater than 0.8 is $\sim 50\%$ (Fig. 5.19C) indicating the correlation is very strong for some molecules although no
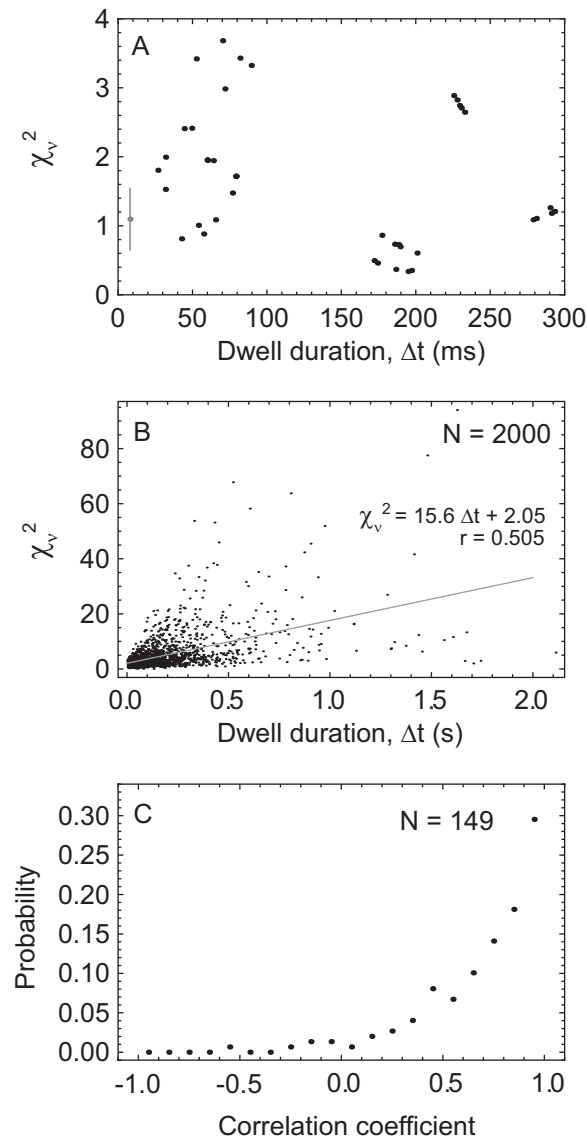
Figure 5.19: $\chi^2_\nu$ depends on dwell duration. (A) For the molecule shown in Fig. 5.12, $\chi^2_\nu$ calculated from the change point intervals (*black*) are similar to those for the binned data (mean±S.D., *gray*), and unlike in other molecules does not depend strongly on the dwell duration $\Delta t$. (B) If all of the dwells from the subset of 149 translocating molecules (Table 5.2) are combined then the total number of dwells is 2000 (*black dots*). The correlation between $\chi^2_\nu$ and the dwell duration results in the average $\chi^2_\nu$ increasing by over an order of magnitude when the dwell increases from 0.1 to 1 s (*gray fit line*). (C) If the correlation of each of the 149 molecules is considered separately, over 80% of the molecules show a strong correlation ($r > 0.5$) between $\chi^2_\nu$ and the dwell duration.

other distinguishing characteristic for such molecules could be determined.

### 5.4.4 Rigor myosin V

In the absence of Mg·ATP, single-headed myosin V molecules bind tightly to actin with their lever arm titled forward in the post power stroke (rigor) state, but EM images of myosin V dimers in the absence of Mg·ATP indicate that both heads do not usually bind simultaneously [127]. In order to investigate the occurrence of singly bound heads, BR-CaM labeled myosin V is attached to actin and the proportion of molecules with large and small wobble parameter were compared.

The PFIs for BR-CaM myosin V's attached to actin in the absence of Mg·ATP generally show few, if any, abrupt intensity changes. For the molecule shown in Fig. 5.20, the total intensity indicates a single bleaching event at 2.5 s (Fig. 5.20A) with a relatively constant intensity (Fig. 5.20B). By eye, the individual PFIs (Fig. 5.20C-J) suggest a change point at ∼0.5 s, that is confirmed by the MICP analysis in addition to a second change point corresponding to the bleaching event.

As before, both the binned and change point intensities are input into the dipole model in order to determine the probe's orientation and wobble during the recording. The signal to background ratio of ∼3 is quite high, and is the upper limit of what is typically measured under these conditions (Fig. 5.21A). The $\chi_\nu^2$ values for the change point intensities are more than an order of magnitude greater than those for the binned intensities (Fig. 5.21B), despite good agreement between the measured intensities and those predicted by the model (data not shown). The large $\chi_\nu^2$ is common in other molecules and is correlated with very long duration dwells (Fig. 5.19B,C). The wobble parameter increases from a moderate value of $\sim 40°$ during the first 0.5 s to a large value $\sim 70°$ for the remaining 2 s (Fig. 5.21G). $\theta = 90°$ during the
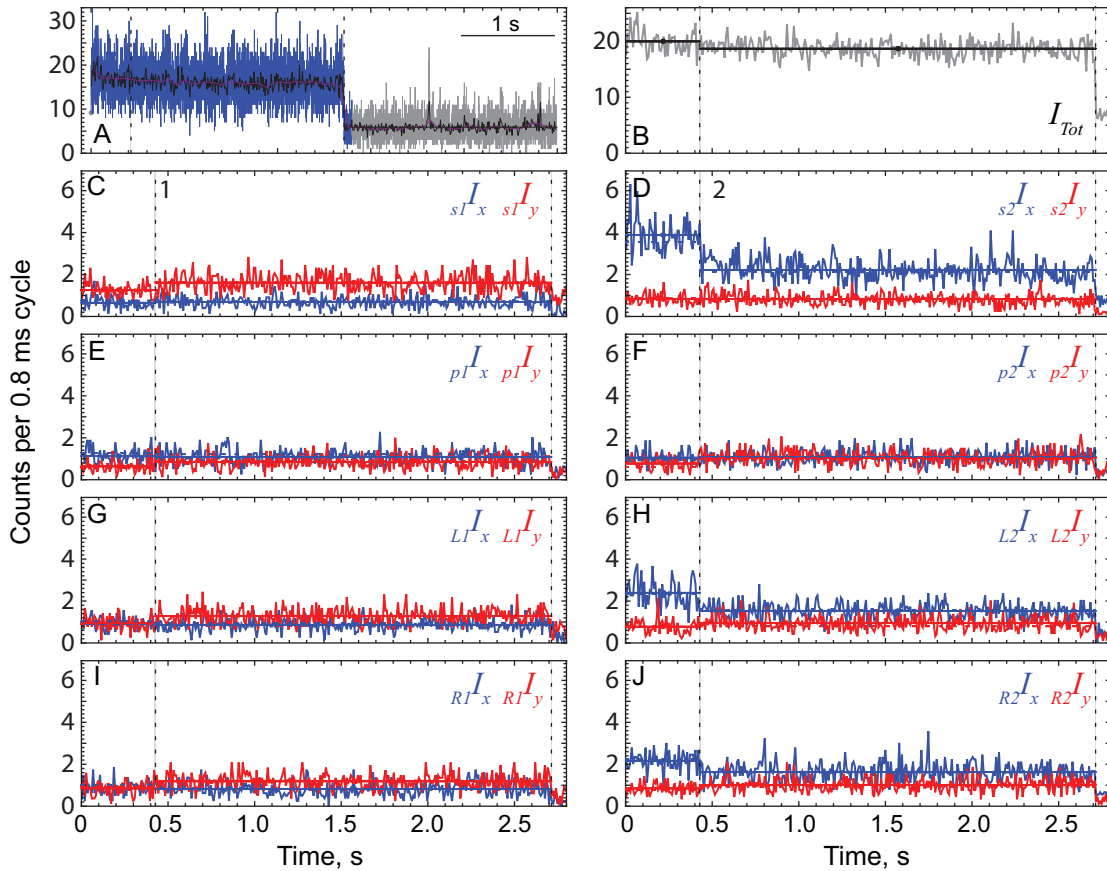
Figure 5.20: Total intensity, individual PFIs and change points for a BR-CaM myosin V molecule bound to actin in absence of Mg·ATP. (A) Total intensity of the BR-CaM, binned after each complete 0.8 ms cycle of the polarizations *(gray, blue)* and averaged over 10 cycles *(black)*, photo-bleaches to background in a single step at ∼2.5 s. (B) Zoomed-in view of the region to be analyzed has a relatively constant intensity. (C-J) Individual PFIs including the superimposed change points *(dotted vertical line)* with their confidence interval *(gray shaded box)* on the intensities of data binned at 8 ms for APDx *(blue)* and APDy *(red)*. Estimates of the intensities between adjacent change points are shown as horizontal lines. Aside from the photobleaching event, there is only one other change point at ∼0.5 ms.

initial interval indicates that the probe is oriented parallel the *x-y* plane (Fig. 5.21C) and is thus likely to be measured at symmetric orientations obtained by reflection about the *x-z* and *y-z* planes, as indicated by the large fluctuations in $\phi$ (Fig. 5.21D). The orientations identified in the second dwell are unreliable since orientation is not well-defined during periods of large $\delta$. $\beta$ and $\alpha$ orientations in the actin frame are similarly noisy (Fig. 5.21E,F) during the period of large wobble.
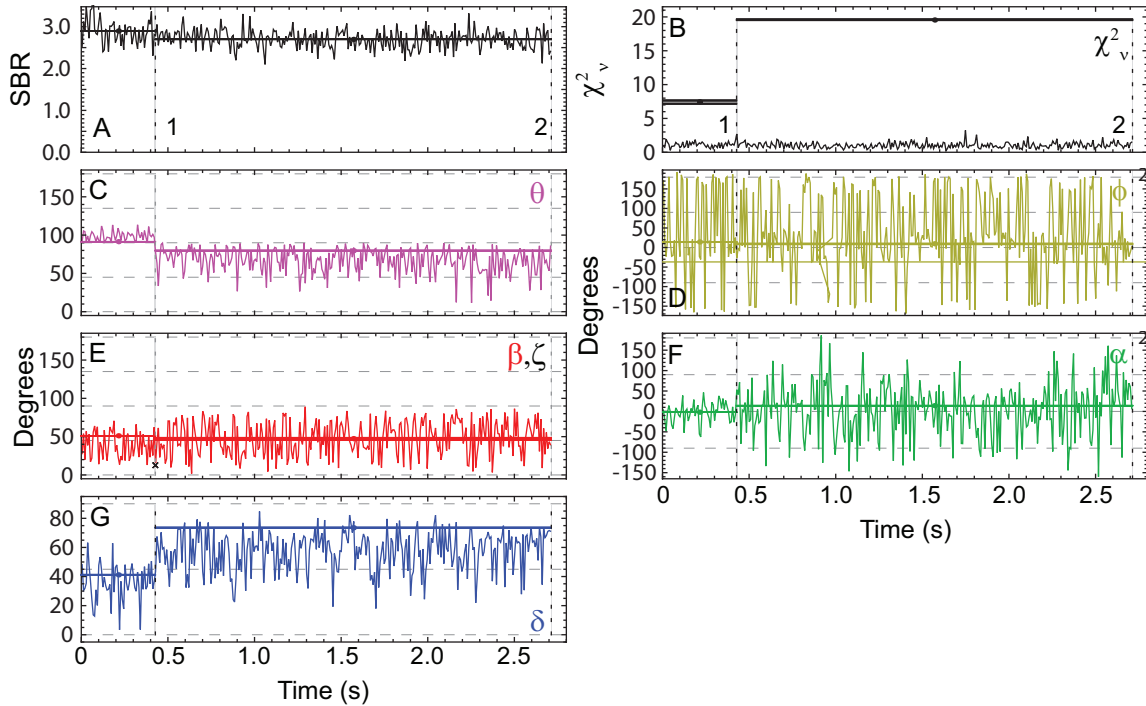
Figure 5.21: Orientation and wobble parameters for a BR-CaM myosin V molecule bound to actin in the absence of Mg·ATP. The binned and MICP intensities from Fig. 5.20 were input to the dipole model to determine the orientation and wobble of the probe. (A) The signal to background ratio is relatively large at ~3. (B) Large values for the reduced $\chi^2$ are probably influenced by the long duration dwells (see Fig. 5.19) (C) $\theta$ and (D) $\phi$ for the orientation in the microscope frame. The angle of the actin filament equals $-37°$ *(horizontal line)*, and is determined from the CCD image of the Alexa-647 labeled actin filaments. (E) The change in absolute angular displacement $\zeta$ (×'s), and the polar angle $\beta$ and (F) azimuthal angle $\alpha$ for the orientation in the actin frame of reference. Angles in the second dwell are not reliable due to large wobble parameter (G) Slow wobble cone $\delta$ is large for most of the recording suggesting the BR-CaM is labeled near the detached head. Large changes in angle for the binned data typically occur between angles related by symmetries in the setup (see text). The hemisphere for these molecules is centered about the director axis pointing in the direction $\{\beta, \alpha\} = \{48.8°, 5.9°\}$ or equivalently $\{\theta, \phi\} = \{85.6°, 48.6°\}$.

Two populations of molecules are expected in the data since BR-CaM bound near a head

that is attached to actin would presumably have a well-defined orientation and lower wobble

than a BR-CaM bound near the highly mobile detached head. In order to separate these two

kinds of molecules, the fraction of the recording time that $\delta > 75°$ is calculated. Sorting

these values from lowest to highest separates the number of molecules that rarely experience

very large wobble from those that often experience large wobble. In the absence of Mg·ATP,
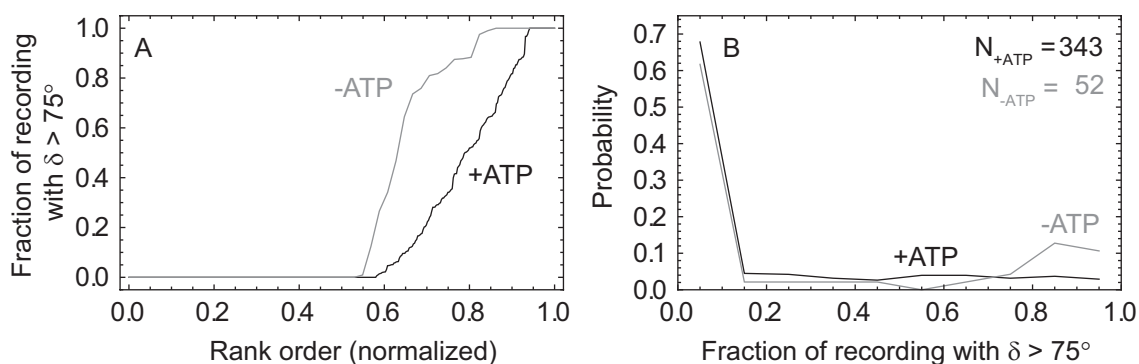
Figure 5.22: Fraction of molecules with periods of large wobble. (A) The fraction of the recording that each molecule has wobble greater than 75° is calculated and plotted in increasing order for molecules with *(black)* and without Mg·ATP *(gray)* present. (B) Same data as in A, but histogrammed according to the fraction of molecules with low and high wobble. 55-60% of the molecules in both cases have a relatively low fraction of their recording in a high wobble state (peak at 0.05). In the absence of Mg·ATP, ~30% of molecules experience large wobble for over 80% of the recording, whereas less than 10% of molecules in the presence of 5-40 $\mu$M Mg·ATP experience this degree of wobble (peak at 0.9 in *gray* only).
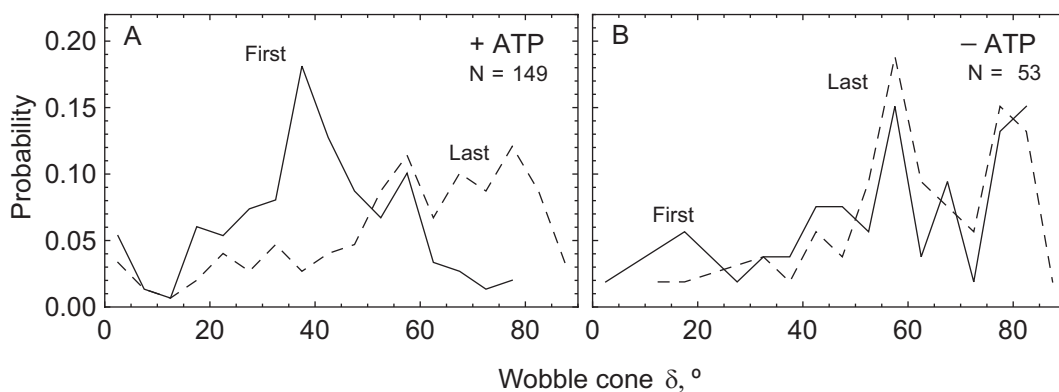


Figure 5.23: Wobble cone distribution. (A) The wobble parameter during the first *(solid)* and last *(dashed)* dwell for myosin V molecules in the presence of Mg·ATP shifts to larger values later in the recording, suggesting that the molecule bleaches or dissociates from a one-head bound state. The peak at $\sim 40°$ may indicate the wobble of the two-head bound state. (B) Molecules attached to actin in the absence of Mg·ATP have a similar distribution of wobble parameters during the first and last dwells with two peaks, suggesting two populations of BR-CaM: one attached near a bound myosin head with wobble $\sim 55$-$60°$ and the other attached near a free head with wobble 80-85°.

~55% of the molecules never experience large wobble events, but the wobble fraction for the

remaining molecules increases sharply such that ~20% experience periods of large wobble

for greater than ~90% of the recording (*gray line* Fig. 5.22A). ~ 60% of the molecules in the

presence of Mg·ATP also rarely experience large wobble events (*black line* Fig. 5.22A), and

the remaining 40% experience some amount of large wobble, but with no apparent preference in how long the wobble persists (*black line* Fig. 5.22B). Similarly, a histogram of the data in Fig. 5.22A results in a peak at zero with and without Mg·ATP, but only data without Mg·ATP indicates a peak at large wobble $\delta = 80 - 90°$ (Fig. 5.22B).

The fraction of translocating molecules with some amount of large wobble ($\sim 40\%$ in Fig. 5.22) is consistent with the raw data of many molecules that show a long duration dwell with high wobble near the end of the trace. In order to explore this trend, the magnitude of the wobble parameter during the first and last dwell are compared for molecules in the presence (Fig. 5.23A) and absence (Fig. 5.23B) of Mg·ATP. With Mg·ATP present in solution, there is a large shift in the distribution of wobble parameter from $\delta \sim 40°$ during the first dwell (*solid line* Fig. 5.23A) to a large fraction with $\delta > 60°$ during the last dwell (*dashed line* Fig. 5.23A). As a control, the wobble during the first and last dwells of molecules without Mg·ATP present in solution were also compared (Fig. 5.23B); both distributions are similar with two peaks at $\delta = 55°$ and $80°$.

## 5.5   Discussion

### 5.5.1   Increased polTIRF time resolution

The maximum time resolution of a polarized TIRF setup was improved 100 fold by increasing the polarization cycle frequency from 100 to 10 000 Hz (Fig. 5.9) and tagging each photon with its arrival time and polarization state using a time-correlated single photon counting device (Fig. 5.5). Additional hardware circuits were built to filter out photons detected during the

brief period ($\sim$1 $\mu$s) when the polarizations change due to the finite time response of the

Pockels cell high voltage amplifier (Fig. 5.6 and Fig. 5.7). A second circuit establishes a

10 MHz oscillator as the master clock for the experiment by converting the sine wave clock

output from the delay generator to a short duration, negative sync pulse that is input into

the SPC circuit and used as the macrotime clock (Fig. 5.8). A third circuit combines the

polarization signal from the Pockels cell driver circuit with the SPC routing bits in order to

encode the polarization state of the excitation laser (not shown). A more sensitive EM-CCD

camera replaced the intensified CCD camera, necessitating new software for controlling the

experiment, which was written in LabView.

Fast time resolution is critical for detection of short-lived substeps in the myosin ATPase

cycle. Previous polTIRF measurements were typically conducted with gate intervals of 10

ms, which correspond to cycle times of 40 ms for the 4 polarization case [61, 62, 65] and

80 ms for the 8 polarization case [2, 123, 124]. Despite decreasing the time resolution, most

experiments were conducted with 8 input polarizations (i.e., 16 PFIs) instead of half that

number, in order to better characterize the orientation of the probe. As shown in in Fig. 4.9B,E,

the wobble is also better characterized with 16 PFIs due to a symmetry between $\delta = 90°$ and

$(\theta, \phi) = (54.7°, 45°)$ in the 8 PFI case. Because these polTIRF experiments are restricted

to measuring orientation, individual substeps must be distinguished from steps by a distinct

wobble state, e.g., the high wobble state during the diffusive search. Absent this feature,

substeps can be distinguished by their kinetics, assuming they are substantially different from

the stepping kinetics.

The laser intensity is increased $\sim$3 fold compared with the twirling experiments (Sect. 3)

in order to maximize the number of photons detected during the short duration substeps in the myosin ATPase cycle. The rate of photon emission from the BR-CaM fluorophore at these laser intensities is $\sim 30/\text{ms}$ and provided a limit on the achievable time resolution. The simulations in Sect. 4 indicate that for an SBR of 3, approximately 800 photons are required to detect 50% of diffusive search type substeps in myosin V [98, 160, 173]. At these photon rates, 800 photons would be recorded in $\sim$25 ms, which serves as a more practical estimate of the time resolution than the 0.8 ms cycle time. Considering this detection efficiency and the expected distribution of event durations, only a fraction of the number of substeps are likely to be detected, even if they occur with every cycle of the motor.

Faster emission rates would result in a higher fraction of detected substeps, and are possible at higher laser powers; however, this would increase the rate of photobleaching, thus minimizing the number of events measured per molecule. This tradeoff can be mitigated by increasing the Mg·ATP concentration and thus the number of steps, but recording quickly moving molecules is a challenge due to the $\sim 1\,\text{s}$ latency currently required to center the stage above the APDs and change the optics from imaging at the microscope's camera port to imaging at the APD port.

polTIRF experiments using a CCD camera instead of APDs measured position and orientation simultaneously [109] with 150-500 ms exposure times using two input polarizations. Alternating between focused and defocused imaging of BR-CaM myosin V [111] and VI [190], also allows simultaneous position and orientation at 500-1000 ms exposure times. Detecting short-lived substeps is not feasible with these relatively slow experiments, however longer-lived states between angle changes that were not correlated with a stepping

event were detected [109]. The polTIRF experiments described here have a faster time time resolution and larger angular range than these previous efforts. Substeps detected via optical traps [170, 171, 173] or high speed tracking of non-fluorescence particles [98] have submillisecond time resolution, but also a relatively large particle attached to the myosin which may slow down or interfere with rebinding. The polTIRF experiments described here do not match the speed of these measurements, but the small fluorescence probe is unlikely to interfere with rebinding of the free head.

In principle, polTIRF experiments would be sensitive to both the diffusive search and substeps that consist of a kink forming in the lead head lever arm prior to a step (i.e., the telemark state). The highly mobile diffusive state would be represented as brief, large wobble event with a poorly defined orientation, flanked on either side by low wobble states with well-defined orientations in the trailing- and leading- head configurations.

## 5.5.2 Myosin V translocating along actin

The orientation and wobble of BR-CaM myosin V molecules translocating along actin in the presence of Mg·ATP were measured with the high time resolution polTIRF setup. Abrupt changes in the magnitude of individual PFIs occurred simultaneously (Fig. 5.10C-J) with some increasing and other decreasing such that total intensity was constant (Fig. 5.10B), indicative of orientation changes of a single molecule [61, 63, 123]. The intensity changes are visible by eye in the binned intensity traces and only occur when Mg·ATP is present in solution. Other work has shown that the frequency of orientation changes are correlated with the concentration of Mg·ATP [61, 124] and often accompany a myosin step [109, 111]. Substeps are not typically

evident by eye in the binned data, but statistically significant ones were identified using the multiple intensity change point (MICP) algorithm.

## MICP algorithm

Single photon counting data does not impose a bin size on the recorded photons. After the experiment, the data can be binned with arbitrary time resolution and analyzed in the conventional manner. Alternatively, a change point analysis [100] can be performed on the raw photon arrival times to determine if there is a change in intensity, and if so, its location in time. For example, Hanson et al. [191] use a similar change point analysis on FRET data to study the dynamics of adenylate kinase with 2 ms time resolution. In Sect. 4, the change point analysis was extended to also detect changes in individual polarized fluorescence intensities that can occur even when the total photon detection rate is constant (Fig. 5.12). The magnitude of the PFIs between adjacent change points are then input to a model of the dipole orientation [63] to characterize the state of the molecule during the entire interval instead of in constant width bins as was done previously [2, 61–63, 123, 124].

A major advantage of the change point approach is that it reduces the Poisson shot noise by maximizing the number of photons used to estimate the state of the molecule. In contrast, binning the data fixes the shot noise at the mean number of photons per bin. Smoothing the data by averaging successive bins improves the signal to noise ratio, but at the expense of a loss of time resolution. This filtering approach is especially deleterious for detecting substeps in myosin V polarization data because as the filter sweeps across an abrupt intensity change point, it blurs the boundary, effectively introducing an artificial state with intensities

that are the average of the two on either side. Importantly, these average intensities are often comparable to the intensities that would be expected for a high wobble state, resulting in a high incidence of false positive change points and parameters that are misleadingly reported by the dipole model. The MICP algorithm avoids this, by decoupling the time resolution used to detect events from the time resolution used to characterize the state of the molecule.

Improving the signal to background ratio (SBR) of each PFI using the MICP algorithm has the additional benefit of minimizing fluctuations between spatial orientations that are far apart but have closely related PFIs. This scenario corresponds to the orientation of a probe and its reflection about the cartesian planes, e.g., $(\theta, \phi)$ and $(\theta, -\phi)$ which are resolved by the $L1$ and $R1$ polarizations. Low photon counts and random fluctuations in these PFIs, however, can cause the apparent orientation of the probe to hop between these two symmetric orientations. Similar symmetry points occur across the $x$-$z$ plane.

The rapid cycling of the polarizations also minimizes the impact of an angle change occurring in the middle of a cycle. With the slower cycle frequencies used in earlier work [2, 61, 62, 65, 123, 124], if the probe's orientation or wobble changed during the course of the cycle, then the resulting parameters from the dipole model would not be meaningful for that cycle. Faster cycling of the polarizations combined with the flexible location of the change point using the MICP algorithm eliminates this issue. The drawback to faster cycle frequencies are the greater fraction of photons that are rejected during each change of voltage on the Pockels cell. Here the fraction of rejected photons was 3% whereas for the slower cycling frequency it was 1%.

The MICP algorithm for the molecule in Fig. 5.10, finds 9 significant peaks in the like-

lihood functions (Fig. 5.11), some of which correspond to the long-lived change points that were obvious by eye in the binned data and some that correspond to short-lived states that seem to indicate substeps in myosin V cycle (Fig. 5.12C-J). The change points and substeps determined by the MICP algorithm are the result of the raw photon data and do not depend on an underlying model. In order to verify that they correspond to rotational motions of the myosin, the PFIs during each interval are used as input to the dipole model and the probe's orientation and wobble are determined. The model therefore acts as an independent verification on the validity of the detected change points.

**Orientation and wobble**

Because of the probe's dipole symmetry, two equivalent orientations, related by a $180°$ end-on rotation, can be used to describe its 3D direction in space. This ambiguity complicates interpretation of the data since rotation of the protein by $\zeta$ could also be interpreted as a rotation by $180° - \zeta$ in the opposite direction. Definitively choosing one end of the dipole is impossible, but the issue can be mitigated by a wise choice for the range of $\theta$ and $\phi$ that is likely to contain the same end of the dipole for the entire recording. For myosin VI, Sun et al. [124] reported the orientation for the end of the dipole that was contained in a hemisphere, which was rotated around the actin filament by $60°$ in a direction opposite to its helical twist. In this work, a hemisphere was defined separately for each molecule by aligning its polar axis along a direction that minimized the variance amongst the different dipole orientations estimated during its recording (i.e., the director).

A caveat to this approach is that if the protein is known to rotate by more than $90°$ in a

single step then the reported change in angle will be less than $90°$. For example, a probe that rotates from $(\beta, \alpha) = (20°, 20°)$ to $(140°, 40°)$ would instead be reported as the opposite end of the dipole at $(40°, -140°)$, and the large change in $\beta$ would become a large change in $\alpha$. EM images of myosin V indicate that the lever arm in the trailing head makes an angle of $\sim 40°$ with the barbed ('+') end of the actin filament [127], and an angle of $90°$ to $150°$ with the leading head (with an average of $115°$). The corresponding lever arm swing would be $50$-$110°$, but as discussed in Sect. 5.3.3, the lever arm swing is not necessarily equal to the change in orientation of the probe, which is estimated to be tilted away from the lever arm axis by $40°$. Using polTIRF with angles restricted to $1/8$ of a hemisphere Forkey et al., [61] measured the probe angles for BR-CaM myosin V and found two peaks for $\beta$ at $30°$ and $75°$, but the latter was interpreted as $105°$ due to symmetries in the setup. $\beta = 30°$ was assigned to the trailing head because a similar peak was also detected for myosin molecules bound in the rigor state in the absence of Mg·ATP. The resulting $65°$ change in angle of the probe would likely remain within the chosen hemisphere.

For the molecule in Fig. 5.12, the orientations in either the microscope (Fig. 5.13C,D) or actin frames (Fig. 5.13E,F) appear to alternate between two well-defined values and the orientations determined between change points are in reasonable agreement with the orientations determined from the binned data. The absolute angular displacement $\zeta$, which includes both azimuthal and polar angle changes independent of the reference frame, shows large changes of $\sim 90°$ during the supposed steps, which are preceded by small changes for the two putative substeps ($\zeta$ Fig. 5.13E). $\zeta$ is larger than $\beta$ here due to the large contribution in the angle change from $\alpha$.

The wobble parameter for this molecule showed alternating low and high wobble events. Interestingly, the low wobble events ($\delta \sim 30°$) corresponded to the long dwells after large changes in $\beta$, whereas the high wobble events occur during the putative substeps when $\beta$ changes from $85°$ to $125°$ at 0.15 and 0.6 s. If these large wobble events corresponded to the free head's diffusive search for the next actin binding site then $\beta = 85°$ would correspond to the probe on the trailing head and $\beta = 125°$ to the probe on the leading head. The molecule also terminates in a high wobble state, which will be discussed below.

Even though this pattern for increasing wobble is consistent with expectations for the diffusive search, it was only occasionally detected. Of the subset of 149 molecules with at least 4 angle changes, 18 potential diffusive search events in 12 different molecules were manually identified if the wobble parameter increased by at least $20°$ compared to the neighboring dwells. The average dwell of these events was 36 ms and ranged from 7.5 to 80 ms. Detecting the diffusive search substep is at the limits of detection due to its short duration and insufficient photon counts under these experimental conditions. Conversely, the dwells for the high-wobble substeps measured for the molecule considered here are long compared to other measurements (10 ms [98, 173]) and theoretical estimates of the diffusive search ($\sim 1$ ms [174, 175]). A distribution of dwell times for the diffusive search is expected, but if the results reported for this molecule were from the tail of a distribution, then one would expect many more 10-20 ms substeps, which were not observed. Possible explanations for the extended diffusive search experienced by this and other molecules are an obstacle along the actin filament such as a streptavidin molecule, a damaged section of the actin filament with compromised myosin binding, or interaction of the myosin with the surface of the slide.

### 5.5.3  Myosin translocation in the presence of BDM

Numerous groups [98, 109, 171] have determined that the myosin II inhibitor BDM slows the rate of myosin V translocation on actin. There are some differences, however, as to its role in prolonging substeps in the myosin V ATPase cycle. Uemura et al. [171] determined that 100 mM BDM stabilizes the ADP bound-head state on both the trailing and the lead head, where it also delays the power stroke. Dunn et al. [98] found that BDM slows the rate at which the free head re-binds actin, but it did not affect their measurement of the power stroke. Syed et al. [109] found that BDM increased the fraction of 'extra' re-orientations that occurred accompanied by a small ±5 nm step.

**Distribution of dwell times**

Histograms of all the intervals between change points of BR-CaM myosin translocating along actin in the presence of 10 $\mu$M Mg·ATP includes both steps and substeps. If the kinetics of these states are sufficiently different, then the histograms should be better described with a 2-exponential fit than with a 1-exponential fit, but this is not the case. Instead, the distribution is well fit by a single exponential (Fig. 5.15) with time constant $\tau_- = 116$ ms (where the '−' indicates no BDM). Including 100 mM BDM in solution increased the duration of the dwells so that the single exponential fit resulted in $\tau_+ = 174$ ms (where the '+' indicates the presence of BDM in solution), consistent with a slower velocity.

The ratio of the time constants for the data with and without BDM ($\tau_+/\tau_- = 1.5$) is in excellent agreement with the increase in dwell time in the velocity measurements. The corresponding time constants for the velocity data, assuming constant 36 nm steps, however,

are $\sim$ 33% slower indicating that there are more dwells than steps in the polarization data, which is indirect evidence of the existence of substeps in the polTIRF data. Distinguishing between substeps and steps by their potentially different kinetics by using a two-exponential function was not successful as the fit was no better than a single exponential.

**Distribution of orientations**

The distribution of orientation and wobble for molecules with and without BDM were very similar (Fig. 5.16). In either case, the distribution of the polar angle $\beta$ (Fig. 5.16A) did not indicate two peaks as would be expected from the tilting motion seen in the raw data and as reported previously [61, 124]. One possible explanation is that during the periods of large probe wobble, which were better estimated in this work, the probe orientation would be poorly defined and result in random $\beta$ values that would obscure any potential peaks. Filtering out high wobble events and weighting orientations by their dwell duration, however, did not affect the shape of the distributions (data not shown) suggesting that this is not the explanation.

Another possible reason for the lack of expected peaks in the $\beta$ distribution is that if the probe changed by an angle greater than 90° then restricting it's orientation to a single hemisphere would resulted in a smaller reported angle. This seemed to be the case in certain molecules that exhibited large orientation changes that were consistently more prominent in $\alpha$ than $\beta$. In principle this could be true, however if the dipole was not restricted to a hemisphere, then it would likely have resulted in large tilting motions in $\beta$, more consistent with a molecule translocating along actin. A higher incidence of substeps in $\beta$ may also explain the lack of a two-peak distribution, since substeps consisting of intermediate $\beta$ angle could

obscure the peaks.

The distribution of orientations around the actin filament ($\alpha$) is relatively constant, as expected for molecules that can land on actin at any azimuth due to the helical distribution of binding sites (Fig. 5.16B). Both distributions show a small tendency for probes to orient parallel to the $x$-$y$ plane (i.e., $\alpha = 0°$ and $\pm180°$). The origin of this preference in angle is not clear, however it could arise from the geometry of the BR-Cam labeled myosin, such as if translocation was preferred on the actin binding sites oriented away from the quartz slide. If these binding sites corresponded to $\alpha = 0°$ and $\pm180°$ then these values would be over-represented in the distribution.

The wobble parameter is distributed about $\delta = 45°$ similarly for molecules with and without BDM (Fig. 5.16C). If BDM increased the occurrence of high wobble events, even if they were short in duration, then they would be represented by a peak near $\delta \sim 90°$, which was not observed. However, if BDM lengthens the duration of large wobble events, then this effect would not be represented in the distributions. There is a shoulder to the right side of the central peak at $\delta \sim 70°$ indicating that high wobble events are present, but their probability does not seem to increase with BDM.

**Distribution of angle changes**

Changes in orientation $(\Delta\beta, \Delta\alpha)$ and wobble $\Delta\delta$ between successive dwells are similar for molecules with and without BDM. The 3 peaks in the $\Delta\beta$ distribution for molecules without BDM in solution (Fig. 5.17A) indicate that when tilting events occur they are often $\pm50°$. The peak at zero indicates a large fraction of events with little or no change in $\beta$, such as

when other parameters (e.g., wobble) change. Large changes in $\beta$ may be under-represented since the automated choice of hemisphere suppresses angle changes greater than $90°$. When BDM is present, the peak at $+50°$ is reduced and the peak at zero is slightly broadened, possibly indicating that substeps are more likely to break up the $+50°$ angle change into smaller changes.

The distributions of the change in azimuths $\Delta\alpha$ are similar, but there is a slight preference for large $\Delta\alpha$ with BDM present in solution (Fig. 5.17B). Large $\Delta\alpha$ may correspond to non-36 nm steps, which would include an additional rotational component when the head binds to an actin monomer that is rotated around the actin filament. As discussed in Sect. 3.4.4, the difference in azimuthal angle of monomer 11 or 15 compared to monomer 13 is $\sim 28°$ for a 13/6 actin helix. Alternatively, the large $\Delta\alpha$ might be explained by the probe tilting out of the hemisphere and the opposite end being reported. The mean of either distribution is within $3°$ of zero indicating that even though large angle changes are possible, the net rotation around the actin filament is small. These results do not contradict the numerous studies [115, 116, 192, 193], which show myosin following a long $\sim$micron pitch helical path along actin filaments suspended above the surface, because the long pitch of these motions only requires a small shift in the average azimuthal angle (e.g., $10°$-$15°$).

The distribution of changes in wobble ($\Delta\delta$) are nearly identical with and without BDM. The absolute angular displacement $\zeta$ indicates a large fraction of $\sim 90°$ changes for molecules with and without BDM, indicative of the large tilting events accompanying the lever arm swing. The molecules with BDM, however, also have a significant peak at $\zeta = 20°$. This second peak might represent the re-orientations measured by Syed et al. [109] that increased

in frequency in the presence of 100 mM BDM.

In order to explore the significance of these steps further, the dwell immediately following a 'large' angle change (here $\zeta > 50°$, Fig. 5.18A) was histogrammed separately from the 'small' angle changes (here $\zeta < 50°$, Fig. 5.18B). Single exponential fits to the 'large' $\zeta$ histogram result in time constants that are within 10% of the time constants discussed previously in Fig. 5.15, whereas fits to the 'small' $\zeta$ histogram are $\sim 25\%$ faster. The time constants for the fits to the dwells when BDM is present are $\sim 30\%$ longer than the data when no BDM is present. If the dwells corresponding to large $\zeta$ changes are productive steps then at these low Mg·ATP concentrations they would be predicted to depend proportionally on Mg·ATP concentration. If the population of dwells corresponding to small $\zeta$ are substeps when the rear head detaches from actin before the power stroke occurs on the lead head then they would be predicted to not depend on Mg·ATP concentration [171].

## Dependence of $\chi_\nu^2$ on dwell interval

The $\chi_\nu^2$ for this molecule fluctuates about unity for the binned intensities (Fig. 5.13B) indicating that the number of unknown parameters estimated from the data (5) is adequate for the number of measured PFIs (16) given the noise in the signal [88]. For the molecule shown in Fig. 5.13, the correlation between $\chi_\nu^2$ and the dwell duration $(\Delta t)$ is not strong (Fig. 5.19A). However, when all of the dwells and their respective $\chi_\nu^2$ for the set of molecules are considered together, there is a trend between large $\chi_\nu^2$ and long duration dwells (Fig. 5.19B). Similarly, when the correlation is calculated for each molecule, $\sim 80\%$ of the molecules have a very strong correlation $(> 0.8)$ between these two parameters. In principle there could be a

physical phenomena missing from the model that only becomes apparent with the larger signal to noise ratio achieved in the longer duration dwells. A more likely explanation, perhaps, is that small errors in estimating the calibration factors or subtracting the background become more obvious during the longer dwells and result in a higher $\chi_\nu^2$.

## 5.5.4   Myosin bound to actin in rigor

Molecules of myosin V, in the absence of Mg·ATP, bind to actin with the lever arm tilted forward in the post power stroke (i.e., rigor) state [127, 194]. These molecules do not move on actin, but they do colocalize with it so distinguishing them from background contaminants is not an issue. Typically, polarization recordings show very few changes in the PFIs, although 1 or 2 are not uncommon (Fig. 5.20). The orientation and wobble for these molecules is characterized by either a well-defined orientation with moderate wobble or a large wobble state with poorly-defined orientation. The molecule shown in Fig. 5.20 illustrates both of these states with a low wobble ($\delta \sim 40°$) and well-defined orientation $(\beta, \alpha) = (50°, 0°)$ during the initial 400 ms followed by a large wobble ($\delta \sim 70°$) for the remaining 2 s until photo-bleaching.

Two distributions of molecules are expected since the intermolecular strain is too large for both heads of myosin V to bind actin in the rigor configuration, unless the lead head lever arm is kinked, as proposed in the telemark state. Consequently, many molecules are attached to actin in the one-head bound state [127], therefore a BR-CaM near the attached head would have a well-defined orientation whereas a BR-CaM near the free head would have a large wobble and poorly defined orientation.

The fraction of each molecule's recording where the wobble parameter is large (i.e., $\delta > 75°$) is calculated for all the analyzed molecules to illustrate the fraction that rarely or frequently experience high wobble. In the absence of Mg·ATP (Fig. 5.22A,B), two distributions of wobble states is clear from the peak at 0.1, which indicates that $\sim 65\%$ of the molecules experience high wobble for only 10% of the recording, and the peak at 0.85, which indicates that $> 20\%$ of the molecules experience high wobble for nearly the entire recording ($> 85\%$). This is in contrast to molecules in the presence of Mg·ATP(Fig. 5.22A,B), which mostly show no high wobble events.

This result is consistent with the data presented in reference [61] which showed two distributions of molecules when no Mg·ATP was present. The smaller peak was identified as the trailing head with $\delta = 36°$ and the larger peak as the detached head with $\delta = 46°$. Symmetries in the setup prevented $\delta = 90°$ from being measured; instead the orientation $(\theta, \phi) = (54.7°, 45°)$, which has an equivalent distribution of PFIs as $\delta = 90°$, was usually returned by the fitting procedure (see Sect. 4.3.4 for details).

The tail of the Mg·ATP wobble distribution (Fig. 5.22B) indicates that 40% of translocating molecules experience high wobble for 10-100% of their recording. This result is evident in the molecule shown in Fig. 5.12, which indicates an interval with large wobble before photobleaching or dissociating from actin (Fig. 5.13G). In order to investigate this trend further, the distribution of wobble during the first and last dwell of a recording were compared for myosin with and without Mg·ATP present in solution (Fig. 5.23A,B). With Mg·ATP present, the first dwell is likely to be in the ATP-waiting state with two heads bound and has a relatively low wobble of $\sim 40°$ (*solid line* Fig. 5.23A). At the end of the recording, the probability that

the last dwell contains a high wobble event is considerably more likely (*dashed line*). In the absence of ATP, the distribution of the first and last dwell are nearly identical with two peaks, one at $\delta = 55°$ and the other at $\delta = 80°$. Presumably, the $85°$ peak is the detached head, whereas the $55°$ peak is the attached head, which has a slightly higher wobble than in the two head bound state.

Thus, it seems that a myosin run is likely to terminate in a one head bound state before either photobleaching or dissociating from actin. Often these terminal dwells are much longer in duration than the previous dwells, assumed to be due to stepping (data not shown). If the abrupt reduction in fluorescence was due to the molecule dissociating from actin then this would likely occur from a singly bound state, however the duration of the final dwell would not be significantly different than the others unless it encountered an obstacle or the end of the actin filament. An alternate hypothesis is that that translocation is being impaired as the molecule is illuminated, for example photodamage of Alexa-647 actin may prevent binding by myosin. The high intensity laser seems like a likely culprit since it is continuously illuminating the sample during a polarization measurement. This is in contrast to short exposure movies, where each frame is exposed for only a fraction of the frame rate, and the myosin is observed to translocating over many microns for 10's of seconds.

## 5.6   Conclusions

The maximum time resolution of a polarized TIRF setup was increased $100\times$ by increasing the frequency that different polarizations illuminate the sample and incorporating a modified TCSPC device that records the arrival times of individual photons and their polarization state.

The maximum time resolution is limited by the response of the high-voltage amplifiers to the Pockels cells that modulate the laser polarizations. Currently, 3% of the detected photons are rejected due to the 2-3 $\mu$s required to change the polarization state after each 100 $\mu$s illumination interval. In practice however, the time resolution is limited by the number of photons emitted ($\sim 30/\text{ms}$) from a single fluorescence molecule, here bifunctional rhodamine attached to calmodulin.

The multiple intensity change point algorithm developed in Sect. 4 was applied to translocating myosin V molecules to detect changes automatically in the polarized fluorescence intensities with the only user defined parameters being the rates of false positive and negative events. Longer duration dwells, presumably corresponding to the ATP-waiting state before the next step occurs, and shorter duration dwells, which sometimes corresponded to discernable substeps in the myosin ATP cycle, were detected. Some of these substeps corresponded to the proposed diffusive search of the free myosin head for the next actin binding site, but they were rarely observed, probably due to the insufficient number of photons detected during the short events.

Future experiments varying the concentration of ADP and phosphate may slow down the substeps and make them easier to detect. Also simultaneous position and orientation measurements would help distinguish substeps from actual steps that produce forward motion.

## 5.7 Biological assays

Protocols for expressing the myosin, labeling the myosin, and conducting the processivity experiment are described in the following sections. When possible, all solutions were prepared

using 0.2 $\mu$m filtered de-ionized water in a clean hood while wearing gloves to prevent sample contamination.

### 5.7.1 Protocol for myosin V expression and purification

The myosin V construct, kindly provided by M. Ikebe (University of Massachusetts), contains amino acids 1-1105 of the native mouse myosin V as well as a C-terminal His tag and N-terminal His, FLAG and TEV protease sites. The heavy chain molecular weight is 137 kDa (240.3 kDa including the 6 calmodulins). Myosin with bound calmodulin was purified from SF9 cells that were coinfected with baculovirus (pFast HT FLAG) containing the myosin construct [187] and a separate virus containing a calmodulin expression plasmid. After incubating 2 L of cells for 60 h at 27 °C, cells were harvested by centrifugation at low speed and the myosin purified according to El Mezgueldi et al. [186].

Briefly, the cells were suspended in lysis buffer (10 mM Tris pH 7.5, 200 mM NaCl, 2 mM ATP, 4 mM MgCl$_2$, 5 mM DTT, 1 mM EGTA, 0.5% Igepal, 1 mM BME, 0.01 mg/ml protease inhibitor) and homogenized 5 times with a Dounce homogenizer. The cell contents were removed by centrifugation at $100\,000 \times g$ for 1 h at 4 °C, and the supernatant containing the myosin retained (Fig. 5.24, lanes S, S/10, P/10, P/100 indicate the supernatant and pellet at 10 and 100× dilution). Two columns (each 120 mm × 8 mm) containing 2 ml of FLAG resin (A2220 Sigma) are cleaned by washing with 3 × 1.5 ml of 100 mM Glycine, pH 3.5 and equilibrated with 3×10 ml of wash buffer (lysis buffer without Igepal). The columns are loaded with the myosin containing supernatant (Fig. 5.24, lane LT) and washed with 5×5 ml of wash buffer to remove unwanted protein (Fig. 5.24, lane WT). The myosin is competed off

the resin with excess FLAG peptide by rinsing with 2 ml of elution buffer (100 mM NaCl, 10 mM Tris pH 8.0, 1 mM EGTA 1 mM DTT, 5 $\mu$M calmodulin, 0.2 mg/ml FLAG peptide), incubated for 1 h and the effluent collected. This elution step is repeated three times to collect all of the myosin $\sim$14 ml total, (Fig. 5.24, lanes E1 to E1+E2+E3), .

Half of the eluted myosin is dialyzed into storage buffer and the other half is further puri-fied on a Mono Q column using fast protein liquid chromatography (FPLC). Before dialysis (Fig. 5.24, lane Dia-PreC), the first half is concentrated from 7 to 1.5 ml using a centrifugal filter (Amicon Ultracel-10k, Millipore) with 5 spins at $2\,500 \times g$ for 5 min each. After concen-trating, the myosin is dialyzed overnight (Slide-A-Lyzer Dialysis cassette, Thermo Scientific 10 0000 MWCO) with 3 buffer exchanges into storage buffer (200 mM NaCl, 20 mM MOPS pH 7.0, 1 mM EGTA-K (Fluka stock), 1 mM DTT) to remove excess FLAG antibody and free nucleotide (Fig. 5.24, lanes Dia-PreC). The last dialysis contains 10% sucrose (Fig. 5.24, lane Dia-PostC).

The other half of the eluted protein is loaded onto a Mono-Q column (8 ml, Amersham Biosciences), equilibrated in column buffer (10 mM Tris, pH 8.0, 25 mM KCl, 1 mM DTT) and eluted with a linear $25\,\text{mM} - 1\,\text{M}$ KCl gradient. The Mono-Q column separates the myosin from free FLAG peptide, nucleotides, free CaM and a $\sim$42 kDa protein that is presumably actin (Fig. 5.24, lane Dia-PostC). Fractions containing myosin were pooled (Fig. 5.24, lane MQ-PreC), concentrated from 8 to 0.2 ml using a centrifugal filter as before(Fig. 5.24, lane MQ-PostC), and dialyzed into storage buffer containing 10% sucrose (Slide-A-Lyzer mini dialysis unit, 10 000 MWCO, Pierce).

Western blots using antibodies to the FLAG sequence and to the Dil 2-123 sequence in
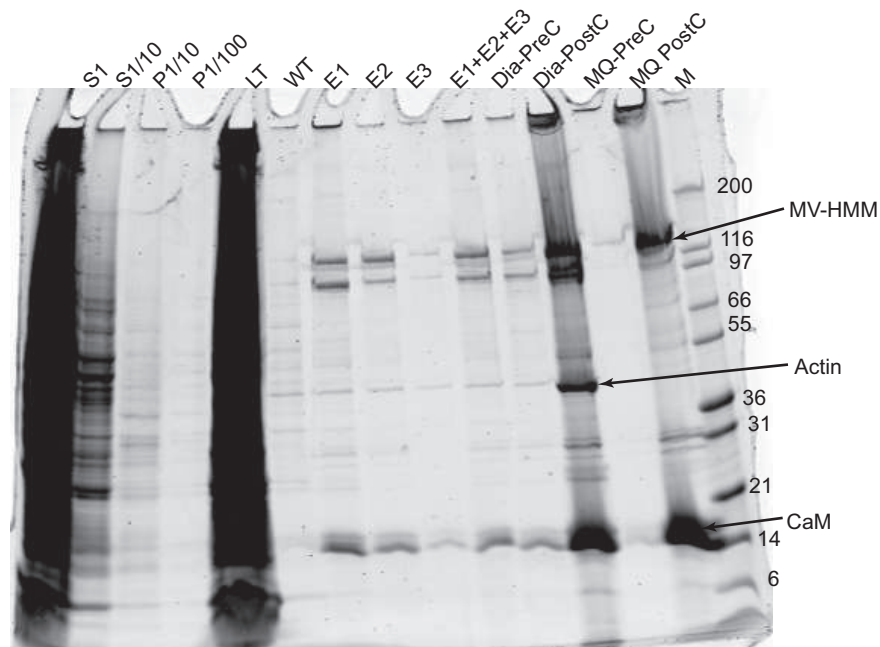
Figure 5.24: Recombinant myosin V purification. Sypro-Red stained SDS-PAGE gel of various steps in the myosin V purification: S1, supernatant; P1, pellet; LT, load through the FLAG column; WT, wash through the FLAG column; E1,E2,E3, elutions from the FLAG column, Dia-PreC/PostC, dialyzed myosin before and after concentrating; MQ-PreC/PostC, Mono-Q purified myosin before and after concentration; M, Marker, in kDa (see text for details). The final myosin V product (MV-HMM) is either concentrated and dialyzed myosin V (lane Dia-PostC) or concentrated and Mono-Q purified myosin V (lane MQ PostC). There appears to be a proteolytic myosin fragment at $\sim 97$ kDa that was not removed by dialysis, but was largely removed by the Mono-Q column.

the first section of the coiled-coil of Myosin V (generously provided by John Hammer, NIH) indicate dominant bands for the full-length myosin. The myosin V antibody, but not the FLAG antibody, also detects a much lower weight proteolytic fragments for both the Mono-Q and dialyzed purification schemes (Fig. 5.25).

The concentration of the myosin dimers obtained via the two purification schemes was determined by a Bradford assay with a BSA standard to be $\sim 2.5$ mg/ml ($\approx 5$ $\mu$M) with a total volume of 0.35 and 0.54 ml for the dialyzed and Mono-Q purified myosins, respectively. Both sets of myosin were divided into aliquots and snap frozen in liquid nitrogen for storage at -80 °C.
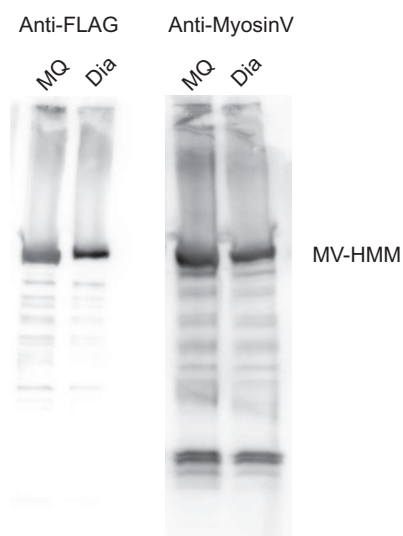
Figure 5.25: Western blot of dialyzed (Dia) and Mono-Q (MQ) purified myosin using antibodies to FLAG or myosin V. The myosin V antibody (a generous gift from John Hammer, NIH) is to an $\sim 300$ amino acid region of coiled-coil from rabbit (see text for details). The MV-HMM band is likely full length myosin V since the FLAG/Myosin-V antibodies are to the N- and C- terminus, respectively. The lower band myosin-V antibody lanes may be a proteolytic fragment that was not separated by the Mono-Q column.

## 5.7.2 Protocol for myosin V exchange

Bisiodoacetamidorhodamine (bifunctional rhodamine, BR), which has two iodoacetamide linkers flanking the chromophore, is cross-linked to a calmodulin (CaM) containing only two Cystines at amino acids P66C and A73C, see Fig. 5.1. The BR-CaM is attached to the myosin V lever arm by exchanging the wild type calmodulin (WT-CaM) for the BR-CaM. Briefly, $\sim$ 100 nM myosin V is incubated at room temperature with an exogenous calmodulin mixture of 1 BR-CaM to 10 WT-CaM in exchange buffer (20 mM Imidazole pH 7.6, 25 mM KCl, 2 mM MgCl$_2$, 1.000 mM EGTA (accurate concentration is important, Fluka 03778), 5 mM DTT). The calmodulin affinity to the lever arm is reduced by adding calcium to a final concentration of 1.001 mM. After a 10 min incubation, the concentration of calcium is reduced by adding a high concentration of EGTA forcing the free calmodulins to rebind to the lever arm. The

BR-CaM is exchanged at low stoichiometry ($\sim$0.4 BR-CaM per double-headed myosin V) to obtain myosin V molecules with one BR-CaM and to minimize the proportion of myosins with two or more probes. Note that the exchange stoichiometry is very sensitive to the calcium concentration during the exchange reaction [195]. After exchanging the myosin, the free BR-CaM remaining in solution is removed by using a 100 kDa centrifugal filter (Pall Corporation, Nanosep OD100C33) at $2\,000 \times g$ for 2-3 min, which passes the low molecular weight calmodulin and retains the high molecular weight myosin. Approximately a half to a third of the solution is spun through the filter, discarded and replaced with the exchange solution containing 10% sucrose. After 4-5 iterations, the retentate is predominately BR-CaM labeled myosin V in the sucrose storage solution, which is then divided into aliquots and stored at $-80°$. The final concentration of BR-CaM myosin V is $\sim$ 10-50 nM.

### 5.7.3 Protocol for single molecule processivity assay

Single molecule processivity experiments of myosin V translocating along fixed actin filaments are performed in a flow cell consisting of a PMMA-coated quartz slide and glass cover slip (Fisher, No 1.) held together by pieces of double–sided tape (Scotch, Cat. No. 665). Typically, four $\sim$1 mm wide pieces of tape are spaced to create three 10 $\mu$l individual flow cells on one slide. An equal volume of solution is flowed through the chamber using a pipette while wicking out the previous contents with filter paper. The flow rate can be controlled roughly by adjusting the contact area between the filter paper and the solution.

First, quartz slides (Quartz Scientific, HPFS grade quartz, 212000-001) are cleaned by sonication (Branson 3510) at 40°C in 3 steps: Acetone for 10 min, 200 mM KOH for 20

min, and 10 min Ethanol. Slides are rinsed 3 times in deionized water between the first two steps and allowed to air dry after the ethanol wash in a clean hood. Immediately before use, a prepared slide is plasma-cleaned (Harrick, PDC-32G) for 2 min on hi power. 20 $\mu$l PMMA ($\sim$ 2 mg/ml PMMA (Aldrich Chemical, secondary standard grade 37 003-7) dissolved in methylene chloride) is spin-coated (Laurell WS-400A-6NPP/Lite) at 5 000 rev/min onto the clean slide and transferred immediately into sealed container for transport to a clean hood where the flow cell is constructed.

After constructing the flow cells, 1 mg/ml biotinylated BSA (Sigma, A8549) is flowed in to one of the lanes using filter paper to wick out any excess liquid. After incubating for 5 min the flow cell is rinsed with myosin V buffer (M5B, 25 mM KCl, 20 mM Hepes pH = 7.6, 2 mM MgCl$_2$, and 1 mM EGTA-K in filtered deionized water) and then 0.5 mg/ml streptavidin (Sigma, S-4762) is flowed in and incubated for 2 min. After rinsing out the excess streptavidin with MVB, a 0.25 $\mu$M solution of biotin-Alexa 647-actin filaments (filaments polymerized in the ratio 1 biotin actin monomer (Cytoskeleton, Inc., AB07) to 5 Alexa-647 labeled actin (prepared by labeling G-actin with Alexa Fluor 647 as described for AEDANS actin in reference [61]) monomers to 20 unlabeled actin monomers) are flowed into the cell and quickly rinsed to achieve filaments that are well aligned with the direction of flow. Blocking of the surface is achieved by an additional 2 min incubation with 1 mg/ml unlabeled BSA (Sigma A0281). Finally, motility assay buffer containing labeled myosin V, excess calmodulin and Mg·ATP is flowed into the cell (MAB, 0.01-1 nM BR-CaM Myosin V, 100 mM DTT, 0.1 mg/ml WT-CaM, 1-40 $\mu$M ATP dissolved in M5B). The Alexa actin and BR-CaM myosin V can be imaged independently but displayed on the monitor simultaneously so that spots of

myosin moving along actin filaments can be clearly identified and recorded for polarization analysis. All solutions are prepared fresh monthly, except for DTT and the PMMA solution which are prepared daily from powder.

Slight variations in the protocol were also implemented, including substituting the biotin-BSA, streptavidin and biotin-Alexa 647-actin filaments with NEM (N-Ethylmaleimide) treated myosin II and 1:5 Alexa 647-actin filaments (one Alexa-647 labeled actin monomer to five unlabeled monomers). The advantage of NEM myosin is that the long, highly-charged tail binds to the PMMA-coated quartz slide while the head attaches but does not release actin. Myosin V can translocate along actin filaments and never encounter biotin-streptavidin obstacles that can act as an impediment if too many are incorporated into the filament. In order to slow down the rebinding rate of the free myosin V head to the next actin binding site, 100 mM BDM is sometimes included in the final motility assay buffer.

# Chapter 6

# Conclusions

In this work two biological systems were studied at the single molecule level: DNA looping in tethered particle experiments and translocation between myosin and actin using polarized TIRF microscopy. In the DNA looping system, a new analysis tool was developed to determine the kinetics of loop formation and breakdown without filtering the raw data. In the acto-myosin work, modifications to a polarized TIRF setup were described that increased the range of detectable orientations 4-fold and increased the maximum time resolution 50-fold, in part by measuring the arrival time of each detected photon. A new analysis tool was also developed for these higher time resolution experiments that avoided binning of the raw photon data. Experiments using single molecule polTIRF determined the handedness of actin filament twirling as it translocated on myosin in a gliding assay and substeps in myosin V molecules as they translocated along a stationary actin filament.

Aside from very general similarities, i.e., both projects investigated single molecules using light microscopy, these two areas of research were quite distinct; however, the analysis tools

that were developed for each provide a common link. Both methods use the data in its raw form with no filtering or binning, common practices that are often used to improve the signal to noise ratio at the expense of lower time resolution. Avoiding these post-processing steps entirely removes any concerns that the conclusions may depend on them. Rigorous analyses like these are especially useful in single molecule experiments because the data are inherently statistical. Objectively identifying events minimizes selection bias from skewing the results.

## 6.1   Tethered particle experiments

In the DNA work discussed here, kinetics of protein-DNA interactions were investigated using the tethered particle method (TPM); a technique in which protein binding and dissociating to specific sites on the DNA induces loops to form and break, thereby abruptly changing the motion of the tethered particle. The kinetics of these loops provides information on the chemical affinity of protein binding as well as on the physical properties of the DNA such as its elasticity and geometry. Determining the effect of these and other variables on the kinetic rates is one of the main objectives of TPM. Thus reliable methods that do this, such as the Diffusive Hidden Markov Method (DHMM) developed here, are useful.

The DHMM method relies on the large amount of data that can be collected using single particle tracking techniques on images of the tethered microspheres that are recorded for 30-60 min. The resulting data consists of the $(x, y)$ position of the particle every 30-100 ms. These high speeds allow the diffusive motion of the tethered particle to be accurately modeled in the looped and unlooped states of the DNA, which can then be used in the analysis of experimental data to predict the state of a tether that is dynamically switching between these configurations.

No binning or filtering of the raw data is required and the underlying kinetic scheme of the hidden Markov model can be as simple or complex as required to describe the protein-DNA kinetics and determine the desired rates.

Potential avenues for future TPM work will likely include broadening into other biologically interesting proteins that bind to nucleic acids besides repressor proteins, for example References [83, 84, 101], studying the physical properties of DNA to form loops at short length scales [28], and expanding the complexity of the kinetic looping scheme to include multiple looped states and binding sites [72]. 3D tracking of the particle has already been implemented [85] and could be incorporated into future DHMM models. Smaller particles such as quantum dots or tiny particles of gold would have a faster diffusive time scale and yet still be bright enough for rapid imaging so that new kinetic regimes might become available. Interesting physics might also be revealed, such as hydrodynamic coupling between the bead and the wall, or conformational dynamics of the tether. Combining TPM with other single molecule techniques such as fluorescence imaging or FRET could provide direct information on the protein-DNA interactions that are inferred from the particle.

### 6.1.1   Polarized-TIRF experiments on acto-myosin

In the polTIRF work, interactions between myosin and actin were studied to better understand the molecular mechanisms underlying translocation. The polTIRF assay determines the orientation and wobble of a single fluorophore, independent of its spatial position. For myosin and other molecular motors this is a particularly useful assay because the lever arm of the molecule undergoes a large rotation as it produces force during a forward step. A fluorophore rigidly

attached to the lever arm at two points reports these angle rotations via the magnitude of the polarized fluorescence emission. The 3D orientation of the probe can be inferred if multiple polarized illuminations are used to excite the fluorophore [61, 63].

One improvement to the polTIRF setup made here was to increase the number of input polarization states of the laser illumination. Light polarized in the two beams at $\sim 45°$ to the cartesian axes breaks the reflection symmetries in the setup and allows the orientation of the probe to be measured within a hemisphere [123]. This is the largest range that can be achieved since the probe has an intrinsic dipole symmetry that cannot be resolved. Using this expanded range of angles, the handedness of an actin filament translocating on skeletal myosin II in a gliding assay was determined to be left-handed [123], opposite to the intrinsic actin helix. Twirling of actin by myosins V [123] and VI [124] were also determined using this assay and found to be left- and right- handed, respectively.

The second major improvement was the increase in time resolution that was achieved by faster cycling of the input polarizations and tagging each photon with its arrival time and polarization state using a modified time-correlated single photon counting circuit. The raw data for these experiments consists of a list of photon arrival times and tag numbers. A new analysis, the Multiple Intensity Change Point algorithm, was developed to detect intensity change points [100] from the polarization information of individual photons, without requiring any binning of the raw data. The increased time resolution allowed substeps within the myosin V ATPase cycle to be measured. Due to the limited number of photons emitted during these rapid events, substeps consistent with the diffusive search of the free myosin head for the next actin binding site were only occasionally detected. Short duration angular states, possibly

corresponding to a molecule transiently bending its leading lever arm as a precursor to a step (i.e., the telemark state), were detected before and after long duration dwells, which were shown to correlate with stepping in other work [61].

A key development for future polTIRF experiments will be to combine position and orientation, as has been accomplished in other similar assays albeit at lower time resolution [111] and limited angular resolution [109]. More widely applicable bifunctional labeling schemes, e.g., the ReAsH molecule, which binds to two pairs of Cysteines in the motif (C-C-P-G-C-C), could greatly expand the usefulness of polTIRF in other biological systems. Currently, most of the polarized TIRF experiments have utilized BR-CaM with various myosin isoforms [61, 62, 124] and kinesin with bifunctional sulforhodamine [177]. The third classical motor, dynein, may also undergo interesting rotational motions as part of its movement on microtubules and would be a good candidate for polTIRF experiments. Another avenue of future research is simultaneous measurement of the orientation of two probes attached to the same molecule, as is done with position by using two different color fluorophores and orthogonal labeling schemes. This would allow domain rotations within a molecule to be determined independent of the molecule's overall orientation in space.

In general, measuring the orientation of single molecules is much less common than measuring their position, although many macromolecules are known to exhibit essential rotational motions [2]. There remains much unexplored territory with exciting discoveries waiting to be made. Novel analysis tools based on statistical models of a single molecule's dynamics or its fluorescence properties can aid in this search by quantify the large amount of data generated in single molecule biophysics experiments. These tools are especially advantageous if they

221

minimizing the number of user defined parameters such as bin sizes and thresholds that can

lead to different conclusions from the same set of data.

# Bibliography

[1] W. E. Moerner. Illuminating single molecules in condensed matter. *Science*, 283:1670–6, 1999.

[2] J. F. Beausang, Y. Sun, M. E. Quinlan, J. N. Forkey, and Y. E. Goldman. Orientation and rotational motions of single molecules by polarized total internal reflection fluorescence microscopy. In P. R. Selvin and T. Ha, editors, *Single molecule techniques*, pages 121–148. Cold Spring Harbor, NY, 2008.

[3] S. Weiss. Fluorescence spectroscopy of single biomolecules. *Science*, 283:1676–83, 1999.

[4] C. Bustamante, J. C. Macosko, and G. J. Wuite. Grabbing the cat by the tail: Manipulating molecules one by one. *Nature Reviews. Molecular Cell Biology*, 1(2):130–6, 2000.

[5] W. J. Greenleaf, M. T. Woodside, and S. M. Block. High-resolution, single-molecule measurements of biomolecular motion. *Annual review. Biophysics and Biomolecular Structure*, 36:171–90, 2007.

[6] F. Ritort. Single-molecule experiments in biological physics: methods and applications. *Journla of Physics: Condensed Matter*, 18:R531–83, 2006.

[7] P. R. Selvin and T. Ha. *Single molecule techniques*. Cold Spring Harbor, 2008.

[8] C. Gell, D. Brockwell, and A. Smith. *Handbook of single molecule fluorescence spectroscopy*. Oxford University Press, Oxford, 2006.

[9] P. Hinterdorfer and A. van Oijen. *Handbook of single-molecule biophysics*. Springer, Dordrecht, 2009.

[10] E. Barkai, F. L. H. Brown, M. Orrit, and H. Yang. *Theory and Evaluation of Single-Molecule Signals*. World Scientific, Singapore, 2008.

[11] E. Neher and B. Sakmann. Single-channel currents recorded from membrane of denervated frog muscle fibres. *Nature*, 260:799–802, 1976.

[12] A. Ashkin. Acceleration and trapping of particles by radiation pressure. *Physical Review Letters*, 24:156–9, 1970.

[13] G. Binnig, C. F. Quate, and C. H. Berger. Atomic force microscope. *Physical Review Letters*, 56:930–3, 1986.

[14] A. Ashkin and J. M. Dziedzic. Optical trapping and manipulation of viruses and bacteria. *Science*, 235:1517–20, 1987.

[15] M. S. Kellermayer, Smith S. B., H. L. Granzier, and C. Bustamante. Folding-unfolding transitions in single titin molecules characterized with laser tweezers. *Science*, 276:1112–6, 1997.

[16] K. Svoboda, C.F. Schmidt, B.J. Schnapp, and S.M. Block. Direct observation of kinesin stepping by optical trapping interferometry. *Nature*, 365:721–7, 1993.

[17] H. Yin, M. D. Wang, K. Svoboda, R. Landick, S. M. Block, and J. Gelles. Transcription against an applied force. *Science*, 270(5242):1653–7, 1995.

[18] A. D. Mehta, R. S. Rock, M. Rief, J. A. Spudich, M. S. Mooseker, and R. E. Cheney. Myosin V is a processive actin-based motor. *Nature*, 400(6744):590–3, 1999.

[19] D. E. Smith, S. J. Tans, S. B. Smith, S. Grimes, D. L. Anderson, and C. Bustamante. The bacteriophage $\phi$29 portal motor can package DNA against a large internal force. *Nature*, 413(18):748–52, 2001.

[20] M. Rief, M. Gautel, F. Oesterhelt, J. M. Fernandez, and H. E. Gaub. Reversible unfolding of individual titin inmunoglobulin domains by AFM. *Science*, 276:1109–12, 1997.

[21] S. Chu. Laser manipulation of atoms and particles. *Science*, 253(5022):861–6, 1991.

[22] S. B. Smith, L. Finzi, and C. Bustamante. Direct mechanical measurements of the elasticity of single DNA molecules by using magnetic beads. *Science*, 258:1122–4, 1992.

[23] P. Cluzel, A. Lebrun, C. Heller, R. Lavery, J.-L. Viovy, D. Chatenaly, and F. Caron. DNA: An extensible molecule. *Science*, 271:792–4, 1995.

[24] S. B. Smith, Y. Cui, and C. Bustamante. Overstretching B-DNA: the elastic response of individual doublestranded and single-stranded DNA molecules. *Science*, 271:795–9, 1995.

[25] T. R. Strick, J.-F. Allemand, D. Bensimon, A. Bensimon, and V. Croquette. The elasticity of a single supercoiled DNA molecule. *Science*, 271:1835–7, 1996.

[26] L. Finzi and J. Gelles. Measurement of lactose repressor-mediated loop formation and breakdown in single DNA-molecules. *Science*, 267(5196):378–80, 1995.

[27] P. A. Wiggins, T. van der Heijden, F. Moreno-Herrero, A. Spakowitz, R. Phillips, J. Widom, C. Dekker, and P. C. Nelson. High flexibility of DNA on short length scales probed by atomic force microscopy. *Nature Nanotechnology*, 1(2):137–41, 2006.

[28] L. Han, H. G. Garcia, S. Blumberg, K. B. Towles, J. F. Beausang, P. C. Nelson, and R. Phillips. Concentration and length dependence of DNA looping in transcriptional regulation. *PLoS One*, 4(5):e5621, 2009.

[29] K. B. Towles, J. F. Beausang, H. G. Garcia, R. Phillips, and P. C. Nelson. First-principles calculation of DNA looping in tethered particle experiments. *Physical Biology*, 6(2):025001, 2009.

[30] I. Sase, H. Miyata, J. E. T. Corrie, J. S. Craik, and K. Kinosita Jr. Real time imaging of single fluorophores on moving actin with an epifluorescence microscope. *Biophysical Journal*, 69:323–8, 1995.

[31] T. Hirschfeld. Optical microscopic observation of single small molecules. *Applied Optics*, 15:2965–6, 1976.

[32] K. Morikawa and M. Yanagida. Visualization of individual DNA molecules in solution by light microscopy: DAPI staining method. *Journal of Biochemistry*, 89(2):693–6, 1981.

[33] L. S. Barak and W. W. Webb. Fluorescent low density lipoprotein for observation of dynamics of individual receptor complexes on cultured human fibroblasts. *Journal of Cell Biology*, 90:595–604, 1981.

[34] T. Yanagida, M. Nakase, K. Nishiyama, and F. Oosawa. Direct observation of motion of single f-actin filaments in teh presence of myosin. *Nature*, 307:58–60, 1984.

[35] Moerner W. E. and L. Kador. Optical detection and spectroscopy of single molecules in a solid. *Physical Review Letters*, 62(21):2535–8, 1989.

[36] M. Orrit and J. Bernard. Single pentacene molecules detected by fluorescence excitation in a p-terphenyl crystal. *Physical Review Letters*, 65(21):2716–9, 1990.

[37] E. B. Shera, N. K. Seitzinger, L. M. Davis, R. A. Keller, and S. A. Soper. Detection of single fluorescent molecules. *Chemical Physics Letters*, 174(6):553–7, 1990.

[38] R. Rigler and J. Widengren. Ultrasensitive detection of single molecules by fluorescence correlation spectroscopy. *BioScience*, 3:180–3, 1990.

[39] E. Betzig and R. J. Chichester. Single molecules observed by near-field scanning optical microscopy. *Science*, 262(5138):1422–5, 1993.

[40] J. J. Macklin, J. K. Trautman, T. D. Harris, and L. E. Brus. Imaging and time-resolved spectroscopy of single molecules at an interface. *Science*, 272(5259):255–8, 1996.

[41] J. K. Trautman and J. J. Macklin. Time-resolved spectroscopy of single molecules using near-field and far-field optics. *Chemical Physics*, 205(1-2):221–9, 1996.

[42] T. Funatsu, Y. Harada, M. Tokunaga, K. Saito, and T. Yanagida. Imaging of single fluorescent molecules and individual ATP turnovers by single myosin molecules in aqueous solution. *Nature*, 374(6522):555–9, 1995.

[43] J. R. Lakowicz. *Principles of fluorescence spectrosocpy*. New York, 3rd edition.

[44] T. Ha, T. Enderle, D.F. Ogletree, D.S. Chemla, P.R. Selvin, and S. Weiss. Probing the interaction between two single molecules: fluorescence resonance energy transfer between a single donor and a single acceptor. *Proceedings of the National Academy of Sciences of the USA*, 93(13):6264–8, 1996.

[45] B. Schuler, E. A. Lipman, P. J. Steinbach, M. Kumke, W. A. Eaton, and R. M. Hochstrasser. Polyproline and the 'spectroscopic ruler' revisited with single-molecule fluorescence. *Proceedings of the National Academy of Sciences of the USA*, 102(8):2754–9, 2005.

[46] R. Roy, S. Hohng, and T. Ha. A practical guide to single-molecule FRET. *Nature Methods*, 5(6):507–16, 2008.

[47] A. Yildiz, J. N. Forkey, S. A. McKinney, T. Ha, Y. E. Goldman, and P. R. Selvin. Myosin V walks hand-over-hand: single fluorophore imaging with 1.5-nm localization. *Science*, 300(5628):2061–5, 2003.

[48] S. T. Hess, T. P. K. Girirajan, and M. D. Mason. Ultra-high resolution imaging by fluorescence photoactivation localization microscopy. *Biophysical Journal*, 91:4258–72, 2006.

[49] S. W. Hell and J. Wichmann. Breaking the diffraction resolution limit by stimulated-emission: stimulated emission-depletion fluorescence microscopy. *Optics Letters*, 19:780–2, 1994.

[50] M. J. Rust, M. Bates, and X. Zhuang. Sub-diffraction-limit imaging by stochastic optical reconstruction microscopy (STORM). *Nature Methods*, 3:793–5, 2006.

[51] W. C. Chan, D. J. Maxwell, X. Gao, R. E. Bailey, M. Han, and S. Nie. Luminescent quantum dots for multiplexed biological detection and imaging. *Current Opinion in Biotechnology*, 13(1):40–6, 2002.

[52] Y. Sun, J. D. McKenna, J. M. Murray, E. M. Ostap, and Y. E. Goldman. Parallax: high accuracy three-dimensional single molecule tracking using split images. *Nano Letters*, 9(7):2676–82, 2009.

[53] B. Huang, W. Wang, M. Bates, and X. Zhuang. Three-dimensional super-resolution imaging by stochastic optical reconstruction microscopy. *Science*, 319:810–3, 2008.

[54] H. Yang. Progress in single-molecule spectroscopy in cells. *Current Opinion in Chemical Biology*, 14:1–7, 2009.

[55] S. Wennmalm and S. M. Simon. Studying individual events in biology. *Annual Review of Biochemisty*, 76:419–46, 2007.

[56] X. S. Xie, P. J. Choi, G. W. Li, N. K. Lee, and G. Lia. Single-molecule approach to molecular biology in living bacterial cellstudying individual events in biology. *Annual Review of Biophyiscs*, 37:417–44, 2008.

[57] D. S. Chemla P. R. Selvin S. Weiss T. Ha, T. Enderle. Single molecule dynamics studied by polarization modulation. *Physical Review Letters*, 77(19):3979–82, 1996.

[58] T. Ha, J. Glass, Th. Enderle, D.S. Chemla, and S. Weiss. Hindered rotational diffusion and rotational jumps of single molecules. *Physical Review Letters*, 80:2093–96, 1998.

[59] I. Sase, H. Miyata, S. Ishiwata, and K. Kinosita Jr. Axial rotation of sliding actin filaments revealed by single-fluorophore imaging. *Proceedings of the National Academy Science USA*, 94(11):5646–5650, 1997.

[60] D. M. Warshaw, E. Hayes, D. Gaffney, A.-M. Lauzon, J. Wu, G. Kennedy, K. Trybus, S. Lowey, and C. Berger. Myosin conformational states determined by single fluorophore polarization. *Proceedings of the National Academy of Sciences of the USA*, 95(14):8034–9, 1998.

[61] J. N. Forkey, M. E. Quinlan, M. A. Shaw, J. E. T. Corrie, and Y. E. Goldman. Three-dimensional structural dynamics of myosin V by single-molecule fluorescence polarization. *Nature*, 422(6930):399–404, 2003.

[62] M. E. Quinlan, J. N. Forkey, and Y. E. Goldman. Orientation of the myosin light chain region by single molecule total internal reflection fluorescence polarization microscopy. *Biophysical Journal*, 89(2):1132–42, 2005.

[63] J. N. Forkey, M. E. Quinlan, and Y. E. Goldman. Measurement of single macromolecule orientation by total internal reflection fluorescence polarization microscopy. *Biophysical Journal*, 89:1261–71, 2005.

[64] J. N. Forkey, M. E. Quinlan, and Y. E. Goldman. Protein structural dynamics by single-molecule fluorescence polarization. *Progress in Biophysics and Molecular Biology*, 74(1-2):1–35, 2000.

[65] S. A. Rosenberg, M. E. Quinlan, J. N. Forkey, and Y. E. Goldman. Rotational motions of macro-molecules by single-molecule fluorescence microscopy. *Accounts of Chemical Research*, 38:583–93, 2005.

[66] H. Xu and T. R. Hoover. Transcriptional regulation at a distance in bacteria. *Current Opinion in Microbiology*, 4(2):138–44, 2001.

[67] R. Schleif. DNA looping. *Annual Review Biochemistry*, 61:199–223, 1992.

[68] J. Müller, Oehler S., and B. Müller-Hill. Repression of lac promoter as a function of distance, phase and quality of an auxiliary lac operator. *Journal of Molecular Biology*, 257:21–9, 1996.

[69] P. J. Choi, L. Cai, K. Frieda, and X. S. Xie. A stochastic single-molecule event triggers phenotype switching of a bacterial cell. *Science*, 322(5900):442–6, 2008.

[70] C. Zurla, A. Franzini, G. Galli, D. D. Dunlap, D. E. A. Lewis, S. Adhya, and L. Finzi. Novel tethered particle motion analysis of cI protein-mediated DNA looping in the regulation of bacteriophage lambda. *Journal of Physics-Condensed Matter*, 18(14):S225–34, 2006.

[71] P. C. Nelson. *Biological Physics*. W.H. Freeman and Co., New York, 2004.

[72] J. M. G. Vilar and L. Saiz. DNA looping in gene regulation: from the assembly of macromolecular complexes to the control of transcriptional noise. *Current Opinion in Genetics and Development*, 15:136–44, 2005.

[73] J. D. Moroz and P. Nelson. Torsional directed walks, entropic elasticity, and DNA twist stiffness. *Proceedings of the National Academy of Science USA*, 94(26):14418–22, 1997.

[74] D. Swigon, B. D. Coleman, and W. K. Olson. Modeling the Lac repressoroperator assembly: the influence of DNA looping on Lac repressor conformation. *Proceedings of the National Academy of Science USA*, 103:9879–84, 2006.

[75] P. K. Purohit and P. C. Nelson. Effect of supercoiling on formation of protein-mediated DNA loops. *Phsyical Review E*, 74:061907–1–14, 2006.

[76] P. C. Nelson, C. Zurla, D. Brogioli, J. F. Beausang, L. Finzi, and D. Dunlap. Tethered particle motion as a diagnostic of DNA tether length. *Journal of Physical Chemistry B*, 110(34):17260–17267, 2006.

[77] D. E. Segall, P. C. Nelson, and R. Phillips. Volume-exclusion effects in tethered-particle experiments: Bead size matters. *Physical Review Letters*, 96(8):088306–(1–4), 2006.

[78] H. Qian and E. L. Elson. Quantitative study of polymer conformation and dynamics by single-particle tracking. *Biophysical Journal*, 76(3):1598–605, 1999.

[79] O.K. Wong, M. Guthold, D. A. Erie, and J. Gelles. Interconvertible lac repressor-DNA loops revealed by single-molecule experiments. *PLoS Biology*, 6(9):e232, 2008.

[80] D. A. Schafer, J. Gelles, M. P. Sheetz, and R. Landick. Transcription by single molecules of RNA–polymerase observed by light-microscopy. *Nature*, 352(6334):444–8, 1991.

[81] F. Vanzi, C. Broggio, L. Sacconi, and F. S. Pavone. Lac repressor hinge flexibility and DNA looping: single molecule kinetics by tethered particle motion. *Nucleic Acids Research*, 34(12):3409–20, 2006.

[82] M. Lewis, G. Chang, N. C. Horton, M. A. Kercher, H. C. Pace, M. A. Schumacher, R. G. Brennan, and P. Lu. Crystal structure of the lactose operon repressor and its complexes with DNA and inducer. *Science*, 271:1247–54, 1996.

[83] F. Vanzi, S. Vladimirov, C. R. Knudsen, Y. E. Goldman, and B. S. Cooperman. Protein synthesis by single ribosomes. *RNA*, 9:1174–9, 2003.

[84] B. van den Broek, F. Vanzi, D. Normanno, F. S. Pavone, and G. J. L. Wuite. Real-time observation of DNA looping dynamics of type IIE restriction enzymes NaeI and NarI. *Nucleic Acids Research*, 34(1):167–74, 2006.

[85] S. Blumberg, A. Gajraj, M. W. Pennington, and J. C. Meiners. Three-dimensional characterization of tethered microspheres by total internal reflection fluorescence microscopy. *Biophysical Journal*, 89(2):1272–81, 2005.

[86] J. F. Beausang, C. Zurla, C. Manzo, D. Dunlap, L. Finzi, and P. C. Nelson. DNA looping kinetics analyzed using diffusive hidden Markov model. *Biophysical Journal*, 92:L64–L66, 2007.

[87] D. Colquhoun and F. J. Sigworth. Fitting and statistical analysis of single-channel records. In B. Sakmann and E. Neher, editors, *Single-Channel Recording*, pages 191–263. Plenum, New York, 1983.

[88] P. R. Bevington and D. K. Robinson. *Data reduction and error analysis for the physical sciences*. McGraw–Hill, Boston, 3rd edition, 2003.

[89] D. A. Smith, W. Steffen, R. M. Simmons, and J. Sleep. Hidden-Markov methods for the analysis of single-molecule actomyosin displacement: The variance-hidden-Markov method". *Biophysical Journal*, 81:2795–2816, 2001.

[90] L. E. Baum and T. Petrie. Statistical inference for probabilistic functions of finite state Markov chains. *Annals of Mathematical Statistics*, 37:1554–63, 1966.

[91] L. R. Rabiner. A tutorial on hidden Markov-models and selected applications in speech recognition. *Proceedings of the IEEE*, 77(2):257–86, 1989.

[92] F. Qin, A. Auerbach, and F. Sachs. A direct optimization approach to hidden Markov modeling for single channel kinetics. *Biophysical Journal*, 79(4):1915–27, 2000.

[93] F. Qin, A. Auerbach, and F. Sachs. Hidden Markov modeling for single channel kinetics with filtering and correlated noise. *Biophysical Journal*, 79(4):1928–44, 2000.

[94] L. S. Milescu, A. Yildiz, P. R. Selvin, and F. Sachs. Maximum likelihood estimation of molecular motor kinetics from staircase dwell-time sequences. *Biophysical Journal*, 91(4):1156–68, 2006.

[95] L. S. Milescu, A. Yildiz, P. R. Selvin, and F. Sachs. Extracting dwell time sequences from processive molecular motor data. *Biophysical Journal*, 91(9):3135–50, 2006.

[96] S. A. McKinney, C. Joo, and T. Ha. Analysis of single-molecule FRET trajectories using hidden Markov modeling. *Biophysical Journal*, 91(5):1941–51, 2006.

[97] J. F. Beausang, C. Zurla, L. Finzi, L. Sullivan, and P. C. Nelson. Elementary simulation of tethered Brownian motion. *American Journal of Physics*, 75:520–23, 2007.

[98] A. R. Dunn and J. A. Spudich. Dynamics of the unbound head during myosin V processive translocation. *Nature Structural and Molecular Biology*, 14(3):246–9, 2007.

[99] W. H. Press, B. P. Flannery, S. A. Teukolsky, and W. T. Vetterling. *Numerical Recipes in C*. Cambridge University Press, Cambridge, 2nd edition, 1992.

[100] L. P. Watkins and H. Yang. Detection of intensity change points in time-resolved single-molecule measurements. *The Journal of Physical Chemistry B*, 109(1):617–28, 2005.

[101] N. Laurens, S. R. Bellamy, A. F. Harms, Y. S. Kovacheva, S. E. Halford, and G. J. Wuite. Dissecting protein-induced DNA looping dynamics in real time. *Nucleic Acids Research*, 37(16):5454–64, 2009.

[102] I. Rayment, H. M. Holden, M. Whittaker, C. B. Yohn, M. Lorenz, K. C. Holmes, and R. A. Milligan. Structure of the actin-myosin complex and its implications for muscle contraction. *Science*, 261(5117):58–65, 1993.

[103] R. Cooke. Actomyosin interaction in striated muscle. *Physiology Review*, 77(3):671–97, 1997.

[104] M. A. Geeves and K. C. Holmes. The molecular mechanism of muscle contraction. *Advances in Protein Chemistry*, 71:161–93, 2005.

[105] D. M. Warshaw. Lever arms and necks: A common mechanistic theme across the myosin superfamily. *Journal Muscle Research and Cell Motility*, 25(6):467–74, 2004.

[106] I. Dobbie, M. Linari, G. Piazzesi, M. Reconditi, N. Koubassova, M. A. Ferenczi, V. Lombardi, and M. Irving. Elastic bending and active tilting of myosin heads during muscle contraction. *Nature*, 396(6709):383–7, 1998.

[107] J. M. Gillis and E. J. O'Brien. The effect of calcium ions on the structure of reconstituted muscle thin filaments. *Journal of Molecular Biology*, 99(3):445–59, 1975.

[108] Y. Maeda, I. Matsubara, and N. Yagi. Structural changes in thin filaments of crab striated muscle. *Journal of Molecular Biology*, 127:191–201, 1979.

[109] S. Syed, G. E. Snyder, C. Franzini-Armstrong, P. R. Selvin, and Y. E. Goldman. Adaptability of myosin V studied by simultaneous detection of position and orientation. *Embo Journal*, 25(9):1795–803, 2006.

[110] J. L. Ross, M. Y. Ali, and D. M. Warshaw. Cargo transport: Molecular motors navigate a coplex cytoskeleton. *Currrent Opinion in Cell Biology*, 20:41–7, 2008.

[111] E. Toprak, J. Enderlein, S. Syed, S. A. McKinney, R. G. Petschek, T. Ha, Y. E. Goldman, and P. R. Selvin. Defocused orientation and position imaging (DOPI) of myosin V. *Proceedings of the National Academy Science USA*, 103(17):6495–6499, 2006.

[112] I. Matsubara, Y. E. Goldman, and R. M. Simmons. Changes in the lateral filament spacing of skinned muscle fibres when cross-bridges attach. *Journal of Molecular Biology*, 173(1):15–33, 1984.

[113] T. Nishizaka, T. Yagi, Y. Tanaka, and S. Ishiwata. Right-handed rotation of an actin filament in an in vitro motile system. *Nature*, 361(6409):269–71, 1993.

[114] N. Suzuki, H. Miyata, S. Ishiwata, and K. Kinosita Jr. Preparation of bead-tailed actin filaments: estimation of the torque produced by the sliding force in an in vitro motility assay. *Biophysical Journal*, 70(1):401–8, 1996.

[115] M. Y. Ali, S. Uemura, K. Adachi, H. Itoh, K. Kinosita Jr., and S. Ishiwata. Myosin V is a left-handed spiral motor on the right-handed actin helix. *Nature Structal Biology*, 9(6):464–7, 2002.

[116] M. Y. Ali, K. Homma, A. H. Iwane, K. Adachi, H. Itoh, Jr. K. Kinosita, T. Yanagida, and M. Ikebe. Unconstrained steps of myosin VI appear longest among known molecular motors. *Biophyiscal Journal*, 86(6):3804–10, 2004.

[117] M. Prummer, B. Sick, B. Hecht, and U. P. Wild. Three-dimensional optical polarization tomography of single molecules. *Journal of Chemical Physics*, 118(21):9824–9, 2003.

[118] S. S. Margossian and S. Lowey. Preparation of myosin and its subfragments from rabbit skeletal-muscle. *Methods in Enzymology*, 85:55–71, 1982.

[119] J. A. Spudich and S. Watt. Regulation of rabbit skeletal muscle contraction: 1. biochemical studies of interaction of tropomyosin-troponin complex with actin and proteolytic fragments of myosin. *Journal of Biological Chemistry*, 246(15):4866–71, 1971.

[120] J. E. Corrie and J. S. Craik. Synthesis and characterization of pure isomers of iodoacetamido-tetramethylrhodamine. *Journal of Chemical Society Perkin Transactions 1*, pages 2967–74, 1994.

[121] W. S. Rasband. *ImageJ, http://rsb.info.nih.gov/ij*. U.S. National Institutes of Health, Bethesda, 2007.

[122] T. Q. P. Uyeda, S. J. Kron, and J. A. Spudich. Myosin step size. estimation from slow sliding movement of actin over low densities of heavy meromyosin. *Journal of Molecular Biology*, 214(3):699–710, 1990.

[123] J. F. Beausang, H. W. Schroeder 3rd, P. C. Nelson, and Y. E. Goldman. Twirling of actin by myosins II and V observed via polarized TIRF in a modified gliding assay. *Biophysical Journal*, 95(12):5820–31, 2008.

[124] Y. Sun, H. W. Schroeder 3rd, J. F. Beausang, K. Homma, M. Ikebe, and Y. E. Goldman. Myosin VI walks "wiggly" on actin with large and variable tilting. *Molecular Cell*, 28(6):954–64, 2007.

[125] R. Dominguez, Y. Freyzon, K. M. Trybus, and C. Cohen. Crystal structure of a vertebrate smooth muscle myosin motor domain and its complex with the essential light chain: Visualization of the pre-power stroke state. *Cell*, 94(5):559–71, 1998.

[126] I. Rayment, W. R. Rypniewski, K. Schmidt-Bäse, R. Smith, D. R. Tomchick, M. M. Benning, D. A. Winkelmann, G. Wesenberg, and H. M. Holden. Three-dimensional structure of myosin subfragment-1: A molecular motor. *Science*, 261(5117):50–8, 1993.

[127] M. L. Walker, S. A. Burgess, J. R. Sellers, F. Wang, J. A. Hammer, J. Trinick, and P. J. Knight. Two-headed binding of a processive myosin to F-actin. *Nature*, 405(6788):804, 2000.

[128] A. Vilfan. Influence of fluctuations in actin structure on myosin V step size. *Journal of Chemical Information and Modeling*, 45(6):1672–5, 2005.

[129] N. Yagi and I.Matsubara. Structural changes in the thin filament during activation studied by X-ray diffraction of highly stretched skeletal muscle. *Journal of Molecular Biology*, 208:359–63, 1989.

[130] A. Yildiz, H. Park, D. Safer, Z. Yang, L.-Q. Chen, P. R. Selvin, and H. L. Sweeney. Myosin VI steps via a hand-over-hand mechanism with its lever arm undergoing fluctuations when attached to actin. *Journal of Biological Chemistry*, 279:37223–6, 2004.

[131] Vilfan A. Twirling motion of actin filaments in gliding assays with nonprocessive myosin motors. *Biophysical Journal*, 97(4):1130–7, 2009.

[132] K. A. Taylor, M. C. Reedy, L. Cordóva, and M. K. Reedy. Three-dimensional reconstruction of rigor insect flight muscle from tilted thin sections. *Nature*, 310:285–91, 1984.

[133] S. C. Hopkins, C. Sabido-David, U. A. van der Heide, R. E. Ferguson, B. D. Brandmeier, R. E. Dale, J. Kendrick-Jones, J. E. T. Corrie, D. R. Trentham, M. Irving, and Y. E. Goldman. Orientation changes of the myosin light chain domain during filament sliding in active and rigor muscle. *Journal of Molecular Biology*, 18(5):1275–91, 2002.

[134] L. P. Watkins and H. Yang. Quantitative single-molecule conformational distributions: a case study with poly-(L-proline). *The Journal of Physical Chemistry A*, 110(15):5191–203, 2006.

[135] C.S. Xu, H. Kim, C.C. Hayden, and H. Yang. Joint statistical analysis of multichannel time series from single quantum dot-(Cy5)n constructs. *The Journal of Physical Chemistry. B*, 112(19):5917–23, 2008.

[136] B. C. Carter, M. Vershinin, and S. P. Gross. A comparison of step-detection methods: How well can you do? *Biophysical Journal*, 94(1):306–19, 2008.

[137] J. W. J. Kerssemakers, E. L. Munteanu, L. Laan, T. L. Noetzel, M. E. Janson, and M. Dogterom. Assembly dynamics of microtubules at molecular resolution. *Nature*, 442:709–12, 2006.

[138] M. Andrec, R. M. Levy, and D. S. Talaga. Direct determination of kinetic rates from single-molecule photon arrival trajectories using hidden Markov models. *Journal of Physical Chemistry A*, 107(38):7454–64, 2003.

[139] D. S. Talaga. Information theoretical approach to single-molecule experimental design and interpretation. *Journal of Physical Chemistry A*, 110:9743–57, 2006.

[140] A.W.F. Edwards. *Likelihood*. Cambridge University Press, London, 1st edition, 1972.

[141] M. Noé. The calculation of distributions of two-sided Kolmogorov-Smirnov type statistics. *The Annals of Mathematical Statistics*, 43(1):58–64, 1972.

[142] K.J. Worsley. Percentage points of the likelihood-ratio test for a change-point hazard-rate model. *Biometrics*, 44(1):259–63, 1988.

[143] R. Henderson. A problem with the likelihood ratio test for a change-point hazard rate model. *Biometrika*, 77(4):835–43, 1990.

[144] T. Sakamoto, M. R. Webb, E. Forgacs, H. D. White, and J. R. Sellers. Direct observation of the mechanochemical coupling in myosin Va during processive movement. *Nature*, 455(7209):128–32, 2008.

[145] E. Bertrand, P. Chartrand, M. Schaefer, S. M. Shenoy, R. H. Singer, and R. M. Long. Localization of ASH1 mRNA particles in living yeast. *Molecular Cell*, 2(4):437–45, 1998.

[146] X. Wu, B. Bowers, K. Rao, Q. Wei, and J. A. Hammer 3rd. Visualization of melanosome dynamics within wild-type and dilute melanocytes suggests a paradigm for myosin V function in vivo. *Journal of Cell Biology*, 143(7):1899–918, 1998.

[147] S. L. Reck-Peterson, D. W. Provance Jr., M. S. Mooseker, and J. A. Mercer. Class V myosins. *Biochimica et biophysica acta*, 1496(1):36–51, 2000.

[148] A. K. Satoh, B. X. Li, H. Xia, and D. F. Ready. Calcium-activated myosin V closes the Drosophila pupil. *Current Biology*, 18(13):951–1, 2008.

[149] S. Woolner and W. M. Bement. Unconventional myosins acting unconventionally. *Trends in Cell Biology*, 19(6):245–52, 2009.

[150] D. W. Provance Jr., M. Wei, V. Ipe, and J. A. Mercer. Cultured melanocytes from dilute mutant mice exhibit dendritic morphology and altered melanosome distribution. *Proceedings of the National Academy of Sciences of the USA*, 93(25):14554–8, 1996.

[151] R. E. Larson, D. E. Pitta, and J. A. Ferro. A novel 190 kDa calmodulin-binding protein associated with brain actomyosin. *Brazilian Journal of Medical and Biological Research*, 21(2):213–7, 1988.

[152] R. E. Cheney, M. K. O'Shea, J. E. Heuser, M. V. Coelho, J. S. Wolenski, E. M. Espreafico, P. Forscher, R. E. Larson, and M. S. Mooseker. Brain myosin V is a two-headed unconventional myosin with motor activity. *Cell*, 75(1):13–23, 1993.

[153] K. A. Taylor. Regulation and recycling of myosin V. *Current Opinion in Cell Biology*, 19(1):67–74, 2007.

[154] K. M. Trybus. Myosin V from head to tail. *Cellular and Molecular Life Sciences*, 65(9):1378–89, 2008.

[155] R. D. Vale and R. A. Milligan. The way things move: Looking under the hood of molecular motor proteins. *Science*, 288:88–95, 2000.

[156] E. M. De La Cruz, A. L. Wells, S. S. Rosenfeld, E. M. Ostap, and H. L. Sweeney. The kinetic mechanism of myosin V. *Proceedings of the National Academy of Sciences of the USA*, 96(24):13726–31, 1999.

[157] S. Burgess, M. Walker, F. Wang, J. R. Sellers, H. D. White, P. J. Knight, and J. Trinick. The prepower stroke conformation of myosin V. *Journal of Cell Biology*, 159(6):983–91, 2002.

[158] O. A. Oke, S. A. Burgess, E. Forgacs, P. J. Knight, T. Sakamoto, J. R. Sellers, H. White, and J. Trinick. Influence of lever structure on myosin 5a walking. *Proceedings of the National Academy of Sciences of the USA*, 2010.

[159] T. Sakamoto, I. Amitani, E. Yokota, and T. Ando. Direct observation of processive movement by individual myosin V molecules. *Biochemical and Biophysical Research Communications*, 272(2):586–90, 2000.

[160] K. Shiroguchi and K. Kinosita Jr. Myosin V walks by lever action and Brownian motion. *Science*, 316(5828):1208–12, 2007.

[161] A. O. Olivares and E. M. De La Cruz. Holding the reins on myosin V. *Proceedings of the National Academy of Sciences of the USA*, 102(39):13710–20, 2006.

[162] J. R. Sellers and C. Veigel. Walking with myosin V. *Current Opinion in Cell Biology*, 18(1):68–73, 2006.

[163] J. E. Baker, E. B. Krementsova, G. G. Kennedy, A. Armstrong, K. M. Trybus, and D. M. Warshaw. Myosin V processivity: Multiple kinetic pathways for head-to-head coordination. *Proceedings of the National Academy of Sciences of the USA*, 101(15):5542–6, 2004.

[164] P. D. Coureux, H. L. Sweeney, and A. Houdusse. Three myosin V structures delineate essential features of chemo-mechanical transduction. *EMBO*, 23:4527–37, 2003.

[165] C. Veigel, S. Schmitz, F. Wang, and J. R. Sellers. Load-dependent kinetics of myosin V can explain its high processivity. *Nature Cell Biology*, 7(9):861–9, 2005.

[166] S. S. Rosenfeld and H. L. Sweeney. A model of myosin V processivity. *The Journal of Biological Chemistry*, 279(39):401000–11, 2004.

[167] A. Vilfan. Elastic lever-arm model for myosin V. *Biophsyical Journal*, 88:3792–805, 2005.

[168] Y. Oguchi, S. V. Mikhailenko, T. Ohki, A. O. Olivares, E. M. De La Cruz, and S. Ishiwata. Load-dependent ADP binding to myosins V and VI: Implications for subunit coordination and function. *Proceedings of the National Academy of Sciences of the USA*, 105(22):7714–9, 2008.

[169] K. Kinosita Jr., M. Y. Ali, K. Adachi, K. Shiroguchi, and H. Itoh. How two-foot molecular motors may walk. *Advances in Experimental Medicine and Biology*, 565:205–18, 2005.

[170] C. Veigel, F. Wang, M. L. Bartoo, J. R. Sellers, and J. E. Molloy. The gated gait of the processive molecular motor, myosin V. *Nature Cell Biology*, 4(1):59–65, 2002.

[171] S. Uemura, H. Higuchi, A. O. Olivares, E. M. De La Cruz, and S. Ishiwata. Mechanochemical coupling of two substeps in a single myosin V motor. *Nature Structural and Molecular Biology*, 11(9):877–83, 2004.

[172] E. M. Ostap. 2,3-Butanedione monoxime (BDM) as a myosin inhibitor. *Journal of Muscle Research and Cell Motility*, 23:305–8, 2002.

[173] G. Cappello, P. Pierobon, C. Symonds, L. Busoni, J. C. Gebhardt, M. Rief, and J. Prost. Myosin V stepping mechanism. *Proceedings of the National Academy of Sciences of the USA*, 104(39):15328–33, 2007.

[174] D. A. Smith. How processive is the myosin V motor? *Journal of Muscle Research and Cell Motility*, 25(3):215–7, 2004.

[175] E. M. Craig and H. Linke. Mechanochemical model for myosin V. *Proceedings of the National Academy of Sciences of the USA*, 106(43):18261–6, 2009.

[176] S. Rice, A. W. Lin, D. Safer, C. L. Hart, N. Naber, B. O. Carragher, S. M. Cain, E. Pechatnikova, E. M. Wilson-Kubalek, M. Whittaker, E. Pate, R. Cooke, E. W. Taylor, R. A. Milligan, and R. D. Vale. A structural change in the kinesin motor protein that drives motility. *Nature*, 402(6763):778–84, 1999.

[177] A. B. Asenjo and H. Sosa. A mobile kinesin-head intermediate during the ATP-waiting state. *Proceedings of the National Academy of Sciences of the USA*, 106(14):5657–62, 2009.

[178] N. R. Guydosh and S. M. Block. Direct observation of the binding state of the kinesin head to the microtubule. *Nature*, 461(7260):125–8, 2010.

[179] X. Nan, P. A. Sims, and X. S. Xie. Organelle tracking in a living cell with microsecond time resolution and nanometer spatial precision. *Chemphyschem*, 9(5):707–12, 2008.

[180] R. Rigler. Fluorescence and single molecule analysis in cell biology. *Biochemical and Biophysical Research Communications*, 396(1):170–5, 2010.

[181] H. Yang and X. S. Xie. Probing single-molecule dynamics photon by photon. *Journal of chemical physics*, 117(24):10965–79, 2002.

[182] Y. W. Tan, J. A. Hanson, and H. Yang. Direct Mg(2+) binding activates adenylate kinase from Escherichia coli. *Journal of Biological Chemistry*, 284(5):3306–13, 2009.

[183] S. Verbrugge, S. M. van den Wildenberg, and E. J. Peterman. Kinesin's step dissected with single-motor FRET. *Proceedings of the National Academy of Sciences of the USA*, 106(42):17741–6, 2009.

[184] J. A. Levitt, D. R. Matthews, S. M. Ameer-Beg, and K. Suhling. Fluorescence lifetime and polarization-resolved imaging in cell biology. *Current Opinion in Biotechnology*, 20(1):28–36, 2009.

[185] W. Becker. *The bh TCSPC handbook*. Becker and Hickl GmbH, Berlin, 2008.

[186] M. El Mezgueldi, N. Tang, S. S. Rosenfeld, and E. M. Ostap. The kinetic mechanism of Myo1e (human myosin-Ic). *Journal of Biological Chemsitry*, 277(24):21514–21, 2002.

[187] K. Homma, J. Saito, R. Ikebe, and M. Ikebe. Ca(2+)-dependent regulation of the motor activity of myosin V. *Journal of Biological Chemistry*, 275(44):34766–71, 2000.

[188] P. M. Chaikin and T. C. Lubensky. *Principles of condensed matter physics*. Cambridge University Press, Cambridge, 1995.

[189] A. Houdusse, J. F. Gaucher, E. Krementsova, S. Mui, K. M. Trybus, and C. Cohen. Crystal structure of apo-calmodulin bound to the first two IQ motifs of myosin V reveals essential recognition features. *Proceedings of the National Academy of Sciences of the USA*, 103(51):19326–31, 2006.

[190] J. G. Reifenberger, E. Toprak, H. Kim, D. Safer, H. L. Sweeney, and P. R. Selvin. Myosin VI undergoes a 180 degrees power stroke implying an uncoupling of the front lever arm. *Proceedings of the National Academy of Sciences of the USA*, 106(43):18255–60, 2009.

[191] J. A. Hanson, K. Duderstadt, L. P. Watkins, S. Bhattacharyya, J. Brokaw, J. W. Chu, and H. Yang. Illuminating the mechanistic roles of enzyme conformational dynamics. *Proceedings of the National Academy of Sciences of the USA*, 104(46):18055–60, 2007.

[192] M. E. Arsenault, Y. Sun, H. H. Bau, and Y. E. Goldman. Using electrical and optical tweezers to facilitate studies of molecular motors. *Physical Chemisty and Chemical Physics*, 11(24):4834–9, 2009.

[193] Y. Sun, O. Sato, F. Ruhnow, M. E. Arsenault, M. Ikebe, and Y. E. Goldman. Single-molecule stepping and structural dynamics of myosin X. *Nature Structural and Molecular Biology*, 17(4):485–91, 2010.

[194] P. D. Coureux, A. L. Wells, J. Ménétrey, C. M. Yengo, C. A. Morris, H. L. Sweeney, and A. Houdusse. A structural state of the myosin V motor without bound nucleotide. *Nature*, 425(6956):419–23, 2003.

[195] H. Nguyen and H. Higuchi. Motility of myosin V regulated by the dissociation of single calmodulin. *Nature Structural and Molecular Biology*, 12(2):127–32, 2005.

# Glossary

**ADC**                 Analog to digital converter

**AFM**                Atomic Force Microscope,

**APD**                 Avalanche photodiode


**BDM**                2,3-butanedione monoxime, a myosin inhibitor

**BR-CaM**          Bifunctional rhodamine labeled calmodulin


**CaM**                Calmodulin

**CCD**                Charge coupled device

**CFD**                Constant fraction discriminator

**cI**                    *lambda* repressor protein


**DHMM**            Diffusive hidden Markov method


**FCS**                 Fluorescence Correlation Spectroscopy,

| | |
|---|---|
| **FIFO** | First in-First out mode for operating the TCSPC circuit |
| **FIONA** | Fluorescence imaging at one nanometer accuracy |
| **FLAG** | Polypeptide sequence DYKDDDDK used in protein purification |
| **FLIM** | Fluorescence lifetime imaging |
| **FPLC** | fast protein liquid chromatography |
| **FRET** | Förster resonance energy transfer |
| **GFP** | Green Fluorescent Protein |
| **HMM** | Hidden Markov method, or Heavy meromysoin depending on the context |
| **IQ motif** | A short peptide sequence that binds calmodulin that sometimes begins with an Isoleucine(I) and Glutamine(Q) |
| **M5B** | Myosin V buffer |
| **MICP** | Multiple intensity change point |

| | |
|---|---|
| **NSOM** | Near-Field Scanning Optical Microscopy, |
| **pdf** | probability distribution function |
| **PEG** | polyethylene glycol, |
| **PFI** | Polarized fluorescence intensity |
| **polTIRF** | Polarized total internal reflection fluorescence microscopy |
| **SBR** | Signal to background ratio |
| **SPC** | Single photon counting |
| **TAC** | Time-to-amplitude converter |
| **TCSPC** | Time-correlated single photon counting |
| **TEV protease site** | Sequence from the Tobacco etch virus used to cleave off portions of a protein after it has been expressed. |
| **TIR** | Total Internal Reflection, |
| **TIRF** | Total internal reflection fluorescence microscopy |
| **TPM** | Tethered particle method |
| **WT-CaM** | Wild-type calmodulin |